R-1406
CU- 376
NEVIS- 270

Nevis Laboratories
Columbia University
Physics Department
Irvington, NY

NUCLEON STRUCTURE FUNCTIONS FROM HIGH ENERGY NEUTRINO AND ANTINEUTRINO INTERACTIONS IN IRON

Edward Oltman

Reproduction in whole or in part
is permitted for any purpose by the
United States Government.

Submitted in partial fulfillment of
the requirements for the degree
of Doctor of Philosophy in the
Graduate School of Arts and Sciences,
Columbia University

1989

National Science Foundation
NSF PHY 86-10898

AA01884

NUCLEON STRUCTURE FUNCTIONS FROM HIGH ENERGY NEUTRINO AND ANTINEUTRINO INTERACTIONS IN IRON*†

Edward Oltman
Columbia University, New York, NY

*Research supported by the National Science Foundation.
†Submitted in partial fulfillment of the requirement for the degree of Doctor of Philosophy in the Graduate School of Arts and Sciences, Columbia University.

Abstract

Charged current nucleon structure functions obtained from high energy neutrino and antineutrino interactions in iron are presented. These were extracted from two separate exposures using the Fermilab narrow band beam. The structure functions were used to test the validity of two Quark Parton Model predictions: (1) F_2 measurements from this analysis were compared to those from charged lepton scattering experiments, indicating that both probes reveal the same nucleon structure. (2) The Gross–Llewellyn Smith sum rule, which measures the valance quark content of the nucleon, was evaluated at $Q^2 = 3$ (GeV/c)^2, yielding the value $2.79 \pm 0.08 \pm 0.13$ which lies below the Quark Parton Model prediction of three. When perturbative QCD corrections to this prediction are included, the measurement is consistent with a value of the QCD scale parameter $\Lambda_{\overline{MS}} < 435$ MeV/c. Scaling violations were analysed in the context of perturbative QCD through the Altarelli–Parisi evolution equations. A nonsinglet fit to xF_3, which is independent of the unmeasured gluon density, yielded $\Lambda_{\overline{MS}} = 251^{+134}_{-115} \pm 89$ MeV/c. A singlet analysis of F_2, which does depend on the gluon density, yielded $\Lambda_{\overline{MS}} = 255^{+73}_{-63} \pm 101$ MeV/c. By simultaneously evolving F_2 and xF_3, this error was reduced by about 30% and the shape of the gluon density was significantly constrained by the difference $F_2 - xF_3$ which measures the virtual $q\bar{q}$ content of the nucleon.

FERMILAB
LIBRARY

Acknowledgements

I take pleasure in acknowledging the contributions of the many people who made this dissertation possible. First I would like to thank the members of the CCFR collaboration: Priscilla Auchincloss, Bob Blair, Carl Haber, Sanjib Mishra, Martin Ruiz, Frank Sciulli, Mike Shaevitz, Wesley Smith and Runsheng Zhu from Columbia University; Dave Garfinkle, Frank Merritt, Mark Oreglia and Pat Reutens from the University of Chicago; Rick Coleman, Gene Fisk, Binyang Jin, Taka Kondo, Dave Levinthal, Bill Marsh, Petros Rapidis, Herman White and Drasko Yovanovitch from Fermi National Accelerator Laboratory; and Arie Bodek, Fred Borcherding, Nikos Giokaris, Karol Lang and Ian Stockdale from the University of Rochester. I would also like to thank the past collaborators, in particular Dave MacFarlane and Milind Purohit. They have made tremendous contributions to my understanding of neutrino physics.

I would like to thank my advisor, Frank Sciulli, for his patience, understanding and wisdom. I have benefited greatly, not only from his knowledge and style, but from his trust.

Wesley Smith, Mike Shaevitz and Bob Blair deserve special thanks for their generous help and guidance throughout my long stay at Nevis. My "fellow" graduate students provided me with stimulation and friendship. Carl, Priscilla and Sanjib

made many contributions to my analysis.

Finally, I would like to thank the Nevis staff for their assistance over the years.

I dedicate this thesis to my parents.

1 Introduction **1**

1.1 Overview 1

1.2 Theory 3

1.2.1 A Brief History 3

1.2.2 Cross Section Formalism 6

1.2.3 Structure Functions in the Parton Model 10

1.2.4 Quark Parton Model Formalism 14

1.2.5 Strong Interactions 19

2 The Neutrino Source **27**

2.1 Introduction 27

2.2 The Primary Beam 29

2.3 The Secondary Beam 30

2.4 Secondary Beam Monitoring 31

2.5 The Neutrinos 34

2.5.1 Dichromatic Monte Carlo 35

2.5.2 Wideband Neutrinos 38

3 The Lab E Detector **40**

3.1 General Requirements 40

3.2 Overview of Detector 41

3.3 The Muon Tracking System 42

3.4 Scintillation Counters 44

3.4.1 The Calorimetry Counters 45

3.4.2 The Trigger Counters 46

3.5 Triggering 46

3.6 Data Acquisition 48

4 Event Analysis **50**

4.1 Introduction 50

4.2 Muon Reconstruction 51

4.2.1 The Target Track: θ_μ, v_x, v_y 51

4.2.2 Momentum Fitting in the Toroid 53

4.2.3 Muon Energy Losses 56

4.3 Hadron Energy Determination 57

4.3.1 Muon Peaks 57

4.3.2 Gain Drifts 58

4.3.3 Counter Maps 59

4.3.4 Longitudinal Extent of Hadron Shower 60

4.4 Energy Calibrations 61

4.5 Structure Function Analysis 64

5 Structure Function Extraction **68**

5.1 Overview 68

5.2 Differential Cross Sections: Experimental Corrections 70

5.2.1 The Event Monte Carlo 72

5.2.2 Relative Flux Determination 76

5.3 Differential Cross Sections: Model Corrections 78

5.4 Statistical Errors 82

5.5 Systematic Errors 83

6 Comparisons and Conclusions **85**

6.1 Comparisons With Other Neutrino Experiments 86

6.2 Quark Parton Model Tests 94

6.2.1 Mean Squared Charge Test 95

6.2.2 Gross–Llewellyn Smith Sum Rule 97

6.3 Scaling Violations 101

6.3.1 Fitting Procedure 102

6.3.2 Nonsinglet Fit Results 105

6.3.3 Singlet Fit Results 108

6.3.4 Comparisons With Other Analyses 113

6.4 Conclusions 114

A Absolute Flux Normalizations **116**

A.1 Overview 116

A.2 Event Analysis 119

A.3 y–Distribution Analysis 121

B Parton Parametrizations **125**

B.1 Valence Densities 126

B.2 Sea Densities 127

B.3 R 129

B.4 Fitting Procedure 129

C Physical Differential Cross Section Model **131**

C.1 Flavor Asymmetries 131

C.2 Charm Production Threshold 133

C.3 Radiative Effects 136

D CCFR Collaboration **137**

References **138**

List of Tables **144**

List of Figures **147**

Tables **158**

Figures **177**

Chapter 1

Introduction

1.1 Overview

This thesis is concerned with the inelastic charged current reactions

$$\nu_\mu(\overline{\nu}_\mu) + N \rightarrow \mu^-(\mu^+) + X \tag{1.1}$$

measured with high energy beams of neutrinos and antineutrinos on an iron target. Here, N refers to the (almost) isoscalar or "nucleon" target and X refers to the inclusive hadronic final state. Figure 1.1 depicts the reaction as occurring through the exchange of a single virtual $W^\pm$ between the leptonic (ν–μ) and hadronic (N–X) currents. The use of high energy neutrino beams (more generally, lepton beams) offers an attractive means for probing nucleon structure: (i) The properties of the lepton vertex are well understood in terms of the V–A interaction [1] (V in the case of charged lepton probes) and (ii) Dominance of the single particle exchange mechanism is guaranteed by the small ν–W coupling constant (or ℓ–γ coupling, in the case of

charged lepton scattering). Combining these properties with Lorentz invariance allows the experimentally accessible cross sections, depending on three invariants, e.g. $p \cdot k_1$, $p \cdot q$ and q^2 (Figure 1.1), to be expressed in terms of *structure functions*, which depend only on the two invariant quantities needed to specify the hadronic vertex ($p \cdot q$ and q^2). Our present understanding of the nucleon's constituent nature (parton content) and the dynamics governing the constituent interactions (QCD) is largely based on studies of deep inelastic structure functions.

Measurements of structure functions are presented from the combined data of Fermilab experiments E616 and E701 using the dichromatic (narrow band) beam. The neutrino source and flux analysis is discussed in Chapter 2. Approximately 250K neutrino and 30K antineutrino induced events were measured and recorded by the Lab E target/detector (Chapter 3). Of these, approximately 90K ν and 10K $\overline{\nu}$ events surviving fiducial, reconstruction and kinematic cuts were used in the structure function analysis. Reconstruction of the final state muon's angle and momentum and the hadronic energy, sufficient quantities for specifying the inclusive reaction of Equation 1.1, are presented in Chapter 4. Measured event sums were then combined with the calculated fluxes to form differential cross sections. In Chapter 5, the technique used to correct the cross sections and extract structure functions is presented. F_2 and xF_3 were extracted with an assumed parametrization of $R = \sigma_L/\sigma_T$ predicted by QCD. The concluding chapter contains comparisons with other experiments and comparisons with Quark Parton Model predictions and QCD.

1.2 Theory

Figure 1.2 shows the kinematic plane describing the hadronic vertex. $Q^2 = -q^2$ is the magnitude of the 4–momentum transfer squared, ν is the energy transfer in the lab frame and M is the nucleon mass ($p \cdot q = 2M\nu$). Elastic scattering off the nucleon occurs at $Q^2 = 2M\nu$, where the invariant mass of the final state is $W^2 = M^2$ and is shown as the solid line labeled $x = 1$. The resonance region ($X = \Delta(1238), N(1450), \Delta(1688)\ldots$) occurs for $W^2 = M^2 + 2M\nu - Q^2$ less then a few GeV^2 and is shown as dotted lines. The measurements and analysis presented in this thesis correspond to the large (Q^2,ν) area on the right, referred to as the deep inelastic region. Before going into the significance of this region, a brief historical digression on the subject of electron scattering is presented.

1.2.1 A Brief History

Early elastic scattering experiments [2] using 400 to 600 MeV electrons on nuclear targets (A) measured cross sections which deviated from those expected from a structureless target. These deviations were parametrized in terms of nuclear form factors, $F_A(Q^2)$ which for small energy transfers, ν, correspond to the Fourier Transforms of nuclear charge densities. At higher energies and correspondingly higher values of Q^2, these nuclear form factors suppressed the elastic e^-–nucleus cross sections as well as the nuclear excitations observed in the recoil spectrum for $\nu > Q^2/2M_A$. $|F_A(Q^2)|^2$ is a measure of the probability that the nucleus (or its excited states) will recoil *coher-*

ently. However, a broad quasi–elastic structure visible in the recoil spectrum below the elastic and resonance peaks (larger ν) was observed to persist with increasing q^2. This corresponded to *incoherent* elastic electron scattering off the nuclear constituents – individual nucleons, its broad shape arising from the Fermi motion of nucleons in the nucleus. Higher energy (400 MeV to 16 GeV) elastic electron scattering measurements [3] using hydrogen targets indicated, through the deviations of cross sections expected from a pointlike proton, the emergence of nucleon structure. Nucleon form factors[1], as in the case of nuclear scattering, suppressed the elastic and resonance peaks with increased Q^2.

In 1968, the SLAC–MIT collaboration undertook the first extensive study of the continuum or deep inelastic region of electron–proton scattering [4]. Contrary to the expectation that cross sections (relative to the Mott cross section) would be suppressed by $(Q^2)^{-4}$ from the proton's form factor [3], something quite different was observed. Figure 1.3 shows the measured cross sections as a function of Q^2 for various values of W^2; the gentle Q^2 variation of the inelastic relative to the elastic cross section is evident. When plotted as a function of $\omega = 2M\nu/Q^2$ (see below), the measured structure functions were found to be Q^2 independent over a large range in ω [5], provided the low–W^2 data was excluded. This property is known as scaling.

A year prior [6] to the completion of SLAC data analysis, Bjorken [7] found, based on studies of current commutation relations at infinite momentum, that in the

[1] At these larger Q^2–values, a second form factor is required to describe the magnetic interaction.

limit $Q^2 \to \infty$ with $\omega = 2M\nu/Q^2$ fixed, the inelastic structure functions *remain finite and depend only on* ω. Feynman [8] provided an intuitive interpretation of this asymptotic behaviour through the introduction of the parton model (See discussion in Section 1.2.4): Deep inelastic lepton–nucleon scattering is viewed as the incoherent sum of elastic lepton–parton scatterings, analogous to the relationship between inelastic electron–nucleus scattering to elastic electron–nucleon scattering. The scaling variable $x \equiv 1/\omega$ represents the nucleon's momentum fraction carried by the struck parton. Structure functions, in turn, are proportional to the momentum densities of partons inside the nucleon.

The nuclear scattering phenomena discussed above can be qualitatively reexamined in terms of the scaling variable $x_A = Q^2/2M_A\nu$ where M_A is the *nuclear* mass of atomic number A. In the region $1/R^2 \ll Q^2 \ll 1/r^2$, where R and r are the nuclear and nucleon sizes respectively, the elastic e–nucleon peak *scales* in the variable x_A: it remains approximately constant in area with $\langle x_A \rangle \approx 1/A$. As $Q^2 \to 1/r^2$, a new structure scale emerges and the elastic e–nucleon peak displays *scaling violations*: it acquires a $(Q^2)^{-4}$ dependance from the nucleon form factor. For $Q^2 \gg 1/r^2$ and for non–interacting, structureless partons, scaling once again emerges, with the elastic e–parton peak at $\langle x_A \rangle \approx 1/nA$, where n is the number of partons in the nucleon. Partons at small x, dubbed "wee–partons" by Feynman, complicate this relation though. Wee–partons, hypothesized [9] to be virtual parton–antiparton pairs at small–x, would shift $\langle x_A \rangle$ to a value smaller then that of the n "valence" partons.

This is discussed further in Section 1.2.4.

1.2.2 Cross Section Formalism

Returning now to Figure 1.1, the structure of the neutrino nucleon cross section describing Reaction 1.1 is considered. In the language of current current interactions, the matrix element for the neutrino reaction can be written [10]:

$$\mathcal{M} = \frac{G_F}{\sqrt{2}} \frac{1}{1+Q^2/M_W^2} \underbrace{\overline{u}_\mu(k_2,s_2)\gamma_\alpha(1-\gamma_5)u_\nu(k_1,s_1)}_{\text{lepton}} \underbrace{< X|J_{cc}|N;p,s >}_{\text{hadron}} \tag{1.2}$$

where G_F is the weak coupling constant, $Q^2 = -q^2 = -(k_1 - k_2)^2$ is the magnitude of the square of the four–momentum transferred between the leptonic and hadronic currents and M_W is the $W^\pm$ mass. (k_1, s_1) and (k_2, s_2) are the four momenta and helicities of the incident neutrino and scattered muon respectively and (p, s) is four–momentum and helicity of the target nucleon of mass M. The u's are the lepton spinors, defined using the conventions of Reference [11] (e.g. $\overline{u}(k',s')u(k',s') = 1$). The inclusive, spin–averaged cross section, proportional to $|\mathcal{M}|^2$ takes the form

$$\frac{d^2\sigma^{\nu N}}{d\Omega_\mu dE_\mu} = \frac{1}{(1+Q^2/M_W^2)^2} \frac{G^2}{2} \frac{m_\nu}{E_\nu} \frac{m_\mu}{E_\mu} \frac{E_\mu^2}{(2\pi)^2} L_{\alpha\beta} W^{\alpha\beta}. \tag{1.3}$$

Here, E_ν and E_μ are the energies of the incident neutrino and final state muon in the lab frame (nucleon at rest) and Ω is the solid angle the scattered muon lies in. The leptonic tensor $L_{\alpha\beta}$, is given by (incident neutrinos)

$$L_{\alpha\beta} = \sum_{s_1,s_2} \overline{u}_\mu(k_2,s_2)\gamma_\alpha(1-\gamma_5)u_\nu(k_1,s_1)\overline{u}_\nu(k_1,s_1)\gamma_\beta(1-\gamma_5)u_\mu(k_2,s_2) \tag{1.4}$$

$$= \frac{2}{m_\nu m_\mu}\left[k_{2\alpha}k_{1\beta} + k_{2\beta}k_{1\alpha} - k_1 \cdot k_2 g_{\alpha\beta} - i k_1^\gamma k_2^\delta \epsilon_{\gamma\delta\alpha\beta}\right]. \tag{1.5}$$

For an incident antineutrino, the last term reverses sign. The hadronic tensor is formally given by

$$W^{\alpha\beta} = \frac{1}{2}\sum_{s}\sum_{X} < N;p,s|J_{cc}^{\dagger\beta}|X;p',s' >< X;p',s'|J_{cc}^{\alpha}|N;p,s > (2\pi)^3\delta^4(q+p-p') \tag{1.6}$$

where all final states $|X;p',s'>$ are summed over. The most general Lorentz invariant structure for W is given by [12]

$$\begin{aligned} W^{\alpha\beta} &= -g^{\alpha\beta}W_1 + \frac{p^\alpha p^\beta}{M^2}W_2 - \frac{i\epsilon^{\alpha\beta\gamma\delta}p_\gamma q_\delta}{2M^2}W_3 \\ &+ \frac{q^\alpha q^\beta}{M^2}W_4 + \frac{(p^\alpha q^\beta + p^\beta q^\alpha)}{M^2}W_5 \\ &+ \frac{i(p^\alpha q^\beta - p^\beta q^\alpha)}{2M^2}W_6 \end{aligned} \tag{1.7}$$

where the W_i are real functions depending only invariants constructed from q and p, e.g. $Q^2 = -q^2$ and $p \cdot q$. In the limit of negligible lepton masses,

$$q^\alpha L_{\alpha\beta} = q^\beta L_{\alpha\beta} = 0 \tag{1.8}$$

so that terms proportional to q^α or q^β in $W^{\alpha\beta}$ can be ignored: these are the coefficients of W_4, W_5 and W_6. After contracting the lepton and hadron tensors, Equation 1.3 becomes (neglecting Q^2/M_W^2):

$$\frac{d^2\sigma^{\nu(\bar{\nu})N}}{d\Omega dE_\mu} = \frac{G_F^2}{2\pi^2}E_\mu^2\left[\cos^2\frac{\theta}{2}W_2^{\nu(\bar{\nu})N} + 2\sin^2\frac{\theta}{2}W_1^{\nu(\bar{\nu})N} \pm \frac{E_\nu + E_\mu}{M}\sin^2\frac{\theta}{2}W_3^{\nu(\bar{\nu})N}\right] \tag{1.9}$$

where lepton masses have been ignored. Neutrino and antineutrino scattering corresponds to the positive and negative sign for the W_3 term respectively. In general, the *structure functions* $W_i(q^2, p\cdot q)$s depend on the target and may depend as well on the neutrino helicity.

All kinematic quantities appearing in Equation 1.9 can be expressed in terms of the measured quantities in the lab frame: these are E_μ, $E_{had} = \nu$ and θ, the angle of the final state muon. The relations are given by:

$$E_\nu = E_\mu + E_{had} \tag{1.10}$$

$$Q^2 \equiv -q^2 \approx 4E_\nu E_\mu sin^2\frac{\theta}{2} \tag{1.11}$$

$$p \cdot q = 2M\nu \tag{1.12}$$

An analogous derivation for charged lepton cross sections leads the same form as Equation 1.9 with the following replacements:

$$\frac{G_F^2}{2\pi} \rightarrow \frac{4\alpha^2}{(Q^2)^2} \tag{1.13}$$

$$W_3 \rightarrow 0 \tag{1.14}$$

where W_1 and W_2 are pure VV electromagnetic structure functions. (Aside from the VA interference term (W_3) absent in the electromagnetic case, the weak structure W_1 and W_2 include both VV and AA terms).

The structure functions appearing in Equation 1.9 are related to the nucleon absorption cross sections for different helicity $W^\pm$s. In terms of σ_L, σ_R and σ_S, the absorption cross sections for left–handed, right–handed and scalar Ws, the structure functions can be written as:

$$W_1 = \frac{K}{\pi G_F\sqrt{2}}(\sigma_R + \sigma_L) \tag{1.15}$$

$$W_2 = \frac{K}{\pi G_F\sqrt{2}}\frac{Q^2}{Q^2+\nu^2}(\sigma_R + \sigma_L + 2\sigma_S) \tag{1.16}$$

$$W_3 = \frac{K}{\pi G_F\sqrt{2}}\frac{2M}{\sqrt{Q^2+\nu^2}}(\sigma_R - \sigma_L) \tag{1.17}$$

where K represents the flux of virtual Ws. It is worth noting at this point that for electromagnetic interactions, parity invariance forces $\sigma_L = \sigma_R$ and W_3^{em} vanishes. In this case, W_1^{em} represents the photoabsorption cross section for transverse polarized γs ($\sigma_T = \frac{1}{2}(\sigma_L + \sigma_R)$) and W_2^{em} represents the photoabsorption cross section for the sum of transverse and longitudinal (scalar) γs. While there is some arbitrariness in the definition of K, the ratio of absorbtion cross sections for longitudinal to transverse bosons is well defined:

$$R(\nu, Q^2) \equiv \frac{\sigma_S}{\sigma_T} = \frac{W_2}{W_1}\left(1 + \frac{\nu^2}{Q^2}\right) - 1 \tag{1.18}$$

It is convenient to express the cross section in variables appropriate for the study of scaling and Q^2 violations to scaling. Equation 1.9 can be written in terms of $x = Q^2/2M\nu$ and ,Q^2 through the Jacobian transformation:

$$\frac{d^2\sigma}{dxdQ^2} = \left|\frac{\partial(E_\mu, \Omega)}{\partial(x, Q^2)}\right| \frac{d^2\sigma}{dE_\mu d\Omega} \tag{1.19}$$

where

$$\left|\frac{\partial(E_\mu, \Omega)}{\partial(x, Q^2)}\right| = \frac{\pi(E_\nu - E_\mu)}{E_\nu E_\mu x}. \tag{1.20}$$

The resulting cross section takes the form

$$\frac{d^2\sigma^{\nu(\bar{\nu})}}{dxdQ^2} = \frac{G_F^2}{2\pi x}\left[(1 - y - \frac{Mxy}{2E})\nu W_2^{\nu(\bar{\nu})} + y^2 xMW_1^{\nu(\bar{\nu})} \pm y\left(1 - \frac{y}{2}\right)x\nu W_3^{\nu(\bar{\nu})}\right] \tag{1.21}$$

where

$$y \equiv \frac{\nu}{E} \tag{1.22}$$

is the fraction of the neutrino energy transferred to the nucleon in the lab frame. y is related to the scattering angle in the neutrino–nucleon center of momentum frame

(see Section 1.2.3). In terms of x and y, the differential cross section takes the form

$$\frac{d\sigma^{\nu(\bar{\nu})}}{dxdy} = \frac{G_F^2 ME}{\pi}\left[(1-y-\frac{Mxy}{2E})F_2^{\nu(\bar{\nu})} + \frac{y^2}{2}2xF_1^{\nu(\bar{\nu})} \pm y\left(1-\frac{y}{2}\right)xF_3^{\nu(\bar{\nu})}\right] \quad (1.23)$$

where the modern structure function notation has been used:

$$2xMW_1(\nu,Q^2) = 2xF_1(x,Q^2) \quad (1.24)$$

$$\nu W_2(\nu,Q^2) = F_2(x,Q^2) \quad (1.25)$$

$$x\nu W_3(\nu,Q^2) = xF_3(x,Q^2) \quad (1.26)$$

and $R = \sigma_L/\sigma_T$ is given by:

$$R = \frac{W_2}{W_1}\left(1+\frac{\nu^2}{Q^2}\right) - 1 = \frac{F_2}{2xF_1}\left(1+\frac{Q^2}{nu^2}\right) - 1 \quad (1.27)$$

1.2.3 Structure Functions in the Parton Model

Structure functions in the Parton Model are developed intuitively from the notion that deep inelastic scattering is an incoherent sum of elastic neutrino scatterings off quasi–free, pointlike partons [8]. The elastic neutrino–parton scattering cross sections are first presented. From these, the inelastic structure functions are constructed through the introduction of parton distributions within a nucleon target.

The V–A structure of the charged weak current is assumed: For spin–$\frac{1}{2}$ partons, only left–handed partons and right handed anti–partons participate in the weak interaction (See Figure 1.4). The elastic cross sections depend only on the square of the center–of–momentum energy, s and the spin of the neutrino–parton system:

$$\frac{d\sigma^{\nu}}{d\cos\theta^*} = \frac{G_F^2 s}{2\pi} \times [\text{angular factor}] \quad (1.28)$$

where the angular factor depends on the total neutrino–parton spin. The variable $y = (E_\nu - E_\mu)/E_\nu$ introduced in the previous section is related to the C.M. scattering angle. In terms of the C.M. quantities,

$$y = 1 - \frac{\gamma_{CM}(E^*_\mu + \beta_{CM} p^*_\mu \cos\theta^*)}{\gamma_{CM}(E^*_\nu + \beta_{CM} p^*_\nu)} \tag{1.29}$$

$$\approx 1 - \frac{1}{2}(1 + \cos\theta^*), \tag{1.30}$$

where γ_{CM} and β_{CM} are the Lorentz boost factors relating the C.M. frame to the lab frame and (*) indicates quantities in the C.M. frame. In this expression, the muon mass is ignored and and the elastic scattering condition $E^*_\nu = E^*_\mu$ has been made.

The elastic scattering cross sections take the form (in units of $\frac{G_F^2 s}{2\pi}$):

Interaction	total spin	$\frac{d\sigma}{d\cos\theta^*}$	$\frac{d\sigma}{dy}$
ν-q or $\overline{\nu}$-$\overline{q}$	0	1	2
ν-$\overline{q}$ or $\overline{\nu}$-q	1	$(\frac{1+\cos\theta^*}{2})^2$	$2(1-y)^2$
ν-k or $\overline{\nu}$-k	$\frac{1}{2}$	$2\cos\frac{\theta^*}{2}$	$4(1-y)$

The last row corresponds to scattering off a spin–0 parton k. Other spin constituents are not presented since their angular distributions will appear as linear combinations of spin–0 and spin–$\frac{1}{2}$ partons.

Inelastic structure functions are constructed from these elastic cross sections by considering the constituent nature of a nucleon target. Figure 1.5 depicts the scattering of a single parton in an "infinite momentum" frame, i.e. a frame where the transverse momentum of partons in the target and all masses can be ignored. P is the four momentum of the target nucleon in this frame and ξ represents the (longitudi-

nal) momentum fraction carried by the struck parton. In terms of the 4–momentum carried by the exchanged vector boson, q:

$$(\xi P + q)^2 = 2\xi P \cdot q - Q^2 = 0 \tag{1.31}$$

$$\xi = \frac{Q^2}{2P \cdot q} = \frac{Q^2}{2M\nu} \tag{1.32}$$

$$= x \tag{1.33}$$

Thus, the Bjorken scaling variable x represents the momentum fraction carried by the struck parton.

Parton densities in a target T, as measured by neutrinos ($p^{\nu T}(x)$) or antineutrinos ($p^{\overline{\nu} T}(x)$) are defined such that the probability of "seeing" a parton of type p ($p = q, \overline{q}$ or k) inside T with a momentum fraction in the interval $(x, x + dx)$ is $p(x)dx$. The differential cross section for scattering off a parton p with momentum fraction in the interval $(x, x + dx)$ is obtained from Equation 1.28:

$$\frac{d\sigma^{\nu(\overline{\nu})p}}{dy} = \frac{G_F^2 x s}{\pi} \times [y\text{–factor}]\, p^{\nu(\overline{\nu})}(x)dx \tag{1.34}$$

where the s has been replaced by xs, the square of the $\nu(\overline{\nu})$–parton CM energy. In terms of all target constituents, the double differential cross sections take the form

$$\frac{d^2\sigma^{\nu T}}{dxdy} = \frac{G_F^2 x s}{\pi}\left[q^{\nu T}(x) + (1-y)^2 \overline{q}^{\nu T}(x) + 2(1-y)k^{\nu T}(x)\right] \tag{1.35}$$

$$\frac{d^2\sigma^{\overline{\nu} T}}{dxdy} = \frac{G_F^2 x s}{\pi}\left[\overline{q}^{\overline{\nu} T}(x) + (1-y)^2 q^{\overline{\nu} T}(x) + 2(1-y)k^{\overline{\nu} T}(x)\right] \tag{1.36}$$

These expressions can be compared directly to the cross sections obtained from Lorentz invariance (Equation 1.23), yielding:

$$2xF_1^{\nu(\overline{\nu})T} = 2\left[xq^{\nu(\overline{\nu})T} + x\overline{q}^{\nu(\overline{\nu})T}\right]$$

$$F_2^{\nu(\bar{\nu})T} = 2\left[xq^{\nu(\bar{\nu})T} + x\bar{q}^{\nu(\bar{\nu})T} + 2xk^{\nu(\bar{\nu})T}\right] \tag{1.37}$$

$$xF_3^{\nu(\bar{\nu})T} = 2\left[xq^{\nu(\bar{\nu})T} - \bar{q}^{\nu(\bar{\nu})T}\right] \tag{1.38}$$

where the term proportional to Q^2/ν^2 has been neglected. Thus, in the Parton Model, deep inelastic structure functions are equal to the momentum fractions of partons in the target.

The Parton Model expressions for charged lepton scattering are analogous. Instead of Equation 1.28, the elastic scattering cross section takes the form

$$\frac{d\sigma^{\ell^\pm}}{d\cos\theta^*} = \frac{4\pi\alpha^2 e_i^2 s}{Q^4} \times [\text{ angular factor}] \tag{1.39}$$

where e_i is the ith parton's electric charge (in units of proton charge) of the parton and α is the electromagnetic coupling constant. A consequence of The pure vector nature of the electromagnetic current (ignoring electroweak interference) is that ℓ^+ and ℓ^- couple to a given parton or its anti-parton with the same strength. The resulting electromagnet structure functions are given by

$$2xF_1^{\ell T} = \sum_i e_i^2\left[xq_i^{\ell T} + x\bar{q}_i^{\ell T}\right] \tag{1.40}$$

$$F_2^{\ell T} = \sum_i e_i^2\left[xq_i^{\ell T} + x\bar{q}_i^{\ell T} + 2k_i^{\ell T}\right] \tag{1.41}$$

where the sum is over all parton charges. While neutrino scattering is sensitive to the helicity content of the target, electromagnetic scattering measures the charge content.

It is worth noting that the structure functions presented in this section follow from the assumption that the partons carry no transverse momentum. At available

energies, partons will have non–negligible transverse momenta, which, in the absence of spin–0 constituents, will contribute to the difference between F_2 and $2xF_1$.

1.2.4 Quark Parton Model Formalism

The Parton model does not make any predictions about the quantum numbers of the constituents. Identification of the partons with the quarks introduced by Gell–Mann [13] and Zwieg [14] to rationalize the the proliferation of "elementary particles" appearing in the early 1960's enhanced the status of both models to what is now called the Quark Parton Model (QPM). Callen and Gross [15] found an asymptotic relation which tested the current algebra assumption Bjorken used in his scaling hypothesis, that currents consist of spin–$\frac{1}{2}$ particles:

$$\lim_{\substack{q^2 \to \infty \\ x \text{ fixed}}} F_2(x) = 2xF_1(x) \tag{1.42}$$

The physical content can be seen from comparing Equations 1.15 and 1.16, and noting that a spin–0 constituent can not absorb a transversely polarized particle. Early electron scattering measurements [5] indicated $R = \sigma_L/\sigma_T$ was small.

The charge assignments of quarks is tested through the comparison of structure functions measured with charged lepton and neutrino beams. In the electroweak theory [16] quarks and leptons form weak iso–doublets and the charged current interaction is mediated through the exchange of $W^{\pm}$, the $I_3 = \pm 1$ members of a weak iso–triplet. Consequently, neutrinos interact with $I_3 = -\frac{1}{2}$ quarks or $I_3 = +\frac{1}{2}$ antiquarks and antineutrinos interact with $I_3 = +\frac{1}{2}$ quarks or $I_3 = -\frac{1}{2}$

antiquarks. In terms of the quark and antiquark probability densities for a proton target, $d^p(x), \overline{d}^p(x), u^p(x), \overline{u}^p(x)\ldots$, the parton densities appearing in Equations 1.37 take the form (proton target):

$$\begin{aligned} q^{\nu p}(x) &= d^p(x) + s^p(x) \\ \overline{q}^{\nu p}(x) &= \overline{u}^p(x) + \overline{c}^p(x) \\ q^{\bar{\nu} p}(x) &= u^p(x) + c^p(x) \\ \overline{q}^{\bar{\nu} p}(x) &= \overline{d}^p(x) + \overline{s}^p(x) \end{aligned}$$

By appealing to symmetry arguments, parton densities for neutron and nucleon targets can be constructed from these same proton densities. *Strong isospin* invariance suggests the following flavor symmetries between the proton and neutron densities of the valence flavors (u and d):

$$d(x) \equiv d^p(x) = u^n(x) \quad ; \quad u(x) \equiv u^p(x) = d^n(x) \tag{1.43}$$

$$\overline{d}(x) \equiv \overline{d}^p(x) = \overline{u}^n(x) \quad ; \quad \overline{u}(x) \equiv \overline{u}^p(x) = \overline{d}^n(x). \tag{1.44}$$

It is reasonable to assume that the non–valence flavors satisfy:

$$s(x) \equiv s^p(x) = s^n(x) \quad ; \quad c(x) \equiv c^p(x) = c^n(x) \tag{1.45}$$

$$\overline{s} \equiv \overline{s}^p(x) = \overline{s}^n(x) \quad ; \quad \overline{c} \equiv \overline{c}^p(x) = \overline{c}^n(x) \tag{1.46}$$

Thus, the neutron's parton densities take the form

$$\begin{aligned} q^{\nu n}(x) &= u(x) + s(x) \\ \overline{q}^{\nu n}(x) &= \overline{d}(x) + \overline{c}(x) \end{aligned}$$

$$q^{\bar{\nu}n}(x) = d(x) + c(x)$$

$$\bar{q}^{\bar{\nu}n}(x) = \bar{u}(x) + \bar{s}(x)$$

Finally, the isoscalar parton densities, $\frac{1}{2}$(proton + neutron), become:

$$q^{\nu N} = \frac{1}{2}\left(u(x) + d(x) + 2s(x)\right) \tag{1.47}$$

$$q^{\bar{\nu}N} = \frac{1}{2}\left(u(x) + d(x) + 2c(x)\right) \tag{1.48}$$

$$\bar{q}^{\nu N} = \frac{1}{2}\left(\bar{u}(x) + \bar{d}(x) + 2\bar{c}(x)\right) \tag{1.49}$$

$$\bar{q}^{\bar{\nu}N} = \frac{1}{2}\left(\bar{u}(x) + \bar{d}(x) + 2\bar{s}(x)\right) \tag{1.50}$$

The isoscalar structure function F_2 for neutrino scattering are obtained from substituting these densities into Equations 1.37:

$$F_2^{\nu N}(x) = xu(x) + x\bar{u}(x) + xd(x) + x\bar{d}(x) + xs(x) + x\bar{s}(x) \tag{1.51}$$

$$= F_2^{\bar{\nu}N}(x) \tag{1.52}$$

where $s(x) = \bar{s}(x)$ is assumed and charm is neglected from now on. $F_2^{\ell p}$ and $F_2^{\ell n}$ are constructed from Equation 1.41 using the same parton densities as above and the quark charges:

$$F_2^{\ell p} = \left(\frac{1}{3}\right)^2\left(xd(x) + x\bar{d}x + xs(x) + x\bar{s}(x)\right) + \left(\frac{2}{3}\right)^2\left(xd(x) + x\bar{d}(x)\right) \tag{1.53}$$

$$F_2^{\ell n} = \left(\frac{1}{3}\right)^2\left(xu(x) + x\bar{u}x + xs(x) + x\bar{s}(x)\right) + \left(\frac{2}{3}\right)^2\left(xu(x) + x\bar{u}(x)\right). \tag{1.54}$$

$$\tag{1.55}$$

Combining these expressions gives the isoscalar structure function $F_2^{\ell N}$:

$$F_2^{\ell N} = \frac{1}{2}\left(F_2^{\ell p} + F_2^{\ell n}\right) \tag{1.56}$$

$$= \frac{5}{18}\left(xu + x\overline{u} + xd + x\overline{d} + xs + x\overline{s} - \frac{3}{5}(xs + x\overline{s})\right). \tag{1.57}$$

Dividing by Equation 1.52 yields:

$$\frac{F_2^{\ell N}}{F_2^{\nu N}} = \frac{5}{18}\left(1 - \frac{3}{5}\frac{xs + x\overline{s}}{xq + x\overline{q}}\right) \tag{1.58}$$

where $q = u + d + s$ and $\overline{q} = \overline{u} + \overline{d} + \overline{s}$. The small correction term in brackets is a consequence of the asymmetry of the s–c doublet. The flavor changing nature of the charged current neutrino interaction induces a kinematic suppression for production of heavy flavors (e.g. charm) which is not present in the electromagnetic interaction. This is discussed in Chapter 5 and Appendix C.

Another test of the QPM has to do with the valence content of nucleon. In the simplest formulation of quark model (three flavors, no orbital angular momentum) hadrons are constructed from the fundamental ($q = \mathbf{3}$) and adjoint ($\overline{q} = \overline{\mathbf{3}}$) representations of flavor $SU(3)$: Mesons are constructed as $q\overline{q} = \mathbf{3} \otimes \overline{\mathbf{3}}$ and baryons as $qqq = \mathbf{3} \otimes \mathbf{3} \otimes \mathbf{3}$. The three quarks which comprise the proton or neutron are referred to as the *valence* quarks. The anti–partons appearing in the structure function assignments in the previous section are part of the flavor–singlet "sea" of virtual q–$\overline{q}$ pairs, the "wee partons" in Feynman's model. Thus, the parton densities include both valence (nonsinglet) and sea quarks:

$$q(x) = q_v(x) + q_s(x) = (q(x) - \overline{q}(x)) + q_s(x) \tag{1.59}$$

or

$$q_v(x) = q(x) - \overline{q}(x) \tag{1.60}$$

where the subscripts v and s indicate valence and sea densities respectively. From the form of Equation 1.38, xF_3 represents the momentum density of valence quarks. Substitution of the isoscalar parton densities into Equation 1.38 yields:

$$xF_3^{\nu N}(x) = xu_v(x) + xd_v(x) + 2xs(x) \tag{1.61}$$

$$xF_3^{\bar{\nu} N}(x) = xu_v(x) + xd_v(x) - 2xs(x) \tag{1.62}$$

where $u_v \equiv u - \bar{u}$ and $d_v \equiv d - \bar{d}$ are the proton's valence densities. The asymmetry of the s–c doublet results $xF_3^{\nu N} \neq xF_3^{\bar{\nu} N}$. The reported structure functions are averages of neutrino and antineutrino:

$$xF_3(x) = xu_v(x) + xd_v(x) \tag{1.63}$$

Dividing the momentum density by the momentum fraction x yields the *number density* of valence quarks in the nucleon. Integration of the number density over all x leads to the Gross–Llewellyn Smith (GLS) sum rule [17]:

$$\int_0^1 \frac{dx}{x} xF_3(x) = N_v \tag{1.64}$$

where the value of N_v prescribed by the QPM is three. Since xF_3 does not contain Feynman's wee–partons, the value of n discussed in Section 1.2.1 is N_v, that is, xF_3 should have a mean value $1/3A$ when x is taken as the *nuclear* momentum fraction.

While agreement between measured structure functions is in reasonable agreement with the QPM predictions, certain puzzles remained. Four examples are:

- The notion of incoherent scattering off quasi–free quarks posed a serious dynamics problem: What holds the nucleon together?

- Higher statistics electron scattering experiments preformed by the SLAC–MIT group and subsequent higher energy muon and neutrino scattering experiments displayed weak violations to the predicted scaling law.

- The measured integral of $F_2^{\nu}(x)$ ($F_2^{\ell N}(x)$, equal to ($\frac{5}{18}\times$) the proton's momentum carried carried by quarks and antiquarks, only accounted half of the proton's momentum. Kuti and Weisskopf [18] suggested that neutral "gluons" which do not directly interact with the lepton current carry this missing momentum. Presumably an interaction between quarks mediated by gluons holds the nucleon together.

Each of these puzzles are related to the dynamics of the strong interaction, issues not addressed by the parton model.

1.2.5 Strong Interactions

A field theory of interacting quarks called Quantum Chromodynamics (QCD) emerged [19] in the 1970s which satisfied the generally accepted requirements of locality, causality and renormalizability [20] *and appeared to coincide with the QPM in the Bjorken limit* [21], a property known as asymptotic freedom. It is an example of a nonabelian gauge theory introduced by Yang and Mills [22] and based on the local gauge group $SU(3)_c$: The color degree of freedom (global $SU(3)_c$) introduced by Han and Nambu [23] to solve the statistics problem (example: $\Delta^{++} = uuu$ should be a totally symmetric $L = 0$ wave function, in conflict with Fermion statistics) and pursued by by

others in an attempt to explain the saturation problem (the question of why only $q\overline{q}$ and qqq states are realized in nature) was *gauged* through the introduction of eight massless vector gluons in analogy to the gauging the global $U(1)$ symmetry (charge) of electromagnetism through the photon.

The matter fields in QCD are colored quarks; their interactions are mediated through the exchange of the QCD gauge fields. Each quark flavor appears in the QCD Lagrangian as a 3–component vector (color) field of quark spinors. The QCD Lagrangian conserves flavor, which corresponds to the conservation of electric charge, baryon number, the third component if isospin (I_3), strangeness, charm, etc. The gauge coupling to all flavors is *necessarily* identical. This is in contrast to QED where the photon can couple to any electric charge. To the extent that quark masses can be ignored, QCD is flavor symmetric.

Asymptotic freedom is a direct consequence of the nonabelian gauge structure of the theory [24], i.e. the gluon–gluon self coupling. This can be contrasted with (abelian) QED which displays the opposite behavior. In QED, virtual e^+e^- pairs surrounding a test charge polarize the vacuum, effectively screening the bare charge at large distances (α_{em} decreases with increasing distance). In QCD, virtual $q\overline{q}$ also polarize the vacuum, screening the color charge at long distances. However, the effect of virtual gluons, which are themselves colored, is to *anti*–screen at long distances. For eight colored gluons and fewer then seventeen quark flavors, the anti–screening effect dominates. This means that the strong interaction coupling constant, α_S, *decreases*

at short distances, corresponding to large momentum transfers. As $Q^2 \to \infty$, $\alpha_S \to 0$ and the quarks are free: scale invariance is an asymptotic property of QCD.

To leading order in perturbation theory, the running (i.e. renormalized) QCD coupling constant is given by:

$$\alpha_S(Q^2) = \frac{4\pi}{(11 - \frac{2}{3}n_f)\ln(Q^2/\Lambda^2)} \tag{1.65}$$

where n_f is the number of quark flavors and Q^2 is the momentum scale characterizing a given process. Λ is the "hidden scale parameter" of QCD. It enters the theory because the gluons couple to themselves inducing gluon–gluon scattering but no scale[2] to measure it with. These scattering amplitudes are renormalized for off–shell gluons, $m^2_{gluon} = -\Lambda^2$: Since QCD is infra–red divergent they can not be renormalized for real gluons ($\Lambda = 0$).

Contact with structure functions is made through the application of the operator product expansion [25] and renormalization group equations [26] to perturbative QCD. Structure function moments, related to the product of currents at small distance, can be written in the factorized form [27]:

$$\int dx x^{n-1} F_k(x, Q^2) = \sum_i C^{q_i}_{k,n}(\alpha_S(Q^2))\langle O^{q_i}_n(Q^2)\rangle + C^G_{k,n}(\alpha_S(Q^2))\langle O^G_n(Q^2)\rangle \tag{1.66}$$

where F_k is either $F_1, x^{-1}F_2$ or F_3 and the sum runs over flavors. $\langle O^{q_i}_n\rangle$ and $\langle O^G_n\rangle$ are the reduced quark and gluon operator matrix elements and $C^{q_i}_{k,n}$ and $C^G_{k,n}$ are the Wilson Coefficient functions. The coefficient functions, which satisfy the renormalization

[2]In the absence of quark masses, all quantities entering the QCD Lagrangian are dimensionless. Quark masses have no bearing on this discussion

group equations, are calculable in perturbative QCD,

$$\begin{aligned} C^q_{k,n}(Q^2) &\propto 1 + \frac{\alpha_S(Q^2)}{4\pi} C^{q(1)}_{k,n} + \mathcal{O}(\alpha_S^2) \\ C^G_{k,n}(Q^2) &\propto \frac{\alpha_S(Q^2)}{4\pi} C^{G(1)}_{k,n} + \mathcal{O}(\alpha_S^2) \end{aligned} \tag{1.67}$$

while only the Q^2 evolution of the operator matrix elements are specified:

$$\langle O^p_n(Q^2)\rangle = T \exp\left[\frac{1}{2}\int_{t_0}^{t} \gamma^{pp'}_n dt'\right] \langle O^{p'}_n(Q^2_0)\rangle. \tag{1.68}$$

Here, p and $p' = q_i, \bar{q}_i$ or G, $t = \ln Q^2/\Lambda^2$ and T means the t'–ordering of the exponential. The anomalous dimensions of the p–operator, $\gamma^{pp'}_n$, which governs the Q^2 evolution of the p–operator are also calculable in perturbation theory:

$$\gamma_n(Q^2) = \frac{\alpha_S(Q^2)}{4\pi}\gamma^{(0)}_n + \left(\frac{\alpha_S(Q^2)}{4\pi}\right)^2 \gamma^{(1)}_n + \mathcal{O}(\alpha_S^3). \tag{1.69}$$

The short distance (large Q^2) behaviour of the structure function moments are dominated by the coefficient functions of the "leading twist" operators: QCD predicts deviations to Bjorken scaling that are logarithmic in Q^2. Inclusion of higher twist operators contributes to scaling violations that depend on inverse powers of Q^2 which can be ignored at large Q^2.

Another way to describe the Q^2 variation of the structure functions is through Altarelli–Parisi equations [28]. Application of the inverse Mellin transform to Equation 1.66 leads to a set of evolution equations in x–space. The transformed operator matrix elements are identified with the QCD–improved parton densities:

$$p(x, Q^2) = \frac{1}{2\pi i}\int_{-i\infty}^{i\infty} dn x^{-n} \langle O^p_n(Q^2)\rangle, \tag{1.70}$$

where $p = G, u, \bar{u}, d, \bar{d}, \ldots$ Their Q^2 evolutions, corresponding to Equation 1.68 are given by:

$$\frac{dq_i(x,t)}{dt} = \int_x^1 \frac{dy}{y}\left[\sum_j P_{q_iq_j}\left(\frac{x}{y},t\right) q_j(y,t) + \sum_j P_{q_i\bar{q}_j}\left(\frac{x}{y},t\right)\bar{q}_j(y,t) + P_{q_iG}\left(\frac{x}{y},t\right) G(y,t)\right] \tag{1.71}$$

$$\frac{d\bar{q}_i(x,t)}{dt} = \int_x^1 \frac{dy}{y}\left[\sum_j P_{\bar{q}_iq_j}\left(\frac{x}{y},t\right) q_j(y,t) + \sum_j P_{\bar{q}_i\bar{q}_j}\left(\frac{x}{y},t\right)\bar{q}_j(y,t) + P_{\bar{q}_iG}\left(\frac{x}{y},t\right) G(y,t)\right] \tag{1.72}$$

$$\frac{dG(x,t)}{dt} = \int_x^1 \frac{dy}{y}\left[\sum_j P_{Gq_j}\left(\frac{x}{y},t\right) q_i(y,t) + \sum_j P_{G\bar{q}_j}\left(\frac{x}{y},t\right)\bar{q}_j(y,t) + P_{GG}\left(\frac{x}{y},t\right) G(y,t)\right] \tag{1.73}$$

where $t = \ln(Q^2/\Lambda^2)$ and the sums are over quark flavors. The splitting functions $P_{pp'}$, which are related to the inverse Mellin transforms of the anomalous dimensions, express the tendency for a parton of type p' carrying a momentum fraction y to be resolved as a parton of type p, with momentum momentum fraction $x < y$. Examples of QCD processes contributing to the $P_{pp'}$'s are shown in Figure 1.6.

By exploiting the symmetries of QCD, contact with the nucleon structure functions can be made. Charge invariance implies:

$$P_{q_iq_j} = P_{\bar{q}_i\bar{q}_j}; \qquad P_{q_i\bar{q}_j} = P_{\bar{q}_iq_j}; \tag{1.74}$$

$$P_{q_iG} = P_{\bar{q}_iG}; \qquad P_{Gq_i} = P_{G\bar{q}_i}. \tag{1.75}$$

Additional symmetries follow from the equivalence of flavors in the massless theory:

$$P_{q_iq_i} = P_{q_jq_j}; \tag{1.76}$$

$$P_{q_i q_j} = P_{q_k q_l} \qquad (i \neq j \text{ and } k \neq l); \tag{1.77}$$

$$P_{q_i G} = P_{q_j G}; \qquad P_{G q_i} = P_{G q_j} \tag{1.78}$$

with analogous expressions involving antiquarks. The parton density evolution equations can be expressed as

$$\frac{dq_{ns}(x,t)}{dt} = \int_x^1 \frac{dy}{y} P_{qq}^{ns}\left(\frac{x}{y},t\right) q_{ns}(y,t) \tag{1.79}$$

$$\frac{dq_s(x,t)}{dt} = \int_x^1 \frac{dy}{y}\left[P_{qq}^{s}\left(\frac{x}{y},t\right) q_s(y,t) + 2N_f P_{qG}\left(\frac{x}{y},t\right) G(y,t)\right] \tag{1.80}$$

$$\frac{dG(x,t)}{dt} = \int_x^1 \frac{dy}{y}\left[P_{Gq}\left(\frac{x}{y},t\right) q_s(y,t) + P_{GG}\left(\frac{x}{y},t\right) G(y,t)\right] \tag{1.81}$$

where

$$q_{ns}(x,t) = \sum_i (q_i(x,t) - \overline{q}_i(x,t)) \tag{1.82}$$

$$q_s(x,t) = \sum_i (q_i(x,t) + \overline{q}_i(x,t)) \tag{1.83}$$

are the nonsinglet and singlet quark densities respectively, and the sum is over all N_f flavors. Since quarks and antiquarks couple with equal strength to the gluons, there is no gluon contribution to the evolution of q_{ns}. Note that at leading order in α_S, $P_{q_i \overline{q}_j} = P_{\overline{q}_i q_j} = 0$ for all $i \neq j$ and $P_{qq}^{ns} = P_{qq}^{s}$.

The physically measurable quantities are not the parton densities, but the structure functions. Transforming the product of parton operators and coefficient functions in Equation 1.66 into x–space requires the convolution of their inverse Mellin Transforms:

$$2F_1(x,Q^2) = \int_x^1 \left[C_1^q\left(\frac{x}{y},Q^2\right) q_s(y,Q^2) + C_1^G\left(\frac{x}{y},Q^2\right) G(y,Q^2)\right] \tag{1.84}$$

$$x^{-1}F_2(x,Q^2) = \int_x^1 \left[C_2^q\left(\frac{x}{y},Q^2\right) q_s(y,Q^2) + C_2^G\left(\frac{x}{y},Q^2\right) G(y,Q^2)\right] \quad (1.85)$$

$$F_3(x,Q^2) = \int_x^1 C_3^q\left(\frac{x}{y},Q^2\right) q_{ns}(y,Q^2). \quad (1.86)$$

Equations 1.84–1.86 are of the form of a "product" of calculable short distance cross sections, the C's, and non–perturbative pieces describing the soft nucleon interior. A consequence of this "factorization" is the universality of the parton densities: They should depend only on the target and not the process under study, e.g. leptoproduction, Drell–Yan, etc. To leading order in α_S, the transformed quark coefficient functions are proportional to $\delta(1-x/y)$ and the transformed gluon coefficient functions vanish (See Equation 1.67). In this case, $F_2 = xq_s$ and $xF_3 = xq_{ns}$ identically. The QCD expressions for the structure functions coincide with the Quark Parton Model, apart from the Q^2 dependance arising from Equations 1.79 and 1.80. The Gross–Llewellyn Smith sum rule, the Callen–Gross relation and other QPM relations hold. The nucleon's momentum not carried by quarks, roughly half, is accounted for by the gluons.

When next–to–leading order (NLO) corrections are included, the coefficient functions vitiate the quark assignments given by the QPM and other QPM predictions [29]. Definitions of parton densities, coefficient functions and Λ acquire a degree of ambiguity when NLO effects are included. Ultraviolet divergences encountered beyond the tree level must be regulated and removed by some renormalization programme, of which there are infinitely many to choose from [30]. To any finite order (> 1) in perturbation theory, Λ depends on this choice. The factorization of structure

functions into a product of short distance cross sections and parton densities (Equation 1.66 or 1.84–1.86) is not unique. This freedom of choice leads to ambiguities in the definitions of both [31].

Figure 1.7 illustrates scaling violations predicted by QCD for the valence–quark, antiquark and gluon densities. Each of these momentum densities shrinks to lower values of x with increasing Q^2. There is a similarity between the the scaling violations dipicted in Figure 1.7 and that discussed at the end of Section 1.2.1: in both cases, as new structure is revealed, more constituents emerge, each carying a smaller fraction of the target's momentum. In QCD, the new structure is the sea of $q\overline{q}$ pairs and gluons. However, the rate at which cross sections change as this new structure appears is only logarithmic in Q^2 as compared with the $(Q^2)^{-4}$ dependance of the elastic e^-–nucleon cross sections.

Chapter 2

The Neutrino Source

2.1 Introduction

A beam of muon type neutrinos is formed when charged pions and kaons decay in flight. In this experiment, a primary beam of protons was targeted on a BeO target forming a wide band secondary hadron beam. These secondaries were then sign– and momentum–selected ($\langle p \rangle$ ranging from 120 to 250 GeV/c for each polarity with $\Delta p/\langle p \rangle \approx 0.1$) before entering an evacuated decay pipe where a fraction of the pions and kaons subsequently decayed:

$$\pi \text{ or } K \rightarrow \mu + \nu_\mu. \tag{2.1}$$

The small momentum bite results in the characteristic dichromatic neutrino spectrum. Figure 2.1 shows the correlation of reconstructed event energy verses event radius at

the Lab E[1] detector for a +250 GeV/c momentum setting. The high–energy band corresponds to neutrinos originating from kaon decays and the low–energy band corresponds to neutrinos from pion decays. A more detailed description of the dichromatic beam is presented in Section 2.5.

Traditionally, calculation of the dichromatic flux spectrum was based entirely on the measured properties of the secondary beam: (a) The energy and radial dependance of the flux was computed from the measured momentum spectrum (mean and rms spread) and angular divergence of the secondary beam and (b) the normalizations were computed from the measured intensities and particle fractions. In this analysis, only the secondary beam measurements pertaining to (a) were used. The ability to separate pion–induced from kaon–induced events together with consistency requirements applied to the measured event distributions were used to establish the neutrino flux normalizations. The methods used to normalize the fluxes are presented in Appendix A.

At each setting i, of the secondary beam the neutrino flux $\phi_i(E,r)$ = number of ν's/GeV/cm^2 at the Lab E detector, can be expressed as:

$$\phi_i(E,r) = N_\pi^i \phi_i^\pi(E,r) + N_K^i \phi_i^K(E,r) + \phi_i^{WB}(E,r), \tag{2.2}$$

where N_π and N_K are the total pion and kaon intensities. The flux analysis presented in this chapter is restricted to the calculation of ϕ^π and ϕ^K, the neutrino fluxes at

[1]Lab E is the name of the building that houses the neutrino detector. Its position relative to the neutrino source is shown in Figure 2.2

Lab E per pion or kaon respectively and ϕ^{WB}, the wideband neutrino flux originating from secondary decays prior to momentum selection.

2.2 The Primary Beam

Pions and kaons were produced by 400 GeV/c protons from the accelerator striking a 33 cm long beryllium oxide target. Figures 2.2 and 2.3 shows the layout of the accelerator, primary target and Lab E detector. The accelerator was able to provide a burst of protons roughly every ten to twenty seconds. Three different extraction modes were employed during the two running periods[2]: E616 had a 2 msec and 500 msec extraction; E701 had in addition, a series of up to five "pings" or mini fast extractions separated by approximately one second. The Lab E detector was gated on during the extraction period for normal data triggers; the shorter spill times reduced the cosmic ray contamination of the triggers. On the other hand, due to the long dead time of the spark chambers ($\sim$ 50 msec) a maximum of one event could be logged per fast spill. The advent of pings in E701 allowed several fast spill events to be logged per machine cycle.

Three devices were used to measure the primary beam intensity: a secondary emission monitor, a resonant cavity tuned to the radio frequency of the machine (rf cavity) and a beam current transformer. The primary beam intensity was required

[2]Throughout this thesis, the Fermilab experiment numbers E616 and E701 are used to designate the running periods.

for the wideband background calculation discussed in Section 2.5. Typical intensities of protons on target were 10^{13} protons/pulse for normal fast spill and one fifth that for individual pings. Figure 2.4 shows the accelerator magnet current and proton beam intensity over one acceleration/extraction cycle.

2.3 The Secondary Beam

The secondaries enter a system of dipoles quadrupoles and beam collimators (see Figure 2.5a), referred to as the dichromatic train, which perform sign and momentum selection and focusing. The following is a simple description of the dichromatic train's operation (see Figure 2.5b). First, the quadrapole magnets just downstream of the target provided a point-to-parallel focus. The beam was separated according to momentum by the first of two sets of dipoles. Momentum selection was achieved by passing this beam through a collimator which absorbed all but a narrow momentum bite ($\Delta p/\langle p\rangle \approx 0.1$). Primaries not interacting with the target were dumped in a steel block which was moved to an appropriate location in the train according to the sign and momentum setting of the train. The second set of dipoles recombine the diverging portion of the beam emerging from the collimator. Bending occurred primarily in the horizontal plane, although the entire train was laid out like a corkscrew to prevent the beam from pointing directly towards Lab E. This design helped minimize the wideband contamination.

The secondary beam emerged from the train through a 13 cm $\times$ 4 cm aperture,

having an angular dispersion of approximately .2 mrad in both vertical and horizontal planes. Composition of the beam varied with momentum and polarity. For positive settings, protons made up the dominant fraction and pions less then 50% and kaons less then 5%. For the negative settings, pions made up the dominant fraction with kaons less then about 6%. Figure 2.6 shows the number of secondary particles produced and transmitted, per proton on target for E616 [32].

Ten different settings of the train were used during the two running periods. Nominal momentum settings of ±250, ±200, ±165, ±140, and ±120 Gev/c were used in E616 ("±" refers to sign of secondaries selected) and +250, +200, ±165, +140 and +100 Gev/c in E701. Table 2.1 summarizes these running modes.

2.4 Secondary Beam Monitoring

Two secondary beam monitoring stations were located in the decay region 132 m (target manhole) and 310 m (expansion port) from the downstream end of the train (see Figure 2.3). Two types of ionization chambers were located in each of these, providing beam position, profile and total intensity measurements. A focusing Čerenkov counter and rf cavity were also located in the expansion port. The use and calibration of each device are detailed in the references [32,33]. The measurements required for the calculation of ϕ^{π} and ϕ^{K} in Equation 2.2 are the transverse position, angular divergence, mean momentum $\langle p \rangle$ and rms spread in momentum σ_p, of the beam in the decay region.

Position measurements were made with a set of split–plate ion chambers which measured the average vertical and horizontal position of the beam on a spill–by–spill basis. This information was used online as a feedback for beam steering and offline to insure stability of the neutrino beam center at Lab E. The secondary beam profile was monitored with vertical and horizontal segmented wire ion chambers (SWICs) having a spatial resolution of about 8 mm. Two separate profiles provided a measure of the angular divergence. Figure 2.7 shows typical expansion port and target manhole beam profiles.

The Čerenkov counter provided information about both the composition and the momentum spectrum of the secondary beam. Two different counters were used for the E616 and E701 runs; the latter was designed to reduce diffraction (the E701 counter had a 212 cm radiator verses 189 cm for E616) and to remove the pressure dependence of the optics. Figure 2.8 shows the counter used in the E701 running. Both counters operate by measuring light collected at a fixed angle as a function of the radiator's pressure, P, related to the index of refraction by

$$n \approx 1 + \kappa P \qquad \kappa = 4.605 \times 10^{-8}\text{mm Hg at } 273^{\circ}\text{K}. \tag{2.3}$$

An ideal beam of charged particles traversing an infinitely long medium with $\beta > 1/n$, induces coherent radiation at the Čerenkov angle

$$\cos\theta_C = \frac{1}{\beta n}. \tag{2.4}$$

For relativistic particles of mass m

$$\beta \approx 1 - \frac{m^2}{2p^2} \tag{2.5}$$

Combining this expression with Equation 2.3 leads to the approximation

$$P \approx \frac{1}{2\kappa}\left[\theta_C^2 + \frac{m^2}{p^2}\right]. \tag{2.6}$$

Differentiating yields the relationship between the momentum spread and pressure spread:

$$\frac{\Delta P}{P} \approx 2\frac{\Delta p}{p}. \tag{2.7}$$

The area under the pressure curve is proportional to the intensity of particles of mass m.

Beam interactions with upstream material produced low energy debris which contributed to the pressure curve. Light not originating in the radiator also contributed to the pressure curve. These backgrounds were measured (pressure curves were taken with additional material placed in the beam and with the shutter closed) and subtracted. Figure 2.9 shows a background–subtracted pressure curve superimposed on fits to the modeled response for positrons, pions, kaons and protons. The model includes the broadening of peaks due to finite angular acceptance (light was collected from the angular region $.7 < \theta < 1$ mrad) and diffraction [34] of the counter, angular dispersion, momentum spread and decay products (mostly muons) of the secondary beam and transition radiation. The fit parameters were the intensities and means and widths of the pion, kaon and proton momenta. A 200 GeV/c proton beam trans-

ported from the accelerator with the production target removed was used to calibrate the counter response.

2.5 The Neutrinos

Decays yielding muon type neutrinos along with their branching ratios are shown here:

$$\begin{aligned} \pi^+ &\rightarrow \mu^+ + \nu_\mu & 100\% \\ K^+ &\rightarrow \mu^+ + \nu_\mu & 64\% \\ K^+ &\rightarrow \pi^0 + \mu^+ + \nu_\mu & 3\% \end{aligned} \tag{2.8}$$

plus charge conjugates. The most important of these are the two–body decay modes: it is these that give rise to the dichromatic spectrum. Conservation of 4–momentum in the two–body decays demands a monoenergetic neutrino in the meson rest frame. Boosting the neutrino to the lab frame results in an energy which is dependent only on its angle or radial position at the Lab E detector. In terms of the parent meson's Lorentz boost factor, $\gamma = E_p^{lab}/m_p c^2$, and the mean distance from the decay point to Lab E, L, the radial dependance (at Lab E) of the neutrino energy is given approximately by

$$E_\nu(r) = \frac{E_{max}}{1 + \gamma^2 r^2 / L^2} \tag{2.9}$$

where

$$E_{max} = \frac{m_p^2 - m_\mu^2}{m_p^2} E_p^{lab} \tag{2.10}$$

is the maximum neutrino energy. For neutrinos originating from kaon decay, the maximum energy is roughly 96% of the parent kaon energy while for pion decay the maximum is about 43% of the pion energy. The finite spread in the secondary beam momentum and angle does not change the qualitative energy–radius correlation as is apparent in Figure 2.1. The solid line in Figure 2.1, known as the energy separatrix, is parametrized in analogy to Equation 2.9:

$$E^{SEP}(r) = \frac{E_s}{1 + (\beta r)^2}, \tag{2.11}$$

where E_s and β were chosen to optimize the separation. Fully reconstructed events in the Lab E detector were categorized as pion or kaon events for $E_{meas} < E^{SEP}(r)$ or $E_{meas} > E^{SEP}(E)$ respectively. The separatrix parameters are listed in Table 2.2 for each secondary setting.

2.5.1 Dichromatic Monte Carlo

The calculation of ϕ^{π} and ϕ^{K} in Equation 2.2 consisted of three steps. Pion and kaon rays with the measured properties of the secondary beam were generated. Their decays were then simulated in accordance with the known branching ratios and kinematic constraints. Finally, the daughter neutrinos were propagated to the Lab E detector, binned in E and r and normalized to the generated number of secondary rays.

Hadron rays were generated by using measured [35] secondary production spectra from p–BeO as an input to the ray–tracing program, *DECAY TURTLE* [36]. This

program used the surveyed coordinates of the beam line magnets and collimators to produce rays at the exit aperture of the dichromatic train. Since thin lens approximations were employed, rays transported far from the optical axis were not expected to be reliably modeled. The transported rays were compared to the measured profiles, $\langle p \rangle$ and σ_p of the secondary beam and the daughter neutrinos generated from these rays (see below) were compared with the measured event spectra at the Lab E detector. Small adjustments to the *DECAY TURTLE* rays were then made to optimize these comparisons:

Angular Divergence: This effects both the overall normalization and radial dependance of the neutrino flux at Lab E. Neutrinos from pion decay are most sensitive due to large Lorentz factor. Adjustments to the angular divergence were made based on both SWIC profiles and radial dependance of pion–induced events at Lab E. Uncertainties in angular divergence limited usable pion flux to $r < 30$ in at Lab E.

Mean Momentum: Shapes of pion Čerenkov peaks are dominated by angular divergence and diffraction. Small adjustments in the mean momenta were made which were based on the kaon Čerenkov peaks and on event energies observed at Lab E at small radii.

rms Momentum Spread : The momentum spread of secondary beam was measured from both the kaon and the proton Čerenkov peaks. Variations in this spread were found to have little effect on the predicted event spectra at Lab E.

Consequently, the momentum spreads predicted by *DECAY TURTLE* were not adjusted.

Beam Centers : Secondary beam centers at the exit aperture of the train were adjusted to match event beam centers at Lab E.

Adjustments to the *DECAY TURTLE* rays were of the form

$$x_0 \rightarrow x_0 + \delta_x \tag{2.12}$$

$$\theta_x \rightarrow (1 + \alpha_{\theta_x})\theta_x \tag{2.13}$$

$$\langle p \rangle \rightarrow (1 + \alpha_p)\langle p \rangle \tag{2.14}$$

where x_0, θ_x and $\langle p \rangle$ are the position, angle with respect to the z–direction and momentum of the ray at the train exit aperture, with analogous expressions for y_0 and θ_y. Detailed comparisons for E616 and E701 settings can be found in References [37] and [33] respectively.

Neutrino rays were generated from the (adjusted) secondary rays and binned in E and r with a separate Monte Carlo. The probability for a pion or kaon at the exit aperture of the train to decay before reaching the dump, $1 - e^{-L/\gamma c\tau}$, ranges from 2.5% to 5% for pions and 17% to 31% for kaons for the secondary momentum settings used in this experiment. Rather then using the actual decay probabilities, a decay point z was generated for *each* ray according to the normalized distribution

$$\frac{1}{\gamma c\tau(1 - e^{-L/\gamma c\tau})} e^{-z/\gamma c\tau} \tag{2.15}$$

where L is the total decay length. Each daughter neutrino was then assigned a weight equal to the actual probability. Two–body decays for pions and two– and three–body decays for kaons were simulated in accordance with the branching ratios shown in 2.8.

Neutrinos from the two–body decay modes were histogrammed in energy for each 5–inch beam centered radial bin at Lab E. Gaussian fits to each energy histogram were used to parametrize the number and energy of neutrinos per pion or kaon as a function of radius. Neutrinos from three–body decays were binned in 5–inch radial and 5 GeV energy bins. Figure 2.10a shows the integrated neutrino flux spectra at Lab E originating from pion, kaon 2–body, kaon 3–body and wideband decays, integrated over radii less then 10 inches for the +250 GeV/c secondary setting. Figure 2.10b shows the same flux spectra integrated over the fiducial area used in the structure function analysis: $r < 30$ inch for $E < E^{SEP}(r)$ and $r < 50$ inch in for $E > E^{SEP}(r)$. Figure 2.11 shows the neutrino and antineutrino flux spectra integrated over the fiducial area for all settings combined.

2.5.2 Wideband Neutrinos

The neutrino flux arising from secondary decays prior to momentum selection, ϕ^{WB} in Equation 2.2, was taken [38] to be independent of position at Lab E and proportional to the total primary intensity on target:

$$\phi^{WB}(E,r) = N_{prim} f_{WB/prim} \mathcal{W}(E) \tag{2.16}$$

where N_{prim} is the number of protons on target, $f_{WB/prim}$ is a normalization and $\mathcal{W}$ is an empirical function of the form:

$$\mathcal{W}(E) = \begin{cases} (1 - e^{-E/E_0}) & E \leq b \\ (1 - e^{-E/E_0})e^{-(E-b)/c} & E > b \end{cases} \tag{2.17}$$

Special runs taken with the momentum-defining collimator in the dichromatic train closed were used to model the wideband flux spectrum. The event spectrum is related to the wideband flux as follows

$$N(E)dE = N_t\sigma(E)\left[\int 2\pi r dr \phi^{WB}(E,r)\right] dE \tag{2.18}$$

$$= N_t N_{prim} f_{WB/prim} A\mathcal{W}(E)dE, \tag{2.19}$$

where N_t is the number of target nuclei, A is the transverse area and σ is the total cross section. Since the wideband flux was expected to depend on the position of the primary beam dump, the constants E_0, b, c, and $f_{WB/prim}$ were fit independently for each position of the primary dump used: one position for all negative settings of the train, and one position for each of the positive settings. Since the closed-slit running was very limited in E701, fits to E616 data were used. Table 2.4 lists the constants for each secondary setting.

Chapter 3

The Lab E Detector

3.1 General Requirements

The properties of a detector capable of measuring neutrino induced interactions are largely dictated by the weak interaction. In particular, the "smallness" of $G_F \sim 1/M_W^2$ imposes the most obvious requirement: the target must be quite massive in order to allow sufficient opportunity for an interaction to occur. As the interaction's final state is likely to be absorbed within such a target (with the exception of muons or neutrinos) the target must permit for both triggering and measurement. The two major types of neutrino detectors are the bubble chamber and the electronic detector. This experiment employs the later. In the former case, the target is the liquid in the bubble chamber: its ionization by charged particles makes the entire fiducial mass active. Triggering is done off–line: one picture is taken per machine cycle and a (human) scanner's recognition of an event constitutes a trigger. The

main advantage of the bubble chamber is its ability to make detailed measurements of the final state. However, the fiducial mass, hence event rate, is limited by the low densities of liquids and the difficulty of superheating a large volume of liquid. Electronic detectors, on the other hand, achieve higher event rates by using a passive high density solid sandwiched between active layers. Triggering is done online and the digitized information is written directly to magnetic tape for offline analysis. Because of the high average density, detailed information about the final state is unavailable; however, structure function analysis requires only the final state muon momentum and angle and the total hadronic energy, quantities which are readily measurable.

3.2 Overview of Detector

Lab E, located 940 m downstream of the secondary beam dump, housed the neutrino detector. The apparatus was divided into two pieces: the upstream part functioned as both the neutrino target and hadronic calorimeter; the downstream part was the muon spectrometer (Figure 3.1). Both parts were made of iron instrumented with spark chambers for tracking muons and scintillation counters for triggering and calorimetry. Figure 3.2 shows a detailed view of one of the six (four in E701) moveable target carts. Each cart consisted of approximately 140 cm of steel: between each 10 cm ($\sim$ 1.7 interaction lengths) was a scintillation counter — the active medium of the sampling calorimeter; between each 20 cm ($\sim$ 11 radiation lengths) was a spark chamber for measuring the x– and y–views of the final state muon. The transverse size of the target

was a square with a 3 m edge. The muon spectrometer, a magnetized ($\sim$ 17 kG) steel toroid of radius 1.8 m, was divided into three moveable carts (Figure 3.2). Each consisted of approximately 80 cm of steel: between each 20 cm was a scintillator; between each 40 cm (80 cm in E701) was a spark chamber.

The entire apparatus weighs about 1000 ton of which the target portion weighs 680 tons. The fiducial region (a beam centered cylinder of 50 inch radius and 40 ft length) corresponds to 280 tons for E616 and 160 tons for E701, or in terms of density, 5360 gm/cm^2 and 3090 gm/cm^2 respectively. The probability for a 100 GeV neutrino to interact in the fiducial volume is on the order of 10^{-9}

3.3 The Muon Tracking System

The spark chambers provided the information required to reconstruct the final state muon angle and momentum. By tracking the muon in the target upstream towards the event vertex, its angle was determined and by tracking it through spectrometer, its momentum was determined. Multiple scattering was the limiting factor in the resolution of both measurements.

Each spark chamber was constructed from two 1 in thick aluminum clad Hexcell panels held apart by .5 in plexiglas spacers (see Figure 3.3). Glued to the inside face of each panel were mylar backed planes of wires (1 mm spacing), one each of horizontal and vertical orientation. A gas system provided one atmosphere of a neon-helium-ethanol mixture (89%, 10% and 1% respectively) which was constantly recycled and

purified. The wire planes, in each view, were connected to magnetostrictive wands running along two of the edges of the chamber. When the detector triggered, a 5 kV pulse was applied across the planes of wires. An ionizing particle (e.g. muon) which passes through the chamber just prior to pulsing causes a violent electrical discharge (spark) to occur at the location of the lingering ion trail. An electromagnetic pulse, in turn, occurs in the nearest wires in each view. These pulses travel to magnetostrictive wands creating acoustic pulses which propagate to their ends. The measurement of the arrival time, together with the known velocity of sound in the wand, provide the coordinate measurement.

Transformer coils at the end of each wand translate the acoustic pulses into electrical signals. The readout electronics for each wand (i.e. view) consisted of a preamplifier, a spark chamber interface (SCI) and a multitime digitizer (MTD). The SCI processed the preamplified analog signal (found the center of the pulse and converted it to a digital pulse) and the MTD associated a time and saved each of up to 16 arriving pulses. By comparing the arrival times of these pulses to fiducial pulses generated on each wand, the position of the spark (in each view) could be calculated. The intrinsic spatial resolution of the spark chambers was $\pm$ .5 mm.

The high voltage pulse was $\sim$ 6.5kV for E616 and $\sim$ 10kV for E701. In both experiments the pulse duration was 200 ns. A DC clearing field of 90V (30V) was applied to the chambers in the target (toroid) as well as a 10–ms 600V pulsed field. The memory time was thereby reduced to approximately 30 ms.

Instrumentation of the Wonder Building detector for E701 depleted the capabilities of the Lab E detector. Table 3.1 summarizes the differences between the two experiments.

3.4 Scintillation Counters

Scintillation counters served two purposes in the Lab E apparatus: they constituted the active media for calorimetry and defined the various triggering conditions. All of the counters employed a technique using wavelength shifters to minimize the number of photomultiplier tubes needed to view the large active areas involved. The basic principles governing their operation are described here. Ionization produced by the passage of a charged particle through the counter stimulated the emission of UV light from the primary fluor. This light, having a short attenuation length, $\lambda_{atten} \sim 1$ mm, was absorbed by the secondary fluor and reemitted isotropically as blue light with $\lambda_{atten} \sim 1.5$ m. The blue light entered the light pipes, separated from the counter by an air gap, and was wavelength shifted again to green light with $\lambda_{atten} \sim 3$ m. That green light satisfying the condition of total internal reflection propagated through the guides to the phototubes. While this technique of using successive wavelength shifts allowed a large area to be read out with a small number of phototubes, the spatial variation of the counter response was large: near the corners of the counters, the pulse height resulting from a given energy deposition was as much as twice that of an equivalent deposition at the center.

3.4.1 The Calorimetry Counters

The target portion of the detector functioned as a sampling calorimeter. Hadrons produced at the neutrino interaction vertex initiate a hadronic cascade through subsequent strong interactions in the target steel. Eventually the total energy is absorbed in the steel. The primary mechanism of energy dissipation is through ionization losses. Scintillation counters interspersed in the steel sample these ionization losses. On average, the sum of the sampled energy is proportional to the total hadronic energy.

The target counters were constructed from 10 ft $\times$ 10 ft $\times$ 1 in lucite tanks filled with a mixture of liquid scintillator and wave shifter. Along the edges of the tank were eight 5 ft BBQ doped (wavelength shifter) light pipes that fed into four RCA 6342A photomultiplier tubes. Figures 3.4 show construction details.

The counter front–end electronics (Figure 3.5) distributed phototube pulse–height for triggering and recording. Linear sums of the four phototube pulse–heights were used by the triggers in the form of energies and thresholds. Delayed signals were integrated and digitized by three separate ADCs: individual tubes were read into 15–bit Lecroy 2280 ADCs (minimum ionizing particle typically at $\sim$ 100 channels above pedestal and hadron showers rarely saturate); linear sums of the four phototubes on each counters were read into 10–bit Lecroy 2249 ADCs (minimum ionizing a few channels above pedestal, saturation also rare); phototubes from distant counters were summed to recover catastrophic depositions which saturated the 10–bit ADCs and were read into a separate 10–bit ADC.

A monitoring system for tracking the relative gains of the four phototubes was necessary for proper energy reconstruction. Each counter was provided with an external light source for this purpose. Between beam spills, a fiber optic system delivered a light pulse to the center of each counter and the response of the four tubes was recorded.

3.4.2 The Trigger Counters

While the counters described above were also used for triggering (see below), additional counters located immediately downstream of each toroid cart and at the extreme upstream end of the detector were used exclusively for triggering purposes. The toroid trigger counters were constructed from two 5 ft $\times$ 10 ft $\times$ 1.5 in acrylic sheets, each fitted with four shifter bars and two RCA 56AVP photomultiplier tubes. A veto wall located at the upstream end of Lab E was fashioned out of twelve 10 ft $\times$ 2.5 ft acrylic scintillators, each viewed by two photomultiplier tubes. The total area covered was about 15 ft $\times$ 20 ft.

3.5 Triggering

Several different triggers were used for both physics and diagnostic purposes. Deep inelastic neutrino interactions have a distinct signature: the appearance of energy deposition in the detector with no visible agent initiating it. Charged current events are further distinguished by the presence of a final state muon. All physics triggers

included the condition that the veto wall did not fire ($\overline{\text{VETO}}$) insuring that the interaction was not initiated by a charged particle. This was the only element common to all physics triggers. Additional diagnostic triggers for monitoring the efficiency of the physics triggers and supplying calibration data were also used. A description of the triggers used in the structure function analysis is presented here.

Trigger 1: The Muon Trigger This is the primary charged current trigger used in the structure function analysis. In addition to $\overline{VETO}$, it required a muon to pass through (1) the first target cart and (2) at least the first third of the toroid. No hadron energy requirement was made. Its efficiency is high for the low $y = E_{had}/E_\nu$ events in which the final state muons are very forward.

Trigger 3: The Penetration Trigger This trigger requires (1) $\overline{VETO}$, (2) at least 4 GeV of hadronic energy deposited in the target, and (3) a net penetration (muon or hadronic shower) of at least 16 consecutive planes of counters. Penetration trigger efficiency is high for events with E_{had} above $\sim$ 10 GeV. Apart from a small region (very large–y) the Muon and Penetration triggers cover the entire charged–current phase–space, with a sizable overlap region. Penetration triggers are used in the structure function analysis for events which point towards the T2 counter but range out before reaching it. Penetration triggers are also used in the flux normalization procedure discussed in Appendix A.

Trigger 4: The Efficiency Trigger This diagnostic trigger was redundant with and independent of (except for the $\overline{VETO}$ requirement) the Muon Trigger for

a subset of charged current events. It was used to monitor the efficiency of the Muon Trigger.

Trigger 6: The Straight Through Trigger As the name implies, this trigger selected a sample of muons passing through the entire detector.

Figure 3.6 shows the logic for the muon trigger. S9–S12 and S1–S4 are discriminated signals from the upstream and downstream four counters in the most downstream target cart. T2, T3 and T4 are discriminated signals from the trigger counters downstream from the first, second and third toroid carts. The more stringent trigger requirement for slow spill cycles was imposed to reduce cosmic rays.

3.6 Data Acquisition

The Lab E apparatus was alive during specific times (gates) during the accelerator cycle. In addition to the normal beam gates, triggers were accepted during separate cosmic ray gate to monitor backgrounds from that source. (The integrated time for which cosmic ray triggers were accepted was roughly ten times the actual beam gated time.) Special computer generated triggers were also taken to measure the ADC pedestals. It was necessary to read each triggered event directly into the computer before the next trigger could be accepted[1] The digitized information from the various components of the detector (times from the spark chamber MTDs, ADC channels from

[1]Not all triggers were read out: Trigger sums for each run were recorded with scalars and used to monitor deadtimes.

the phototubes and individual hardware bits) were read into a PDP 11/50 computer using a serial CAMAC interface. The computer performed online diagnostics and spooled the data onto magnetic tape. Beamline information was made available by a Lockheed MAC computer during data taking and recorded as well. The MAC also allowed the experimenter to monitor and make (or request) necessary adjustments to the beamline magnets.

Chapter 4

Event Analysis

4.1 Introduction

In this chapter, the event analysis required for extraction of structure functions is presented. The kinematic quantities required to specify the inclusive reaction

$$\nu_\mu(\overline{\nu}_\mu) + N \rightarrow \mu^-(\mu^+) + X \tag{4.1}$$

are E_μ and θ_μ, the final state muon's energy and angle with respect to the neutrino direction and E_{had}, the hadronic energy of the final state X. Reconstruction of these quantities, along with their resolutions, are presented here. Event cuts and binning in the variables x and Q^2, required for structure function extraction, are also discussed. Finally, energy calibrations and their uncertainties, which contribute to the systematic errors in the extracted structure functions, are discussed.

4.2 Muon Reconstruction

Reconstruction of the final state muon — the determination of its energy, E_μ, and angle at the event vertex, θ_μ, — follows from the analysis of the spark chamber data. Both measurements are largely limited by multiple Coulomb scattering. Multiple scattering induces correlations between the measured points which must be taken into account by the track–fitting procedure. Furthermore, the degree of correlation depends on the muon momentum. A fit to the measured track positions in the target, incorporating momentum dependent multiple scattering correlations, was used to determine θ_μ. The momentum determination required both the angle and projected position of the muon at the toroid front face (i.e. a target track fit) together with the measured track positions in the toroid chambers. This interdependence between target and toroid fits required iteration.

4.2.1 The Target Track: θ_μ, v_x, v_y

First the event vertex position was estimated: The z–position (v_z) was determined by locating the most upstream counter in the target with pulse height above threshold (see Section 4.3). The transverse vertex position (v_x, v_y) was estimated as the centroid of spark chamber hits in the shower. Next, the muon track was found and fit to a straight line (no multiple scattering). The muon momentum was estimated from a fit to the projected position and angle at the toroid front face together with the toroid chamber hit. In the next iteration, both θ_μ and the muon angle at the toroid front face

were determined from a multiple scattering fit (using the estimated momentum) to the target track. The transverse vertex measurement was improved by extrapolating this fit backwards into the shower.

Track parameters (position and angle of the track at the interaction vertex or toroid front face) were determined from a χ^2 minimization,

$$\chi^2 = \sum_i \sum_j (x_i - x_i^p) M_{ij}^{-1} (x_j - x_j^p), \tag{4.2}$$

where the sum is over the measurement planes, i: x_i and x_i^p are the measured and predicted (straight line) track positions respectively. M_{ij} is the error matrix,

$$M_{ij} = \langle (x_i - x_i^p)(x_j - x_j^p) \rangle = \sum_{k=1}^{i} \sigma_k^2 \left[\frac{L_k^2}{3} + \frac{L_k}{2}(z_{kj} + z_{ki}) + z_{ki} z_{kj} \right] + \sigma_0^2 \delta_{ij} \tag{4.3}$$

where L_k is the distance between the kth and $(k+1)^{st}$ measurement planes and $z_{ki} = \sum_{m=k+1}^{i} L_m$ is the distance from the kth to i^{th} plane, and

$$\sigma_k = \frac{.015}{|\mathbf{p}|} (L_k / L_{rad})^{1/2} \tag{4.4}$$

is the mean multiple scattering deflection in the interval L_k. The last term in Equation 4.3, σ_0, is the intrinsic resolution of the spark chamber. In the absence of multiple scattering, $\sigma_k = 0$ and M_{ij} would be diagonal.

From Equation 4.3, it is clear that for a given z–position, the fit position and angle are most sensitive to nearby points. Thus, θ_μ is most sensitive to the measured track positions closest to the interaction point. Its resolution improves for cases where the track positions can be reliably found near the vertex; and, through Equation 4.4, it improves with increasing muon momentum. The minimum tracking

distance from the vertex, limited by spark chamber saturation in the shower region, has been parametrized [38] in terms of the measured hadronic energy deposition. The θ_μ–resolution was parametrized as

$$\sigma_{\theta_\mu} = a + \frac{b}{|\mathbf{p}|} \tag{4.5}$$

where a and b depend on E_{had} and are given in Table 4.1.

4.2.2 Momentum Fitting in the Toroid

Momentum finding was achieved by a χ^2 minimization. The fit parameters were the muon momentum, position and angle at the toroid front face. However in this case, the M_{ij} in equation 4.2 depend on one of the fit parameters. The minimization problem was linearized by alternately calculating the error matrix from the most recent estimate of the momentum and minimizing the χ^2 with fixed error matrix. Convergence was specified by the requirement that the muon momentum change by less then 2% in an iteration. The treatment of fit failures is discussed below. The predicted track points, x_i^p, were calculated by propagating the muon from the toroid front face through the magnetized steel in small steps. In each step, the muon momentum acquired a small transverse component, induced by the magnetic field and a reduction in magnitude associated with the ionization losses (Section 4.2.3).

The magnetic field map used to propagate the muon through the spectrometer is a parametrization of a numerical solution to the magnetostatic boundary value problem for the toroid. Measurements of the magnetic field in the gaps of each steel

disk comprising the toroid and the measured current in the toroidal winding were supplied to the computer program *POISSON* [39]. The field measurements were made with a Hall Probe at several different radii. The measured integral $\int |\mathbf{B}| d\ell$ constitutes one of the absolute energy calibrations used in this analysis. Including uncertainties in the magnetization curve and susceptibility of the steel, the absolute calibration of the spectrometer is estimated accurate to about 1%. This value is supported by Fermilab experiment E595 [40] which used the same spectrometer and a momentum–analysed muon beam for direct calibration.

We can estimate the spectrometer's resolution as follows: For small angles with respect to the toroid axis (a fair approximation for all but the lowest momentum muons), the muon sees a uniform magnetic field and its trajectory lies in a plane. The radius of curvature, r, for a unit charge in a uniform magnetic field is given by $|\mathbf{p}| = .3|\mathbf{B}|r$ (MKSA units and $|\mathbf{p}|$ in GeV/c). For a uniform magnetic field region of length L, the angular deflection is $\theta = L/r$ or $|\mathbf{p}| = .3|\mathbf{B}|L/\theta = p_t/\theta$, where p_t is the transverse momentum kick supplied by the field. (Using 1.7 T as the mean field strength and noting that the toroid steel fills roughly half of the length $L = 9.9$ m, $p_t = 2.45$ GeV/c). Thus, the resolution is limited by the ability to measure the trajectory's net angular displacement. In the expressions below, '$m.s.$' refers to multiple scattering, Δ refers to the effective transverse resolution of the spark chambers, L is the length of the toroid and L_{rad}^{eff} is the effective radiation length of the toroid ($\sim L/2$). Δ is taken to be .5 mm/$\sqrt{3}$, since there are three spark chambers

immediately downstream of the toroid, each with .5 mm resolution.

$$(\delta|\mathbf{p}|)^2 = \left(\frac{p_t}{\theta^2}\right)^2 (\delta\theta)^2 \tag{4.6}$$

$$\delta\theta_{m.s.} = \frac{.015}{|\mathbf{p}|}\left(L/L_{rad}^{eff}\right)^{1/2} \sim \frac{.245}{|\mathbf{p}|} \tag{4.7}$$

$$\delta\theta_{\Delta} = \frac{\Delta}{L/2} \sim .0001 \ll \delta\theta_{m.s.}; \tag{4.8}$$

therefore,

$$(\delta|\mathbf{p}|)^2 \sim \left(\frac{p_t}{\theta^2}\right)^2 (\delta\theta_{m.s.})^2 \Rightarrow \frac{\delta|\mathbf{p}|}{|\mathbf{p}|} \sim 9.6\%. \tag{4.9}$$

A detailed analysis of realistic trajectories, with chamber inefficiencies and bad hits, yields similar results: the resolution is multiple scattering limited and $\delta|\mathbf{p}|/|\mathbf{p}| \simeq 11\%$. This resolution was used in the Monte–Carlo simulation described in Chapter 5.

Several types of momentum reconstruction failures were common. If after five iterations the procedure led to a non–physical momentum, or the χ^2 surface was very flat, or χ^2 was too large ($\chi^2/dof > 9$ for E616 and $\chi^2/dof > 25$ for E701) the event was cut. About 3% (8%) of the E616 (E701) data with $E_{had} > 10$ GeV failed the reconstruction requirements. For the E701 data, roughly a third of the failures were refit by hand. Most failures were found to occur at low momenta. Figure 4.1 shows the reconstruction efficiency as a function of the muon momentum at the toroid front face. The solid line is a fit to the efficiency used in the event Monte Carlo (Chapter 5) to simulate these losses. For the E616 data, all of the failures were refit by hand [41] yielding an overall efficiency of about 99%.

4.2.3 Muon Energy Losses

Muons, like all charged particles, undergo energy losses when passing through matter. Collisions with atomic electrons give rise to a Landau distribution of energy losses with the most probable value of about $dE/dx = 11.6$ MeV/cm for relativistic muons in steel. These losses were accounted for in both momentum fitting and calculation of E_μ, the muon energy at the event vertex. In calculating the x_i^p in Equation 4.2, 11.6 MeV was *subtracted* from the muon energy for each centimeter of path–length as the predicted trajectory was propagated through the toroid. E_μ was calculated by *adding* 11.6 MeV for each centimeter of path–length between the vertex and toroid front face to the energy supplied by the toroid analysis. For muons that ranged out before reaching the toroid, E_μ was determined to within 0.4 GeV from known range–energy in steel.

Catastrophic losses (the high energy tail of the Landau spectrum) were accounted for in two different ways. Between the end of the hadronic shower and the toroid front face, the calorimetry information was used directly. Any excess energy deposition above a minimum ionizing threshold was added back to E_μ. However, within the hadronic shower, there was no way to isolate such losses from the hadron energy on an event by event basis. As a consequence, the measured hadron (muon) energies were systematically higher (lower) then the true values. This effect was simulated in the event Monte Carlo discussed in Section 5.2.1. The simulation required a parametrization of the catastrophic losses as a function of muon momentum. Figure 4.2 shows

cumulative probabilities for catastrophic losses for various muon momenta. These probabilities were determined from a study of "visible" losses between the shower and and toroid front face. Twelve P_μ bins between 0 and 240 GeV/c and 60 energy loss bins between 1.5 and 61.5 GeV were used.

4.3 Hadron Energy Determination

The extraction of hadron shower energy from the calorimeter involved several steps. For each scintillation counter i, pulse–heights from the four photomultiplier tubes was converted to an equivalent number of minimum ionizing particles, N_i^{MIP}. This conversion accounted for both the phototube gain drifts with time and the spatial variation of the counter response. Since the primary mechanism for the shower's energy dissipation is through ionization losses, the total energy is proportional, on average, to $\sum_i N_i^{MIP}$ where the sum is over all counters in the shower. Finally, the hadron shower was obtained by multiplying N^{MIP} by the calibration constant (Section 4.4) and subtracting off the muon's ionization losses.

4.3.1 Muon Peaks

Conversion of phototube pulse–height into an equivalent number of minimizing ionizing particles afforded a convenient means of maintaining relative and absolute calibrations. The calorimeter was continuously exposed to a flux of muons which, on average, deposited a fixed amount of ionization energy in each counter. Figure 4.3 shows the

energy loss spectrum, in units of N^{MIP}s, for muons passing through a counter. The "muon peak" is defined as a measure the most probable pulse–height, in units of pedestal–subtracted ADC channels, corresponding to the passage of a muon through the center of a balanced counter (see Section 4.3.3). Rather then defining the muon peak as the average pulse–height which is subject to fluctuations arising from the tails of the distributions, a truncated mean value was used. The algorithm for determining the truncated mean is unimportant, as long as it is consistently used. (Unfortunately, two different definitions were used in the E616 and E701 running periods. The resolution of these differences are discussed in Section 4.4.) Both algorithms were iterative: the muon peak was defined as the mean value, μ, in the interval 0.0μ to 2.0μ for E616 and 0.1μ to 2.0μ for E701. The muon peaks were used for two different purposes: they were used to monitor and correct for temporal and spatial variation of the counters with time; and they were used in the absolute conversion if N^{MIP} to GeV. The former use relates only to relative calibrations and do not depend on the definition chosen. However, the absolute calibration does depend on the definition of muon peak and is discussed in Section 4.4.

4.3.2 Gain Drifts

Over the course of several months running, the phototube gains drifted from their initial values. At the beginning of each running period, the gains were adjusted to produce equal responses to a radioactive source placed at the the center of each counter. Relative gain shifts were monitored during the run by tracking the relative

pulse–heights in each of the four phototubes induced by hadronic energy depositions in the center of each counter. A set of corrections was calculated and updated roughly every three days and used to restore the original balance. Drifts in the overall gains of each counter were monitored through the muon peaks. These were also updated every three days and used to generate corrections.

4.3.3 Counter Maps

The raw pedestal–subtracted pulse–height is proportional to the number of photons reaching the phototubes. Light attenuation in the scintillator and the shifter bars resulted in a variation with position of the number photons reaching each phototube for a given energy deposition. This variation was modeled and removed by dividing the raw pulse–height in each counter by its own map correction. Since the drifts in gains were removed first, the counter maps were determined only once per running period. Two different techniques were employed to determine the maps. E616 employed a physical model [41] of each counter based on its geometry and attenuation lengths. Pulse–heights in each of the four phototubes from hadronic energy depositions over the area of each counter were fit to this model. In E701, the spatial response was measured directly with muons. For each counter, muon peaks were determined in each 8–inch cell of a 15 $\times$ 15 grid. The resulting grid of muon peaks was then fit to a 4th order polynomial in x and y. Figure 4.4 shows contours of equal response for a typical counter using this technique. The map corrections used in E616 and E701, averaged over the 54 counters in the E701 fiducial region, did not display systematic

differences.

4.3.4 Longitudinal Extent of Hadron Shower

A typical charged–current event has an easily recognized signature in the calorimeter. Looking from the upstream to the downstream end of the target, the signature is characterized by a set of counters with no pulse–height followed by a set of counters with large pulse–height followed by a set of counters with small pulse–height (Figure 4.5). The first region indicates that the interaction is induced by a neutrino. The second region arises from the cascade of hadrons induced by the fragmentation of the target nucleon. Finally, the outgoing muon leaves the shower and continues to deposit energy in each counter until it leaves the calorimeter.

Fluctuations in energy deposition, especially near the downstream end of the shower, cloud the demarcation of the three regions. By scanning the counters from upstream to downstream, the event vertex and the downstream end of the shower were determined as follows. The z–position of the event vertex was defined as the upstream counter of the first occurrence of two consecutive counters with $N_i^{MIP} > .25$. Two different algorithms for determining the z–position of the downstream shower end were used in E616 and E701: In E616 (E701) SHEND was defined as the counter immediately upstream of the first occurrence of three consecutive counters with $N_j^{MIP} < 2(4)$ with $\langle N^{MIP} \rangle < 2(4)$ for the next three beyond that. For a given hadronic deposition, the E616 algorithm yields a longer shower length, hence more counters to sum over. This difference is discussed in the next section.

4.4 Energy Calibrations

A calibration run in 1980 using a beam of momentum–analysed hadrons and muons (E = 25, 50, 90, 200 and 250 GeV) established the conversion from N^{MIP} to GeV and is shown in Figure 4.6. The calibration and resolution are

$$1N^{MIP} = (.2157 \pm .0006) \text{ GeV} \tag{4.10}$$

and

$$\sigma_{E_{had}} = (.72 \pm .20) + (.81 \pm .03)\sqrt{E_{had}} \tag{4.11}$$

where the energies appearing in Equation 4.11 are in GeV. Since the the calibration data was analysed with the E616 muon peak and SHEND algorithms (apart from the muon's energy loss subtraction), N^{MIP} was converted directly to GeV by Equation 4.10. With the E701 algorithms, the same data yielded a definition of muon peak that is larger (lower limit of truncated interval was higher) and a hadron shower length that is smaller, resulting in

$$1N^{MIP} < .2157 \text{ GeV} \tag{4.12}$$

In fact, the E701 data was mistakenly analysed with the calibration given by Equation 4.10. This error was detected and corrected by examining the self–consistency of the data. Consider the miscalibrations of the hadron energy, muon energy and neutrino energy (Chapter 2) resulting in

$$E_{\mu}^{MEAS} \rightarrow (1 + \alpha_{\mu})E_{\mu}^{TRUE} \tag{4.13}$$

$$E_{had}^{MEAS} \rightarrow (1+\beta_{had})E_{had}^{TRUE} \tag{4.14}$$

$$E_{\nu}^{PRED} \rightarrow (1+\delta_{\nu})E_{\nu}^{TRUE}. \tag{4.15}$$

Then the ratio of the measured to predicted energy (from the event Monte Carlo, discussed in Chapter 5) as a function of $y = E_{had}^{MEAS}/E_{\nu}^{MEAS}$ takes the form

$$R(y) = \frac{E_{\nu}^{MEAS}}{E_{\nu}^{PRED}} \tag{4.16}$$

$$= \frac{1+\alpha_{\mu}}{1+\delta_{\nu}}\left[1+\frac{(\beta_{had}-\alpha_{\mu})y}{1+\beta_{had}-(\beta_{had}-\alpha_{\mu})y}\right] \tag{4.17}$$

$$\simeq 1+\alpha_{\mu}-\delta_{\nu}+(\beta_{had}-\alpha_{\mu})y. \tag{4.18}$$

Thus, the slope of $R(y)$ corresponds to the relative hadron energy to muon energy calibration and the offset from unity of the intercept corresponds to to the relative muon energy to neutrino energy (e.g. secondary beam momentum for events near the beam axis – see Chapter 2) calibrations.

The usable y–region for this test is limited by acceptance. For neutrino events with energy E_{ν} and muon angle θ_{μ}, the maximum value of y for which the entire x–interval is accessible is

$$y_{max} = \frac{E_{\nu}(1-\cos\theta_{\mu})}{E_{\mu}(1-\cos\theta_{\mu})+M} \tag{4.19}$$

where M is the nucleon mass and the muon mass has been ignored. Since good geometrical acceptance is limited to $\theta_{\mu} < 200$ mr, only high energy data was used for this test (for $E_{\nu} = 100$ GeV, $y_{max} = .68$), i.e. events induced by neutrinos originating from kaon decays. Figure 4.7 shows the ratio of measured to predicted energy of kaon events for E701 using the calibration relation given by Equation 4.10. A simultaneous

fit to the five energy settings of the form 4.17 was performed in the region $.05 < y < y_{max}$ with seven free parameters: A δ_ν for each setting and an overall α_μ and β_{had} were fit for. The fit parameters, summarized in Table 4.2 yielded $\alpha_\mu = .0107 \pm .0031$ and $\beta_{had} = -.0447 \pm .0049$ with a χ^2 of 71 for 68 degrees of freedom. As expected, the hadron energy calibration given in Equation 4.10 was too low. This procedure was repeated twice, changing only the hadron energy calibration. The final hadron energy adjustment, $E_{had} \rightarrow 1.048 E_{had}$ yielded, for the simultaneous fit, $\alpha_\mu = .0014 \pm .0033$ and $\beta_{had} = -.0015 \pm .0055$. Figure 4.8 shows $R(y)$ after this adjustment and Table 4.2 summarizes the fit. The E616 fits are shown in Table 4.3.

The question remains: Is the 4.8% adjustment applied to the E701 hadron energy numerically consistent with the differences between the E616 and E701 analysis? The effects of the different algorithms discussed above (E616 or E701) were determined by applying them separately to the same data and are summarized here:

- Definition of equivalent number of minimum ionizing particles (Section 4.3.1): The number of ADC channels corresponding to a minimum ionizing particle ($N^{MIP} = 1$) was found to be 5% higher for the E701 algorithm. This results in a lower E_{had} for E701.

- Definition of hadronic shower end (Section 4.3.4): E_{had} is calculated by summing counter pulse–height from the vertex to the shower end. E_{had} was systematically higher for the E701 algorithm by two N^{MIP}s, independent of neutrino energy. For the kaon data, which was used in the E vs. y studies, this amounted to a

0.6% increase in E_{had} for the E701 algorithm.

Taken together, these two effects suggest the need for a 4.4% correction. In addition to the individual algorithm comparisons, an overall comparison was made. Using the E616 and E701 definitions of N^{MIP} on the E616 and E701 data sets respectively, the mean pulse–heights for muons, in N^{MIP}s, was fit to a linear function of muon momentum:

$$\begin{aligned} N_{616}^{MIP} &= 1.218 + .0012 \times \langle p_\mu \text{ (in GeV)} \rangle \\ N_{701}^{MIP} &= 1.177 + .0011 \times \langle p_\mu \text{ (in GeV)} \rangle. \end{aligned} \tag{4.20}$$

This comparison, suggesting the need for 3.5% correction to the E701 hadron energy, together with the 4.4% estimate given above is consistent with the 4.8% adjustment made.

4.5 Structure Function Analysis

Structure function extraction requires measured event sums in bins of $(x, \log Q^2)$. Bin sizes were chosen on the basis of resolution and event statistics. Twelve x–bins,

$$\begin{array}{lll} 0.00 < x < 0.03 & 0.15 < x < 0.20 & 0.40 < x < 0.50 \\ 0.03 < x < 0.06 & 0.20 < x < 0.25 & 0.50 < x < 0.60 \\ 0.06 < x < 0.10 & 0.25 < x < 0.30 & 0.60 < x < 0.70 \\ 0.10 < x < 0.15 & 0.30 < x < 0.40 & 0.70 < x < 1.00 \end{array} \tag{4.21}$$

and twelve $\log_{10} Q^2$ of constant width, $\Delta \log_{10} Q^2 = .2$ between 0.0 and 2.4 were used in this analysis.

Figures 4.9a and 4.9b show the x– and $\log Q^2$–resolutions as a function of x and Q^2: The solid lines indicate the total resolutions; the dotted, dashed and dot–dashed lines indicate the contributions from the θ_μ–, E_μ– and E_{had}–resolutions. All resolutions were calculated using the neutrino flux energy spectrum shown in Figure 2.11. Except for the low–x bins, the x–resolution is dominated by the E_{had}–resolution at low Q^2 and the E_μ–resolution at high Q^2. At small x, the x– and $\log Q^2$–resolutions are both dominated by the θ_μ resolution. Above $x = .05$, the $\log Q^2$–resolution is dominated by the E_μ resolution.

Separate histograms were maintained for each energy setting and secondary type (above or below the energy separatrix). The measured event sums were formed after applying fiducial, acceptance, "quality" and kinematic cuts.

1. Fiducial: Depends on the spatial coordinate of the event vertex

   (a) Longitudinal containment of the hadron shower was insured by cutting events with less then 2 m. of steel between the vertex and downstream end of the calorimeter.

   (b) Muon induced backgrounds were eliminated by requiring at least two quiet counters upstream of the event vertex to augment the $\overline{\text{VETO}}$ requirement of the trigger.

   (c) Transverse containment of the hadron shower was insured by cutting events with a vertex beyond an apparatus centered square of 2.79 m edge. A beam centered circle cut of 1.27 m radius was also applied, eliminating

regions with large map corrections. The latter cut was required for the flux normalization procedure (Appendix A).

2. Acceptance: The straight line projection of the final state muon was required to

   (a) lie inside an apparatus centered circle of 1.75 m. radius at the toroid front face,

   (b) lie inside of an apparatus centered square of 2.79 m. side at the position of the T2 trigger counter,

   (c) have less then 30% of its path length within an apparatus centered cylinder of 12.7 cm. within the toroid.

   For muons that do not range out before T2, these cuts insure good momentum-reconstruction efficiency. These cuts, collectively referred to as the acceptance cut, are discussed further in Section 5.2.

3. Quality: Several cuts to insure the quality of the data were applied. These include:

   (a) Reconstruction failures in both the target and toroid were eliminated.

   (b) A beam centered circle cut of 76.2 cm. was applied to events originating from pion decays. Beyond this, the neutrino flux modeling becomes unreliable, due to uncertainties in the secondary beam's angular divergence.

(c) Data taking cycles were eliminated when the secondary beam profile monitors indicated a large departure from nominal centers.

4. Kinematic: These cuts are related to the above categories but are presented separately to indicate the kinematic range of the reported structure functions:

   (a) Cutting events with $E_\mu < 4$ GeV insures that the final state muon was energetic enough to penetrate the longest anticipated hadron shower.

   (b) Cutting events with $E_{had} < 10$ Gev limits the reliance on an extrapolation of the calorimeter's calibration. The calibration run measured the calorimeter response down to 25 GeV.

   (c) Cutting events with $\theta_\mu > 200$ mrad. insured reasonable geometric acceptance.

Table 4.4 traces the measured event sums through the various cuts. Measured event distributions are shown in Chapter 5 where they are compared with the Monte Carlo generated distributions

Chapter 5

Structure Function Extraction

5.1 Overview

Apart from small corrections (typically less then a few percent) discussed below, the differential cross section for the reaction $\nu(\overline{\nu}) + N \rightarrow \mu^-(\mu^+) + X$ takes the form (See Chapter 1)

$$\frac{d^2\sigma^{\nu(\overline{\nu})}}{dx d\log Q^2}(E, x, Q^2) = \frac{G_F^2 M E y}{\pi}\left[\left(1 - y - \frac{Mxy}{2E} + \frac{y^2}{2}\frac{1 + 4M^2x^2/Q^2}{1 + R(x, Q^2)}\right) F_2(x, Q^2) \pm \left(y - \frac{y^2}{2}\right) xF_3(x, Q^2)\right]. \quad (5.1)$$

The structure function $R(x, Q^2) \equiv \sigma_L/\sigma_T$ appearing in Equation 5.1, the ratio of cross sections for longitudinally and transversely polarized $W^\pm$, is not measured in this analysis. Instead, the structure functions F_2 and xF_3 are extracted with an assumed parameterization of R predicted by QCD (See Appendix B).

It follows from Equation 5.1 that for *fixed* neutrino energy E, the structure function F_2 (xF_3) is proportional to the sum (difference) of the neutrino and antineutrino

cross sections. Since the cross sections depend on (E, x, Q^2) while the structure functions depend only on (x, Q^2), cross sections measured at different energies must be averaged: The mean cross sections, evaluated at (x_0, Q_0^2) and averaged over the flux energy spectrum, are *defined* as:

$$\left\langle \frac{d^2\sigma^{\nu(\bar{\nu})}}{dx\,d\log Q^2} \right\rangle_{\nu(\bar{\nu})} (x_0, Q_0^2) \equiv \frac{1}{\int dE\Phi^{\nu(\bar{\nu})}(E)} \int dE\Phi^{\nu(\bar{\nu})}(E) \frac{d^2\sigma^{\nu(\bar{\nu})}}{dx\,d\log Q^2}(E, x_0, Q_0^2). \quad (5.2)$$

Here $\Phi^{\nu(\bar{\nu})}(E)dE$ is the number of neutrinos (antineutrinos) in the energy interval $[E, E + dE]$. The relation between the structure functions and the averaged cross sections is obtained by averaging Equations 5.1 over the same flux spectra:

$$\left\langle \frac{d^2\sigma^{\nu}}{dx\,d\log Q^2} \right\rangle_{\nu} (x_0, Q_0^2) = \langle a_2 \rangle_\nu F_2(x_0, Q_0^2) + \langle a_3 \rangle_\nu x F_3(x_0, Q_0^2) \quad (5.3)$$

$$\left\langle \frac{d^2\sigma^{\bar{\nu}}}{dx\,d\log Q^2} \right\rangle_{\bar{\nu}} (x_0, Q_0^2) = \langle a_2 \rangle_{\bar{\nu}} F_2(x_0, Q_0^2) - \langle a_3 \rangle_{\bar{\nu}} x F_3(x_0, Q_0^2) \quad (5.4)$$

where a_2 and a_3 are the coefficients of F_2 and xF_3 appearing in Equation 5.1. Note that $\langle a_i \rangle_\nu \neq \langle a_i \rangle_{\bar{\nu}}$ since the neutrino and antineutrino flux spectra have different shapes (See Figure 2.11). Flux–weighted mean values of y and y^2 for neutrinos and antineutrinos are listed in Table 5.2.

The extraction of structure functions was complicated by various experimental effects and model corrections. Resolution smearing of the measured quantities, acceptance and finite event statistics required a Monte Carlo simulation for the calculation of differential cross sections. Corrections to Equation 5.1 were required to describe scattering off a real iron target. Both the experimental and model corrections required for the structure function extraction depended on the structure functions

themselves. A self–consistent, iterative approach was used: the required corrections for the $(n+1)^{th}$ iteration were parametrized in terms of the nth iteration structure functions. Figure 5.1 depicts the structure of the analysis presented in this chapter.

In Section 5.2, the derivation of mean cross sections from measured event sums and flux integrals is presented. Corrections to Equation 5.1 for scattering off a physical iron target are discussed in Section 5.3. The techniques used to calculate the statistical errors and estimate the systematic errors are presented in Sections 5.4 and 5.5. Details of the differential cross section modeling and flux normalizations can be found in the appendices.

5.2 Differential Cross Sections: Experimental Corrections

Experimentally, the measured cross sections in a given kinematic bin takes the form

$$\left\langle \frac{d^2\sigma^{\nu(\bar{\nu})}}{dx d\log Q^2} \right\rangle_{\nu(\bar{\nu})}^{meas} (x_0, Q_0^2) = C^{\nu(\bar{\nu})} \frac{\sum data^{\nu(\bar{\nu})}}{\int dE \Phi^{\nu(\bar{\nu})}(E) \Delta x \Delta \log Q^2} \tag{5.5}$$

where $\sum data^{\nu(\bar{\nu})}$ is the event sum in the (x, Q^2) bin and $C^{\nu(\bar{\nu})}$ are corrections for the following experimental effects:

- Geometrical Acceptance - The finite transverse size of the apparatus induces an inefficiency for triggering on events with large θ_μ.

- Resolution Smearing - The measured quantities are smeared by the intrinsic resolution of the apparatus.

- Bin Center - The variation of the cross sections within a finite bin shifts the mean x and Q^2 values from the geometric center (x_0, Q_0^2).

These effects were modeled with a Monte Carlo simulation. As input, the calculation used the flux spectra, a model for the physical differential cross sections (see Appendix C), the detector geometry and a parametrization of its resolution. The corrected mean differential cross section for neutrinos or antineutrinos is:

$$\left\langle \frac{d^2\sigma}{dx d\log Q^2} \right\rangle^{meas} (x_0, Q_0^2) = \frac{\sum data}{\int dE\Phi(E)\Delta x \Delta \log Q^2} \times$$
$$\frac{\sum SMR^{A=1}}{\sum SMR} \times \frac{\sum GEN^{A=1}}{\sum SMR^{A=1}} \times \frac{\Delta x \Delta \log Q^2}{\sum GEN^{A=1}} \int dE\Phi(E) \frac{d^2\sigma^{model}}{dx d\log Q^2}(E, x_0, Q_0^2)$$

where $\sum GEN$ and $\sum SMR$ are the Monte Carlo event sums before and after resolution smearing in the (x, Q^2) bin. $A = 1$ indicates perfect acceptance and σ^{model} is the cross section assumed in the Monte Carlo. The individual corrections appearing on the second line are: acceptance correction, which depend on the smeared quantities; resolution smearing correction; and bin center corrections where the numerator ($\Delta x \Delta \log Q^2$ times integral) corresponds to all events occurring at the geometric center as would be the case for an infinitesimal bin size. Each of these corrections, along with their statistical errors (from the Monte Carlo) are listed in Table 5.1. After factoring, the expression takes a much simpler form:

$$\left\langle \frac{d^2\sigma}{dx d\log Q^2} \right\rangle^{meas} (x_0, Q_0^2) = \frac{\sum data}{\sum SMR} \times \left\langle \frac{d^2\sigma^{model}}{dx d\log Q^2} \right\rangle (x_0, Q_0^2). \tag{5.6}$$

Thus, it was only necessary to accumulate Monte Carlo sums for smeared events passing the acceptance requirements.

5.2.1 The Event Monte Carlo

The Monte Carlo was broken into two pieces, as indicated in Figure 5.1 The DST writer generated events with unit weight according to the neutrino spectrum together with an *initial* parameterization of the cross sections. For each setting of the secondary beam, events were generated such that in a given energy and radial interval

$$d^2N_j(E,r) = \rho L N_A \int_0^1 dx \int_0^1 dy \phi_j(E,r) \frac{d^2\sigma^{model}}{dxdy}(E,x,y) dE r dr. \tag{5.7}$$

Here, $\rho L N_A$ is the number of target nuclei per cm^2 and j labels the flux category (neutrinos originating from pion, kaon or wide–band decays). For j = pion or kaon, $\phi_j(E,r)$ are the *unnormalized* neutrino fluxes (# of ν's/GeV/cm^2) at Lab E. Their energy and radial dependance are discussed in Chapter 2 and their normalizations were roughly estimated. The required adjustments to their normalizations are discussed in Section 5.2.3 and Appendix A. $\phi_{WB}(E,r)$ is the *normalized* wide–band flux, also discussed in Chapter 2.

The cross section model used in the event generation was constructed from an initial parametrization of the structure functions (0th iteration). Within each energy interval, the scaling variables x and y were thrown with the cross section as the parent distribution. The z-coordinate of each event vertex was thrown from a distribution proportional to the target density and the azimuthal angle was thrown flat. A separate file was made for each primary setting used in the analysis. The number of generated events was chosen to be roughly ten (twenty) times the measured number of events for positive (negative) settings.

A separate program was used to calculate the Monte Carlo event sums: iterating was accomplished by re–weighting the DST events by the ratio of new to initial cross sections. For every DST event, the generated quantities were smeared in accordance with the resolutions presented in Chapter 4. The event weight was calculated in terms of the generated quantities, while the kinematic and acceptance cuts were applied to the smeared variables before binning. Since each iteration used the same events, statistical fluctuations between iterations were eliminated.

Resolution smearing of the generated events was carried out in several steps. First, the hadron shower length was thrown from a gaussian distribution. Its mean and rms were parametrized in terms of the generated hadron energy,

$$\begin{aligned} \langle L \rangle &= -6.4 + 64.8 \log_{10}(E_{had}) \\ \sigma_{\langle L \rangle} &= 17.1 + 6.5 \log_{10}(E_{had}), \end{aligned} \tag{5.8}$$

where the lengths are in cm of steel and E_{had} is in GeV. This parametrization was obtained from data taken with the apparatus placed in a momentum–analysed hadron beam [42]. Catastrophic energy losses for the muon within the shower were thrown from the probability distributions of Figure 4.2. Since this energy is not accessible experimentally, it was added to the generated hadron energy and subtracted from the generated muon energy. The smeared hadron energy was then calculated as:

$$E_{had} \rightarrow N \frac{\sigma^2_{E_{had}}}{E_{had}} \tag{5.9}$$

where N was thrown from a Poisson distribution with mean μ, constructed from the

calorimeter resolution:

$$\begin{aligned} \mu &= \left(\frac{E_{had}}{\sigma_{E_{had}}}\right)^2 \\ \sigma_{E_{had}} &= 0.72 + 0.81\sqrt{E_{had}}. \end{aligned} \tag{5.10}$$

For large E_{had} (large μ), the hadron energy smearing becomes gaussian, while at low E_{had} the poisson smearing insures a non–negative result.

θ_μ, the angle of the final state muon, was then thrown from a gaussian distribution with rms given by

$$\sigma_{\theta_\mu} = a + \frac{b}{|\mathbf{P}_\mu|} \tag{5.11}$$

where a and b depend on the smeared hadron energy and are given in Table 4.1. Finally, the muon was propagated to the spectrometer front face with ionization and catastrophic energy losses subtracted. The muon's smeared momentum at the spectrometer front face was thrown from a gaussian distribution with an rms given by

$$\sigma_{p_\mu} = 0.11 p_\mu. \tag{5.12}$$

Ionization losses incurred from the vertex to the spectrometer and catastrophic losses from the hadron shower end to the spectrometer were then added back to the smeared muon energy yielding the smeared muon energy at the event vertex.

The acceptance cut discussed in Section 4.5 was designed to guarantee that passing events could, in general, be momentum analysed: Since the polarity of the spectrometer current was chosen to focus (bend towards beam axis) the final state muon (μ^-'s

for positive settings and μ^+'s for negative settings of the secondary beam), the requirement that the muon's straight line projection intersects the trigger counter is a conservative guarantee that the apparatus triggers. The additional requirements that the straight line projection intersect the front face of the toroid and spend less then 30% of its path length inside the hole (zero field region) eliminated the small number of events with muons passing through little or no magnetic field. Thus, these geometric requirements on the final state muon allowed for a simple means of acceptance simulation.

As discussed in Section 4.2, the reconstruction efficiency for events passing these cuts was not perfect. The solid curve in Figure 4.1 was used to simulate the reconstruction efficiency for E701 by cutting Monte Carlo events with $r > \epsilon_{eff}(P_\mu^{FF})$ where r is a random number on (0,1) and P_μ^{FF} is the smeared muon momentum at the toroid front face. For E616, all reconstruction failures were refit by hand. The residual failures (about 1%) were assumed to independent of momentum and the efficiencies given in Table 4.6 of Reference [41] were used.

The inefficiencies associated with the veto deadtime (common to all neutrino triggers) and target track reconstruction failures do not depend on the event kinematics. Thus, these inefficiencies only affected the overall levels of the Monte Carlo predictions. These small, unknown levels were combined with and treated as part of the unknown flux levels, discussed in the next section and Appendix A

Figures 5.2a–d show comparisons between the Monte Carlo and data for the raw

measured quantities: (a) beam centered event radius; (b) θ_μ; (c) E_{had}; and (d) E_μ. Figures 5.3a–c show the comparisons for the derived quantities: (a) $E_\nu = E_\mu + E_{had}$; (b) $y = E_{had}/E_\nu$; and (c) $x \approx E_\mu E_\nu \theta_\mu^2$. Figures 5.4a and b show event sums in each x and $\log Q^2$ bin.

5.2.2 Relative Flux Determination

The event Monte Carlo was used to calculate the $\sum SMR$ appearing in Equation 5.6. Since these event sums, generated through Equation 5.7, are proportional to the unknown flux levels, a total of 30 adjustments (pion and kaon fluxes for each of the fifteen energy settings) to the ϕ_j's were required. These adjustments were obtained in two steps: Relative flux normalizations for the settings of each polarity (seventeen relative adjustments for the positive settings and eleven for the negative) were fixed by assuming the the energy dependance predicted by the cross section model. At each secondary setting, the adjustments were found by forcing agreement between measured and predicted event sums, accumulated over the kinematic range used in the structure function analysis. The adjustments calculated at each iteration of the extraction procedure reflected the cross section's energy dependance predicted by the previous iteration's structure functions. Since the cross section model appearing in Equation 5.7 was constructed from structure functions (depending only on x and Q^2) multiplying known kinematic factors, the procedure is internally consistent. However, this procedure can not provide the overall level or the relative neutrino–to–antineutrino level. These remaining normalizations are described in Appendix A.

For each primary setting, six categories of Monte Carlo event sums were maintained: events were generated from three flux categories (neutrinos originating from pion, kaon and wide–band decays) each of which could lie above or below the energy separatrix after smearing. These sums were then compared with the measured "pion" and "kaon" event sums to determine the (relative) adjustments to the ϕ_j in Equation 5.7:

$$\begin{aligned} N_\pi^i &= \frac{1}{S}\left[f_\pi^i M_{\pi\to\pi}^i + f_K^i M_{K\to\pi}^i + M_{WB\to\pi}^i\right] \\ N_K^i &= \frac{1}{S}\left[f_\pi^i M_{\pi\to K}^i + f_K^i M_{K\to K}^i + M_{WB\to K}^i\right] \end{aligned} \tag{5.13}$$

where N_π^i (N_K^i) is the observed event sum at secondary setting i with $E_\nu < E^{SEP}(r)$ ($E_\nu > E^{SEP}(r)$). S is the statistical factor indicating the relative number of simulated to measured events: $S = 10$ (20) for positive (negative) settings. $M_{a\to b}$ are the re–weighted Monte Carlo sums for events of generated type a and reconstructed type b. All sums were accumulated over the entire kinematic range used in the structure function analysis. The $M_{\pi\to K}$ and $M_{K\to\pi}$ account for events miss–classified on the basis of the energy separatrix.

The Monte Carlo event sums appearing in Equation 5.6, for each $(x, \log Q^2)$ bin, were expressed in terms of the f_π^i's and f_K^i's and the event sums generated by Equation 5.7:

$$\sum SMR^{\nu(\bar\nu)} = f_{abs}^{\nu(\bar\nu)} \frac{1}{S^{\nu(\bar\nu)}} \sum_{\substack{i=\nu(\bar\nu)\\ \text{sets.}}} \sum_{a=\pi,K} \sum_{b=\pi,K} f_a^i \left(\sum SMR_{a\to b}\right)^i . \tag{5.14}$$

The constant appearing in front of the sum is the overall neutrino (antineutrino) adjustment, also calculated at each iteration, and is discussed in Appendix A. At

each iteration, the $(\sum SMR_{a\to b})^i$ are sums of weights, each calculated as the ratio of the cross section from the previous iteration to the cross section appearing in Equation 5.7. These weights were calculated in terms of the *generated* variables, while the event cuts and binning were based on the *smeared* variables. The Monte Carlo event sums from the wideband component, proportional to the measured intensity of primary protons on target, were subtracted off the measured event sums:

$$\sum data^{\nu(\bar{\nu})} = \sum_{\substack{i=\nu(\bar{\nu})\\ \text{sets.}}} \left[\sum data^i - \frac{1}{S^{\nu(\bar{\nu})}}\left(\sum SMR_{WB\to\pi,K}\right)^i\right]. \tag{5.15}$$

Finally, the total neutrino (antineutrino) flux is given by

$$\Phi^{\nu(\bar{\nu})}(E) = f_{abs}^{\nu(\bar{\nu})} \sum_{\substack{i=\nu(\bar{\nu})\\ \text{sets.}}} \sum_{a=\pi,K} f_a^i \Phi_a^i(E). \tag{5.16}$$

These flux spectra are shown in Figure 2.11. They were used to calculate the flux averaged quantities (Equation 5.2) appearing in Equations 5.24 and 5.25

5.3 Differential Cross Sections: Model Corrections

Various effects not present in Equation 5.1 are required of a physical description of neutrino–iron scattering. Physical effects incorporated in the cross section model include:

- Non-Isoscalar Correction: Iron has a 6.85% excess of neutrons over protons. This increases the neutrino and decreases the antineutrino cross sections relative to an isoscalar target.

- Strange Sea Correction: $s - c \neq 0$ results $xF_3^{\nu} \neq xF_3^{\bar{\nu}}$ The strange sea was assumed to have the same functional dependance on x and Q^2 as the nonstrange sea: $s = \bar{s} = \frac{1}{2}\bar{u}$ or $\frac{1}{2}\bar{d}$ [43]. the charmed sea was assumed zero.

- Charm Production Threshold Correction – Production of a heavy flavor (charm) results in a suppression of the inclusive cross sections. The slow rescaling model [44] with $m_c = 1.5\text{GeV/c}^2$ was used to calculate this effect. This correction was required for parton model tests (Section 6.3) and QCD fits (Section 6.4)

- Radiative Corrections – Colinear emission of photons by the outgoing muon shifts the observed muon energy down and hadron energy up. The measured differential cross sections were corrected using the prescription of De Rújula *et al.* [45].

- $W^{\pm}$ Propagator – This was absorbed into the definition of G_F^2:

$$G_F^2 \rightarrow \frac{G_F^2}{(1 + (Q^2/M_W^2)^2)} \tag{5.17}$$

  where M_W was taken to be 81.8 GeV/c^2 [46].

These physical effects were "removed" from the measured cross sections to produce "corrected" structure functions. Removal of these effects allow direct comparisons with experiments using using different probes and targets as well as various quark–based models.

The physical cross section model was constructed from a modified Buras–Gaemers parameterization of quark momentum densities [47]. These include the proton's va-

lence quark densities, $xu_v(x,Q^2)$ and $xd_v(x,Q^2)$, a single sea density, $xS(x,Q^2)$, and $R(x,Q^2)$. A discussion of their parametrizations is presented in Appendix B. These same momentum densities were also used to parametrize the corrected structure functions:

$$\begin{aligned} F_2(x,Q^2) &= \frac{1+R(x,Q^2)}{1+4M^2x^2/Q^2}\left[xu_v(x,Q^2)+xd_v(x,Q^2)+xS(x,Q^2)\right] \\ xF_3(x,Q^2) &= xu_v(x,Q^2)+xd_v(x,Q^2). \end{aligned} \tag{5.18}$$

The physical cross sections were modelled as follows:

1. *Effective* quark momentum densities for iron, $q^{\nu(\bar{\nu})}$ and $\bar{q}^{\nu(\bar{\nu})}$ incorporating flavor asymmetries and charm production were constructed from the momentum densities mentioned above.

2. Uncorrected (i.e. physical) structure functions were formed from these quark densities:

$$2x\mathcal{F}_1^{\nu(\bar{\nu})} = \left[q^{\nu(\bar{\nu})}+\bar{q}^{\nu(\bar{\nu})}\right] \tag{5.19}$$

$$\mathcal{F}_2^{\nu(\bar{\nu})} = \frac{1+\mathcal{R}^{\nu(\bar{\nu})}(x,Q^2)}{1+4M^2x^2/Q^2}2x\mathcal{F}_1^{\nu(\bar{\nu})} \tag{5.20}$$

$$x\mathcal{F}_3^{\nu(\bar{\nu})} = \left[q^{\nu(\bar{\nu})}-\bar{q}^{\nu(\bar{\nu})}\right] \tag{5.21}$$

3. These were then used to form neutrino (antineutrino) cross sections:

$$\frac{d^2\sigma^{\nu(\bar{\nu})}}{dx\,d\log Q^2} = \frac{G^2MEy}{\pi}\left[\frac{y^2}{2}2x\mathcal{F}_1^{\nu(\bar{\nu})}+\left(1-y-\frac{Mxy}{2E}\right)\mathcal{F}_2^{\nu(\bar{\nu})}\pm\left(y-\frac{y^2}{2}\right)x\mathcal{F}_3^{\nu(\bar{\nu})}\right] \tag{5.22}$$

4. These cross sections were then treated as the Born terms in the radiative formulations.

Details of this construction are contained in Appendix C.

Radiative and propagator effects were "removed" from the measured differential cross sections through a modification of Equation 5.6:

$$\left\langle \frac{d^2\sigma}{dx\,d\log Q^2} \right\rangle_{RP}^{meas} (x_0, Q_0^2) = \frac{\sum data}{\sum SMR} \times \left\langle \frac{d^2\sigma_{RP}^{model}}{dx\,d\log Q^2} \right\rangle (x_0, Q_0^2) \tag{5.23}$$

where RP indicates radiative and propagator effects have been removed and σ_{RP}^{model} is given in Equation 5.22. The remaining effects were "removed" from the measured cross sections through the modification of Equations 5.3 and 5.4:

$$\left\langle \frac{d^2\sigma^{\nu}}{dx\,d\log Q^2} \right\rangle_{RP}^{meas} = \langle a_2 \rangle_{\nu} F_2 + \langle a_3 \rangle_{\nu} x F_3 + \delta^{\nu} \tag{5.24}$$

$$\left\langle \frac{d^2\sigma^{\bar{\nu}}}{dx\,d\log Q^2} \right\rangle_{RP}^{meas} = \langle a_2 \rangle_{\bar{\nu}} F_2 - \langle a_3 \rangle_{\bar{\nu}} x F_3 + \delta^{\bar{\nu}} \tag{5.25}$$

where

$$\delta^{\nu(\bar{\nu})} = \left\langle \frac{d^2\sigma_{RP}^{\nu(\bar{\nu})}}{dx\,d\log Q^2} - \frac{d^2\sigma_0^{\nu(\bar{\nu})}}{dx\,d\log Q^2} \right\rangle_{\nu(\bar{\nu})} . \tag{5.26}$$

The unknown structure functions appearing in Equation 5.24 and 5.25 were solved for in terms of the measured, radiatively corrected cross sections. The cross sections appearing in Equation 5.26 are the modeled quantities: $\sigma_0^{\nu(\bar{\nu})}$ is obtained by substituting Equations 5.18 in Equation 5.1 and $\sigma_{RP}^{\nu(\bar{\nu})}$ is given by Equation 5.22. Figures 5.5a and 5.5b show the effects of the various model corrections on the extracted structure functions. The curves were obtained by turning off each effect one at a time.

The measured, differential cross sections, with radiative and propagator corrections applied (lefthand sides of Equations 5.24 and 5.4) are listed in Table 5.2. The mean values of y and y^2, from which $\langle a_2 \rangle_{\nu(\bar{\nu})}$ and $\langle a_3 \rangle_{\nu(\bar{\nu})}$ can be calculated are also shown.

5.4 Statistical Errors

The error matrix, for a given kinematic bin, was expressed in terms of the likelihood function, $\mathcal{L}$. The probability of observing M^ν neutrino and $M^{\bar{\nu}}$ antineutrino events in a bin is given by

$$\mathcal{L}(F_2, xF_3) = \frac{\mu_\nu^{M^\nu} e^{-\mu_\nu}}{M^\nu!} \cdot \frac{\mu_{\bar{\nu}}^{M^{\bar{\nu}}} e^{-\mu_{\bar{\nu}}}}{M^{\bar{\nu}}!} \tag{5.27}$$

where the "true" numbers of events are given by

$$\mu_{\nu(\bar{\nu})} = \Phi^{\nu(\bar{\nu})} \left[\langle a_2 \rangle_{\nu(\bar{\nu})} F_2 \pm \langle a_3 \rangle_{\nu(\bar{\nu})} x F_3 + \delta^{\nu(\bar{\nu})} \right]. \tag{5.28}$$

Here, Φ represents the flux, including the experimental and radiative corrections and is given by

$$\Phi^{\nu(\bar{\nu})} = \left(\sum SMR^{\nu(\bar{\nu})} \right) \left[\left\langle \frac{d^2 \sigma_{RP}^{\nu(\bar{\nu})}}{dx\, d\log Q^2} \right\rangle_{\nu(\bar{\nu})} \right]^{-1} \tag{5.29}$$

The error matrix V can be expressed [48] in terms of the likelihood function:

$$(V^{-1})_{ij} = -\frac{\partial^2 \log \mathcal{L}(F_2, xF_3)}{\partial F_i \partial F_j} \tag{5.30}$$

Thus,

$$(V^{-1})_{F_2 F_2} = \frac{(\Phi^\nu \langle a_2 \rangle_\nu)^2}{\sigma_{M^\nu}^2} + \frac{(\Phi^{\bar{\nu}} \langle a_2 \rangle_{\bar{\nu}})^2}{\sigma_{M^{\bar{\nu}}}^2} \tag{5.31}$$

$$(V^{-1})_{xF_3xF_3} = \frac{(\Phi^{\nu}\langle a_3\rangle_{\nu})^2}{\sigma^2_{M^{\nu}}} + \frac{(\Phi^{\bar{\nu}}\langle a_3\rangle_{\bar{\nu}})^2}{\sigma^2_{M^{\bar{\nu}}}} \tag{5.32}$$

$$\begin{aligned}(V^{-1})_{F_2xF_3} &= (V^{-1})_{xF_3F_2} \\ &= \frac{(\Phi^{\nu})^2\langle a_2\rangle_{\nu}\langle a_3\rangle_{\nu}}{\sigma^2_{M^{\nu}}} - \frac{(\Phi^{\bar{\nu}})^2\langle a_2\rangle_{\bar{\nu}}\langle a_3\rangle_{\bar{\nu}}}{\sigma^2_{M^{\bar{\nu}}}},\end{aligned} \tag{5.33}$$

where the bin contents in the denominator have been written in terms of their Poisson errors:

$$M^{\nu(\bar{\nu})} \equiv \sigma^2_{M^{\nu(\bar{\nu})}} \tag{5.34}$$

Instead of using the measured event sums ($M^{\nu(\bar{\nu})}$) to calculate the error matrix, predicted event sums were used. This is especially important for bins with small event statistics. The contribution to the bin content errors from the finite Monte Carlo statistics was added in quadrature:

$$\sigma^2_{M^{\nu(\bar{\nu})}} \rightarrow \sum SMR^{\nu(\bar{\nu})} + \left(\frac{f^{\nu(\bar{\nu})}_{abs}}{S^{\nu(\bar{\nu})}}\right)^2 \sum_{\substack{i=\nu(\bar{\nu})\\ \text{sets.}}} \sum_{\substack{a,b=\\ \pi,K}} (f^i_a)^2 \left(\sum SMR^2_{a\rightarrow b}\right)^i \tag{5.35}$$

where $S^{\nu(\bar{\nu})}$ is the statistical factor and $\sum SMR^2_{a\rightarrow b}$ are the sum of the square of the weights (See Equation 5.14 and text following). The structure functions along with their errors are given in Table 5.3. The square roots of the diagonal elements of V are ΔF_2 and ΔxF_3 and the off diagonal piece is $\Delta F_2 \Delta xF_3$.

5.5 Systematic Errors

Systematic errors in the structure functions, arising from uncertainties in the various quantities entering into the analysis, have been estimated. All systematic errors were estimated from Monte Carlo calculations. This is especially important for errors

which effect the measured bin contents since the systematic errors are smaller then the statistical errors. A nominal "data" set was first generated using the Monte Carlo. The event statistics were a factor of 10 and 20 times higher then the actual data for neutrinos and antineutrinos respectively. From these, a nominal set of structure functions was was generated (i.e. $\sigma^{meas} = \sigma^{model}$ in Equation 5.6). For each systematic effect considered, a new "data" set (hadron or muon energy calibration uncertainties) or flux spectrum (secondary energy calibration, angular dispersion or relative neutrino to antineutrino normalization uncertainty) was generated. A new structure set was then extracted from the new "data" and or fluxes using the procedure described in this chapter. Absolute neutrino and antineutrino flux normalizations were determined for each set as described in Appendix A.

Tables 5.4a and 4b list F_2 and xF_3 along with their statistical errors and estimates of the following systematic errors: The first three columns are the estimated changes in the structure functions for a 1% increase the hadron energy, muon energy and secondary beam energy calibrations. The fourth column shows the changes for a simultaneous 1% increase in all three. The last two columns show the changes for a 1.7% increase in the relative antineutrino–to–neutrino flux normalization (keeping the sum of neutrino and antineutrino total cross section slopes fixed, that is $\Phi^{\nu} \rightarrow 0.995\Phi^{\nu}$ and $\Phi^{\bar{\nu}} \rightarrow 1.011\phi^{\bar{\nu}}$) and a 10% increase in the angular dispersion of the secondary beam.

Chapter 6

Comparisons and Conclusions

In this final chapter, the structure functions presented in the previous chapter are compared with other experimental results and some of the theoretical expectations discussed in Chapter 1. Comparisons with recent neutrino scattering results are discussed in Section 6.1. For these comparisons, structure functions have been extracted from the present data set with the same assumptions (total cross section slopes, strange sea, $R = \sigma_L/\sigma_T$ and charm production) that were used in the other analyses. Comparisons with charged lepton scattering results are presented in Section 6.2 in the context of the Quark Parton Model (QPM) prediction, $F_2^{\nu N} \approx \frac{5}{18} F_2^{\ell^\pm N}$. Another QPM test discussed is the Gross–Llewellyn Smith sum rule, which measures the valence quark content of the nucleon. In Section 6.3, observed deviations from scaling behaviour predicted by the QPM are analysed in the context of perturbative Quantum Chromodynamics (QCD) through the Altarelli–Parisi [28] evolution equations. Fits to these equations were used to determine the QCD scale parameter, Λ, and

"QCD–improved" parton densities.

6.1 Comparisons With Other Neutrino Experiments

Comparisons of structure function results from different neutrino experiments are complicated by different assumptions entering into their extraction from the measured differential cross sections. In practice, neutrino experiments using isoscalar (or near isoscalar) targets report two structure functions, F_2 and xF_3. In reality, there are six structure functions (neglecting structure functions multiplying terms proportional to lepton masses) for a given target, T — $2xF_1^{\nu T}, 2xF_1^{\bar{\nu}T}, F_2^{\nu T}, F_2^{\bar{\nu}T}, xF_3^{\nu T}$ and $xF_3^{\bar{\nu}T}$:

$$\frac{d^2\sigma^{\nu(\bar{\nu})T}}{dxdy} = \frac{G^2ME}{\pi}\left[\frac{y^2}{2}xF_2^{\nu(\bar{\nu})T} + \left(1 - y - \frac{Mxy}{E}\right)F_2^{\nu(\bar{\nu})T} + y\left(1 - \frac{y}{2}\right)xF_3^{\nu(\bar{\nu})T}\right], \tag{6.1}$$

where the cross sections shown are radiatively corrected. These structure functions could be extracted, in principle, by fitting the y–dependance of the differential cross sections in each (x, Q^2)–bin. However this is not what is done. Instead, "F_2" and "xF_3" are extracted by combining sums and differences of measured neutrino and antineutrino differential cross sections as discussed in Chapter 5; the results depend on their assumed relationship to the six structure functions mentioned above. Also, since neutrino and antineutrino cross sections are combined, the resulting structure functions depend in a non–trivial way on the assumed total cross section slopes. Table 6.1 lists the assumptions used in the structure function extraction for each experiment considered. Structure functions were extracted from the data set used

in this analysis incorporating each set of assumptions used in the other analyses, allowing direct comparisons.

A summary of the assumed relations between the six structure functions appearing in Equation 6.1 and reported isoscalar structure functions is presented here. Since $R = \sigma_L/\sigma_T$ is small[1], $2xF_1 \approx F_2$ and an *assumed* parametrization of R is used to eliminate $2xF_1$:

$$2xF_1^{\nu(\bar{\nu})T} = \frac{1 + Q^2/\nu^2}{1 + R(x, Q^2)} F_2^{\nu(\bar{\nu})T} \tag{6.2}$$

where $R = R^{\nu T} = R^{\bar{\nu} T}$ is usually assumed. Common choices of R are $R = 0$ and $R =$"R_{QCD}", the later being a parametrization of a next–to–leading order QCD fit.

Experiments using a non–isoscalar target, T, must correct their measured differential cross sections to obtain nucleon structure functions:

$$\frac{d^2\sigma^{\nu(\bar{\nu})T}}{dxdy} = \frac{Z_T}{A_T}\frac{d^2\sigma^{\nu(\bar{\nu})p}}{dxdy} + \frac{A_T - Z_T}{A_T}\frac{d^2\sigma^{\nu(\bar{\nu})n}}{dxdy} \tag{6.3}$$

$$= \frac{d^2\sigma^{\nu(\bar{\nu})N}}{dxdy} + \left(\frac{Z_T}{A_T} - \frac{1}{2}\right)\frac{d^2(\sigma^{\nu(\bar{\nu})p} - \sigma^{\nu(\bar{\nu})n})}{dxdy}, \tag{6.4}$$

where A_T and Z_T are the atomic mass and number respectively, for a target T. Quark Parton Model (QPM) relations are usually assumed to compute the correction term (See Section 1.2.4):

$$F_2^{\nu(\bar{\nu})p} - F_2^{\nu(\bar{\nu})n} = \pm\frac{1 + R}{1 + Q^2/\nu^2} 2\left[(xd - x\bar{d}) - (xu - x\bar{u})\right] \tag{6.5}$$

$$xF_3^{\nu(\bar{\nu})p} - xF_3^{\nu(\bar{\nu})n} = \pm 2\left[(xd + x\bar{d}) - (xu + x\bar{u})\right] \tag{6.6}$$

[1] A review of experimental measurements from high energy neutrino and muon experiments can be found in Reference [49]

where $xu(x\bar{u})$ and $xd(x\bar{d})$ are the momentum densities of u– and d–(anti)quarks in the proton and strong isospin symmetry ($u = u^p = d^n$ and $d = d^p = u^n$) is assumed. Each of the experiments using non–isoscalar targets made the additional assumption: $x\bar{u} = x\bar{d}$. This leads to an isoscalar correction which is proportional to $xd_v - xu_v$, the difference between d and u valence quarks in the proton:

$$xd_v - xu_v \equiv \frac{1 - xu_v/xd_v}{1 + xu_v/xd_v}(xd_v + xu_v) \tag{6.7}$$

$$= \frac{1 - xu_v/xd_v}{1 + xu_v/xd_v} xF_3^N \tag{6.8}$$

where $xF_3^N \equiv \frac{1}{2}(xF_3^{\nu N} + xF_3^{\bar{\nu}N})$ (see below) is the momentum density of valence quarks. Each of the non–isoscalar experiments assumed

$$\frac{xd_v(x, Q^2)}{xu_v(x, Q^2)} = N \cdot (1 - x) \qquad N \approx .53 \text{ to } .57 \tag{6.9}$$

The equations relating the measured differential cross sections to $F_2^{\nu N}, F_2^{\bar{\nu}N}, xF_3^{\nu N}$ and $xF_3^{\bar{\nu}N}$ are given by (for fixed E_ν):

$$\frac{d(\sigma^{\nu N} + \sigma^{\bar{\nu}N})}{dxdy} = \frac{G_F^2 ME}{\pi}\left[g_2(F_2^{\nu N} + F_2^{\bar{\nu}N}) + g_3(xF_3^{\nu N} - xF_3^{\bar{\nu}N})\right] \tag{6.10}$$

$$\frac{d(\sigma^{\nu N} - \sigma^{\bar{\nu}N})}{dxdy} = \frac{G_F^2 ME}{\pi}\left[g_2(F_2^{\nu N} - F_2^{\bar{\nu}N}) + g_3(xF_3^{\nu N} + xF_3^{\bar{\nu}N})\right] \tag{6.11}$$

where

$$g_2 = 1 - y + \frac{y^2}{2}\left(\frac{1 + Q^2/\nu^2}{1 + R} - \frac{1}{2}\frac{Q^2}{\nu^2}\right) \qquad g_3 = y\left(1 - \frac{y}{2}\right) \tag{6.12}$$

The simplest relationship between the four remaining structure functions with the two reported is $F_2 = \frac{1}{2}[F_2^{\nu N} + F_2^{\bar{\nu}N}]$ and $xF_3 = \frac{1}{2}[xF_3^{\nu N} + xF_3^{\bar{\nu}N}]$. In order to solve the above expressions for F_2 and xF_3, it is necessary to assume a parametrization

of the *difference* between neutrino and antineutrino structure functions. The QPM relations connecting these are given by:

$$F_2^{\nu N} = F_2^{\bar{\nu} N} \tag{6.13}$$

$$xF_3^{\nu N} = xF_3^{\bar{\nu} N} + 4x(s - c) \tag{6.14}$$

where xs and xc are the momentum densities of strange and charmed in the nucleon. All experiments compared here assume $xc(x, Q^2) = 0$. Comparing these equations to Equations 6.10 and 6.11 indicate that the extracted values of F_2 depend on the strange sea assumed while xF_3 does not. Different experiments make different assumptions about the amount of the strange. A common parametrization of the total strange sea momentum fraction is given by:

$$\kappa = \frac{\int_0^1 dx[xs(x) + x\bar{s}(x)]}{\int_0^1 dx[x\bar{u}(x) + x\bar{d}(x)]} \tag{6.15}$$

All experiments compared here assume that the strange sea has the same functional dependance on x and Q^2 as the non–strange sea.

Each of the QPM relations discussed above are modified by the threshold effect due to charm production: $F_2^{\nu} - F_2^{\bar{\nu}}$ no longer vanishes, which affects the extraction of xF_3 (Equation 6.11); $F_2^{\nu} - F_2^{\bar{\nu}} \neq 4xs$ where $xs = \kappa x\bar{u}$; and R acquires a mass contribution which is discussed in Appendix C. These effects are most important at low values of x and Q^2. Regardless of whether or not the threshold effect is removed from the reported structure functions, these modifications must be taken into account.

Figures 6.1–6.4 show comparisons of structure functions extracted from the present data sample (E616+E701, called CCFR from now on) with those from other the

neutrino experiments. The points labeled "CCFR" were extracted with the same assumptions (κ, m_c, σ^{ν}/E, $\sigma^{\bar{\nu}}/E$ and R) and x–bins reported by the other analyses. Figure 6.5 and 6.6 show the structure function ratios, F_2^{OTHER}/F_2^{CCFR} and xF_3^{OTHER}/xF_3^{CCFR}, as a function of x. The ratios were formed from interpolations of each data set evaluated at the geometric–mean Q^2 value of the overlap region. Interpolation was performed by fitting the data in the overlap region to power–law in Q^2. These ratios are presented both without (a) and with (b) the adjustment of the CCFR assumptions to match those of the other experiments. Table 6.2 lists the average values of ratios shown in Figures 6.5 and 6.6. Figures 6.7 and 6.8 show the observed pattern of scaling violations: $d\ln F/d\ln Q^2$ is the exponent found in the power–law fits mentioned above. The diamonds correspond to the experiment labeled on each plot. The cross and squares correspond to the CCFR data, with and without matching each set of assumptions respectively. Differences between the appearance of the CCFR slopes (squares) in the different comparisons arise from the different overlapping Q^2 regions.

Comparison With CCFRR (1984)

The CCFR results are compared with previously published results [50] from this collaboration using the E616 data sample alone (CCFRR, 1984) in Figures 6.1, and 6.5–6.8. Since the E616 data set represents about two thirds of the data (neutrinos and antineutrinos) used in the present analysis, the two sets are highly correlated. This is reflected by the small errors shown in Figures 6.5 and 6.6 and Table 6.2. Compar-

isons made with the 1984 assumptions indicate that: (a) the present analysis yields structure functions that are more peaked in x (smaller at low and high x, larger at intermediate values) than the previous analysis; (b) the present analysis yields larger scaling violations at large–x than the previous analysis; (c) the overall level of F_2 is 2.2% lower (0.7% lower for $x > .10$) than the 1984 result; and (d) the overall level of xF_3 is 0.8% higher than the 1984 result. The same systematic tendencies persisted when the E701 data sample was not included in the present analysis. Several improvements to the analysis method are responsible for these small differences. The largest single effect is that due to a new implementation of the resolution smearing correction (Chapter 5). In the 1984 analysis, $\sum GEN/\sum SMR$ was calculated with a Monte Carlo simulation which used a different neutrino flux spectrum and differential cross section model than was used for the rest of the structure function extraction. The simulation used in the present analysis incorporated the final neutrino flux spectrum and a differential cross section model constructed from fits to the data.

The overall effect of the different assumptions used in the present analysis and 1984 analysis, shown in Table 6.1 are largest at low x. The present assumptions result in a decrease of F_2 and increase of xF_3 with respect to the 1984 assumptions by about 3.7% and 5.0% respectively for $x < 0.1$. In both cases, the magnitude of this difference is about half of that due to the differences in analysis technique. The decrease in F_2 is due primarily to the increase in the assumed value of R, while the increase in xF_3 is due primarily to the increase in $\sigma^{\bar{\nu}}/\sigma^{\nu}$.

Comparisons With CDHSW

The CERN–Dortmund–Heidelberg–Saclay–Warsaw (CDHSW) results from the recent high statistics (wide band beam) exposures have been made available in the thesis of B. Vallage [51]. The apparatus used was a massive iron detector similar to the Lab E detector. While the mean energy of the wide band neutrino spectrum is much lower than the dichromatic spectrum used in the present analysis, the high intensity yielded 6 and 38 times more neutrino and antineutrino events respectively. Structure functions were extracted without applying the charm production threshold correction. The strange sea assumed in the CDHSW analysis was given by $\kappa = .22$ which less than half the size reported in their dimuon analysis [52]. This suppression of the strange sea reflects the change in the ratio of two–muon to single–muon rates when the former is not corrected for charm production threshold. No correction was made for xF_3 since $F_2^{\nu} - F_2^{\bar{\nu}} = 0$ was assumed. The value of $R = R_{QCD}$ used in the CDHSW and CCFR analysis was the same, but its interpretation was different: In the CCFR analysis, R_{QCD} was used to relate the threshold corrected F_2 and $2xF_1$ while in the CDHSW analysis it was used to relate the uncorrected F_2 and $2xF_1$. The CDHSW isoscalar correction took a slightly different form then Equation 6.5:

$$F_2^{\nu(\bar{\nu})p} - F_2^{\nu(\bar{\nu})n} = \pm 2[(xd - x\bar{d}) - (xu - x\bar{u})] \tag{6.16}$$

Figure 6.2 shows the CCFR and CDHSW structure functions extracted with the CDHSW assumptions shown in Table 6.1 and the non–isoscalar relation shown above. In addition to the overall improvement in the level agreement due to the 10% upward

revision of the total cross section slopes [53] the x–dependance of the comparison has also improved [54] dramatically. The average value of F_2^{CDHSW}/F_2^{CCFR} in the interval $0 < x < .6$ is $0.99 \pm .01$ with a decreasing trend as x increases. The CDHSW data also displays larger scaling violations at low values of x. The comparison of xF_3 shows little x–dependance (except for $x = 0.08$), but a 7% level difference persists. The level of xF_3 is sensitive to $\sigma^{\bar{\nu}}/\sigma^{\nu}$; deviations from a linear dependance on energy of the total cross sections could affect the interpretation since two experiments are at different mean energies.

Comparison with WA59(1987)

The Big European Bubble Chamber (BEBC) collaboration, using a heavy neon–hydrogen (75 mole-% neon) fill, reported isoscalar structure functions from wide band neutrino and antineutrino exposures [55]. The reported structure functions were limited to relatively low Q^2 values due to the low statistics arising from the small fiducial mass of the neon–hydrogen target and the relatively low energy of the neutrino spectrum. Consequently, direct comparisons with the CCFR results are limited to a small Q^2 overlap region. The WA59 analysis used the same assumptions as the CCFRR (1984) analysis, apart from the total cross section slopes which are 8% and 3% higher for neutrinos and antineutrinos respectively. The average value of F_2^{WA59}/F_2^{CCFR} (using WA59 assumptions) is 1.01 ± 0.01 in the region $x < 0.70$ with a decreasing trend as x increases. The xF_3 level comparison is similar to the CDHSW comparison: xF_3^{WA59} lies $8.8 \pm 2.5\%$ higher then xF_3^{CCFR}. The WA59 and CCFR measurements

of scaling violations are in reasonable agreement.

Comparison with CHARM(1983)

The CERN–Hamburg–Amsterdam–Rome–Moscow (CHARM) collaboration have reported structure function results from a wide band exposure using a marble ($CaCO_3$) target [56]. While the neutrino event sum used in their analysis is slightly more then half of that used in the CCFR analysis, the antineutrino data is more then ten times as much. The cross section slopes assumed in their analysis were 10% lower then those used in the CCFR analysis. The CHARM structure functions were reported without the charm production threshold correction and the corresponding strange sea fraction $\kappa = 0$ and $R = 0$. The average value of F_2^{CHARM}/F_2^{CCFR} (using CHARM assumptions) is $1.03 \pm .01$ in the region $x < .6$ with a decreasing trend as x increases. This trend is more pronounced than that seen in the comparisons with WA59 and CDHSW. The average value of xF_3^{CHARM}/xF_3^{CCFR} is 0.99 ± 0.02 in the same interval with the same systematic tendency as the F_2 comparison. The scaling violations observed in F_2 are consistent, apart for $x = .015$. xF_3^{CHARM} displays larger scaling violations at low values of x.

6.2 Quark Parton Model Tests

Structure function scaling is the most basic prediction of the QPM. While Figures 6.5 and 6.6 indicate that this prediction is clearly inconsistent with measurement, the

degree of scaling violations is much less then that expected from a nucleon of uniform density which would yield structure functions with a $1/Q^8$ dependance. With this in mind, the observation of weak (logarithmic) scaling violations should be viewed as one of the successes of the model. Scaling violations are discussed in the next section in the context of QCD. The QPM tests discussed here are the mean squared charge test and the Gross–Llewellyn Smith (GLS) sum rule. Both act as consistency checks on the data. The mean square charge test, which relates F_2 measured by neutrino and charged lepton scattering experiments, should not be affected by the strong interaction since the probes do not partake in the strong interaction. The GLS sum rule, which measures the valence quark content of the nucleon, is modified by the strong interaction. For this reason, the GLS sum rule is evaluated at a fixed value of Q^2 to make a comparison with the perturbative QCD prediction.

6.2.1 Mean Squared Charge Test

Comparisons of F_2 reported from this analysis with recent measurements from charged lepton scattering experiments are presented. Since flavor changing transitions are not present in electromagnetic scattering, the charm production threshold from neutrino scattering must be removed. The relationship between nucleon structure functions measured in charged lepton and neutrino scattering experiments, derived in Section 1.2.4, is reproduced here:

$$F_2^{\ell^\pm} = \frac{5}{18}\left(1 - \frac{3}{5}\frac{xs + x\bar{s}}{xq + x\bar{q}}\right) F_2^{\nu N} \tag{6.17}$$

where the correction term in parenthesis accounts for the flavor asymmetry of second generation quarks in the nucleon's sea (charm assumed zero). Figures 6.9–6.11 show F_2 as measured by the high energy muon scattering experiments: (6.9) Berkeley–Fermilab–Princeton (BFP) collaboration using an iron target [57]; (6.10) the European Muon Collaboration (EMC) using an iron target [58]; and (6.11) the Bologna–CERN–Dubna–Munich–Saclay (BCDMS) collaboration using a carbon target [59]. Preliminary results from lower energies at SLAC using electrons on deuterium [60] are shown in Figure 6.12. Superimposed on these plots are the CCFR measurements obtained by matching the R assumptions of each experiment: BPF and SLAC used $R = 0$ and the rest used $R = R_{QCD}$

Figure 6.13 shows the ratios of the charged lepton measurements divided by the predicted values (Equation 6.17) from this analysis. These ratios were constructed from interpolated values of the structure functions in the overlap region, as was done for the neutrino comparisons. The EMC measurements have been multiplied by 1.1 in this plot. The kinematic range of the EMC and BFP experiments are comparable to this experiment while the BCDMS results are mostly at high Q^2 and the SLAC results at low Q^2.

Apart from an overall level difference of 10% between the EMC and CCFR results, the charged lepton results are in reasonable agreement with the results from this analysis. F_2^{OTHER}/F_2^{PRED} shows a systematic decrease with increasing x for BFP ($x < 0.6$) and and BCDMS ($x > 0.4$) and a systematic increase with increasing x for

the SLAC ($x < 0.5$) while the EMC shows no x dependance. The average values of F_2^{OTHER}/F_2^{PRED} for the overlap regions are 1.000 ± 0.006 (BFP), $.906 \pm .005$ (EMC), $.985 \pm .009$ (SLAC) and $.985 \pm .012$ (BCDMS). It should be noted that the SLAC measurements were made with a 20 GeV electron beam while the muon beams range from 90 GeV to 280 GeV.

6.2.2 Gross–Llewellyn Smith Sum Rule

In the QPM, xF_3 is interpreted as the momentum density (= momentum fraction times number density) of valence quarks in the nucleon. The Gross–Llewellyn Smith (GLS) sum rule [17] states that the integral of xF_3, weighted by $\frac{1}{x}$ is equal to the total number of valence quarks:

$$\int_0^1 \frac{dx}{x} xF_3(x) = 3 \qquad \text{Quark Parton Model} \tag{6.18}$$

QCD predicts a correction to the sum rule; the lowest order correction is given by [61]

$$\int_0^1 \frac{dx}{x} xF_3(x, Q^2) = 3\left(1 - \frac{\alpha_S(Q^2)}{\pi}\right) \qquad \text{QCD} \tag{6.19}$$

where $\alpha_S(Q^2)$ is the strong interaction coupling constant. To test this prediction, the sum rule was evaluated at a fixed value of $Q^2 = Q_0^2$. By using an assumed Q^2 dependance for xF_3 in each x bin, it was possible to utilize data at all Q^2 through interpolation. For a given choice of Q_0^2, however, the assumed Q^2 dependance was used to extrapolate the data for some values of x.

The $\frac{1}{x}$ weight in the integral amplifies the small x contribution to the sum rule, a

region accessible only at low Q^2 for the energy range of this experiment. The value of $Q_0^2 = 3$ (GeV/c)^2 was chosen to minimize the integral's sensitivity to extrapolation uncertainties. Three different methods were employed for the interpolation: xF_3 was assumed to have a power law dependance in Q^2, a linear dependance in $\log Q^2$ and a Q^2 dependance predicted by QCD. The first two methods are model independent: they were motivated by the empirical observation that, within the kinematic range of this experiment, xF_3 is consistent with either functional form. Both methods required two–parameter fits to the data in each x bin. The third method uses the x–dependant Q^2 variation predicted by next–to–leading order QCD (see Section 6.4). In each x bin, the level of the QCD prediction was fit to data (one–parameter fit). The Q^2 variation predicted by QCD depends primarily on the assumed value of Λ. The Q^2 dependance was calculated from fits discussed in Section 6.3.4 with $\Lambda = 251$, 385 and 136 MeV/c, corresponding to the central value and $\pm 1\sigma$. The error assigned to $xF_3(x, Q_0^2)$ for this method was taken as the sum (in quadrature) of the statistical error on the level and the the spread in $xF_3(x, Q_0^2)$ values resulting from different values of Λ. At small x, the error is dominated by the statistical contribution.

The values of $xF_3(x, Q_0^2)$ obtained from the three methods, along with the cumulative integrals defined as

$$S_x \equiv \sum_{x_i > x} \frac{\Delta x_i}{x_i} x F_3(x_i, Q_0^2) \approx \int_x^1 dx' F_3(x', Q_0^2), \tag{6.20}$$

are shown in Table 6.3. Apart from the large x data the three methods give consistent values, with the QCD method yielding the smallest errors. The differences at large x

do not effect the sum rule, however, since all three methods give consistent values of the cumulative integral S_x for $x < .15$. Figure 6.14 shows $xF_3(x, Q_0^2)$ obtained from the QCD inter/extra–polation as crosses (left scale) and S_x as diamonds (right scale). The data are consistent with the expected behaviour: $xF_3(x, Q_0^2) \rightarrow 0$ as $x \rightarrow 0$.

The statistical error on the sum rule given by Equation 6.20 is dominated by the data point at $x = .005$. Fits to $xF_3(x, Q_0^2)$ were made in an effort to reduce this error by constraining the the small x data with those at larger x. The functional form

$$f(x) = Ax^b(1-x)^c \qquad b > 0 \tag{6.21}$$

was chosen as a simplest parametrization of xF_3 satisfying $\lim_{x\rightarrow 0} f(x) = 0$ required for a finite sum rule result and the expectation $\lim_{x\rightarrow 1} f(x) = 0$. In terms of the fit, the sum rule takes the form:

$$\int_0^1 \frac{dx}{x} xF_3(x, Q_0^2) = \int_0^{x_i^u} \frac{dx'}{x'} f(x') + S_{x_i^u}, \tag{6.22}$$

where x_i^u is the ith bin's upper limit and the data is fit in the region $x < x_i^u$.

The accuracy with which the extrapolation to $x = 0$ can be made is limited by the error on the fit parameter b. One approach is to fix $c = 0$ and fit $f(x)$ to $xF_3(x, Q_0^2)$ in the region $x < x_p$, where x_p is small. For values of $x_p < .04$, the large statistical error in b resulted in sum rule errors as large as S_0. As x_p is increased, the simple power law breaks down and the fit becomes meaningless. Instead, the data were fit to $f(x)$, with c a free parameter and x_p large. The sum rule should be insensitive to the large x data; this was studied by varying x_p. Table 6.4 lists the results (QCD

method of Q^2 interpolation) for two–parameter fits with $0.03 < x_p < 0.07$ and the three–parameter fits with $0.5 < x_p < 1.0$. In each case, the fit was integrated from 0 to x_p. The difference between the values obtained in this way and those obtained by integrating the fit between 0 and .01 are negligible. Figure 6.15 shows the low x data, along with the fits listed in Table 6.4. The data and fits have been divided by $x^{.66}$ in order to show the differences in the fits. The average value for the sum rule obtained from the eight trials is 2.79 with an RMS of 0.03. The global fit ($x_p = 1.0$) yields the value 2.78 $\pm$ .08 (error is statistical, including uncertainty in Λ). The global fits obtained from the power law and linear log inter/extra–polated data are 2.85 $\pm$ 0.11 and 2.79 $\pm$ .10 respectively.

The dominant systematic error comes from the uncertainty in the flux normalizations. The 3.2% correlated uncertainty in the flux levels contributes 3.2% to the integral's error while the 1.7% uncorrelated flux uncertainty contributes 2.6% to the error. Uncertainties in the energy calibrations are small: An increase of 1.0% in the hadron, muon and secondary energy calibrations induce -0.6%, -1.3% and +0.1% changes in the sum rule respectively. A correlated 1.0% increase in all three energy calibrations decreases the sum rule by 1.1%. The value of the GLS sum rule obtained from a global fit of $xF_3(x, Q_0^2)$ to $Ax^b(1-x)^c$ is

$$\int_0^1 \frac{dx}{x} xF_3(x, Q_0^2 = 3\mathrm{GeV}^2/\mathrm{c}^2) = 2.780 \pm .081 \pm .125 \tag{6.23}$$

where the second error is the quadrature sum of the above–mentioned systematic errors. Substitution of this value into Equation 6.19 predicts $\alpha_S(Q_0^2 = 3\mathrm{GeV}^2/\mathrm{c}^2) =$

$.23 \pm .16$

6.3 Scaling Violations

Scaling violations have been studied through the Altarelli–Parisi equations discussed in Section 1.2.5. Perturbative QCD predicts the Q^2 evolution of structure function moments in terms of the single scale parameter of the theory. A computer program based on one supplied by Duke and Owens [62] was used to perform fits to the leading order (LO) and next–to–leading order (NLO in the $\overline{\text{MS}}$ renormalization scheme) approximation of perturbative QCD[2]. The structure of the program was modified to allow for simultaneous fits to to F_2, xF_3 and their correlations. The computer program *MINUIT* [63] was used for the χ^2 minimization. While less efficient than the Duke and Owens minimization routine, it allowed direct control of the parameter space and contained useful features for detection of local minima.

Flavor nonsinglet fits to xF_3 provide the cleanest means of confronting the predictions of QCD since its evolution is independent of the unmeasured gluon evolution (see below). Furthermore, the extracted values of xF_3 are fairly insensitive to the assumed parametrizations of $R = \sigma_L/\sigma_T$ and the strange sea used in the structure function extraction. Any nonsinglet analysis is limited by the large statistical errors incurred by forming differences of cross sections.

[2]Minor errors found in the next–to–leading order splitting functions and coefficient functions were detected and corrected

The evolution of F_2, on the other hand, is coupled to that of the gluons. Gluons in the nucleon with momentum fraction x at one value of $Q^2 = Q_0^2$ will contribute to the presence of virtual $q\bar{q}$ pairs with momentum fraction $y < x$ at $Q_1^2 > Q_0^2$. The sum of these quarks and antiquarks contributes to the Q^2 evolution of F_2 while their difference cancels in xF_3. Likewise, quarks or antiquarks with momentum fraction x at Q_0^2 contribute to the presence of gluons with momentum fraction $< x$ at $Q^2 > Q_0^2$ through gluon Bremsstrahlung. In the nonsinglet case, the quark and antiquark contributions cancel, while in the singlet case they do not. At a given value of x, the Q^2 evolution of the singlet density is governed both by the strength of the strong coupling constant, α_S and the parton densities at $x' > x$ (see Equations 1.79–1.81). Since there is no direct gluon density measurement, the observed scaling violations at a given value of x can be equally well described by a variety of different values of α_S and gluon densities at $x' > x$. However, the measurement of the virtual $q\bar{q}$ sea, related to the difference between F_2 and xF_3, provides a constraint on the gluon density, especially at large x where the difference is small.

6.3.1 Fitting Procedure

Data was compared to the QCD predictions by forming a χ^2 from the measured structure functions and those evolved through the Altarelli–Parisi equations. In the case of simultaneous fits to F_2 and xF_3, their correlations were included (see section 5.5). The χ^2 was minimized through the variation of Λ and the Q_0^2 parameters

of the relevant parton densities. The statistical error in Λ was found by solving:

$$\chi^2(\overline{\Lambda} \pm \Delta_\pm) = \chi^2(\Lambda) + 1 \tag{6.24}$$

while allowing the Q_0^2 parameters of the parton densities to vary. The nonlinear dependance of the evolution on Λ results in asymmetric errors. Individual contributions to the systematic errors on Λ were estimated by performing the χ^2 minimizations on data sets with the structure functions values shifted from their nominal values by their estimated systematic uncertainties given in Table 5.4.

The validity of the perturbative predictions of QCD are expected to be valid in the limit of large Q^2. The logarithmic Q^2 evolution of the structure function moments follows from an analysis of the "leading twist" operators in Equation 1.66. Higher twist operators, which contribute to scaling violations with a strength proportional to inverse powers of Q^2 will dominate the leading twist behavior below some unknown value of Q^2. It would be desirable to impose a conservative Q^2 cut to eliminate this region, however the limited statistics and available range of Q^2 demand a modest choice: In all fits, data below $Q^2 = 6$ (GeV/c)^2 were cut. Barnett suggested [64] that the most appropriate quantity fro describing non–perturbative effects is the invariant hadronic mass, $W^2 = M^2 + Q^2(1-x)/x$. Quark counting rules suggest contributions to scaling violations with strengths proportional to inverse powers of W^2. Again, with statistical and kinematic limitations in mind, data with $W^2 < 10$ GeV^2 were eliminated from the fits. Finally, data at $x > 0.7$ were cut for both experimental and theoretical reasons. The experimental corrections required for the differential

cross sections are quite large (see Table 5.1) and Fermi motion of nucleons in nuclear targets are also large [65]. The kinematic cuts are summarized here:

$$Q^2 > 6\ (\mathrm{GeV/v})^2 \quad 0.03 < x < 0.70 \quad W^2 < 10\ \mathrm{GeV}^2$$

The minimum x cut is implied by the Q^2 cut, but is shown explicitly. A total of 48 F_2 and xF_3 data points passed the cuts.

The finite nucleon mass induces power law (in $1/Q^2$) corrections to the structure function evolution (kinematical higher twist effects). Fits were performed both with and without target mass corrections following the prescription of Georgi and Politzer [66]. Devoto *et al.* [62] point out that this formulation is inconsistent with the assumption that the ordinary moments of $F_i^0(\xi)$, where $\xi = 2x/(1+(1+4M^2x^2/Q^2)^{\frac{1}{2}})$ and F_i^0 is a structure function for a massless target, are equal to the Nachtmann moments [67] of $F_i^{TM}(x)$, the corresponding structure function for a massive target. The effect is important for large values of $4M^2x^2/Q^2$, a region eliminated by the x and W^2 cuts. Since the fit values of Λ obtained with and without application of the Georgi–Politzer target mass correction differed by a small fraction of the statistical error, it was concluded that target mass effects are unimportant. All results are reported without the correction applied.

All parton densities were parametrized at $Q^2 = 1\ (\mathrm{GeV/c})^2$, the point where the Q^2 evolution begins. The validity of perturbation theory at these low values of Q^2 is not an issue since only the densities evolved to $Q^2 > 6\ (\mathrm{GeV/c})^2$ were used in the

fits. The nonsinglet parametrization used is given by:

$$xq_{ns}(x, Q_0^2) = A_{ns}x^{\eta_1}(1-x)^{\eta_2}(1+\gamma x), \tag{6.25}$$

where A_{ns} was fixed by the fermion conservation rule

$$\int_0^1 dx q_{ns}(x, Q_0^2) = 3. \tag{6.26}$$

Fermion conservation is a built–in feature of the nonsinglet operator in the factorization scheme used, valid to all orders of perturbation theory. A numerical check on the evolved nonsinglet density showed that Equation 6.26 was satisfied at the 1% level for 1 $(\mathrm{GeV/c})^2 < Q^2 < 300$ $(\mathrm{GeV/c})^2$.

The singlet fits required parametrizations of both the singlet quark density and the gluon density:

$$xq_s(x, Q^2) = xq_{ns}(x, Q^2) + B_s(1-x)^{\eta_s} \tag{6.27}$$

$$xG(x, Q^2) = A_g(1-x)^{\eta_g}(1+\gamma_g x), \tag{6.28}$$

where A_g was fixed by the momentum sum rule:

$$\int_0^1 dx \left[xq_s(x, Q_0^2) + xG(x, Q_0^2)\right] = 1. \tag{6.29}$$

6.3.2 Nonsinglet Fit Results

The results of the nonsinglet fits are in Table 6.5 and Figure 6.16 shows the NLO fits superimposed on the data. The systematic errors in Λ and α_S at $Q^2 = 12.6$ $(\mathrm{GeV/c})^2$, the mean Q^2 value of this experiment, are listed in Table 6.6. It is worth

noting that both the systematic and statistical errors in Λ are larger in the LO case than the NLO case, apart from the systematic error from the correlated flux uncertainty. The entry labeled R in Table 6.6 is from the difference in fits to xF_3 extracted with $R = 0$ and $R = R_{QCD}$. It is surprising that the Λ_{LO} increases by almost a standard deviation when $R = 0$ is assumed. Figure 6.17 shows xF_3 extracted with the different R assumptions. The point–to–point differences are always a small fraction of the statistical errors. (The reason why xF_3 does depend on R was traced to the differences between the neutrino and antineutrino flux spectra: measured neutrino and antineutrino cross sections were not combined at the same mean energy, i.e. y, resulting in an additional correlation when their differences were formed.) Figure 6.18 shows the χ^2 surfaces as a function of Λ_{LO} and $\Lambda_{\overline{MS}}$ (44 degrees of freedom) for both R assumptions. The large systematic errors in the LO fit, especially due to different R assumptions, may be a reflection physical content of leading order calculations: It has been pointed out [68] that if the change $\Lambda_{LO} \rightarrow \kappa\Lambda_{LO}$ is made *without* changing α_S, the moment evolution equations remains unchanged since κ can always be absorbed in the next–to–leading order correction which is dropped. To fix the numerical value of Λ from experiments, it is necessary retain all expressions up to $\mathcal{O}(\alpha_S^2)$.

The results of the NLO fits are summarized here.

$$\Lambda_{\overline{MS}} = 251^{+134}_{-115} \pm 89 \text{ MeV/c} \tag{6.30}$$

$$\alpha_S = .222 \pm .037 \pm .026 \qquad \text{at } Q^2 = 12.6 \text{ (GeV/c)}^2 \tag{6.31}$$

The errors are statistical followed by systematic. The systematic errors on Λ were

found by adding the systematic errors in α_S in quadrature (only half of the R uncertainty) and then expressing Λ in terms of $\alpha_S \pm \Delta(\alpha_S)_{syst}$. The next–to–leading order value of α_S was found in all calculations by numerically inverting

$$\ln(Q^2/\Lambda_{\overline{MS}}) = \frac{4\pi}{\beta_0 \alpha_S} - \frac{\beta_1}{\beta_0^2} \ln\left[\frac{4\pi}{\beta_0 \alpha_S} + \frac{\beta_1}{\beta_0^2}\right], \tag{6.32}$$

where

$$\beta_0 = 11 - \frac{2}{3}N_f \qquad \beta_1 = 102 - \frac{38}{3}N_f \tag{6.33}$$

and the number of flavors was fixed at $N_f = 4$.

The comparison shown in Figure 6.16 indicates that the fit is consistent with the data. Another way of displaying the level of agreement between theory and measurement is through a direct comparison of the scaling violations. Since both the data and fits are consistent with a power law dependance in Q^2 for a given value of x, the logarithmic derivatives are consistent with being independent of Q^2:

$$\frac{d \ln x F_3(x, Q^2)}{d \ln Q^2} \approx A(x) \tag{6.34}$$

Figure 6.19 shows the measured xF_3 slopes (crosses) calculated in each x bin from fits of the form $a + b \ln Q^2$. The predicted slopes (lines) were calculated by fitting the predicted structure functions, evaluated at the same Q^2 values as the data, to the same functional form, using the measured errors. The solid (dashed) curve is a smooth interpolation of the predicted slopes for $\Lambda_{\overline{MS}} = 251(\pm 2\sigma)$ MeV/c.

The highest x bins suggest a possible trend towards larger measured slopes, although the statistical significance is not compelling. If one assumes that $F_2 \approx xF_3$

for $x > 0.4$ (diamonds in Figure 6.19) this trend persists. Results of fits to xF_3 for $x < 0.4$ and $(1 + Q^2/\nu^2)/(1 + R) \times F_2$ for $x > 0.4$ yielded

$$\Lambda_{LO} = 471^{+104}_{-102} \text{ MeV/c} \tag{6.35}$$

$$\Lambda_{\overline{MS}} = 386^{+78}_{-74} \text{ MeV/c.} \tag{6.36}$$

and are listed in Table 6.7. It should be noted that this parton model inspired approximation is not quite valid in the NLO approximation due the different coefficient functions of F_2 and xF_3. The dotted line in Figure 6.19 is the NLO prediction.

6.3.3 Singlet Fit Results

Two separate types of singlet fits to the data have been performed. The first method involved fitting F_2 by itself to the Altarelli–Parisi equations. In the second method, F_2 and xF_3 were simultaneously fit to the Altarelli–Parisi equations. In the later case, $xq_{ns}(x, Q_0^2)$ and $xq_s(x, Q_0^2)$ were evolved separately with their respective splitting kernels, coupled to each other by the same Λ (through α_S). The purely nonsinglet degrees of freedom served as constraint on Λ. Together with the singlet degrees of freedom, xF_3 also constrained the amount of $q\overline{q}$ content at large x, hence on the level of the gluon density, reducing the correlation between the gluon shape at Q_0^2 and Λ.

Both types of fits yielded very hard (relatively large fraction at high x) gluon densities at Q_0^2. When γ_g in Equation 6.28 was a free parameter it tended to a very large value. The resulting $xG(x, Q_0^2)$ was strongly peaked at $x \sim 0.2$. Figure 6.20 shows $xG(x, Q^2)$ from fits to F_2 at various values of Q^2 for $\gamma_g = 0, 10, 10^2$ and 10^6

for fixed $\Lambda_{\overline{MS}} = 250$ MeV/c (See below). The preferred gluon densities (large γ_g) are larger at intermediate values of x. By $Q^2 = 5$ (GeV/c)^2, all of the gluon densities decrease with increasing x as is intuitively expected. Since the gluon evolution is very rapid at low values of x, its simple functional form given in Equation 6.28 will give different results depending on the choice of Q_0^2. Clearly for $Q_0^2 = 5$ (GeV)/c^2, Equation 6.28 can not describe the large–γ_g gluon densities unless the momentum sum rule constraint is removed in which case the description is valid only for $x > 0.1$. This situation is in contrast to the nonsinglet fit results which were Q_0^2–independent. The choice of $Q_0^2 = 1$ (GeV/c)^2 was made because it effectively offered the greatest flexibility in parameterizing the gluon density in the $Q^2 > 6$ (GeV/c)^2 region.

Figure 6.21 shows the contours for the F_2 fits as a function of $\Lambda_{\overline{MS}}$ for the different values of γ_g. Since the best value of $\Lambda_{\overline{MS}}$ is insensitive to the choice of γ_g, the densities shown in Figure 6.19 are "best fits." All subsequent singlet fits were preformed with $\gamma_g = 10^6$ fixed.

The parametrization given in Equation 6.27 was required for the simultaneous fits because both the singlet and nonsinglet quark densities were evolved. For the fits to F_2 alone, a standard Q_0^2–parameterization of the singlet quark density was also tried:

$$q_s(x, Q_0^2) = A_s(1-x)^{\eta_2}(1+\gamma x) \tag{6.37}$$

where A_s, η_2 and γ were unconstrained, apart from the momentum sum rule. Figure 6.22 shows the χ^2 contours as a function of $\Lambda_{\overline{MS}}$ for the two different singlet quark parametrizations. The best values of $\Lambda_{\overline{MS}}$ and η_g are consistent with each other for

the two cases.

The results of the NLO nonsinglet fits are shown in Table 6.8 and Figure 6.23 shows the fit to F_2 superimposed on the data. The large χ^2s indicate that either the data is consistent with perturbative QCD only at the three sigma level or that the systematic errors are significant. Table 6.9 lists the contributions to the systematic errors in $\Lambda_{\overline{MS}}$ and α_S (using $q_s(x, Q_0^2)$ given in Equation 6.27) indicating that the systematic errors are significant. When all systematic errors on F_2, apart from the correlated flux uncertainty which only affects the overall level, were added in quadrature to to the statistical errors, the χ^2 decreased from 66.8 for 41 degrees of freedom (dof) to 47.6/41 dof indicating a good fit. In this case, the central value of $\Lambda_{\overline{MS}}$ also decreased by 30 MeV/c. This can be understood from Figure 6.24 which shows the comparison between the measured and predicted scaling violations as a functions of x. The large observed scaling violations at large x tend to force Λ to larger values. Since the systematic errors are largest in this region, the relative contribution to the χ^2 from these degrees of freedom were reduced. Figures 6.19 and 6.24 both suggest that at large values of x, scaling violations predicted by QCD are smaller than measured scaling violations. The F_2 comparison indicates that in the region $0.1 < x < 0.4$, the measured scaling violations lie above the predictions.

Also shown in Tables 6.8 are the results of the simultaneous fits. Figure 6.25 shows the χ^2 contours as a function of $\Lambda_{\overline{MS}}$ for the simultaneous fit along with the nonsinglet fit and the F_2 (q_s given in Equation 6.27) fit for comparison. The excellent agreement

between the central values of the singlet and nonsinglet values of Λ is accidental: Changing the kinematic cuts shifts the central values around, although they do remain consistent with each other. Table 6.9 lists the systematic uncertainties in $\Lambda_{\overline{MS}}$. As was the case for the other NLO fits discussed, the dominant systematic error arises from the hadron energy and secondary energy calibrations. The determination of $\Lambda_{\overline{MS}}$ from the simultaneous fit is limited by the systematic error. Adding the structure functions' systematic errors in quadrature with their statistical errors resulted in a reduction of the χ^2 from 116/89 dof to 92/89 dof with a corresponding reduction in $\Lambda_{\overline{MS}}$ of 35 MeV/c.

The quality of the simultaneous fits are in good agreement with both the nonsinglet and singlet (F_2 only) fits: Considering only the F_2 degrees of freedom, the simultaneous fit yielded a χ^2 of 69.1 as compared to 66.8 for the fit to F_2 alone. The xF_3 degrees of freedom for the simultaneous fit yielded a χ^2 of 52.0 as compared to 48.0 for the nonsinglet fit. Another check on the consistency of the fits came from comparing the F_2 fits to xF_3. When the nonsinglet part of the F_2 fit, $q_{ns}(x, Q_0^2)$ in Equation 6.27, was evolved by itself and compared with xF_3, the resulting χ^2 was 59.4 for 48 degrees of freedom as compared to 48.0/44. The nonsinglet part of the F_2 fit is shown as the dashed lines in Figure 6.26 and the purely nonsinglet fit is shown as a solid line.

Figure 6.27 shows the χ^2 contours as a function of the gluon exponent, η_g, for the NLO F_2 and simultaneous fits. This comparison shows the indirect effect xF_3 has

on the shape of the gluons: The simultaneous fits more readily exclude low values of η_g which correspond to a large gluon fraction at high values x. This is because $F_2 - xF_3$, which is related to the momentum density of virtual $q\overline{q}$ in the nucleon sea, is constrained to a small value at large x. Figure 6.28 and 6.29 show the projections of the η_g–$\Lambda_{\overline{MS}}$ correlations onto the $\Lambda_{\overline{MS}}$ and η_g axes respectively. The points with horizontal error bars represent the best parameter value $\pm$ 1σ and the vertical scale indicates the corresponding excursion of the other parameter. Both plots illustrate the reduction in correlation achieved through the inclusion of the nonsinglet evolution.

Figure 6.30 shows the gluon structure densities at different values of Q^2 for $\eta_g =$ 4.13, 6.50 and 2.80, corresponding to the best value and $\pm$ 2σ ($\Lambda_{\overline{MS}} = 253, 265$ and 225 MeV/c respectively). Also shown on these plots are the "soft" (DO 1: $\Lambda_{\overline{MS}} =$ 200 MeV/c) and "hard" (DO 2: $\Lambda_{\overline{MS}} = 400$ MeV/c) densities given in Reference [69] for comparison. At large values of x, the best gluon density from this analysis lies between their two extremes. The $Q^2 = 5$ (GeV/c)^2 plot also shows the gluon density extracted by the BCDMS collaboration using a hydrogen target [70] with $\Lambda_{\overline{MS}} =$ 220 MeV/c. This gluon density is inconsistent with the others shown. In fact, BCDMS makes use of their soft gluon density to justify the the claim that above $x = .25$ and $Q^2 = 20$ (GeV/c)^2, F_2 is approximately nonsinglet [71]. Figure 6.31 shows the difference $0.5 * (F_2 - xF_3) \sim x\overline{q}$, along with the simultaneous NLO fit shown in Table 6.8. This shows that below $x = 0.4$, the nonsinglet approximation of F_2 is not supported.

6.3.4 Comparisons With Other Analyses

Differences in the analysis assumptions and kinematic ranges between the various deep inelastic scattering experiments preclude simple comparisons of QCD results. In spite of these differences, it is remarkable that the reported values of $\Lambda_{\overline{MS}}$ are in such good agreement. Rather than presenting a quantitative comparison of QCD fit results, a qualitative comparison of the data is given. Figure 6.32 show the scaling violations in F_2 and xF_3 for several experiments with Q^2–ranges comparable to this experiment. The solid lines correspond to best value of $\Lambda_{\overline{MS}}$ plus and minus two standard deviations for the simultaneous and nonsinglet fits respectively. The slopes were calculated from power law fits in Q^2 to the data in each x bin, subject to the following cuts: $Q^2 > 6\ (\mathrm{GeV/c})^2$, $W^2 > 10\ \mathrm{GeV}^2$ and $\nu > 10$ GeV. The F_2 comparison shows that, apart from the BCDMS data, there is a tendency for the measured points to lie below the predicted curves at high x and above the curves at intermediate x. Below $x = 0.10$, the BFP and CCFR data are consistent with the QCD predictions, but the other data lie significantly above the prediction. The low x comparison could be improved by increasing the relative fraction of gluons at low x, but the CCFR data, in particular, the large sea–quark content extending to $x = 0.40$, does not favor a softened gluon density. The xF_3 comparison shows the same high x tendency as the F_2 comparison. The CDHSW data also lies above the QCD predictions below $x = 0.40$, as was the case for the F_2 comparison.

6.4 Conclusions

Structure functions extracted from two narrow band neutrino and antineutrino exposures at Fermilab have been presented. These results are in reasonable agreement with recent high statistics results from wide band exposures from neutrino experiments at CERN. In particular, the level of agreement between data from this analysis and the recent CDHSW results have improved greatly. The Quark Parton Model tests provided consistency checks on the data: Apart from an overall 10% level difference between the results reported here and those from EMC, the mean square charge test demonstrated consistency at the few percent level for several charged lepton scattering experiments. The Gross–Llewellyn Smith Sum Rule result,

$$\int_0^1 dx F_3(x, 3\ (\mathrm{GeV/c})^2) = 2.78 \pm .08 \pm .13 \tag{6.38}$$

is consistent, at the 1.5σ level, with the QPM prediction of three. When next–to–leading order perturbative QCD corrections are included, the measured value is consistent with $\Lambda_{\overline{MS}} < 435$ MeV/c with a central value of 135 MeV/c.

Measured deviations from scaling predicted by the QPM were used analysed in the context of perturbative QCD. Three types fits to the Altarelli–Parisi equations were performed. A purely nonsinglet fit to xF_3 yielded:

$$\Lambda_{\overline{MS}} = 251^{+134}_{-115} \pm 89 \text{ MeV/c} \tag{6.39}$$

$$\alpha_S = .222 \pm .037 \pm .026 \qquad \text{at } Q^2 = 12.6\ (\mathrm{GeV/c})^2. \tag{6.40}$$

This value of $\Lambda_{\overline{MS}}$, obtained at large Q^2, is consistent with the value predicted from

the GLS sum rule at lower Q^2. Singlet fits, were performed using F_2 alone and using both F_2 and xF_3 simultaneously. The results of these fits were consistent with the purely nonsinglet fits:

$$\left.\begin{array}{lcll} \Lambda_{\overline{MS}} & = & 255^{+73}_{-63} \pm 101 \text{ MeV/c} & \\ \alpha_S & = & .223 \pm .020 \pm .030 & \text{at } Q^2 = 12.6 \text{ (GeV/c)}^2 \end{array}\right\} F_2 \text{ Only}$$

$$\left.\begin{array}{lcll} \Lambda_{\overline{MS}} & = & 253^{+55}_{-50} \pm 71 \text{ MeV/c} & \\ \alpha_S & = & .223 \pm .015 \pm .021 & \text{at } Q^2 = 12.6 \text{ (GeV/c)}^2 \end{array}\right\} F_2 \text{ \& } xF_3 \tag{6.41}$$

The coupling of the singlet quark density evolution to the gluon evolution was used to constrain the gluon density shape. It was found that the conventional parametrization the gluons, $xG(x, Q_0^2) = A(1-x)^{\eta_g}(1+\gamma_g x)$, provided the best description of the data when a low value of Q_0^2 was chosen. The resulting gluon density was found to be inconsistent with that reported by the BCDMS collaboration. The best gluon result from this analysis lie between the the hard and soft densities given by Duke and Owens [69] for x above 0.2 (high Q^2) to 0.4 (low Q^2).

Appendix A

Absolute Flux Normalizations

A.1 Overview

In Section 5.2.3, the technique used to determine the *relative* flux levels for secondary settings of each polarity was presented. In this appendix, the techniques used to determine the absolute neutrino and antineutrino flux normalizations (f^{ν}_{abs} and $f^{\bar{\nu}}_{abs}$ of Equations 5.14 and 5.16) are presented. A parallel event analysis, using the same fiducial and beam cuts employed in the structure function analysis, was carried out to establish these normalizations: By relaxing the kinematic cuts and making use of the dichromatic beam's energy–radius correlation, the unnormalized (i.e. $f^{\nu(\bar{\nu})}_{abs} = 1$) differential cross sections,

$$\left\langle \frac{1}{E} \frac{d\sigma^{\nu(\bar{\nu})}}{dy} \right\rangle_{\nu(\bar{\nu})} (y) \tag{A.1}$$

were obtained over most of the kinematic range $0 < y < 1$ (See Figure A.1). Their integrals were compared directly with the total cross section slopes reported by this

collaboration (E616) [72],

$$\begin{aligned}(\sigma^{\nu}/E)_{616} &= (.669 \pm .003 \pm .024) \times 10^{-38}\mathrm{cm}^2/\mathrm{GeV} \\ (\sigma^{\overline{\nu}}/E)_{616} &= (.340 \pm .003 \pm .020) \times 10^{-38}\mathrm{cm}^2/\mathrm{GeV}\end{aligned} \tag{A.2}$$

yielding a 3.5% measurement of the relative neutrino–to–antineutrino flux normalization (due primarily to the uncorrelated systematic uncertainties in neutrino and antineutrino flux measurements) and a 3.1% measurement of the overall level (from correlated flux uncertainties). The overall level uncertainty translates directly into overall scale error for both F_2 and xF_3 of 3.1%. However, the relative neutrino–to–antineutrino flux level uncertainty induces much larger errors in xF_3 which is related to the *differences* of neutrino and antineutrino cross sections.

A consistency requirement applied to the data was used to reduce the relative neutrino–to–antineutrino flux uncertainty. The "y–intercept", defined as

$$Y_0 = \lim_{y\to 0} \frac{1}{E}\frac{d\sigma}{dy} \approx \frac{G^2 M}{\pi}\int_0^1 dx F_2(x, Q^2 = 0), \tag{A.3}$$

is approximately (let $y \to 0$ in Equation 5.1) independent of the beam polarity and energy. In terms of the averaged, unnormalized y–intercepts, defined as

$$\overline{Y}_0^{\nu(\overline{\nu})} = \lim_{y\to 0}\left\langle \frac{1}{E}\frac{d\sigma^{\nu(\overline{\nu})}}{dy}\right\rangle_{\nu(\overline{\nu})}(y), \tag{A.4}$$

the constraint takes the form

$$\frac{\overline{Y}_0^{\nu}}{\overline{Y}_0^{\overline{\nu}}} = C_y \frac{f_{abs}^{\overline{\nu}}}{f_{abs}^{\nu}}. \tag{A.5}$$

The constant C_y, estimated from a Monte Carlo calculation, reflects the nucleon flavor asymmetries (charm production and the strange sea) and non–scaling behaviour

which affect the extrapolation to $y = 0$. The 1.3% statistical error on the measured y–intercept ratio and 1.5% systematic uncertainty in C_y provided a 2.0% measurement of the relative flux level. Combined with the 3.5% constraint from the total cross section ratio, $f^{\bar{\nu}}_{abs}/f^{\nu}_{abs}$ was determined to 1.7%.

It should be emphasized that the absolute flux normalization *must* be constrained independently. The overall level constraint came from comparing data collected over a much larger kinematic region then was used in the structure function analysis to assumed total cross sections. There was very little reliance on extrapolation of the differential cross section model in unsampled regions. Constraining the relative neutrino–to–antineutrino normalization did rely on an extrapolation to at low–y (small E_{had}). However, since only the *ratio* of predicted low–y cross sections were used, the sensitivity to model assumptions were small. The 1.5% systematic uncertainty in C_y was estimated by varying the charm quark mass between 0 and 2 GeV/c^2, R between $.5R_{QCD}$ and $2R_{QCD}$, the strange sea between $SU(2)$–symmetric and $SU(3)$–symmetric and a variety of assumed structure function parametrizations.

The $f^{\nu(\bar{\nu})}_{abs}$ were calculated at each iteration. Values of f^{ν}_{abs} or $f^{\bar{\nu}}_{abs}$ different from unity modified the cross section model normalizations used in the next iteration. They converged to their final values quickly. The final overall flux adjustments were

$$\begin{aligned} f^{\nu}_{abs} &= 1.001 \pm .005 \\ f^{\bar{\nu}}_{abs} &= .996 \pm .015. \end{aligned} \tag{A.6}$$

A.2 Event Analysis

The kinematic range was extended by relaxing the cuts and including penetration trigger events (see Section 3.5). Low–y data was recovered by eliminating the 10 GeV hadron energy cut[1]. Inclusion of penetration triggers improved the acceptance cut–off at high–y (large θ_μ and small E_μ). Events not satisfying the muon trigger requirement, e.g. muon momentum not reconstructed, were classified as pion or kaon events on the basis of their hadron energies and the energy separatrix (Section 2.5). For these events y was assigned "the dichromatic" value $y = E_{had}/E_\nu(r)$ where $E_\nu(r)$ is the predicted dichromatic energy. The dashed curves in Figures A.1 indicate the fractions of the total cross sections sampled by this extended kinematic range.

Each event satisfying the trigger, beam, fiducial and reconstruction cuts (see Section 4.5), was assigned a tag indicating that one or both of the following requirements was satisfied:

Muon Tag (MT): Muon Trigger $\cap$ $E_\mu > 10$ GeV $\cap$ $\theta_\mu < .2 \cap (\theta_\mu > .0071 \cup r > 5$ in) $\cap$ Acceptance requirement

Penetration Tag (PT): Penetration Trigger $\cap$ $E_{had} > 10$ GeV $\cap$ $\theta < .37 \cap E_\mu > 2.9$ GeV $\cap$ Acceptance requirement.

The acceptance requirement for muon tag is discussed in Section 4.5. The acceptance requirement for penetration tag is that the muon passes though at least 20 counters

[1] While the x–resolution suffers at low E_{had}, the y–resolution is good.

within a 50 in apparatus centered square cut. Events not satisfying at least one of these requirements were cut. The efficiency for penetration tagging is nearly unity for $E_{had} > 10$ GeV while the efficiency for muon tagging, which depends on θ_μ, is high for low hadron energy events. The following six categories were used to classify events as originating from pion or kaon decays.

No.	Category
1	$\mathrm{MT} \cap E_{had} < 10\ \mathrm{GeV} \cap r < 30\ \mathrm{in} \cap E_{TOT} < E^{SEP}(r)$
2	$\mathrm{MT} \cap E_{had} < 10\ \mathrm{GeV} \cap E_{TOT} > E^{SEP}(r)$
3	$\mathrm{PT} \cap 10\ \mathrm{GeV} < E_{had} < .85E^{SEP}(r) \cap r < 30\ \mathrm{in}$
4	$\mathrm{MT} \cap 10\ \mathrm{GeV} < E_{had} < .85E^{SEP}(r) \cap r < 30\ \mathrm{in} \cap E_{tot} > E^{SEP}(r)$
5	$\mathrm{MT} \cap 10\ \mathrm{GeV} < E_{had} < .85E^{SEP}(r) \cap r > 30\ \mathrm{in} \cap E_{tot} > E^{SEP}(r)$
6	$\mathrm{PT} \cap E_{had} > .85E^{SEP}(r)$

Events with $E_{had} < 10$ GeV (categories 1 and 2) were classified on the basis of total energy. The wide separation of neutrino energies from pion and kaon decays allowed the identification of events with $E_{had} > .85E^{SEP}(r)$ (category 6) as kaon induced. For events with 10 GeV$< E_{had} < .85E^{SEP}(r)$ classification was based on the fact that the MT efficiency is high for kaon events. In this region, the pion events are recovered by subtracting identified kaon events (category 4) from all PT events (category 3). The total number of events classified as pion and kaon events is given by

$$\sum \mathrm{pions} = \sum \mathrm{cat.1} + \sum \mathrm{cat.3} - \sum \mathrm{cat.4} \tag{A.7}$$

$$\sum \mathrm{kaons} = \sum \mathrm{cat.2} + \sum \mathrm{cat.4} + \sum \mathrm{cat.5} + \sum \mathrm{cat.6} \tag{A.8}$$

Figure A.2 shows an E_{had} distribution for one momentum setting. The solid histograms labeled ν_π and ν_K are the measured event sums indicated above and the dashed histogram are the Monte Carlo sums.

Pion and kaon events were each histogrammed in both the measured and dichromatic y–variable. Raw y–distributions for pions (kaons) were formed by using the measured–y histograms for $y < .2$ ($y < .4$) and the dichromatic histograms for $y > .2$ ($y > .4$). Figure A.3 shows both measured and Monte Carlo y–distributions for individual settings of the secondary beam. The excess events at high–y are an artifact of the technique: Use of the dichromatic neutrino energy sometimes results in $y > 1$ and these events end up in the highest y–bin.

A.3 y–Distribution Analysis

Differential cross sections (Equation A.1) were formed in analogy to the double differential cross sections discussed in Section 5.2. The corrected cross sections were obtained by multiplying the ratio of measured to Monte Carlo event sums in each y–bin by the model cross section with radiative and non–isoscalar effects removed:

$$\left\langle \frac{1}{E}\frac{d\sigma^{\nu(\bar{\nu})}}{dy} \right\rangle^{meas}_{\nu(\bar{\nu})}(y) = \frac{\sum data^{\nu(\bar{\nu})}}{\sum SMR^{\nu(\bar{\nu})}} \left\langle \frac{1}{E}\frac{d\sigma_0^{\nu(\bar{\nu})}}{dy} \right\rangle_{\nu(\bar{\nu})}(y) \tag{A.9}$$

Charm production threshold and strange sea corrections were not applied since they are not included in the reported total cross section measurements. Their effects were accounted for in the calculation of C_y (Equation A.5). Radiative effects do not contribute to the total cross sections, but they do modify the shapes of the y–

distributions. The total cross section slope was obtained by numerically integrating Equation A.9 with respect to y on $[0,1]$.

The y–intercept constraint was found as follows. Both the measured (unnormalized) and simulated y–distributions were fit to the functional form:

$$\left\langle \frac{1}{E}\frac{d\sigma}{dy} \right\rangle (y) = A + B(1-y)^2; \tag{A.10}$$

the y–intercept is given by $Y_0 = A + B$. C_y is given by the ratio of simulated y–distributions:

$$C_y = \frac{(A_\nu + B_\nu)^{model}}{(A_{\bar{\nu}} + B_{\bar{\nu}})^{model}} \tag{A.11}$$

Figure A.4 shows the corrected differential cross sections averaged over all energy settings. The solid curves are fits to the data of the form $A + B(1-y)^2$ on the interval $.05 < y < .8$. The high–y data was excluded since this where the acceptance and missing region corrections become large.

The low–y data was excluded since non–scaling contributions to the cross sections may be important here. Figure A.5 shows the raw y–distributions in fine bins for the +140 GeV/c setting of the secondary beam. Note that the excess above the continuum is larger for the pion data. This is consistent with the hypothesis that these events are associated with quasi–elastic like processes[2]. Figure A.6 shows the excess number of events/nucleon/(anti)neutrino/cm^2 as a function of the mean neutrino energies. The excesses were calculated by fitting the raw y–distributions to a straight line in the

[2]These include primarily quasi–elastic scattering resonance production and coherent pion production

interval $y_{min} = 10\text{GeV}/E_\nu < y < .05$ and taking the difference between the measured event sum for $y < y_{min}$ and the area under the fit in the same region.

The ratio $r = f^{\bar{\nu}}_{abs}/f^{\nu}_{abs}$ was calculated from the ratios of unnormalized cross sections $R_\sigma = \sigma^\nu/\sigma_{\bar{\nu}}$ and y–intercepts $R_Y = Y^\nu_0/Y^{\bar{\nu}}_0$:

$$r = \frac{\frac{R_Y R^p_Y}{\Delta^2_Y} + \frac{R_\sigma R^p_\sigma}{\Delta^2_\sigma}}{\frac{R^2_Y}{\Delta^2_Y} + \frac{R^2_\sigma}{\Delta^2_\sigma}} \tag{A.12}$$

where

$$R^p_\sigma = 1.968 \pm .069 \tag{A.13}$$

$$R^p_Y = 1.012 \pm .015 \tag{A.14}$$

are the predicted values. Δ_Y and Δ_σ are the statistical errors on the measured quantities added in quadrature with the systematic errors given above. The overall level constraint is:

$$\frac{1}{f^\nu_{abs}}(\sigma^\nu/E) + \frac{1}{f^{\bar{\nu}}_{abs}}(\sigma^{\bar{\nu}}/E) = (\sigma^\nu/E)_{E616} + (\sigma^{\bar{\nu}}/E)_{E616} \tag{A.15}$$

The final ratios and cross sections are

$$(\sigma^\nu/E) = .676 \times 10^{-38}\text{cm}^2/\text{GeV} \tag{A.16}$$

$$(\sigma^{\bar{\nu}}/E) = .333 \times 10^{-38}\text{cm}^2/\text{GeV} \tag{A.17}$$

$$R_Y = 1.000 \pm .014 \tag{A.18}$$

$$R_\sigma = 2.034 \pm .014 \tag{A.19}$$

where the errors are statistical only.

The energy dependance of the y–intercepts are shown in Table A.1 Their energy independence reflects the degree of consistency between the y–intercept technique and relative flux determination discussed in Section 5.2.3.

Appendix B

Parton Parametrizations

Both the corrected structure functions (Equation 5.18) and physical (e.g. uncorrected) differential cross sections (Appendix C) were modelled in terms of the bare momentum densities of partons *in the proton.* The parametrizations of the parton densities used is based on a modification to those of Buras and Gaemers [47]. These authors found simple analytic expressions for the valence, sea and gluon densities which were consistent, at the few percent level, with the moment evolution equations of leading–order QCD. The modifications include the separation of the valence density into up and down densities, $xu_v(x, Q^2)$ and $xd_v(x, Q^2)$, and the incorporation of some higher order effects. The parametrizations discussed here are intended to provide a smooth representation of the data: Fits to the structure functions extracted in the nth iteration were used to parametrize corrections required for the $n + 1^{th}$ iteration.

B.1 Valence Densities

The nucleon's valence momentum density of Reference [47] is given by

$$xV(x,Q^2) = A_V(s)x^{\eta_1(s)}(1-x)^{\eta_2(s)} \tag{B.1}$$

where

$$s = \log\left(\frac{\log(Q^2/\Lambda^2)}{\log(Q_0^2/\Lambda^2)}\right) \tag{B.2}$$

$$\eta_1(s) = \eta_{10} + \eta_{11}\cdot s \tag{B.3}$$

$$\eta_2(s) = \eta_{20} + \eta_{21}\cdot s \tag{B.4}$$

$$A_V(s) = \frac{3}{\beta(\eta_1(s),\eta_2(s)+1)} \tag{B.5}$$

and the *beta*–function,

$$\beta(a,b) = \frac{\Gamma(a)\Gamma(b)}{\Gamma(a+b)}, \tag{B.6}$$

fixes the number of valence quarks at three.

Deep inelastic electron scattering experiments using hydrogen and deuterium targets [73,74] showed that $\lim_{x\to 1} F_2^{en}/F_2^{ep} = 1/4$, suggesting that for large x, the valence is dominated by u_v–quarks. For this reason, the valence distribution given above was separated into flavors: the d_v–quark falling by a power of $(1-x)$ faster then the u_v–quark. The p–n system form an isodoublet: it is assumed that $xu_v^p(x,Q^2) = xd_v^n(x,Q^2) \equiv xu_v(x,Q^2)$ and $xd_v^p(x,Q^2) = xu_v^n(x,Q^2) \equiv xd_v(x,Q^2)$ where the superscript indicates a proton or neutron target. The functional form of these densities are given by:

$$xu_v(x,Q^2) = c_u(s)x^{\eta_1(s)}(1-x)^{\eta_2(s)} \tag{B.7}$$

$$xd_v(x,Q^2) \;=\; c_d(s)x^{\eta_1(s)}(1-x)^{\eta_2(s)+1} \tag{B.8}$$

The relative normalization of u_v– to d_v–quark densities was supplied by the proton quark counting rule (a weak form of the Adler Sum Rule):

$$\int_0^1 \frac{dx}{x} xu_v(x,Q^2) = 2\int_0^1 \frac{dx}{x} xd_c(x,Q^2). \tag{B.9}$$

Thus, the *nucleon* valence density becomes

$$xu_v + xd_v = A'_V(s)x^{\eta_1(s)}(1-x)^{eta_2(s)}\left[1+\frac{1}{2}\frac{\eta_1(s)+\eta_2(s)+1}{\eta_2(s)+1}(1-x)\right] \tag{B.10}$$

Another modification effected the overall normalization of the valence distributions: Imposing the Gross–Llewellyn Smith sum rule to fix the total number of valence quarks was abandoned in favor of allowing the overall normalization to float, but retaining the Q^2 variation expected of next–to–leading order QCD:

$$\int_0^1 \frac{dx}{x}[xu_v(x,Q^2)+xd_v(x,Q^2)] = A_0\left(1-\frac{12\pi}{25\log(Q^2/\Lambda^2)}\right) \tag{B.11}$$

or

$$A'_V(s) = \frac{2A_0}{\beta(\eta_1(s),\eta_2(s)+1)}\left(1-\frac{12\pi}{25\log(Q^2/\Lambda^2)}\right) \tag{B.12}$$

B.2 Sea Densities

Two sea densities, an $SU(3)$–symmetric piece and a charmed piece were considered in Reference [47]. In this analysis, the the charmed component was assumed to be zero and only the $SU(3)$–symmetric sea was used. This density was assumed to describe,

up to normalization, the remaining three flavors:

$$xS(x,Q^2) = A_S(s)(1-x)^{\eta_s(s)} \tag{B.13}$$

The various flavor densities of the sea are expressed as

$$2xu_s = 2x\bar{u} = 2xd_s = 2x\bar{d} = \frac{1}{2+\kappa}xS(x,Q^2) \tag{B.14}$$

and

$$2s = s\bar{s} = \frac{\kappa}{2+\kappa}xS(x,Q^2) \tag{B.15}$$

where $\kappa = .52$ was used [43]. The Q^2–dependance of $xS(x,Q^2)$ can be expressed in terms of the its first two (Q^2–dependant) moments:

$$A_S(Q^2) = \langle xS(Q^2)\rangle_0 \left(\frac{\langle xS(Q^2)\rangle_0}{\langle xS(Q^2)\rangle_1} - 1\right) \tag{B.16}$$

$$\eta_S(Q^2) = \frac{\langle xS(Q^2)\rangle_0}{\langle xS(Q^2)\rangle_1} - 2 \tag{B.17}$$

where

$$\langle xS(Q^2)\rangle_n = \int_0^1 dx x^n xS(x,Q^2). \tag{B.18}$$

The Q^2 evolution of the $\langle xS(Q^2)\rangle_n$ are specified by leading–order QCD and are given in the reference. Since their evolution is coupled to those of the gluon density, $xG(x,Q^2)$, it was necessary to parametrize $xG(x,Q^2)$. The gluon density parametrization was of the same form as the sea

$$xG(x,Q^2) = A_G(1-x)^{\eta_G} \tag{B.19}$$

B.3 R

R, the ratio of absorption cross sections for longitudinally and transversely polarized $W^{\pm}$'s. was parametrized as

$$R(x, Q^2) = 1.5 \frac{(1-x)^4}{\log(Q^2/.04)}. \tag{B.20}$$

As was the case for the valence density normalization, this feature was borrowed from the next–to–leading order QCD prediction.

B.4 Fitting Procedure

A total of nine free parameters were used to specify the valence and sea densities: They are η_{10}, η_{11}, η_{20}, η_{21}, and A_0 for the valence densities and $\langle xS(Q_0^2)\rangle_0$, $\langle xS(Q_0^2)\rangle_1$ and $\langle xG(Q_0^2)\rangle_1$ for the sea density and Λ. Q_0^2 was fixed at 1 GeV$^2/c^2$ (see Equation B.2). The first two moments of the valence density, required for the evolution of the sea were computed from A_0, η_{10} and η_{20}. The first moment of the gluon density, also required for the evolution of the sea, was fixed by the momentum sum rule

$$\int_0^1 dx \left[xS(x, Q_0^2) + xu_v(x, Q_0^2) + xd_v(x, Q_0^2) + xG(x, Q^2)\right] = 1. \tag{B.21}$$

After each iteration, the extracted structure functions were simultaneously fit to simple combinations of the "bare" momentum densities:

$$F_2^M(x, Q^2) = \frac{1 + R(x, Q^2)}{1 + 4M^2x^2/Q^2} \left[xu_v(x, Q^2) + xd_v(x, Q^2) + xS(x, Q^2)\right] \tag{B.22}$$

$$xF_3^M(x, Q^2) = xu_v(x, Q^2) + xd_v(x, Q^2). \tag{B.23}$$

A χ^2 minimization procedure, incorporating the correlations between the F_2 and xF_3, was used. The errors supplied to the fitting program were calculated from the predicted event sums in each (x, Q^2)–bin used in the extraction procedure. This method eliminates biases caused by measured points lying above (below) the fit values which underestimate (overestimate) the χ^2 contribution. The new parton densities were then used to construct the cross section model used in the next iteration (See Figure 5.1). Table B.1 lists the final fit values used to parametrize the corrections.

Appendix C

Physical Differential Cross Section Model

The differential cross parametrization employed by the event Monte Carlo (Chapter 5) and used to calculate "model" corrections to the structure functions are presented. In particular, the physics assumptions made in the construction of the effective parton momentum densities appearing in Equations 5.19—5.21 are presented. For brevity, the effective quark densities are derived only for neutrinos. The constructions for antineutrinos are analogous and only their results are presented. Throughout this Appendix, xu_v, xd_v and xS refer to the *bare* proton densities discussed in Appendix B.

C.1 Flavor Asymmetries

The non–isoscalarity of iron and the s–c asymmetry of the sea result in $F_i^{\nu} \neq F_i^{\bar{\nu}}$. The following assumptions were made:

1. Isoscalar symmetry of the neutron–proton momentum densities:

$$xu^p(x,Q^2) = xd^n(x,Q^2) \equiv xu(x,Q^2) \tag{C.1}$$

and

$$xd^p(x,Q^2) = xu^n(x,Q^2) \equiv xd(x,Q^2) \tag{C.2}$$

where, for example, $xu = xu_v + xu_s$ is the total u–quark momentum density (valence plus sea) of the proton.

2. Universal functional dependance of the non–charmed sea densities (for neutron or proton)

$$xu_s(x,Q^2) = x\overline{u}(x,Q^2) = xd_s(x,Q^2) = x\overline{d}(x,Q^2) = \frac{1}{2+\kappa}\frac{1}{2}xS(x,Q^2) \tag{C.3}$$

and

$$xs(x,Q^2) = x\overline{s}(x,Q^2) = \frac{\kappa}{2+\kappa}\frac{1}{2}xS(x,Q^2) \tag{C.4}$$

where $\kappa \equiv \int dx 2xs / \int dx(x\overline{u} + x\overline{d})$ is a measure of the flavor–symmetry of the sea: $\kappa = 1$ corresponds to an $SU(3)$ symmetric sea and $\kappa = 0$ corresponds to an $SU(2)$ symmetric sea. It was determined experimentally from dimuon production [43] having the value $\kappa = .52^{+.17}_{-.15}$.

3. The charm content of the sea assumed zero.

Neutrinos scatter off quarks with weak isospin $-\frac{1}{2}$ (d or s) or antiquarks with weak isospin $+\frac{1}{2}$ ($\overline{u}$ or $\overline{c}$). The effective quark momentum density (average for a nucleon in

iron) "seen" by neutrinos is given by

$$
\begin{aligned}
q^{\nu} &= 2\left\{\frac{Z}{A}(xd^p + xs^p) + \frac{A-Z}{A}(xd^n + xs^n)\right\} && \text{(C.5)}\\
&= 2\left\{\frac{Z}{A}(xd + xs) + \frac{A-Z}{A}(xu + xs)\right\} && \text{(C.6)}\\
&= (1-\alpha)xd_v + (1+\alpha)xu_v + xd_s + xs && \text{(C.7)}\\
&= (1-\alpha)xd_v + (1+\alpha)xu_v + \frac{1+\kappa}{2+\kappa}xS && \text{(C.8)}\\
& && \text{(C.9)}
\end{aligned}
$$

where $\alpha = 1 - \frac{2Z}{A}$, while the effective antiquark density seen by neutrinos is

$$
\begin{aligned}
\bar{q}^{\nu} &= 2\left\{\frac{Z}{A}x\bar{u}^p + \frac{A-Z}{A}x\bar{u}^n\right\} && \text{(C.10)}\\
&= \frac{1}{2+\kappa}xS. && \text{(C.11)}
\end{aligned}
$$

The effective momentum densities seen by antineutrinos are

$$
\begin{aligned}
q^{\bar{\nu}} &= (1+\alpha)xd_v + (1-\alpha)xu_v + \frac{1}{2+\kappa}xS && \text{(C.12)}\\
\bar{q}^{\bar{\nu}} &= \frac{1+\kappa}{2+\kappa}xS. && \text{(C.13)}
\end{aligned}
$$

C.2 Charm Production Threshold

The effect of charm production is accounted for in the slow re–scaling scheme [44]. In this scheme, the normal scaling variable x no longer represents the momentum fraction carried by the struck quark, but

$$
\xi = x\left(1 - \frac{m_c^2}{Q^2}\right) \qquad \text{(C.14)}
$$

does. The inclusive cross sections are modeled as a sum of two semi–inclusive cross sections; charm–producing and non–charm–producing pieces. Correspondingly, the effective momentum densities were split into charm–producing and non–charm–producing pieces:

$$q^{\nu}_{ncp} = \left((1-\alpha)xd_v + (1+\alpha)xu_v + \frac{xS}{2+\kappa}\right)\cos^2\theta_C + \frac{\kappa}{2+\kappa}xS\sin^2\theta_C \quad \text{(C.15)}$$

$$q^{\nu}_{cp} = \left((1-\alpha)xd_v + (1+\alpha)xu_v + \frac{xS}{2+\kappa}\right)\sin^2\theta_C + \frac{\kappa}{2+\kappa}xS\cos^2\theta_C \quad \text{(C.16)}$$

$$\bar{q}^{\nu}_{ncp} = \frac{1}{2+\kappa}xS \quad \text{(C.17)}$$

$$\bar{q}^{\nu}_{cp} = 0 \quad \text{(C.18)}$$

$$q^{\bar{\nu}}_{ncp} = (1+\alpha)\,xd_v + (1-\alpha)\,xu_v + \frac{1}{2+\kappa}xS \quad \text{(C.19)}$$

$$q^{\bar{\nu}}_{cp} = 0 \quad \text{(C.20)}$$

$$\bar{q}^{\bar{\nu}}_{ncp} = \frac{1}{2+\kappa}xS\cos^2\theta_C + \frac{\kappa}{2+\kappa}xS\sin^2\theta_C \quad \text{(C.21)}$$

$$\bar{q}^{\bar{\nu}}_{cp} = \frac{1}{2+\kappa}xS\sin^2\theta_C + \frac{\kappa}{2+\kappa}xS\cos^2\theta_C \quad \text{(C.22)}$$

where cp (ncp) indicates charm–producing (non–charm–producing) and $\theta_C = 13.2°$ is the Cabibbo angle [46].

Concentrating now on the charm–producing cross sections, we note that the transformation $x \to \xi$ preserves differential area,

$$\left|\frac{\partial(\xi, y)}{\partial(x, y)}\right| = 1. \quad \text{(C.23)}$$

Therefore, the charm producing cross section in the ξ–variable is obtained by the transformation:

$$2x\mathcal{F}_1^{\nu(\bar{\nu})cp}(x) \;\to\; \frac{x}{\xi}2\xi\mathcal{F}_1^{\nu(\bar{\nu})cp}(\xi)\theta(1-\xi) \quad \text{(C.24)}$$

$$\mathcal{F}_2^{\nu(\bar{\nu})cp}(x) \rightarrow \mathcal{F}_2^{\nu(\bar{\nu})cp}(\xi)\theta(1-\xi) \tag{C.25}$$

$$x\mathcal{F}_3^{\nu(\bar{\nu})cp}(x) \rightarrow \frac{x}{\xi}\xi\mathcal{F}_3^{\nu(\bar{\nu})cp}(\xi)\theta(1-\xi), \tag{C.26}$$

where the θ–function insures sufficient energy transfer to produce charm.

In order to preserve the identity

$$\mathcal{F}_2(x,Q^2) \equiv \frac{1+R(x,Q^2)}{1+4m^2x^2/Q^2}2x\mathcal{F}_1 \tag{C.27}$$

under the transformation $x \rightarrow \xi$, it is necessary to transform R:

$$\begin{aligned} R(x) &\equiv \frac{\mathcal{F}_2^{cp}(x)}{2x\mathcal{F}_1^{cp}}\left(1+\frac{4m^2x^2}{Q^2}\right)-1 \\ \longrightarrow R'(x) &= \frac{\xi}{x}\frac{\mathcal{F}_2^{cp}(\xi)}{2\xi\mathcal{F}_1^{cp}(\xi)}\left(1+\frac{4m^2x^2}{Q^2}\right)-1 \\ &= \frac{\xi}{x}\frac{1+R(\xi)}{1+4m^2\xi^2/Q^2}\left(1+\frac{4m^2x^2}{Q^2}\right)-1. \end{aligned} \tag{C.28}$$

Note $R'(x) = R'([R(x)],\xi)$ and in general will be different for neutrinos and antineutrinos. Substituting R' in Equation C.27 yields

$$\mathcal{F}_2^{\nu(\bar{\nu})cp}(x) \rightarrow \frac{1+R(\xi)}{1+4m^2\xi^2/Q^2}2\xi\mathcal{F}_1^{\nu(\bar{\nu})cp}(\xi) \tag{C.29}$$

Combining the charm–producing and non–charm–producing contributions to the cross sections results in the following physical structure functions:

$$2x\mathcal{F}_1^{\nu}(x) = q_{ncp}^{\nu}(x) + \bar{q}^{\nu}(x) + \frac{x}{\xi}q_{cp}^{\nu}(\xi) \tag{C.30}$$

$$2x\mathcal{F}_1^{\bar{\nu}}(x) = q^{\bar{\nu}}(x) + \bar{q}_{ncp}^{\bar{\nu}}(x) + \frac{x}{\xi}\bar{q}_{cp}^{\bar{\nu}}(\xi) \tag{C.31}$$

$$\mathcal{F}_2^{\nu} = \frac{1+R(x)}{1+4M^2x^2/Q^2}\left(q_{ncp}^{\nu}(x)+\bar{q}^{\nu}(x)\right) + \frac{1+R(\xi)}{1+4M^2\xi^2/Q^2}q_{cp}^{\nu}(\xi) \tag{C.32}$$

$$\mathcal{F}_2^{\bar{\nu}} \doteq \frac{1+R(x)}{1+4M^2x^2/Q^2}\left(q^{\bar{\nu}}(x)+\bar{q}_{ncp}^{\bar{\nu}}(x)\right) + \frac{1+R(\xi)}{1+4M^2\xi^2/Q^2}\bar{q}_{cp}^{\bar{\nu}}(\xi) \tag{C.33}$$

$$x\mathcal{F}_3^{\nu}(x) = q_{ncp}^{\nu}(x) - \overline{q}^{\nu}(x) + \frac{x}{\xi} q_{cp}^{\nu}(\xi) \tag{C.34}$$

$$x\mathcal{F}_3^{\overline{\nu}}(x) = q^{\overline{\nu}}(x) - \overline{q}_{ncp}^{\overline{\nu}}(x) - \frac{x}{\xi} \overline{q}_{cp}^{\overline{\nu}}(\xi) \tag{C.35}$$

where Q^2 dependance and the $\theta(1-\xi)$ terms multiplying the cp terms are suppressed. Figure C.1 shows the effect slow rescaling on the ratio of $\mathcal{F}_2/2x\mathcal{F}_1$: The dashed (dotted) line shows this ratio for neutrinos (antineutrinos) on iron and the solid lines shows the ratio assuming $R = R_{QCD}$. The effect is important only at small-x.

C.3 Radiative Effects

The differential cross sections, constructed from the effective structure functions $\mathcal{F}_i^{\nu(\overline{\nu})}$ presented above, were then used as the Born cross sections in the calculation of radiative corrections. The leading muon mass dependant correction [45] is reproduced here:

$$\frac{d^2\sigma^{obs}}{dxdy} = \frac{d^2\sigma^{Born}}{dxdy} + \frac{\alpha}{2\pi} \log \frac{2mE_\nu(1-y-xy)^2}{\mu^2} \times \int_0^1 dz \frac{1+z^2}{1-z} \left\{ \frac{y\theta(z-z_{min})}{z(y+z-1)} \left[\left. \frac{d^2\sigma^{Born}}{dxdy} \right|_{\substack{x=\overline{x} \\ y=\overline{y}}} \right] - \frac{d^2\sigma^{Born}}{dxdy} \right\} + \mathcal{O}\left(\frac{\alpha}{\in\pi}\right) \tag{C.36}$$

where

$$\overline{x} = \frac{xy}{z+y-1}, \qquad \overline{y} = \frac{z+y-1}{z} \tag{C.37}$$

and

$$z_{min} = (1-y)\left(1 + \frac{E_\nu}{m}(1-\cos\theta_{lab})\right) \tag{C.38}$$

In this expression, α is the electromagnetic coupling constant and μ the muon mass.

Appendix D

CCFR Collaboration

D.Garfinkle, F.Merritt, M.Oreglia, P.Reutens

Enrico Fermi Institute, University of Chicago

P.Auchincloss, R.Blair, C.Haber, S.Mishra

E.Oltman, M.Ruiz, F.Sciulli, M.Shaevitz, W.Smith, R.Zhu

Nevis Laboratory, Columbia University

R.Coleman, H.Fisk, B.Jin, T.Kondo, D.Levinthal

W.Marsh, P.Rapidis, H.White, D.Yovanovitch

Fermi National Accelerator Laboratory

A.Bodek, F.Borcherding

N.Giokaris, K.Lang, I.Stockdale

University of Rochester

References

[1] M.Gell-Mann and R.Feynman, *Phys. Rev.* **109**, 193 (1958);

E.Sudarshan and R.Marshak, *Phys. Rev.* **109**, 1860 (1958)

[2] R.Hofstadter, *Ann. Rev. Nucl. Sci.* **7**, 231 (1957)

[3] G.Weber, "Proceedings of the 1967 International Symposium on Electron and Photon Interactions at High Energies", 59, Stanford, Ca. (1967)

[4] E.Bloom *et al.*, *Phys. Rev. Lett.* **23**, 930 (1968);

M.Breidenbach *et al.*, *Phys. Rev. Lett.* **23**. 935 (1968)

[5] J.Friedman and H. Kendall, *Ann. Rev. Nucl. Sci.*, 203 (1972)

[6] A.Pias "Inward Bound", Oxford University Press, (1988)

[7] J.Bjorken, *Phys. Rev.* **179**, 1547 (1969)

[8] R.Feynman, *Phys. Rev. Lett.* **23**, 1415 (1969);

"Photon–Hadron Interactions", Benjaman, New York (1972)

[9] J.Bjorken and E.Paschos *Phys. Rev.* **185**, 1975 (1969)

[10] S. Adler, in "Proceedings of the Sixth Hawaii Topical Conference in Particle Physics (1975)", edited by P.Dobson *et al.*, Univ. Hawaii Press, (1975).

[11] J.D. Bjorken and S.D.Drell, "Relativistic Quantum Fields", McGraw Hill, New York (1964).

[12] C.H. Llewellyn Smith, *Phys. Rep.* **3C**, No. 5 (1972).

[13] M.Gell-Mann, *Phys. Lett.*, **8**, 214 (1964)

[14] G.Zweig CERN preprint 8182/Th 401 Jan. (1964)

[15] C.Callen and D.Gross *Phys. Rev. Lett.* **22**, 156 (1969)

[16] S.Weinberg, Phys. Rev. Lett. **19**, 1264 (1967);
A.Salam in "Elementary Particle Theory", Ed. N.Svartholm, 367 Stockholm (1968)

[17] D.Gross and C.Llewellyn Smith, *Nucl. Phys.* **B14**, 337 (1969)

[18] J.Kuti and V.Weisskopf, *Phys. Rev.* **D4**, 3418 (1971)

[19] H.Politzer, *Phys. Rep.* **14**, 129 (1974)

[20] G. 't Hooft *Nucl. Phys. B33*, 73 (1973)

[21] D.Gross and F.Wilczek *Phys. Rev. Lett.* **30**, 1343 (1973) ;
H.Politzer *Phys. Rev. Lett.* **30**, 1346, (1973)

[22] C.Yang and R.Mills, *Phys. Rev.* **95**, 631; **96**, 191 (1954)

[23] M.Han and Y.Nambu, *Phys. Rev.* **139B**, 1006 (1965)

[24] S.Coleman and. D.Gross, *Phys. Rev. Lett.* **31**, 1343 (1973)

[25] K.Wilson, *Phys. Rev.* **179**, 1499 (1969)

[26] K.Symanzik *Comm. Math. Phys.* **23**;

C.Callen, *Phys. Rev.* **D5**, 3202 (1972)

[27] H.Georgi and H.Politzer, *Phys. Rev.* **D9**, 416 (1974);

D.Gross and F.Wilczek, *Phys. Rev.* **D9**, 980 (1974)

[28] G.Altarelli and G.Parisi, *Nucl. Phys.* **B126**, 298 (1977)

[29] W.Bardeen, A.Buras, D.Duke and T.Muta *Phys. Rev.* **D18**, 3998 (1978)

[30] D.Duke and R.Roberts *Phys. Rep.* **20**, 120 (1985)

[31] W.Furmanski and R.Petronzio *Z. Phys.* **C11**, 293 (1982)

[32] R. Blair, *et al. NIM*, **226**, 281 (1984)

[33] P.Auchincloss, Ph.D. Thesis, "Measurement of the Cross Section for Charged–Current Neutrino–Nucleon Interactions", Columbia University (1986)

[34] A.Bodek *et al.*, *Z. Phys.* **C18**, 289 (1983)

[35] W.Atherton *et al. CERN Report*, CERN 80–07 (1980)

[36] D.Carey, *Fermilab Report*, NAL–64 204.00 PM–9 (1978)

[37] R.Blair, Ph.D. Thesis, "A total Cross Section and y Distribution Measurement for Muon Type Neutrinos and Antineutrinos on Iron", Caltech (1982)

[38] M.Purohit, Ph.D. Thesis, "Nucleon Structure from ν_μ-Fe Interactions and a study of the Valence Quark Distribution", Caltech (1984)

[39] R.Holsinger, CERN Computer Center Program Library T604

[40] J.Ritchie, PhD. Thesis, "Hadronic Charm production by protons and pions on Iron", Univ. of Rochester (1983)

[41] D.Macfarlane, PhD. Thesis, "Nucleon Structure from Neutrino Interactions in an Iron Target with a Study of the Singlet Quark Distributions", Caltech (1984)

[42] F.S.Merritt *et al*, *NIM* **A245**, 27 (1986)

[43] K. Lang *et al*, *Z. Phys.*, **C33**, 483 (1987)

[44] R.M.Barnett, *Phys. Rev. Lett.*, **36**, 1163 (1976);
H.Georgi and H.Politzer, *Phys. Rev.*,**D14**, 1829 (1976)

[45] A. De Rújula, R.Petronzio and A.Savoy-Navarro, *Nucl. Phys.* **B154**, 393 (1979)

[46] Particle Data Group, "Review of Particle Properties", *Phys. Lett.*, **B170** (1986)

[47] A.J. Buras, *Nucl. Phys.*, **B132**, 249 (1978)

[48] J.Orear, "Notes on Statistics for Physicists", UCRL-8417, U. Cal., Berkeley (1958)

[49] S.Mishra and F.Sciulli *Ann. Rev. Nucl. Part. Sci.*, **39**, ?? (1989)

[50] D.MacFarlane *et al.*, *Z. Phys.* **C26**, 1 (1984)

[51] B.Vallage Ph.D. Thesis, "Determination Precise des Fonctions de Structure du Nucleon dans les Interactions de Type Courant–Charge de Neutrinos sur Cible de Fer", Univ. Paris XI Orsey (1987)

[52] H.Abramowicz *et al.*, *Z. Phys.* **C15**, 19 (1982)

[53] P.Berge *et al.*, *Z. Phys.* **C35**, 443 (1987)

[54] F.Sciulli in "1985 International Symposium on Lepton and Photon Interactions at High Energies", 8, Kyoto (1985)

[55] K.Varvell *et al.*, Z. Phys. **C36**, 1 (1987)

[56] F.Bergsma *et al.*, *Phys. Lett.* **123B**, 269 (1983)

[57] P.Meyers *et al.*, *Phys. Rev.* **D34**, 1265 (1986)

[58] J.Aubery *et al.*, *Nucl. Phys.* **B272**, 158 (1986)

[59] A.Benvenuti *et al.*, CERN-EP/87-100 (1987);
A.Benvenuti *et al.*, Phys. Lett., **195B**, 91 (1987)

[60] L.Whitlow *et al.*, Univ. Rochester Report, UR1102 (1989)

[61] W.Bardeen, A.Buras, D.Duke and T.Muta *Phys. Rev.* **D18**, 3998 (1978)

[62] A.Devoto, D.Duke,, J.Owens and R.Roberts *Phys. Rev.* **D27**, 508 (1983)

[63] F.James and M.Roos, CERN Computer Center Program Library (1971)

[64] R.Barnett *Phys. Rev.* **D27**, 98 (1983)

[65] A.Bodek and J.Ritchie *Phys. Rev.* **D23**, 1070 (1981)

[66] H.Georgi and D.Politzer *Phys. Rev.* **D14**, 1829 (1976)

[67] O.Nachtmann, *Nucl. Phys.* **B63**, 237 (1973)

[68] M.Baće, *Phys. Lett.* **78B**, 132 (1978)

[69] D.Duke and J.Owens *Phys. Rev.* **D30**, 49 (1984)

[70] A.Benvenuti, *et al.*, CERN-EP/89-06 (1989)

[71] A.Benvenuti, *et al.*, *Phys. Lett.* **B195**, 97 (1987);
A.Benvenuti, *et al.*, CERN-EP/89-07 (1989)

[72] R.Blair *et al.*, *Phys. Rev. Lett.*, **51**, 343 (1983)

[73] E.Bloom in "Procedings of the 6th International Symposium on Electron and Photon Interactions," Bonn, West Germany (1973)

[74] A.Bodek *et al.*, em Phys. Lett., **51B**, 417 (1974)

List of Tables

Table 2.1 Summary of the secondary beam properties.

Table 2.2 Energy separatrix parameters for each secondary beam setting.

Table 2.3 Wide band neutrino beam parameters.

Table 3.1 Summary of Lab E detector configurations for the two running periods.

Table 4.1 Angular resolution parameters for the final state muon.

Table 4.2 Results of fits to $R(y)$ (Equations 4.16 and 4.17) for the E701 secondary beam settings. Results are shown both with and without the 4.8% adjustment to the hadron energy.

Table 4.3 Results of fits to $R(y)$ for the E616 secondary beam settings.

Table 4.4 Event sums used in the structure function analysis.

Table 5.1 Multiplicative corrections to the differential cross sections for acceptance, resolution smearing and bin center effects.

Table 5.2 Radiatively corrected differential cross sections for neutrinos and antineutrinos (experimental corrections also applied). $\langle y \rangle$ and $\langle y^2 \rangle$ are the mean values

of y and y^2, averaged over the neutrino and antineutrino spectrum shown in Figure 2.11.

Table 5.3 Structure function results with statistical errors. The last column is the correlation between F_2 and xF_3.

Table 5.4 Structure function results with systematic errors for (a) F_2 and (b) xF_3. The columns labeled E_{had}, E_μ, E and p_{secy} show the changes in the reported structure functions due to an increase of 1% in the hadron energy calibration, the muon momentum calibration, all energy calibrations and the secondary momentum calibration respectively. $\Delta\theta_{sec}$ corresponds to the changes in structure functions for a 10% increase in the angular dispersion of the secondary beam. $\Phi^{\bar{\nu}}/\Phi^{\nu}$ corresponds to the changes in the structure functions for a 1.7% increase in the antineutrino–to–neutrino normalization.

Table 6.1 Differences in assumptions used by various neutrino groups for structure function extraction. Also shown is the total event sums used in the structure function analysis. The two different parametrizations of R_{QCD} are:

$$R_{QCD}^{[a]} = \frac{1.5(1-x)^4}{\ln(Q^2/.04)} \qquad R_{QCD}^{[b]} = \frac{.73(1-x)^{3.7}}{\ln(Q^2/.058)}$$

Table 6.2 Average values of F^{OTHER}/F^{CCFR} for various neutrino (F_2 and xF_3) and charged lepton (F_2) experiments.

Table 6.3 xF_3 and the cumulative integrals, $S_x \approx \int_x^1 F_3(x)dx$, evaluated at $Q^2 = 3$ (GeV/c)^2 for the three different inter/extra–polation methods.

Table 6.4 Results of fits to the x dependence of xF_3. A, b and c are given in Equation 6.21.

Table 6.5 Nonsinglet fit results for LO and NLO fits to xF_3. The errors on η_1, η_2 and γ are parabolic.

Table 6.6 Contributions to the systematic errors in Λ_{LO} and $\Lambda_{\overline{MS}}$ from the nonsinglet fits.

Table 6.7 Nonsinglet fit results using the approximation

$$xF_3 = \frac{1 + Q^2/\nu^2}{1 + R} F_2 \qquad \text{for } x > 0.40$$

Table 6.8 Results of NLO fit to F_2 alone and the simultaneous F_2 and xF_3 fit.

Table 6.9 Contributions to the systematic errors in $\Lambda_{\overline{MS}}$ for the fits shown in columns 3 and 4 of Table 6.8.

Table A.1 y–intercepts, in units of $G_F^2 M/\pi$, for the individual secondary beam settings.

Table B.1 Fit parameters used to model the proton's parton densities.

List of Figures

Figure 1.1 Depiction of deep inelastic neutrino (antineutrino) nucleon scattering through the exchange of a virtual charged boson, $W^{\pm}$. k_1, k_2, p and $q = k_1 - k_2$ are the 4–momenta of the incident neutrino, final state muon, target nucleon and exchanged boson.

Figure 1.2 Q^2–$2m\nu$ plane indicating the elastic, resonance and deep inelastic region.

Figure 1.3 Inelastic e^-–p cross section from Reference [4], normalized to the the structureless (Mott) cross section.

Figure 1.4 Helicity considerations for analyzing neutrino and antineutrino scattering off a structureless spin-$\frac{1}{2}$ parton. Single arrows indicate momenta and double arrows indicate spin.

Figure 1.5 Inelastic neutrino scattering off a nucleon in the infinite momentum frame. The struck parton carries a fraction ξ of the nucleon momentum.

Figure 1.6 Feynman diagrams illustrating (a) $\mathcal{O}(\alpha_S)$ and (b) $\mathcal{O}(\alpha_S^2)$ contributions to the splitting functions.

Figure 1.7 x dependence of the valence–quark, sea–quark and gluon momentum densities at $Q^2 = 5$ and 500 $(\mathrm{GeV/c})^2$.

Figure 2.1 Correlation of measured event energy, $E_\nu = E_\mu + E_{had}$, verses event radius at the Lab E detector for a 250 GeV/c setting of the secondary beam. The solid line is the energy separatrix discussed in Section 2.5.

Figure 2.2 Layout of the Fermilab accelerator, showing the positions of neutrino beamline and Lab E detector

Figure 2.3 Layout of the neutrino source which consists of the primary target, the Dichromatic Beamline (N30 Train), decay region and earth/steel muon shield.

Figure 2.4 Time profiles of the main ring magnet current and beam intensity.

Figure 2.5 (a) Detailed schematic showing positions of the dichromatic beamline elements. (b) Simplified model of the dichromatic beamline illustrating major functions.

Figure 2.6 The number of each type of secondary particle entering the decay region per primary proton on target as a function of the secondary momentum selected.

Figure 2.7 Position profiles of the secondary beam at the two monitoring stations in the decay region, measured with the Segmented Wire Ionization Chambers (SWIC).

Figure 2.8 Schematic of Černekov counter used in the E701 running period.

Figure 2.9 Čerenkov pressure curve from a 140 GeV/c setting of the secondary beam with material and closed shutter backgrounds subtracted.

Figure 2.10 Number of neutrinos (arbitrary units) at the Lab E detector as a function of energy for a +250 GeV/c secondary setting. The solid curves represent the neutrino flux originating from two–body pion (low energy) and kaon (high energy) decays, the dashed lines are from neutrinos originating from $K \rightarrow \pi^0 \mu \nu$ decays and the dotted lines are from secondary decays prior to momentum selection (wide band decays): (a) Neutrino flux integrated over the full fiducial region (E^{SEP} is the energy separatrix); (b) neutrino flux integrated over the inner 10 inch beam centered radial bin.

Figure 2.11 Cumulative neutrino (solid line) and antineutrino (dashed line) flux spectrum at the Lab E detector, integrated over the full fiducial region.

Figure 3.1 Side view and perspective view of the Lab E detector.

Figure 3.2 Detail of a target and a toroid cart.

Figure 3.3 Construction detail of a spark chamber.

Figure 3.4 Construction detail of a liquid scintillation counter.

Figure 3.5 Schematic of target front end electronics for a single scintillation counter. Analog signal E_n is used to form the penetration trigger and digital signal S_n is used for both the penetration and muon triggers.

Figure 3.6 Logic diagram for the muon trigger.

Figure 4.1 Muon momentum reconstruction efficiency as a function of the muon momentum at the toroid front face for the E701 running period.

Figure 4.2 Cumulative probability for muon energy losses in a meter of steel as a function of the muon momentum (in GeV/c) and energy loss.

Figure 4.3 ADC pulse–height spectrum for muons in units of "equivalent number of minimum ionizing particles."

Figure 4.4 Contours of equal response for a scintillation counter in the target.

Figure 4.5 Computer generated display showing vertical and horizontal views of a muon trigger event. The bar graph at the top of the display indicates the hadron shower energy deposition measured by the scintillation counters. The solid lines are the fits to the final state muon trajectory in each view.

Figure 4.6 Test run calibration data showing (a) pulse height in units of equivalent number of minimum ionizing particles as a function of the incident hadron energy and (b) RMS of the pulse–height spectrum (in GeV) as a function of the incident hadron energy.

Figure 4.7 Ratio of the reconstructed kaon–induced neutrino energy from measured E_μ and E_{had} and predicted energy from the event Monte Carlo as a function of $y = E_{had}/(E_{had} + E_\mu)$ for the five secondary settings used in the E701 running

period. The measured hadron energy is *unadjusted.* The dotted lines are from the fits shown in Table 4.2

Figure 4.8 Same as 4.7, but with the hadron energy adjustment $E_{had} \rightarrow 1.048 E_{had}$.

Figure 4.9 (a) x–resolutions and (b) $\log Q^2$–resolutions as a function of x and Q^2 for the neutrino energy spectrum shown in Figure 2.11. The solid curves represent the total resolution and the remaining curves represent the contributions from: hadron energy resolution (dot–dashed); muon momentum resolution (dashed); and angular resolution (dotted).

Figure 5.1 Flow diagram illustrating structure function extraction sequence. The staggered rectangles indicate a separate computer file for each secondary setting and the ovals represent computer programs. The Monte Carlo DST events are re–weighted by the ratio of the new differential cross section to the initial differential cross section until the smeared event sums agree with the measured event sums.

Figure 5.2 Comparisons of measured (crosses) and Monte Carlo generated (histograms) quantities for neutrino and antineutrino events originating from pion and kaon decays: (a) beam centered radius of vertex; (b) Muon angle at event vertex; (c) hadron energy; and (d) muon energy at the event vertex.

Figure 5.3 Same comparisons as Figure 5.2, for derived quantities: (a) total energy, $E_{tot} = E_{had} + E_\nu$ (b) $y = E_{had}/E_{tot}$; and (c) Bjorken variable, $x = Q^2/2ME_{had}$.

Figure 5.4 Comparisons of measured (crosses) and Monte Carlo generated (histograms) event sums in x and $\log Q^2$ bins for (a) neutrino induced and (b) antineutrino induced events.

Figure 5.5 Structure function model corrections for (a) F_2 and (b) xF_3. Each curve shows the ratio of the uncorrected to corrected structure function. The uncorrected structure function was calculated by applying all model corrections *except*: isoscalar (solid lines); charm threshold (dotted line); strange sea (dashed lines – $\kappa = 0$); and radiative (dot–dashed).

Figure 6.1 (a) F_2 and (b) xF_3 as reported by the CCFRR collaboration [50] (diamonds) compared with results from this analysis (crosses) using the CCFRR assumptions.

Figure 6.2 (a) F_2 and (b) xF_3 as reported by the CDHSW collaboration [51] (diamonds) compared with results from this analysis (diamonds) using the CDHSW assumptions.

Figure 6.3 (a) F_2 and (b) xF_3 as reported by the WA59 collaboration [55] (diamonds) compared with results from this analysis (diamonds) using the WA59 assumptions.

Figure 6.4 (a) F_2 and (b) xF_3 as reported by the CHARM collaboration [56] (diamonds) compared with results from this analysis (diamonds) using the CHARM assumptions.

Figure 6.5 Ratio of F_2^{OTHER}/F_2^{CCFR} as a function of x (a) without and (b) with the adjustment of the CCFR assumptions to match the others'.

Figure 6.6 Ratio of xF_3^{OTHER}/xF_3^{CCFR} as a function of x (a) without and (b) with the adjustment of the CCFR assumptions to match the others'.

Figure 6.7 Comparisons of the scaling violations in F_2. The diamonds are for the data set in each title, the crosses are the CCFR data without matching assumptions and the squares are CCFR data with matching assumptions.

Figure 6.8 Comparison of the scaling violations in xF_3. Labeling of data is the same as in Figure 6.7

Figure 6.9 F_2 as reported by the BFP collaboration [57] (diamonds) compared with results from this analysis (diamonds) extracted with $R = 0$.

Figure 6.10 F_2 as reported by the EMC collaboration [58] (diamonds) compared with results from this analysis (diamonds) extracted with R_{QCD}.

Figure 6.11 F_2 as reported by the BCDMS collaboration [59] (diamonds) compared with results from this analysis (diamonds) extracted with $R = 0$.

Figure 6.12 Preliminary F_2 as reported by the recent SLAC experiment [60] (diamonds) compared with results from this analysis (diamonds) extracted with $R = 0$.

Figure 6.13 The mean squared charge test: Ratio of F_2 measured in the charged lepton experiments and the predicted value given in Equation 6.17.

Figure 6.14 The GLS sum rule: The crosses are xF_3 evaluated at $Q^2 = 3$ (GeV/c)^2 (right scale) and the diamonds are the cumulative integrals given in Equation 6.20 (left scale). The solid lines are from Fit No. 8 in Table 6.4.

Figure 6.15 Detail of low x data and fits shown in Table 6.4. Both are divided by $x^{.66}$ for clarity.

Figure 6.16 xF_3 and the NLO nonsinglet QCD fits corresponding to $\Lambda_{\overline{MS}} = 251, 96$ and 437 MeV/c, corresponding to the best (center lines), -2σ (shallow lines) and $+2\sigma$ (steep lines) values.

Figure 6.17 χ^2 contours as a function of (a) Λ_{LO} and (b) $\Lambda_{\overline{MS}}$ for the nonsinglet fits.

Figure 6.18 xF_3 extracted with $R = R_{QCD}$ (crosses) and $R = 0$ (diamonds).

Figure 6.19 Logarithmic derivatives of xF_3 (crosses) and $(1 + Q^2/\nu^2)/(1 + R)F_2$ (diamonds) and predictions from the NLO nonsinglet fits. The solid line corresponds to the $\Lambda_{\overline{MS}} = 251$ MeV/c fit to xF_3 and the dotted line corresponds to the $\Lambda_{\overline{MS}} = 386$ MeV/c fit to xF_3 ($x < 0.40$) and F_2 ($x > 0.40$). The dashed lines are the $\pm 2\sigma$ predictions: 96 MeV/c (shallow line) and 437 MeV/c (steep line).

Figure 6.20 Gluon densities for various values of Q^2 and γ_g: $\gamma_g = 0$ (dot–dashed), 10 (dotted), 100 (dashed) and 10^6 (solid).

Figure 6.21 χ^2 contours as a function of $\Lambda_{\overline{MS}}$ for NLO fits to F_2 alone: $\gamma_g = 0$ (dot–dashed), 10 (dotted), 100 (dashed) and 10^6 (solid)

Figure 6.22 χ^2 contours as a function of $\Lambda_{\overline{MS}}$ for NLO fits to F_2 alone, using different Q_0^2 parametrizations of the singlet quark density: dashed line from Equation 6.37 and solid line from Equation 6.27.

Figure 6.23 F_2 and the NLO simultaneous fits corresponding to $\Lambda_{\overline{MS}} = 253, 187$ and 317 MeV/c, the best (center lines), -2σ (shallow lines) and $+2\sigma$ (steep lines) values.

Figure 6.24 Logarithmic derivatives of F_2 (crosses) and predictions from the NLO simultaneous fits. The solid line corresponds to $\Lambda_{\overline{MS}} = 253$ MeV/c. The dashed lines are the $\pm 2\sigma$ predictions: 187 MeV/c (shallow line) and 317 MeV/c (steep line).

Fugure 6.25 χ^2 contours as a function of $\Lambda_{\overline{MS}}$ for the NLO nonsinglet, F_2 only, and simultaneous fits.

Figure 6.26 xF_3 and results of NLO QCD fits: solid line is from pure nonsinglet fit (same as Figure 6.16) and dashed line is the nonsinglet part of the F_2 only fit, evolved with the nonsinglet kernels and convoluted with the xF_3 coefficient function.

Figure 6.27 χ^2 contours as a function of η_g for the NLO F_2 only and simultaneous fits.

Figure 6.28 η_g as a function of $\Lambda_{\overline{MS}}$ for the NLO F_2 only and simultaneous fits.

Figure 6.29 $\Lambda_{\overline{MS}}$ as a function of η_g for the NLO F_2 only and simultaneous fits.

Figure 6.30 Gluon densities for NLO simultaneous fits at various Q^2 values. The solid lines correspond to $\eta_g = 4.13, 2.80$ and 6.50, the best (center lines), -2σ (hard) and $+2\sigma$ (soft) values. The dashed and dotted lines are the hard and soft densities from Reference [69] and the dotted line is from Reference [70].

Figure 6.31 $0.5[F_2 - xF_3]$ and the NLO simultaneous fit.

Figure 6.32 Comparison of observed scaling violations for several experiments. The fits are the same as in Figures 6.19 and 6.24.

Figure A.1 Fraction of the total cross section sampled with the structure function cuts (solid lines) and total cross section cuts (dotted lines) for neutrinos and antineutrinos.

Figure A.2 Measured (crosses) and simulated (dotted histogram) E_{had} distributions for a +250 GeV/c secondary beam setting. The histograms labeled ν_K and ν_π are found from the statistical subtractions given by Equations A.7 and A.8.

Figure A.3 Raw y–distributions for a −165 GeV/c secondary beam setting.

Figure A.4 Isoscalar and radiatively corrected y–distributions for all positive and negative secondary beam settings combined. The lines are fits to the data in the interval $.05 < y < .8$ using Equation A.10.

Figure A.5 Detail of raw low y distributions for a +140 GeV/c secondary beam setting.

Figure A.6 Flux normalized low y excess in units of $G_F^2 M/\pi$.

Figure C.1 Illustration of the effect slow rescaling has on $R = \sigma_L/\sigma_T$. The solid line corresponds to the parametrization of R given in Equation B.20. The dashed (dotted) line shows the ratio $\mathcal{F}_2/2x\mathcal{F}_1$ given in Equations C.30–C.33.

Nominal Setting		$\langle p^{\pi} \rangle$ GeV/c	$\langle p^{K} \rangle$ GeV/c	$\Delta p/\langle p \rangle$ %	σ_{θ_x} mrad	σ_{θ_y} mrad	Protons $\times 10^{17}$
E616	+250	244	257	9.4	.16	.20	11.06
	+200	197	201	9.6	.15	.20	6.55
	+165	166	170	10.0	.13	.20	5.02
	+140	139	142	9.9	.15	.21	3.25
	+120	120	122	10.1	.16	.23	2.61
	−250	239	238	8.7	.16	.20	11.21
	−200	194	195	9.2	.15	.20	5.31
	−165	164	165	9.6	.13	.20	4.15
	−140	138	139	9.4	.15	.21	2.88
	−120	118	120	9.7	.16	.23	1.98
E701	+250	246	248	9.6	.18	.22	8.61
	+200	201	203	10.3	.17	.21	5.45
	+165	168	169	10.7	.17	.21	4.73
	+140	143	143	10.9	.17	.21	4.86
	−165	167	164	10.4	.18	.21	14.95

Table 2.1

Setting	E_s GeV	β in^{-1}
±250	165	.01768
±200	134	.01550
±165	110	.01440
±140	92	.01260
±120	80	.01190

Table 2.2

Setting	$f_{WB/prim}$	E_0	b	c
	$\times 10^{-11}/\text{in}^2/\text{GeV}$	GeV	GeV	
+250	1.48	7.50	1.32	22.97
+200	1.88	9.87	1.78	19.26
+165	1.39	8.07	0.89	21.81
+140	1.71	8.15	1.20	14.68
+120	1.18	7.36	1.18	21.01
−250	1.35	12.96	17.47	12.63
−200	1.46	12.96	17.47	12.63
−165	1.35	12.96	17.47	12.63
−140	1.34	12.96	17.47	12.63
−120	1.35	12.96	17.47	12.63

Table 2.3

Componant	E616	E701
Target Carts	6	4
Fiducial Mass	5362 gm/cm^2	3099 gm/cm^2
Target Chambers	36	24
Target Counters	82	56
Toroid Carts	3	3
Toroid Chambers	1 $5' \times 10'$ in each of 6 toroid gaps; 4 $5' \times 10'$ and 1 $10' \times 10'$ after each full toroid; 7 $5' \times 10'$ and 2 $10' \times 10'$ behind 3rd toroid	no chambers in toroid gaps; 5 $10' \times 10'$ after each full toroid

Table 3.1

Hadron Energy (GeV)	a (mr)	b (GeV/c–mr)
$0 < E_{had} < 10$	.162	84.35
$10 < E_{had} < 25$	.257	80.25
$20 < E_{had} < 50$	.171	105.38
$50 < E_{had} < 100$	.171	106.23
$100 < E_{had} < 200$	.126	129.22
$200 < E_{had} < 400$	-.031	156.10

Table 4.1

Parameter	E701 Algorithm	E701 Algorithm
		$E_{had} \rightarrow 1.048 E_{had}$
δ_ν^{+250}	.0111 ± .0041	.0069 ± .0043
δ_ν^{+200}	.0080 ± .0047	.0051 ± .0047
δ_ν^{+165}	.0114 ± .0053	.0058 ± .0054
δ_ν^{+140}	-.0078 ± .0056	-.0107 ± .0058
δ_ν^{-165}	.0254 ± .0075	.0197 ± .0080
α_μ	.0107 ± .0031	.0014 ± .0033
β_{had}	-.0447 ± .0049	-.0015 ± .0055
χ^2/dof	71/68	64/68

Table 4.2

Parameter	E616 Algorithm
δ_ν^{+250}	.0046 ± .0029
δ_ν^{+200}	-.0106 ± .0036
δ_ν^{+165}	-.0144 ± .0042
δ_ν^{+140}	-.0143 ± .0059
δ_ν^{+120}	-.0209 ± .0069
δ_ν^{-250}	.0141 ± .0133
δ_ν^{-200}	.0073 ± .0116
δ_ν^{-165}	.0102 ± .0114
δ_ν^{-140}	-.0086 ± .0141
δ_ν^{-120}	.0122 ± .0184
α_μ	-.0011 ± .0023
β_{had}	.0140 ± .0041
χ^2/dof	182/134

Table 4.3

CUT	E616 Settings					E701 Settings				TOTAL
Neutrinos	+250	+200	+165	+140	+120	+250	+200	+165	+140	ν
Beam OK	45092	37565	31330	19917	16000	23505	24253	21032	24992	243686
Fiducial	38459	32517	27290	17203	13732	19692	20358	17728	20927	207906
$\theta_\mu < .37$	38366	32402	27198	17130	13679	19127	19835	17348	20409	205494
Target Fit	38290	32350	27144	17106	13654	19107	19786	17324	20400	205161
Good C.C.	38150	32244	27043	17041	13608	18754	19328	16880	19791	202839
Good Muon	28921	23286	18854	11207	8743	15059	15056	12642	14314	148082
$\theta_\mu < .2$	28807	23178	18757	11162	8696	14999	14998	12582	14225	147404
Hole Cut	28794	23170	18755	11160	8695	14994	14995	12576	14224	147363
$E_{had} > 10$ GeV	22830	17296	13161	7188	5004	12501	11674	9225	9650	108529
Toroid Fit	22671	17071	12898	7111	4981	11794	10882	8387	8610	104405
$r^\pi < 30$ in.	21108	15619	11496	5986	3996	10854	9723	7246	7098	93126
$E_\mu > 4$ GeV	20980	15537	11425	5945	3966	10612	9519	7105	6927	92016
$0 < \log Q^2 < 2.4$	20328	14967	10917	5603	3713	10309	9191	6832	6631	88491
Antineutrinos	-250	-200	-165	-140	-120			-165		$\bar{\nu}$
Beam OK	4156	4471	4710	3950	2830			11986		32109
Fiducial	3645	3992	4220	3480	2426			10218		27981
$\theta_\mu < .37$	3641	3985	4219	3477	2425			10144		27891
Target Fit	3638	3984	4216	3477	2424			10135		27874
Good C.C.	3635	3977	4201	3464	2415			9917		27609
Good Muon	2917	3178	3344	2709	1832			8447		22427
$\theta_\mu < .2$	2912	3174	3341	2707	1828			8434		22396
Hole Cut	2910	3173	3341	2707	1828			8433		22392
$E_{had} > 10$ GeV	1851	1923	1926	1401	809			4764		12674
Toroid Fit	1843	1903	1918	1397	794			4425		12280
$r^\pi < 30$ in.	1581	1659	1584	1125	794			3696		10439
$E_\mu > 4$ GeV	1534	1628	1558	1111	602			3580		10013
$0 < \log Q^2 < 2.4$	1430	1517	1434	1019	531			3321		9252

Table 4.4

		Neutrinos			Antineutrinos		
x	Q^2	Acceptance	Smearing	Bin Center	Acceptance	Smearing	Bin Center
.015	1.26	1.051±.002	0.969±.009	1.411±.012	1.057±.004	0.955±.015	1.423±.021
	2.00	1.052±.002	0.975±.009	1.077±.009	1.052±.004	1.011±.019	0.829±.014
	3.16	1.052±.002	0.969±.011	1.255±.013	1.075±.007	0.961±.026	1.058±.025
	5.01	1.082±.004	0.970±.013	1.024±.012	1.075±.010	0.991±.038	0.402±.014
.045	1.26	1.058±.002	0.943±.010	1.024±.010	1.057±.004	0.972±.015	1.014±.014
	2.00	1.065±.002	0.996±.008	0.997±.008	1.066±.003	0.999±.013	1.033±.013
	3.16	1.091±.002	1.043±.007	1.042±.007	1.089±.004	1.038±.014	1.083±.013
	5.01	1.119±.003	1.003±.008	0.991±.007	1.132±.006	1.012±.017	0.954±.014
	7.94	1.130±.003	0.987±.008	0.964±.008	1.153±.010	1.020±.024	0.954±.021
	12.59	1.187±.005	0.987±.010	1.200±.011	1.201±.018	1.036±.036	0.982±.032
.080	2.00	1.057±.002	0.982±.010	1.052±.009	1.060±.003	0.995±.015	1.048±.014
	3.16	1.077±.002	1.005±.008	1.000±.007	1.069±.003	1.001±.012	1.017±.011
	5.01	1.146±.002	1.026±.006	1.045±.006	1.134±.004	1.019±.012	1.075±.012
	7.94	1.227±.003	1.017±.006	1.074±.006	1.246±.008	1.038±.014	1.070±.014
	12.59	1.224±.004	1.004±.007	0.943±.006	1.264±.012	0.984±.019	0.923±.017
	19.95	1.278±.005	1.011±.008	1.137±.008	1.311±.020	0.937±.026	1.205±.034
.125	3.16	1.062±.002	1.033±.009	1.013±.008	1.058±.003	1.021±.014	1.036±.012
	5.01	1.116±.002	1.031±.007	0.973±.006	1.095±.004	1.058±.012	0.987±.010
	7.94	1.244±.003	1.058±.006	1.037±.005	1.215±.006	1.052±.012	1.021±.010
	12.59	1.348±.004	1.040±.006	1.039±.005	1.375±.011	1.032±.015	1.012±.013
	19.95	1.304±.004	1.020±.007	0.949±.006	1.383±.017	1.000±.021	0.941±.018
	31.62	1.413±.006	1.031±.007	1.098±.007	1.476±.030	1.045±.032	1.065±.031
.175	5.01	1.088±.002	1.059±.010	0.973±.007	1.082±.004	1.032±.015	1.005±.012
	7.94	1.200±.003	1.098±.008	0.956±.006	1.160±.005	1.067±.014	1.003±.011
	12.59	1.402±.005	1.094±.007	0.993±.005	1.369±.010	1.084±.015	0.951±.011
	19.95	1.440±.006	1.049±.007	0.981±.006	1.446±.017	1.027±.019	0.897±.015
	31.62	1.385±.006	1.035±.008	0.961±.006	1.448±.025	1.017±.028	0.976±.025
	50.12	1.592±.010	1.062±.009	1.079±.009	1.777±.070	1.017±.048	0.818±.036
.225	5.01	1.085±.003	1.056±.013	1.141±.011	1.081±.005	1.044±.021	1.189±.018
	7.94	1.166±.003	1.034±.009	1.009±.007	1.145±.006	1.061±.017	1.026±.013
	12.59	1.361±.005	1.079±.008	1.021±.006	1.306±.010	1.041±.016	1.033±.013
	19.95	1.522±.007	1.052±.007	1.034±.006	1.484±.017	1.029±.020	0.985±.016
	31.62	1.448±.007	1.028±.009	0.976±.007	1.472±.027	1.055±.031	0.971±.025
	50.12	1.535±.009	1.050±.009	1.038±.008	1.506±.041	1.071±.045	0.997±.037

Table 5.1

(continued on next page)

		Neutrinos			Antineutrinos		
x	Q^2	Acceptance	Smearing	Bin Center	Acceptance	Smearing	Bin Center
.275	7.94	1.146±.004	1.118±.012	0.971±.008	1.128±.006	1.077±.020	1.025±.015
	12.59	1.335±.006	1.112±.010	0.998±.007	1.294±.010	1.074±.019	1.002±.014
	19.95	1.576±.008	1.102±.009	1.050±.007	1.494±.018	1.082±.022	1.027±.017
	31.62	1.584±.009	1.078±.010	0.971±.007	1.522±.028	0.980±.030	0.967±.025
	50.12	1.518±.009	1.057±.010	0.992±.008	1.478±.039	1.038±.045	1.001±.037
	79.43	1.827±.017	1.070±.012	1.047±.010	1.818±.128	1.042±.092	0.743±.057
.350	7.94	1.138±.004	1.155±.012	1.055±.008	1.118±.005	1.151±.019	1.082±.014
	12.59	1.297±.005	1.133±.008	0.965±.006	1.235±.007	1.145±.016	0.999±.012
	19.95	1.574±.007	1.151±.007	1.017±.005	1.478±.014	1.140±.017	1.010±.013
	31.62	1.697±.008	1.103±.007	0.964±.005	1.583±.022	1.073±.021	0.895±.016
	50.12	1.558±.008	1.073±.008	0.961±.006	1.478±.028	1.003±.029	0.971±.027
	79.43	1.755±.011	1.086±.008	1.054±.008	1.892±.086	1.081±.054	0.962±.045
.450	12.59	1.252±.006	1.169±.013	0.967±.008	1.220±.009	1.183±.023	1.030±.015
	19.95	1.526±.008	1.159±.010	0.990±.007	1.437±.016	1.155±.022	1.019±.016
	31.62	1.759±.011	1.121±.009	1.046±.007	1.686±.028	1.078±.025	1.000±.020
	50.12	1.667±.012	1.076±.010	0.991±.008	1.577±.037	1.025±.036	0.953±.029
	79.43	1.674±.013	1.083±.011	1.001±.009	1.649±.063	0.997±.053	1.025±.049
	125.89	2.153±.026	1.084±.013	1.063±.012	2.171±.263	0.745±.104	0.923±.120
.550	12.59	1.240±.008	1.147±.018	1.012±.012	1.212±.012	1.239±.034	1.040±.021
	19.95	1.460±.011	1.153±.015	0.994±.010	1.403±.019	1.184±.031	1.035±.021
	31.62	1.760±.015	1.172±.014	0.969±.009	1.710±.035	1.120±.032	0.968±.022
	50.12	1.794±.018	1.099±.014	0.960±.010	1.736±.054	1.044±.045	0.937±.033
	79.43	1.643±.017	1.077±.016	0.976±.012	1.590±.069	1.079±.072	0.969±.052
	125.89	2.026±.029	1.055±.016	1.058±.014	1.914±.194	1.176±.142	0.791±.077
.650	12.59	1.212±.012	0.925±.027	1.637±.037	1.230±.021	1.040±.050	1.590±.056
	19.95	1.419±.014	0.933±.018	1.041±.016	1.418±.026	1.050±.038	0.988±.027
	31.62	1.740±.021	1.042±.019	1.024±.014	1.657±.044	1.087±.044	0.996±.031
	50.12	1.828±.026	1.017±.020	0.982±.015	1.667±.065	1.053±.062	0.974±.045
	79.43	1.680±.025	1.005±.022	0.917±.017	1.430±.066	0.886±.080	1.015±.076
	125.89	1.835±.033	1.023±.024	1.003±.020	2.199±.283	1.050±.149	0.898±.103
.850	19.95	1.335±.012	0.519±.013	0.480±.011	1.316±.022	0.646±.027	0.452±.016
	31.62	1.572±.019	0.571±.013	0.466±.010	1.537±.038	0.630±.030	0.495±.021
	50.12	1.754±.027	0.566±.014	0.503±.012	1.728±.068	0.582±.036	0.530±.032
	79.43	1.681±.029	0.503±.015	0.458±.013	1.530±.083	0.577±.061	0.463±.046
	125.89	1.750±.036	0.573±.019	0.407±.013	1.720±.148	0.412±.066	0.517±.081

Table 5.1

(continued from previous page)

x	Q^2	$\frac{\pi}{G^2M}\langle\frac{1}{E}\frac{d^2\sigma^\nu}{dx\,dy}\rangle_\nu$	$\langle y\rangle_\nu$	$\langle y^2\rangle_\nu$	$\frac{\pi}{G^2M}\langle\frac{1}{E}\frac{d^2\sigma^{\bar\nu}}{dx\,dy}\rangle_{\bar\nu}$	$\langle y\rangle_{\bar\nu}$	$\langle y^2\rangle_{\bar\nu}$
.015	1.26	0.7540±0.0216	.6074	.4168	0.4684±0.0306	.6868	.5023
	2.00	0.8071±0.0240	.6097	.4176	0.4884±0.0394	.6887	.5132
	3.16	0.8797±0.0283	.6813	.4820	0.6053±0.0534	.7541	.5810
	5.01	0.7943±0.0336	.8578	.7423	0.4879±0.0770	.8822	.7835
.045	1.26	1.0304±0.0349	.2415	.0682	0.6833±0.0534	.2686	.0794
	2.00	1.1072±0.0282	.3795	.1672	0.6611±0.0399	.4226	.1955
	3.16	1.0160±0.0242	.5517	.3458	0.4869±0.0311	.6182	.4094
	5.01	1.0433±0.0266	.6088	.4195	0.4990±0.0372	.7052	.5340
	7.94	1.2163±0.0318	.6152	.4015	0.5207±0.0590	.6777	.4764
	12.59	1.0787±0.0376	.8005	.6520	0.4103±0.0768	.8643	.7553
.080	2.00	1.2167±0.0349	.2152	.0542	0.8842±0.0520	.2394	.0631
	3.16	1.2123±0.0272	.3392	.1338	0.7108±0.0377	.3778	.1565
	5.01	1.1096±0.0233	.5121	.2997	0.5532±0.0280	.5718	.3524
	7.94	1.1576±0.0244	.6276	.4453	0.4721±0.0288	.7223	.5559
	12.59	1.2339±0.0295	.5945	.3839	0.5273±0.0493	.6529	.4501
	19.95	1.1422±0.0330	.7543	.5832	0.4042±0.0584	.8316	.7014
.125	3.16	1.1376±0.0313	.2182	.0557	0.8253±0.0461	.2428	.0649
	5.01	1.1322±0.0249	.3440	.1377	0.6083±0.0325	.3832	.1610
	7.94	1.1491±0.0219	.5194	.3083	0.4182±0.0238	.5800	.3626
	12.59	1.1314±0.0236	.6142	.4267	0.3085±0.0254	.7092	.5367
	19.95	1.1710±0.0274	.5912	.3776	0.4876±0.0435	.6492	.4432
	31.62	1.1317±0.0308	.7548	.5827	0.2738±0.0465	.8291	.6965
.175	5.01	1.0617±0.0288	.2465	.0709	0.7212±0.0398	.2745	.0829
	7.94	1.0391±0.0239	.3867	.1732	0.4192±0.0277	.4308	.2027
	12.59	1.0584±0.0227	.5359	.3250	0.3078±0.0220	.6041	.3892
	19.95	1.0376±0.0257	.5796	.3799	0.3204±0.0283	.6675	.4807
	31.62	1.0037±0.0279	.6106	.3919	0.2765±0.0386	.6742	.4683
	50.12	0.9994±0.0340	.7963	.6435	0.1815±0.0470	.8473	.7250
.225	5.01	1.0088±0.0333	.1921	.0432	0.7501±0.0484	.2138	.0504
	7.94	0.9877±0.0259	.3029	.1067	0.5055±0.0323	.3374	.1248
	12.59	0.9570±0.0228	.4573	.2390	0.3149±0.0227	.5107	.2811
	19.95	0.9323±0.0238	.5605	.3552	0.2130±0.0211	.6451	.4435
	31.62	1.0055±0.0269	.5558	.3393	0.2318±0.0342	.6119	.3990
	50.12	0.9034±0.0282	.6920	.4931	0.1326±0.0314	.7659	.5964

Table 5.2

(continued on next page)

x	Q^2	$\frac{\pi}{G^2M}\langle\frac{1}{E}\frac{d^2\sigma^\nu}{dxdy}\rangle_\nu$	$\langle y\rangle_\nu$	$\langle y^2\rangle_\nu$	$\frac{\pi}{G^2M}\langle\frac{1}{E}\frac{d^2\sigma^{\bar\nu}}{dxdy}\rangle_{\bar\nu}$	$\langle y\rangle_{\bar\nu}$	$\langle y^2\rangle_{\bar\nu}$
.275	7.94	0.8807±0.0269	.2483	.0719	0.4689±0.0352	.2765	.0840
	12.59	0.8343±0.0229	.3843	.1699	0.3049±0.0245	.4284	.1992
	19.95	0.8691±0.0225	.5246	.3111	0.2067±0.0190	.5936	.3753
	31.62	0.8401±0.0251	.5449	.3345	0.2001±0.0260	.6202	.4161
	50.12	0.7806±0.0264	.6058	.3839	0.0911±0.0288	.6696	.4604
	79.43	0.7147±0.0333	.7859	.6256	0.1017±0.0355	.8269	.6899
.350	7.94	0.6933±0.0203	.1954	.0445	0.4087±0.0282	.2175	.0520
	12.59	0.6625±0.0161	.3064	.1088	0.2867±0.0187	.3414	.1273
	19.95	0.6280±0.0147	.4475	.2275	0.1886±0.0133	.5015	.2694
	31.62	0.6395±0.0156	.5123	.2971	0.1436±0.0137	.5936	.3775
	50.12	0.5780±0.0168	.5303	.3039	0.1489±0.0195	.5824	.3567
	79.43	0.5828±0.0181	.6864	.4829	0.0680±0.0149	.7567	.5808
.450	12.59	0.4459±0.0152	.2400	.0670	0.2148±0.0197	.2674	.0784
	19.95	0.4012±0.0131	.3624	.1501	0.1786±0.0137	.4047	.1765
	31.62	0.4040±0.0130	.4762	.2562	0.0855±0.0107	.5435	.3143
	50.12	0.3772±0.0140	.4939	.2731	0.0546±0.0142	.5542	.3319
	79.43	0.3493±0.0142	.5782	.3484	0.0362±0.0130	.6396	.4190
	125.89	0.3020±0.0181	.7557	.5780	0.0084±0.0126	.7922	.6332
.550	12.59	0.2655±0.0135	.1968	.0451	0.1453±0.0187	.2191	.0527
	19.95	0.2477±0.0109	.3045	.1067	0.1169±0.0125	.3395	.1251
	31.62	0.2192±0.0103	.4157	.1954	0.0491±0.0097	.4704	.2357
	50.12	0.1905±0.0105	.4632	.2427	0.0488±0.0100	.5335	.3070
	79.43	0.1938±0.0107	.5033	.2688	0.0554±0.0125	.5545	.3189
	125.89	0.1521±0.0114	.6736	.4632	0.0054±0.0085	.7364	.5490
.650	12.59	0.1550±0.0121	.1665	.0323	0.0817±0.0181	.1854	.0378
	19.95	0.1275±0.0077	.2599	.0780	0.0546±0.0100	.2897	.0914
	31.62	0.1168±0.0072	.3726	.1573	0.0414±0.0074	.4186	.1872
	50.12	0.0884±0.0069	.4372	.2164	0.0301±0.0072	.5066	.2749
	79.43	0.0731±0.0070	.4617	.2315	0.0334±0.0086	.5070	.2715
	125.89	0.0774±0.0069	.6017	.3728	0.0100±0.0067	.6659	.4509

Table 5.2

(continued from previous page)

x	Q^2	F_2	ΔF_2	xF_3	ΔxF_3	$\Delta F_2 \Delta xF_3$
.015	1.26	1.2278	0.0358	0.2607	0.0456	-0.5466E-03
	2.00	1.2571	0.0434	0.3062	0.0564	-0.1134E-02
	3.16	1.5166	0.0615	0.2361	0.0681	-0.2383E-02
	5.01	1.4460	0.0985	0.2954	0.0865	-0.5829E-02
.045	1.26	1.1808	0.0405	0.6817	0.1469	-0.2212E-02
	2.00	1.3722	0.0360	0.6191	0.0792	-0.8951E-03
	3.16	1.3618	0.0347	0.5812	0.0501	-0.4171E-03
	5.01	1.4457	0.0422	0.5493	0.0554	-0.7553E-03
	7.94	1.6003	0.0620	0.7399	0.0797	-0.2719E-02
	12.59	1.5402	0.0928	0.6497	0.0902	-0.5191E-02
.080	2.00	1.3805	0.0386	0.7043	0.1589	-0.2132E-02
	3.16	1.4177	0.0327	0.7671	0.0818	-0.7809E-03
	5.01	1.4244	0.0305	0.6416	0.0483	-0.2532E-03
	7.94	1.5256	0.0351	0.7038	0.0447	-0.2597E-03
	12.59	1.5654	0.0512	0.7736	0.0700	-0.1686E-02
	19.95	1.5362	0.0690	0.7226	0.0721	-0.2592E-02
.125	3.16	1.2806	0.0344	0.6479	0.1397	-0.1611E-02
	5.01	1.2774	0.0289	0.8022	0.0712	-0.4858E-03
	7.94	1.3363	0.0271	0.8675	0.0424	-0.8042E-04
	12.59	1.3185	0.0315	0.8833	0.0412	-0.9021E-04
	19.95	1.4574	0.0453	0.7477	0.0626	-0.1211E-02
	31.62	1.3788	0.0564	0.8543	0.0596	-0.1323E-02
.175	5.01	1.1841	0.0313	0.6474	0.1111	-0.9716E-03
	7.94	1.1059	0.0269	0.8935	0.0583	-0.1897E-03
	12.59	1.1721	0.0268	0.8743	0.0402	0.4931E-04
	19.95	1.1914	0.0333	0.7912	0.0469	-0.1361E-03
	31.62	1.1407	0.0426	0.7872	0.0561	-0.7424E-03
	50.12	1.1604	0.0590	0.8152	0.0607	-0.1128E-02
.225	5.01	1.1012	0.0353	0.5914	0.1642	-0.1876E-02
	7.94	1.0420	0.0280	0.8203	0.0792	-0.4218E-03
	12.59	1.0172	0.0253	0.8276	0.0454	0.2606E-04
	19.95	0.9968	0.0275	0.8127	0.0392	0.1442E-03
	31.62	1.0525	0.0368	0.9035	0.0548	-0.4533E-03
	50.12	0.9719	0.0401	0.7945	0.0463	-0.1961E-03

Table 5.3

(continued on next page)

x	Q^2	F_2	ΔF_2	xF_3	ΔxF_3	$\Delta F_2 \Delta xF_3$
.275	7.94	0.8922	0.0282	0.8220	0.0994	-0.6422E-03
	12.59	0.8530	0.0245	0.7666	0.0534	-0.5666E-04
	19.95	0.9060	0.0246	0.7839	0.0377	0.1686E-03
	31.62	0.8810	0.0303	0.7432	0.0458	-0.2921E-04
	50.12	0.7723	0.0346	0.7593	0.0459	-0.1270E-03
	79.43	0.7853	0.0480	0.6137	0.0510	-0.1599E-03
.350	7.94	0.6887	0.0209	0.6838	0.0956	-0.5649E-03
	12.59	0.6593	0.0167	0.6378	0.0466	-0.9393E-04
	19.95	0.6415	0.0155	0.5701	0.0283	0.5179E-04
	31.62	0.6519	0.0171	0.5860	0.0268	0.6781E-04
	50.12	0.6019	0.0212	0.5045	0.0330	-0.9902E-04
	79.43	0.6018	0.0219	0.5320	0.0256	0.1100E-03
.450	12.59	0.4308	0.0157	0.4721	0.0574	-0.1956E-03
	19.95	0.4206	0.0136	0.3237	0.0314	-0.7874E-05
	31.62	0.3942	0.0135	0.3949	0.0228	0.6567E-04
	50.12	0.3488	0.0160	0.4001	0.0268	0.1210E-05
	79.43	0.3319	0.0166	0.3501	0.0230	0.3695E-04
	125.89	0.2884	0.0210	0.2970	0.0233	0.1703E-03
.550	12.59	0.2571	0.0140	0.2836	0.0632	-0.2454E-03
	19.95	0.2515	0.0112	0.2162	0.0314	-0.3591E-04
	31.62	0.2058	0.0107	0.2296	0.0210	0.1963E-04
	50.12	0.1893	0.0114	0.1746	0.0201	0.1576E-04
	79.43	0.2015	0.0132	0.1637	0.0216	-0.4163E-04
	125.89	0.1414	0.0131	0.1516	0.0157	0.6088E-04
.650	12.59	0.1446	0.0127	0.2040	0.0690	-0.3041E-03
	19.95	0.1213	0.0081	0.1384	0.0272	-0.4921E-04
	31.62	0.1164	0.0075	0.1081	0.0167	0.1951E-06
	50.12	0.0920	0.0077	0.0719	0.0143	-0.1149E-05
	79.43	0.0824	0.0086	0.0464	0.0155	-0.2547E-04
	125.89	0.0758	0.0084	0.0725	0.0112	0.3548E-05

Table 5.3

(continued from previous page)

x	Q^2	F_2	Stat.	E_{had}	E_μ	E	p_{secy}	$\Delta_{\theta_{rec}}$	$\Phi^{\bar{\nu}}/\Phi^{\nu}$
.015	1.26	1.2278	0.0358	0.0013	-.0157	-.0171	-.0015	0.0015	-.0006
	2.00	1.2571	0.0434	0.0084	-.0196	-.0198	-.0096	0.0005	-.0007
	3.16	1.5166	0.0615	0.0244	-.0169	-.0134	-.0193	0.0011	-.0007
	5.01	1.4460	0.0985	0.0179	-.0286	-.0373	-.0259	0.0002	-.0008
.045	1.26	1.1808	0.0405	-.0102	-.0192	-.0191	0.0073	-.0012	-.0015
	2.00	1.3722	0.0360	-.0086	-.0192	-.0194	0.0053	-.0005	-.0009
	3.16	1.3618	0.0347	0.0029	-.0169	-.0185	-.0023	0.0025	0.0002
	5.01	1.4457	0.0422	0.0128	-.0185	-.0166	-.0135	0.0006	0.0007
	7.94	1.6003	0.0620	0.0162	-.0193	-.0235	-.0174	-.0006	0.0003
	12.59	1.5402	0.0928	0.0341	-.0186	-.0110	-.0325	0.0059	0.0011
.080	2.00	1.3805	0.0386	-.0105	-.0177	-.0247	0.0087	-.0023	-.0017
	3.16	1.4177	0.0327	-.0042	-.0176	-.0163	0.0075	0.0015	-.0007
	5.01	1.4244	0.0305	-.0039	-.0218	-.0220	-.0010	0.0036	0.0007
	7.94	1.5256	0.0351	0.0201	-.0134	-.0131	-.0144	0.0010	0.0018
	12.59	1.5654	0.0512	0.0145	-.0162	-.0094	-.0158	0.0003	0.0011
	19.95	1.5362	0.0690	0.0287	-.0136	-.0174	-.0286	0.0055	0.0023
.125	3.16	1.2806	0.0344	-.0141	-.0124	-.0146	0.0098	-.0009	-.0012
	5.01	1.2774	0.0289	-.0085	-.0138	-.0154	0.0055	0.0017	-.0002
	7.94	1.3363	0.0271	0.0025	-.0121	-.0121	-.0031	0.0044	0.0014
	12.59	1.3185	0.0315	0.0135	-.0071	-.0089	-.0142	0.0023	0.0024
	19.95	1.4574	0.0453	0.0107	-.0161	-.0124	-.0139	-.0017	0.0020
	31.62	1.3788	0.0564	0.0293	-.0046	-.0053	-.0248	0.0079	0.0033
.175	5.01	1.1841	0.0313	-.0075	-.0103	-.0109	0.0071	0.0009	-.0006
	7.94	1.1059	0.0269	-.0019	-.0034	-.0044	0.0033	0.0028	0.0006
	12.59	1.1721	0.0268	0.0067	-.0071	-.0079	-.0071	0.0037	0.0021
	19.95	1.1914	0.0333	0.0139	-.0055	-.0059	-.0131	0.0000	0.0025
	31.62	1.1407	0.0426	0.0079	-.0084	-.0096	-.0109	0.0017	0.0025
	50.12	1.1604	0.0590	0.0296	-.0003	-.0033	-.0316	0.0079	0.0037
.225	5.01	1.1012	0.0353	-.0146	-.0076	-.0100	0.0073	0.0000	-.0009
	7.94	1.0420	0.0280	-.0058	-.0050	-.0032	0.0051	0.0021	0.0002
	12.59	1.0172	0.0253	0.0006	-.0012	-.0024	-.0003	0.0046	0.0015
	19.95	0.9968	0.0275	0.0081	0.0005	-.0014	-.0110	0.0014	0.0025
	31.62	1.0525	0.0368	0.0065	0.0019	-.0048	-.0089	0.0000	0.0023
	50.12	0.9719	0.0401	0.0137	-.0017	-.0012	-.0137	0.0033	0.0033

Table 5.4a

(continued on next page)

x	Q^2	F_2	Stat.	E_{had}	E_μ	E	p_{secy}	$\Delta_{\theta_{sec}}$	$\Phi^{\bar{\nu}}/\Phi^{\nu}$
.275	7.94	0.8922	0.0282	-.0039	0.0051	0.0024	0.0048	0.0010	-.0001
	12.59	0.8530	0.0245	-.0018	0.0034	0.0031	0.0003	0.0030	0.0010
	19.95	0.9060	0.0246	0.0060	0.0050	-.0028	-.0075	0.0020	0.0022
	31.62	0.8810	0.0303	0.0056	-.0038	0.0008	-.0098	0.0000	0.0023
	50.12	0.7723	0.0346	0.0051	0.0034	-.0021	-.0085	0.0017	0.0024
	79.43	0.7853	0.0480	0.0292	0.0075	0.0063	-.0247	0.0061	0.0033
.350	7.94	0.6887	0.0209	-.0068	0.0074	0.0024	0.0041	0.0008	-.0003
	12.59	0.6593	0.0167	-.0057	0.0014	0.0004	0.0017	0.0021	0.0004
	19.95	0.6415	0.0155	-.0008	0.0066	0.0028	-.0034	0.0023	0.0013
	31.62	0.6519	0.0171	0.0039	0.0108	0.0078	-.0070	0.0007	0.0019
	50.12	0.6019	0.0212	0.0013	0.0043	0.0021	-.0055	0.0006	0.0016
	79.43	0.6018	0.0219	0.0086	0.0076	0.0053	-.0110	0.0032	0.0025
.450	12.59	0.4308	0.0157	-.0023	0.0109	0.0071	0.0014	0.0013	0.0000
	19.95	0.4206	0.0136	-.0034	0.0082	0.0047	-.0013	0.0010	0.0006
	31.62	0.3942	0.0135	-.0013	0.0088	0.0055	-.0039	0.0004	0.0011
	50.12	0.3488	0.0160	0.0001	0.0091	0.0038	-.0040	-.0002	0.0010
	79.43	0.3319	0.0166	-.0004	0.0053	0.0019	-.0039	0.0010	0.0012
	125.89	0.2884	0.0210	0.0106	0.0094	0.0087	-.0089	0.0023	0.0014
.550	12.59	0.2571	0.0140	-.0054	0.0071	0.0056	0.0011	0.0007	-.0001
	19.95	0.2515	0.0112	-.0009	0.0083	0.0056	-.0005	0.0009	0.0002
	31.62	0.2058	0.0107	-.0008	0.0064	0.0032	-.0018	0.0008	0.0004
	50.12	0.1893	0.0114	-.0004	0.0088	0.0049	-.0026	0.0001	0.0005
	79.43	0.2015	0.0132	-.0004	0.0113	0.0080	-.0016	0.0003	0.0006
	125.89	0.1414	0.0131	0.0027	0.0048	0.0041	-.0031	0.0009	0.0006
.650	12.59	0.1446	0.0127	-.0024	0.0017	-.0012	0.0001	0.0005	-.0001
	19.95	0.1213	0.0081	-.0023	0.0067	0.0047	-.0002	0.0006	0.0000
	31.62	0.1164	0.0075	-.0009	0.0066	0.0044	-.0008	0.0004	0.0002
	50.12	0.0920	0.0077	-.0013	0.0053	0.0042	-.0012	0.0001	0.0002
	79.43	0.0824	0.0086	-.0009	0.0033	0.0020	-.0011	0.0001	0.0002
	125.89	0.0758	0.0084	-.0008	0.0059	0.0049	-.0010	0.0006	0.0003

Table 5.4a

(continued from previous page)

x	Q^2	xF_3	Stat.	E_{had}	E_μ	E	p_{secy}	$\Delta_{\theta_{sec}}$	$\Phi^{\bar{\nu}}/\Phi^{\nu}$
.015	1.26	0.2607	0.0456	-.0017	-.0042	-.0048	0.0018	0.0014	0.0106
	2.00	0.3062	0.0564	0.0001	-.0061	-.0046	0.0033	0.0027	0.0123
	3.16	0.2361	0.0681	-.0024	-.0045	-.0031	0.0012	0.0013	0.0081
	5.01	0.2954	0.0865	0.0000	-.0005	0.0018	0.0001	0.0021	0.0085
.045	1.26	0.6817	0.1469	-.0144	-.0280	-.0213	0.0153	0.0121	0.0509
	2.00	0.6191	0.0792	-.0071	-.0186	-.0092	0.0129	0.0055	0.0266
	3.16	0.5812	0.0501	-.0047	-.0156	-.0141	0.0053	0.0034	0.0158
	5.01	0.5493	0.0554	0.0000	-.0171	-.0141	0.0039	0.0041	0.0134
	7.94	0.7399	0.0797	0.0043	-.0116	-.0048	0.0066	0.0046	0.0183
	12.59	0.6497	0.0902	0.0083	-.0073	-.0041	-.0034	0.0020	0.0124
.080	2.00	0.7043	0.1589	-.0049	-.0049	0.0092	0.0159	0.0085	0.0450
	3.16	0.7671	0.0818	-.0115	-.0220	-.0310	0.0136	0.0018	0.0288
	5.01	0.6416	0.0483	-.0026	-.0070	-.0013	0.0059	0.0036	0.0147
	7.94	0.7039	0.0447	0.0023	-.0146	-.0100	0.0008	0.0030	0.0127
	12.59	0.7736	0.0700	-.0037	-.0162	-.0203	0.0016	0.0018	0.0155
	19.95	0.7226	0.0721	0.0016	-.0089	-.0106	-.0035	0.0044	0.0109
.125	3.16	0.6479	0.1397	-.0053	-.0251	-.0145	0.0130	0.0049	0.0330
	5.01	0.8022	0.0712	-.0126	-.0286	-.0346	0.0122	0.0033	0.0240
	7.94	0.8675	0.0424	-.0026	-.0127	-.0069	0.0047	0.0058	0.0158
	12.59	0.8833	0.0412	0.0047	-.0107	-.0091	-.0012	0.0041	0.0130
	19.95	0.7477	0.0626	0.0026	-.0126	-.0162	-.0008	0.0013	0.0119
	31.62	0.8543	0.0596	0.0086	-.0048	-.0016	-.0043	0.0068	0.0101
.175	5.01	0.6474	0.1111	-.0105	-.0010	-.0043	0.0104	0.0004	0.0244
	7.94	0.8936	0.0583	-.0020	-.0022	0.0025	0.0088	0.0030	0.0197
	12.59	0.8743	0.0402	-.0016	-.0091	-.0092	0.0008	0.0060	0.0128
	19.95	0.7912	0.0469	0.0053	-.0091	-.0059	-.0029	0.0013	0.0106
	31.62	0.7872	0.0561	-.0066	-.0132	-.0111	-.0006	0.0011	0.0098
	50.12	0.8152	0.0607	0.0198	-.0072	-.0056	-.0096	0.0069	0.0078
.225	5.01	0.5914	0.1642	0.0115	-.0050	-.0042	0.0115	0.0056	0.0264
	7.94	0.8203	0.0792	-.0204	-.0108	0.0016	0.0124	0.0025	0.0216
	12.59	0.8276	0.0454	-.0014	-.0104	-.0107	0.0046	0.0045	0.0131
	19.95	0.8127	0.0392	-.0011	0.0010	-.0003	-.0030	0.0026	0.0097
	31.62	0.9035	0.0548	0.0088	-.0092	-.0098	-.0026	0.0007	0.0114
	50.12	0.7945	0.0463	0.0007	-.0049	-.0038	-.0043	0.0032	0.0074

Table 5.4b

(continued on next page)

x	Q^2	xF_3	Stat.	E_{had}	E_μ	E	p_{secy}	$\Delta_{\theta_{sec}}$	$\Phi^{\bar{\nu}}/\Phi^{\nu}$
.275	7.94	0.8220	0.0994	-.0109	-.0149	-.0339	0.0112	0.0042	0.0250
	12.59	0.7666	0.0534	-.0107	-.0201	-.0091	0.0060	0.0037	0.0137
	19.95	0.7839	0.0377	0.0044	-.0028	-.0076	-.0021	0.0033	0.0094
	31.62	0.7432	0.0458	0.0001	0.0013	-.0009	-.0047	0.0012	0.0086
	50.12	0.7593	0.0459	-.0013	-.0010	-.0003	-.0002	0.0013	0.0075
	79.43	0.6137	0.0510	0.0152	0.0039	0.0001	-.0146	0.0047	0.0047
.350	7.94	0.6838	0.0956	-.0135	0.0073	-.0131	0.0107	0.0024	0.0251
	12.59	0.6378	0.0466	-.0125	0.0045	0.0045	0.0070	0.0038	0.0138
	19.95	0.5701	0.0283	-.0034	0.0077	0.0042	0.0010	0.0027	0.0076
	31.62	0.5860	0.0268	0.0007	0.0018	0.0030	-.0032	0.0021	0.0064
	50.12	0.5045	0.0330	-.0021	0.0047	0.0020	0.0004	0.0011	0.0055
	79.43	0.5320	0.0256	0.0058	0.0086	0.0083	-.0056	0.0029	0.0041
.450	12.59	0.4721	0.0574	-.0131	0.0121	0.0140	0.0080	0.0026	0.0130
	19.95	0.3237	0.0314	-.0053	0.0013	0.0000	0.0014	0.0023	0.0053
	31.62	0.3949	0.0228	-.0020	0.0081	0.0029	-.0019	0.0015	0.0045
	50.12	0.4001	0.0268	-.0004	0.0118	0.0082	-.0020	0.0003	0.0045
	79.43	0.3501	0.0230	-.0025	0.0049	-.0005	-.0018	0.0014	0.0031
	125.89	0.2970	0.0233	0.0093	0.0081	0.0075	-.0090	0.0022	0.0020
.550	12.59	0.2836	0.0632	0.0031	0.0080	0.0041	0.0059	0.0018	0.0098
	19.95	0.2162	0.0314	-.0036	0.0078	0.0079	0.0011	0.0015	0.0044
	31.62	0.2296	0.0210	-.0016	0.0072	0.0051	0.0001	0.0014	0.0031
	50.12	0.1746	0.0201	0.0009	0.0085	0.0076	-.0008	0.0004	0.0020
	79.43	0.1637	0.0216	-.0035	0.0042	0.0015	-.0009	0.0002	0.0017
	125.89	0.1516	0.0157	0.0021	0.0057	0.0048	-.0024	0.0011	0.0011
.650	12.59	0.2040	0.0690	-.0059	0.0055	0.0132	0.0015	-.0025	0.0084
	19.95	0.1385	0.0272	-.0037	0.0100	0.0009	0.0014	0.0014	0.0034
	31.62	0.1081	0.0167	-.0015	0.0053	0.0032	0.0000	0.0004	0.0017
	50.12	0.0719	0.0143	-.0015	0.0041	0.0029	-.0005	0.0004	0.0009
	79.43	0.0464	0.0155	-.0001	0.0023	0.0017	-.0004	0.0003	0.0005
	125.89	0.0725	0.0112	-.0015	0.0049	0.0028	-.0006	0.0008	0.0006

Table 5.4b

(continued from previous page)

	CCFR (89)	CCFRR (84)	CHARM (83)	CDHSW (87)	WA59 (87)
Target	Fe	Fe	$CaCO_3$	Fe	Ne–H_2
ν's $\times 10^3$	88	59	50	565	8
$\bar{\nu}$'s $\times 10^3$	9	6	110	344	13
σ^{ν}/E (GeV/cm^2)	.676	.669	.604	.686	.723
$\sigma^{\bar{\nu}}/E$ (GeV/cm^2)	.333	.340	.301	.339	.351
κ	0.50	0.50	0.00	0.22	0.50
m_c GeV/c^2	1.5	1.5	0.0	0.0	1.5
$R = \sigma_L/\sigma_T$	$R_{QCD}^{[a]}$	$R_{QCD}^{[b]}$	0	$R_{QCD}^{[a]}$	$R_{QCD}^{[b]}$
Fermi Motion	No	No	Yes	No	No

Table 6.1

Exp.	S.F.	x–lim.	Adjusted	Unadjusted
CCFRR(84)	F_2	0.00–1.00	1.022±.003	1.001±.002
	xF_3	"	0.992±.006	0.960±.006
CDHSW(87)	F_2	0.00–0.70	0.990±.005	0.983±.005
	xF_3	"	0.932±.010	0.933±.010
CHARM(83)	F_2	0.00–0.60	1.028±.013	0.902±.011
	xF_3	"	0.992±.022	0.876±.019
WA59(87)	F_2	0.00–0.70	1.014±.013	1.064±.014
	xF_3	"	0.912±.025	0.987±.027
BFP(86)	F_2	0.06–0.70	1.003±.006	—
EMC(86)	F_2	0.04–0.70	0.906±.005	—
SLAC(prel.)	F_2	0.06–0.70	0.985±.009	—
BCDMS(88)	F_2	0.25–0.70	0.985±.012	—

Table 6.2

	QCD fit		linear log fit		power law fit	
x	xF_3	S_x	xF_3	S_x	xF_3	S_x
.005	.177 ± .088	2.783 ± .184	.232 ± .228	2.843 ± .463	.290 ± .326	3.002 ± .657
.015	.273 ± .053	2.429 ± .052	.230 ± .071	2.379 ± .073	.229 ± .074	2.422 ± .079
.025	.390 ± .049	2.247 ± .038	.399 ± .050	2.226 ± .056	.393 ± .049	2.270 ± .062
.035	.490 ± .047	2.091 ± .033	.497 ± .049	2.066 ± .052	.497 ± .049	2.112 ± .059
.045	.598 ± .048	1.951 ± .030	.598 ± .057	1.924 ± .050	.593 ± .057	1.970 ± .057
.055	.679 ± .049	1.818 ± .028	.687 ± .067	1.791 ± .049	.688 ± .067	1.839 ± .056
.065	.679 ± .050	1.695 ± .027	.672 ± .079	1.667 ± .047	.671 ± .077	1.714 ± .054
.075	.588 ± .051	1.590 ± .026	.591 ± .089	1.563 ± .046	.590 ± .087	1.610 ± .053
.085	.664 ± .051	1.512 ± .025	.729 ± .098	1.484 ± .044	.725 ± .100	1.532 ± .052
.095	.730 ± .051	1.434 ± .024	.693 ± .106	1.399 ± .043	.698 ± .101	1.446 ± .050
.125	.826 ± .026	1.357 ± .023	.844 ± .056	1.326 ± .041	.843 ± .056	1.373 ± .049
.175	.860 ± .023	1.027 ± .021	.846 ± .065	0.988 ± .034	.845 ± .066	1.036 ± .044
.225	.898 ± .025	0.781 ± .020	.856 ± .069	0.747 ± .029	.854 ± .072	0.794 ± .039
.275	.870 ± .032	0.582 ± .019	.847 ± .073	0.557 ± .024	.851 ± .082	0.604 ± .036
.350	.720 ± .039	0.423 ± .018	.736 ± .050	0.403 ± .020	.764 ± .067	0.450 ± .033
.450	.551 ± .048	0.218 ± .014	.464 ± .050	0.192 ± .015	.496 ± .062	0.231 ± .027
.550	.335 ± .042	0.095 ± .009	.313 ± .043	0.089 ± .009	.373 ± .078	0.127 ± .023
.650	.170 ± .030	0.034 ± .005	.175 ± .032	0.032 ± .005	.335 ± .114	0.059 ± .018
.850	.023 ± .006	0.008 ± .002	.015 ± .004	0.005 ± .001	.022 ± .010	0.076 ± .004

Table 6.3

Fit No.	Fit limits	A	b	c	χ^2/dof	$\int_0^1 dx F_3$
1	0.00 – 0.04	3.97 ± 1.79	.63 ± .12	0	.2/2	2.79 ± .14
2	0.00 – 0.05	4.62 ± 1.69	.68 ± .10	0	.3/3	2.75 ± .12
3	0.00 – 0.06	4.91 ± 1.42	.68 ± .09	0	.3/4	2.75 ± .11
4	0.00 – 0.07	3.79 ± 0.92	.61 ± .08	0	1.5/5	2.82 ± .13
5	0.00 – 0.50	4.15 ± 0.62	.62 ± .05	2.48 ± .27	13.0/13	2.84 ± .11
6	0.00 – 0.60	4.47 ± 0.54	.64 ± .04	2.64 ± .20	14.1/14	2.81 ± .10
7	0.00 – 0.70	4.77 ± 0.50	.66 ± .04	2.77 ± .16	15.3/15	2.77 ± .09
8	0.00 – 1.00	4.76 ± 0.41	.66 ± .03	2.77 ± .12	15.3/16	2.78 ± .08

Table 6.4

Pure Nonsinglet Fit		
Parameter	LO	$\overline{\text{MS}}$
Λ (MeV)	282^{+156}_{-136}	251^{+134}_{-115}
η_1	.546 ± .076	.828 ± .032
η_2	3.28 ± 0.31	3.66 ± 0.14
γ	4.63 ± 2.70	0.67 ± 0.39
χ^2/dof	46.2/44	48.0/44
α_S 12.6 (GeV/c)^2	.298 ± .062	.222 ± .037

Table 6.5

		LO		$\overline{\text{MS}}$	
Syst.	Δ(Syst.)	$\Delta\Lambda_{LO}$ (MeV)	$\Delta\alpha_S$	$\Delta\Lambda_{\overline{MS}}$ (MeV)	$\Delta\alpha_S$
E_{had}	+1%	−91	−.040	−57	−.017
E_μ	+1%	−13	−.005	+2	+.001
All E	+1%	−28	−.012	−2	−.001
P_{secy}	+1%	+87	+.035	+56	+.016
$\sigma_{\theta_{secy}}$	+10%	—	—	−3	−.001
$\Phi^{\bar{\nu}}/\Phi^{\nu}$	+ 1.7%	+51	+.021	+1	—
$(\Phi^{\bar{\nu}} + \Phi^{\nu})$	+ 3.2%	−3	−.001	+36	+.010
R	$R_{QCD} - 0$	+123	+.050	+28	+.008
Total		±150	±.064	±89	±.026
Stat		±146	±.062	±124	±.037

Table 6.6

xF_3 for $x < 0.4$ & F_2 for $x > 0.4$		
Parameter	LO	$\overline{\text{MS}}$
Λ (MeV)	471^{+104}_{-102}	386^{+78}_{-74}
η_1	.647 ± .058	.944 ± .014
η_2	2.70 ± 0.13	2.79 ± 0.09
γ	2.57 ± 0.97	-.569 ± 0.14
χ^2/dof	43.5/44	46.5/44
α_S 12.6 (GeV/c)^2	.373 ± .041	.259 ± .020

Table 6.7

	MS Singlet Fit		
	$q_s = A_s(1-x)^{\eta_2}(1+\gamma x)$	$q_s = q_{ns} + B_s(1-x)^{\eta_s}$	
Parameter	F_2	F_2	F_2 & xF_3
$\Lambda_{\overline{MS}}$ (MeV)	244^{+71}_{-54}	255^{+73}_{-63}	253^{+55}_{-50}
η_1	—	0.823±.020	0.865±.017
η_2	3.162±.054	2.678±.039	2.887±.033
γ	4.764±.806	-.674±.032	−.593±.027
A_s	1.334±.083	—	—
B_s	—	1.103±.081	1.271±.160
η_s	—	7.435±.294	8.983±1.167
η_g	3.695±.973	3.720±1.413	4.131±1.139
χ^2/dof	68.1/43	66.8/41	116/89
α_S @ 12.6 (GeV/c)^2	.220±.018	.223±.020	.223±.015

Table 6.8

		F_2		F_2 & xF_3	
Syst.	Δ(Syst.)	$\Delta\Lambda_{\overline{MS}}$ (MeV)	$\Delta\alpha_S$	$\Delta\Lambda_{\overline{MS}}$ (MeV)	$\Delta\alpha_S$
E_{had}	+1%	−61	−.018	−44	−.015
E_μ	+1%	+5	+.002	+5	+.001
All E	+1%	+7	+.002	−8	−.002
P_{secy}	+1%	+77	+.022	+36	+.010
$\sigma_{\theta_{secy}}$	+10%	+10	+.003	−10	−.003
$\Phi^{\bar{\nu}}/\Phi^{\nu}$	+1.7%	−13	−.004	−21	−.006
$(\Phi^{\bar{\nu}} + \Phi^{\nu})$	+3.2%	+20	+.006	+28	+.008
Total		±101	±.030	±71	±.021
Stat		±68	±.020	±53	±.015

Table 6.9

		pion		kaon	
Exp.	Setting	$\langle E_\nu \rangle$	$\frac{1}{E}\frac{d\sigma}{dy}\|_{y=0}$	$\langle E_\nu \rangle$	$\frac{1}{E}\frac{d\sigma}{dy}\|_{y=0}$
	GeV/c	GeV	$\times 10^{-38}$ cm^2	GeV	$\times 10^{-38}$ cm^2
E616	+250	62.7	.775 ± .019	206	.799 ± .019
	+200	53.8	.773 ± .018	174	.756 ± .022
	+165	47.9	.780 ± .020	151	.740 ± .026
	+140	42.5	.774 ± .024	129	.723 ± .039
	+120	38.3	.766 ± .028	113	.772 ± .051
	−250	61.9	.787 ± .030	199	.764 ± .063
	−200	53.3	.760 ± .026	169	.729 ± .054
	−165	47.5	.752 ± .026	148	.710 ± .050
	−140	42.2	.747 ± .029	126	.632 ± .055
	−120	38.0	.793 ± .037	110	.784 ± .087
E701	+250	63.4	.759 ± .026	206	.775 ± .027
	+200	54.8	.719 ± .023	175	.766 ± .030
	+165	48.3	.795 ± .027	151	.830 ± .037
	+140	43.2	.790 ± .024	130	.819 ± .037
	−165	48.0	.807 ± .018	147	.730 ± .034

Table A.1

Buras Gaemers Parameters	
Λ (GeV/c)	.2379
A	1.126
η_{10}	.5424
η_{11}	-.0232
η_{20}	2.588
η_{21}	2.167
$\langle xS(Q_0^2)\rangle_0$	.1135
$\langle xS(Q_0^2)\rangle_1$	.0116
$\langle xG(Q_0^2)\rangle_1$	.0585
Q_0^2 (GeV/c)^2	1.00

Table B.1

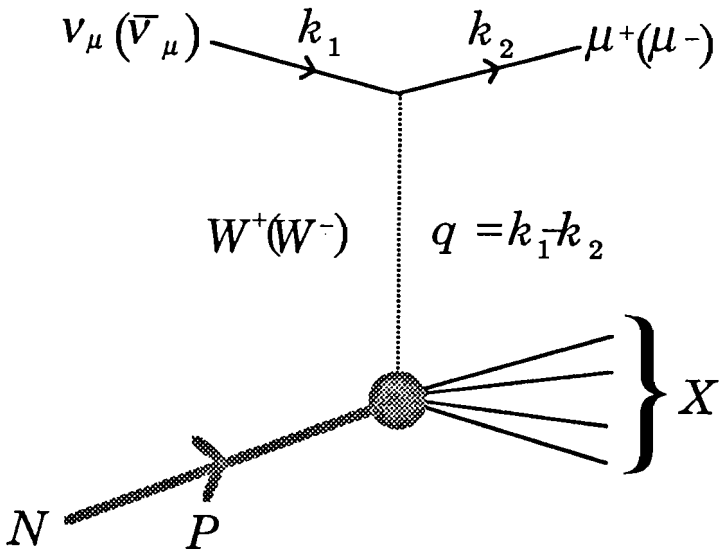

Figure 1.1

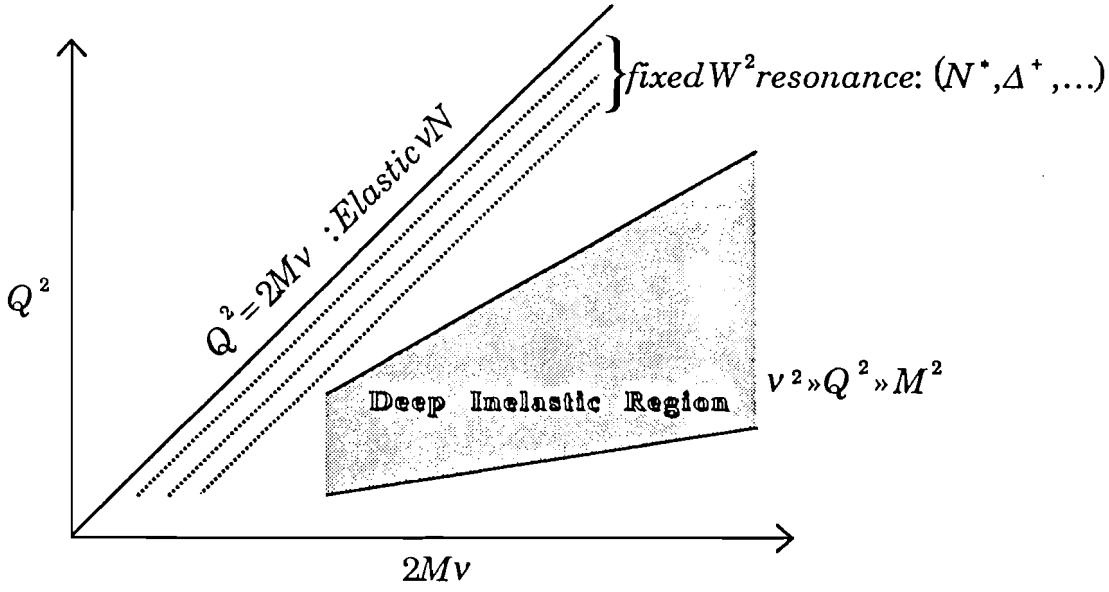

Figure 1.2

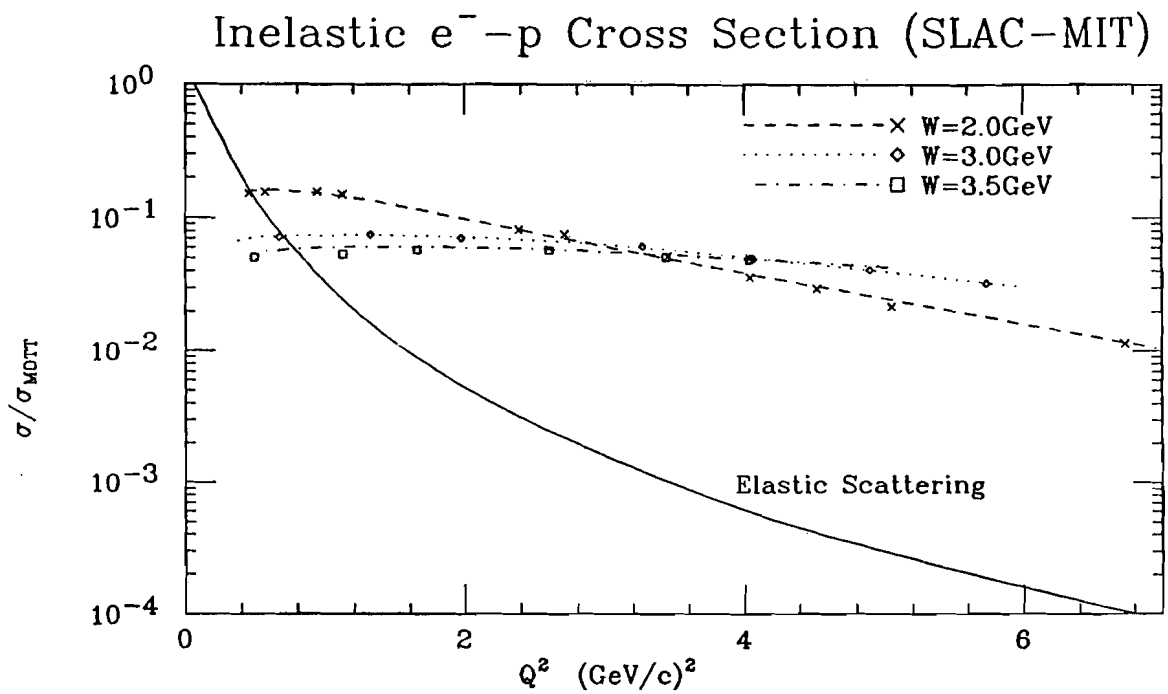

Figure 1.3

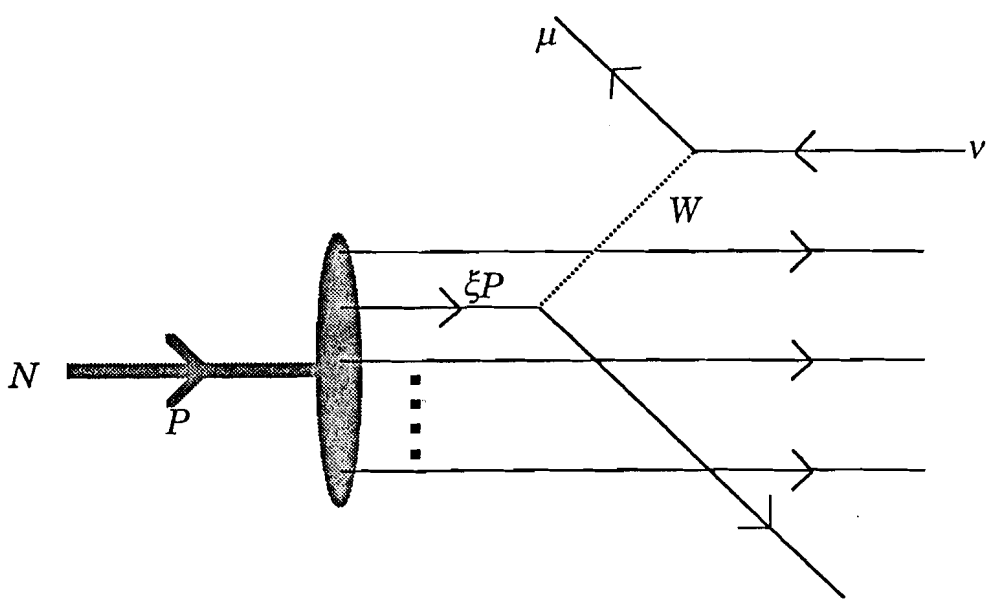

Figure 1.4

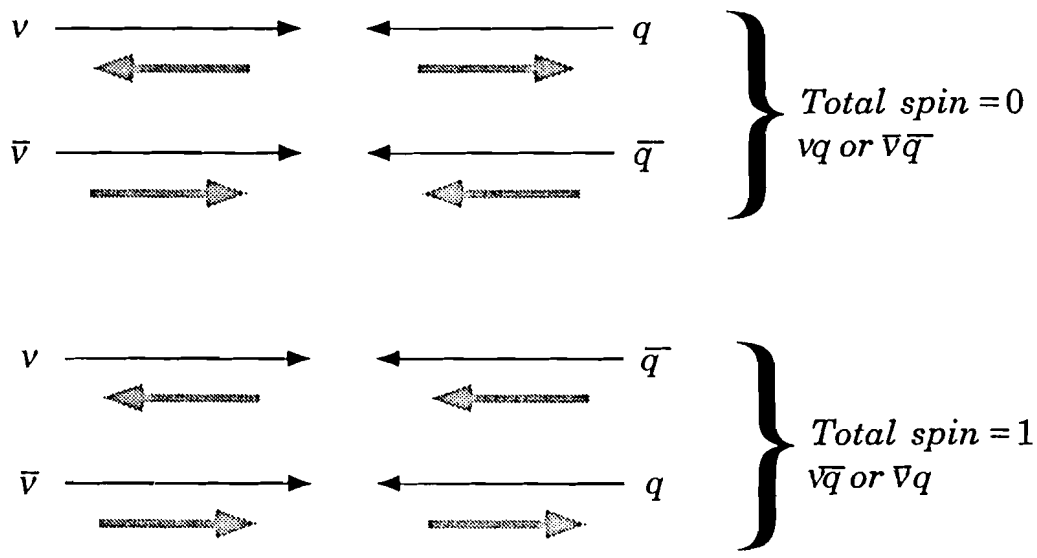

Figure 1.5

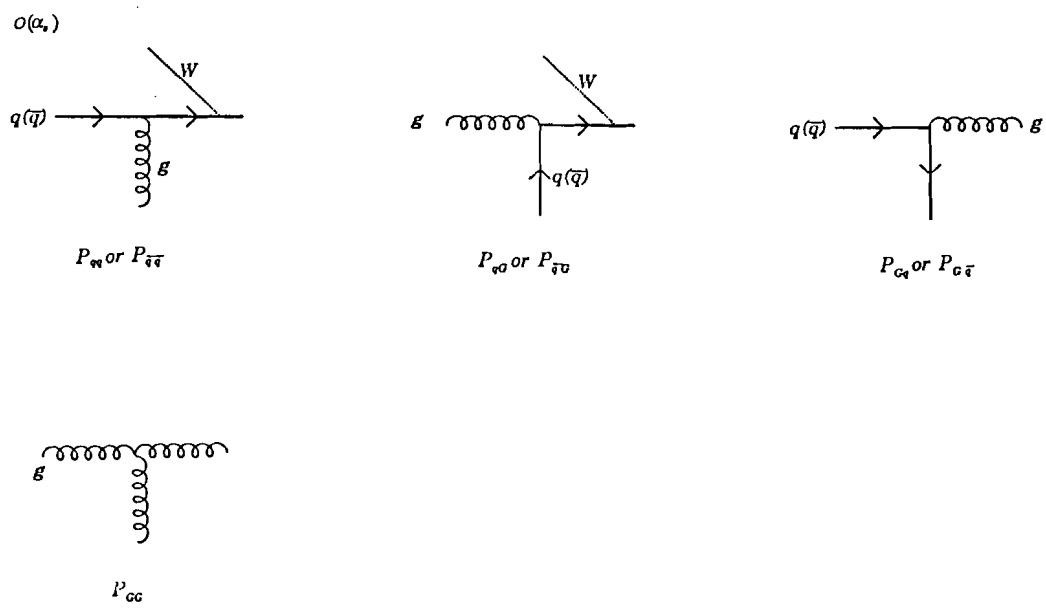

Figure 1.6a

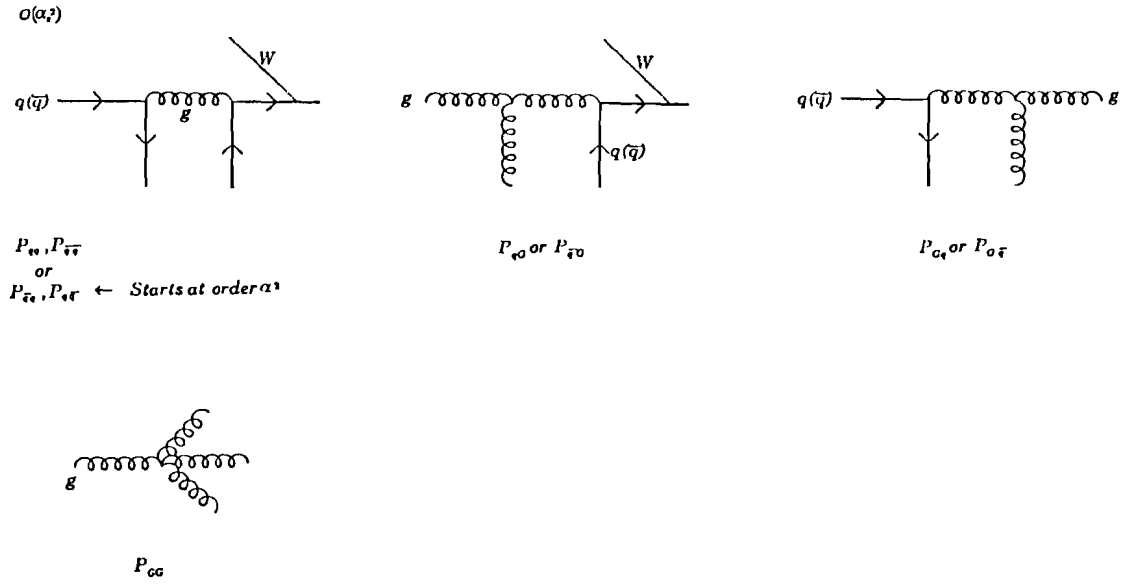

Figure 1.6b

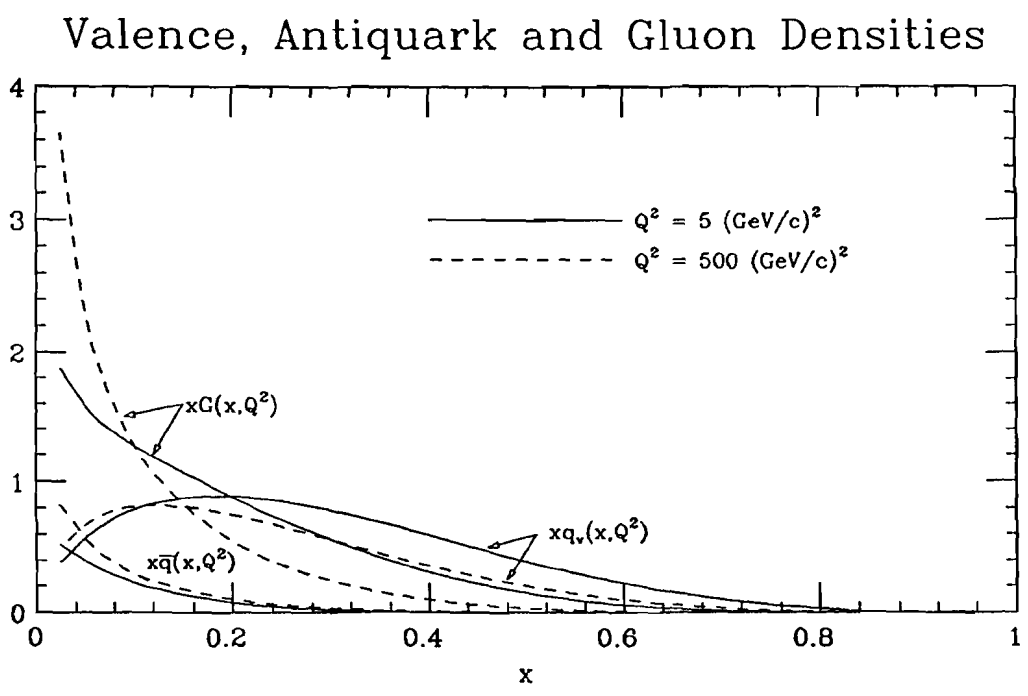

Figure 1.7

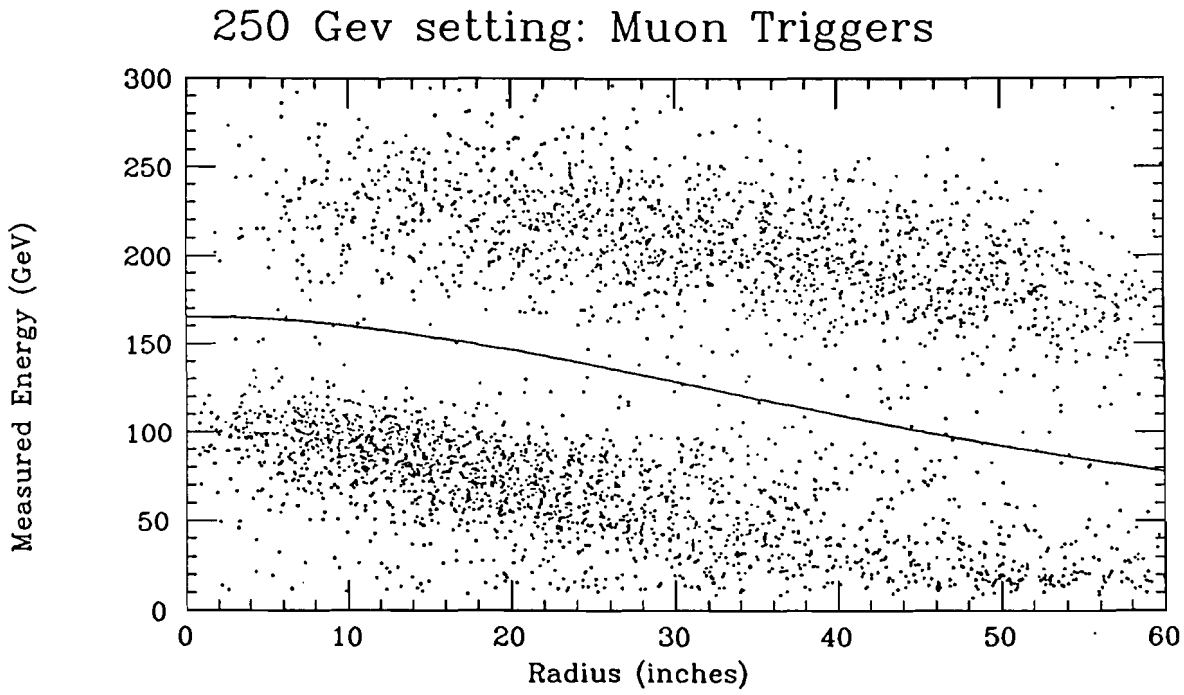

Figure 2.1

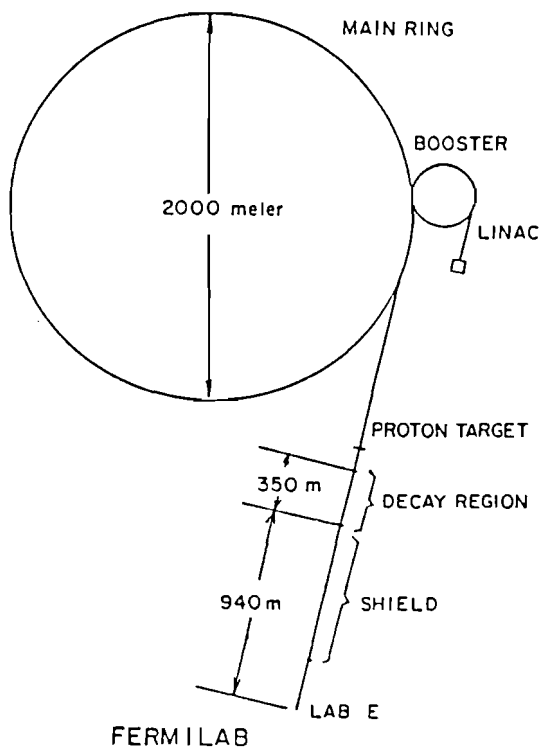

Figure 2.2

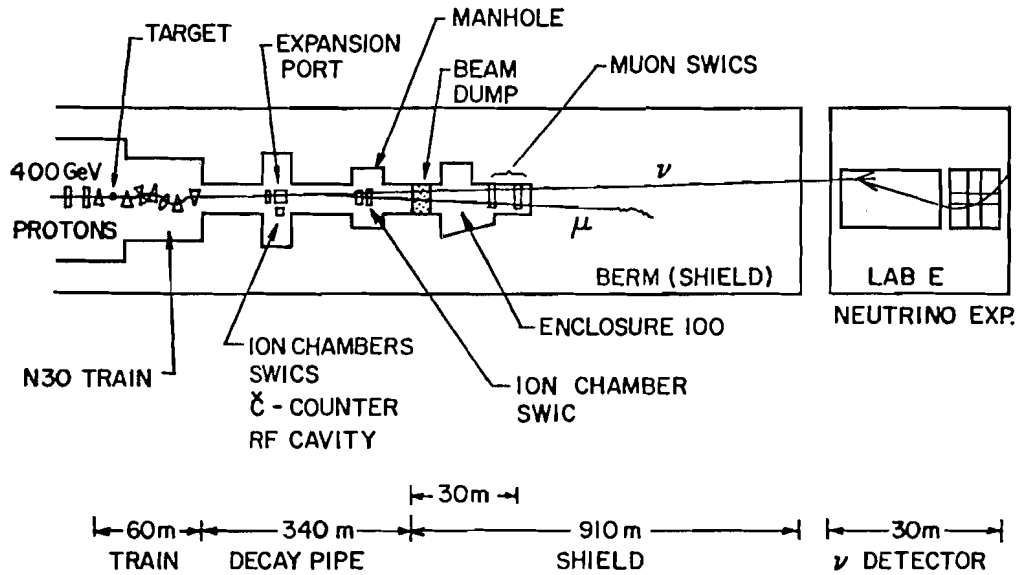

Figure 2.3

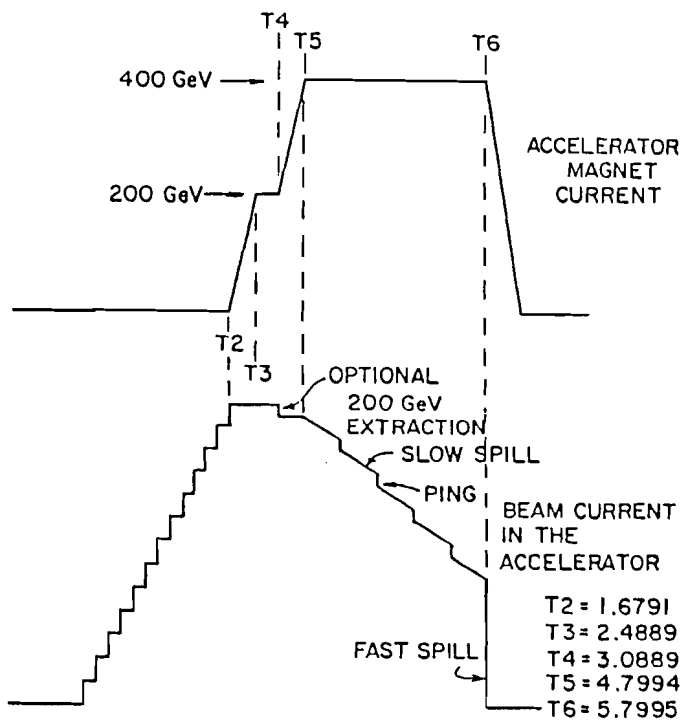

Figure 2.4

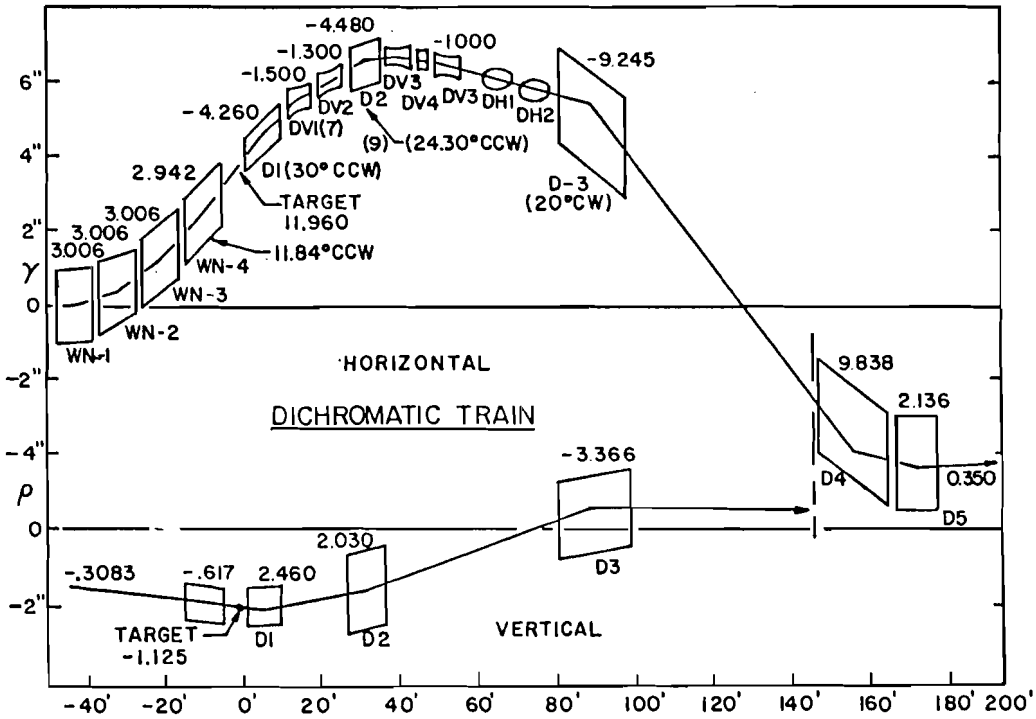

Figure 2.5a

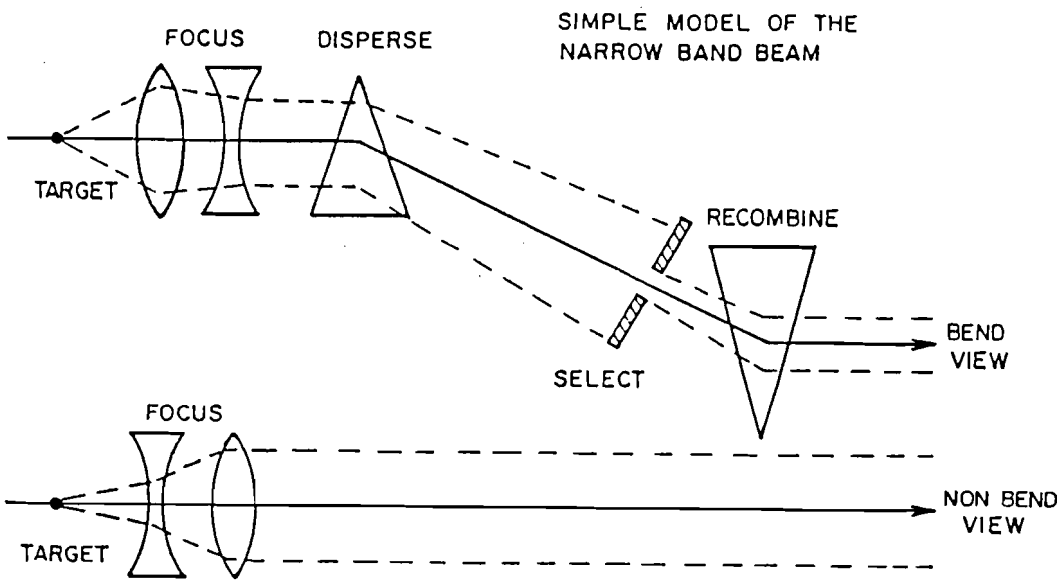

Figure 2.5b

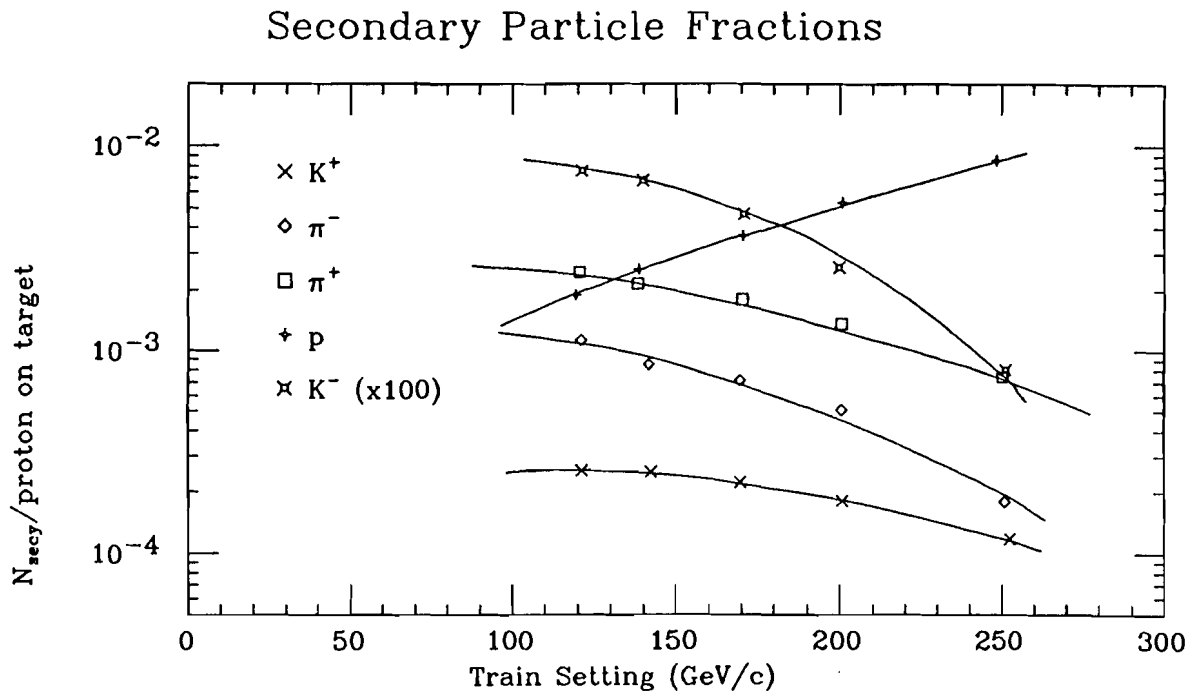

Figure 2.6

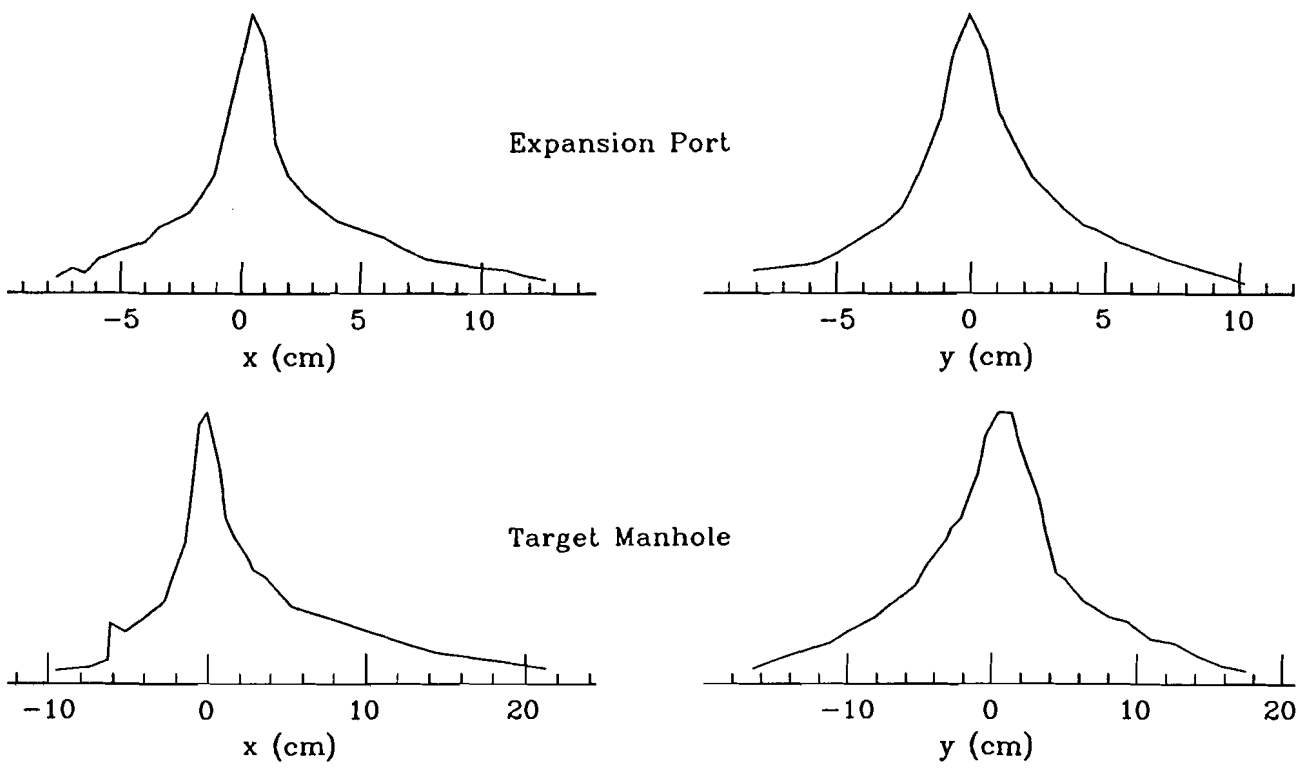

Figure 2.7

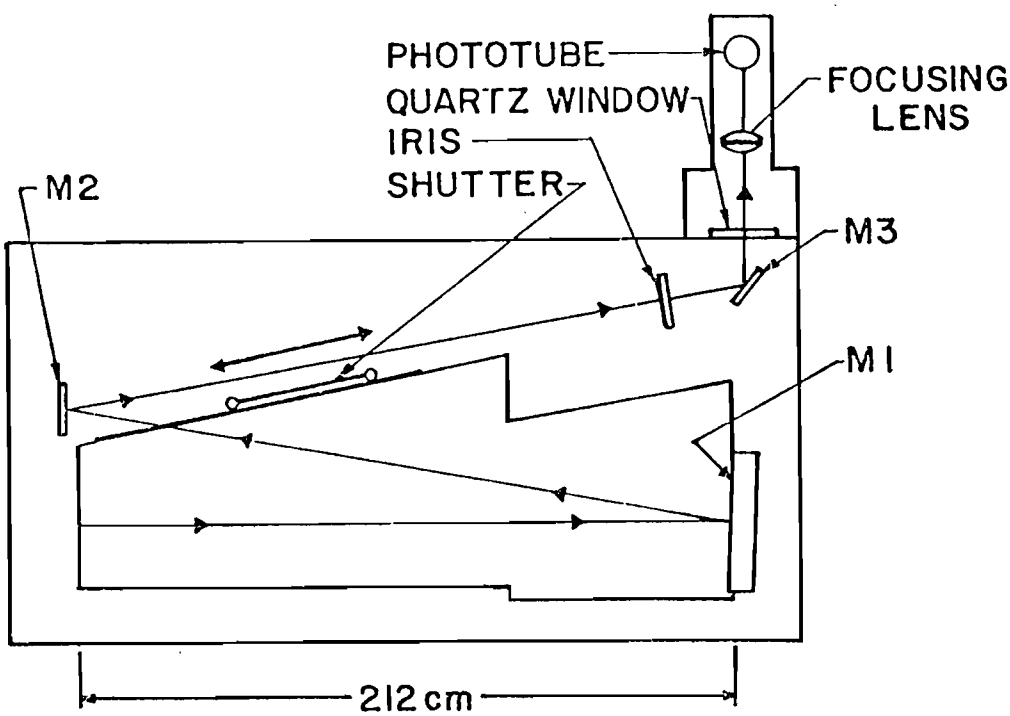

Figure 2.8

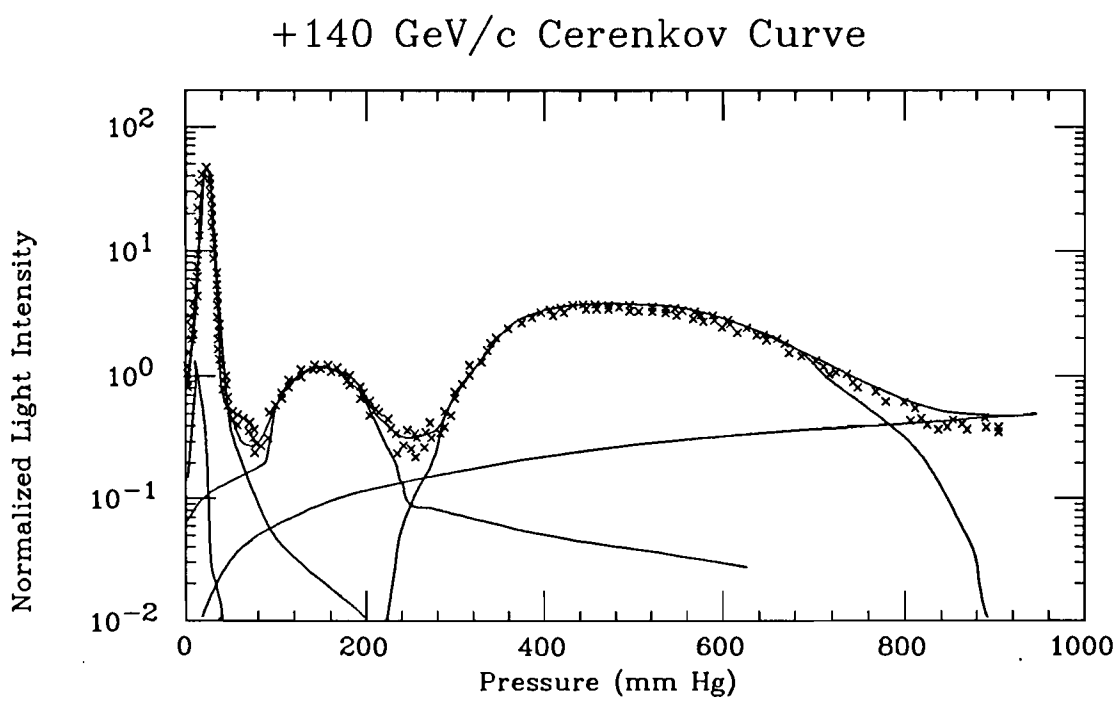

Figure 2.9

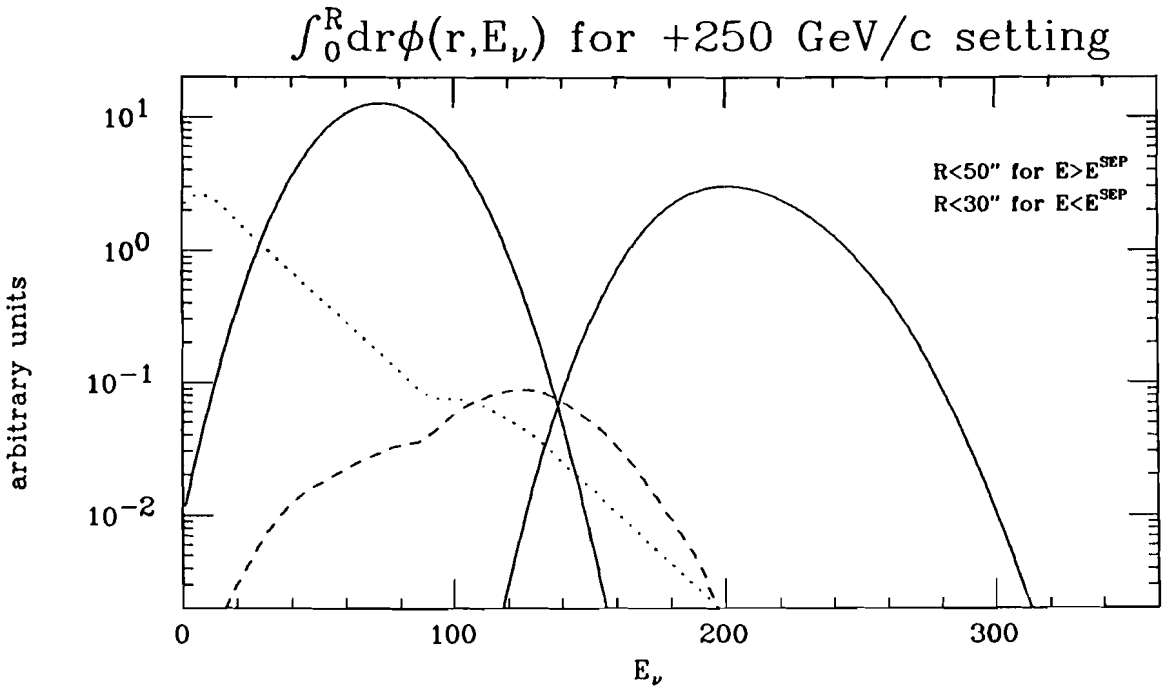

Figure 2.10a

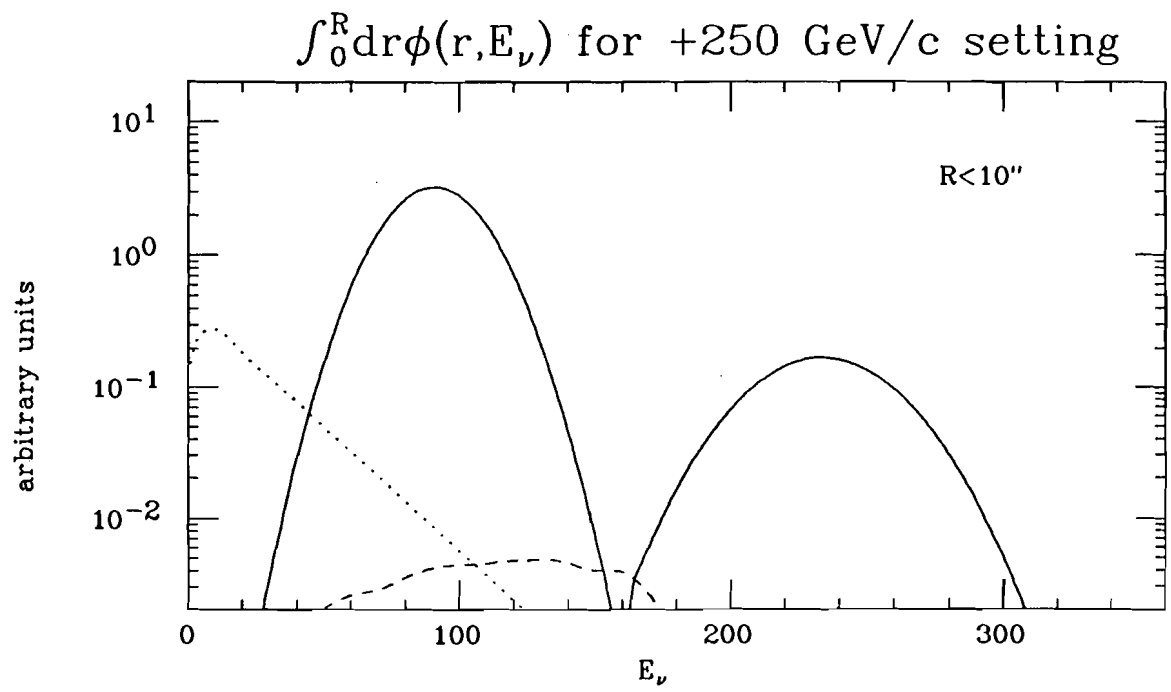

Figure 2.10b

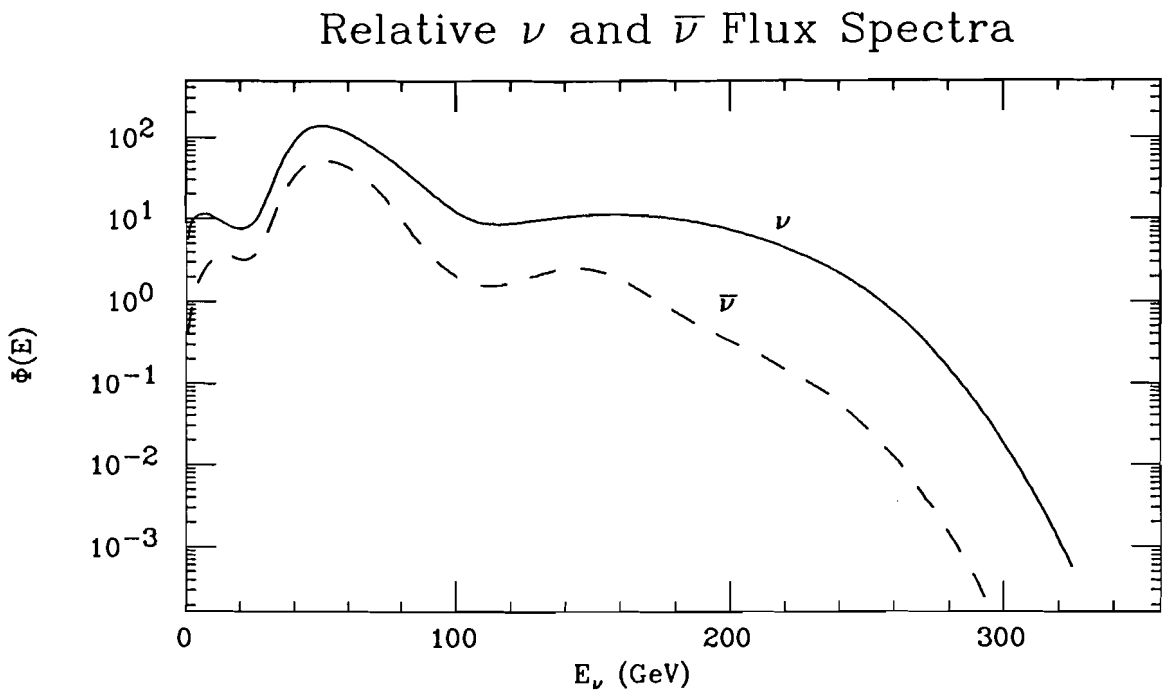

Figure 2.11

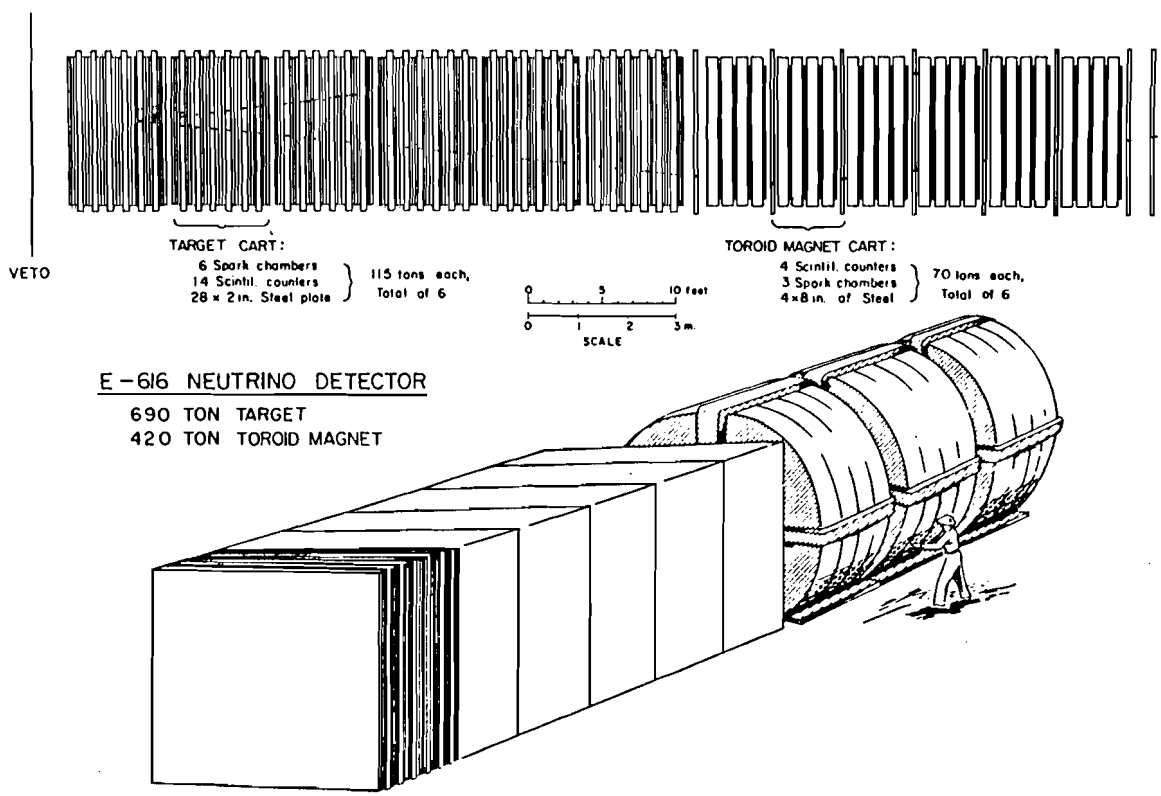

Figure 3.1

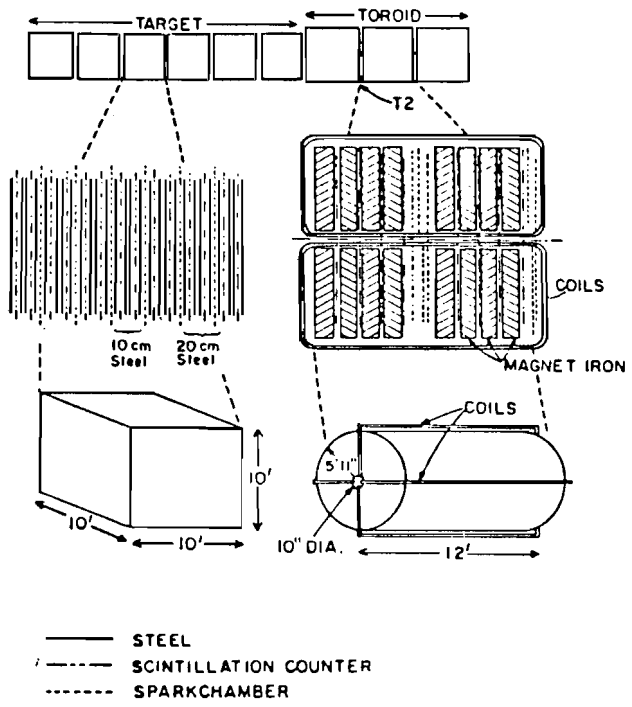

Figure 3.2

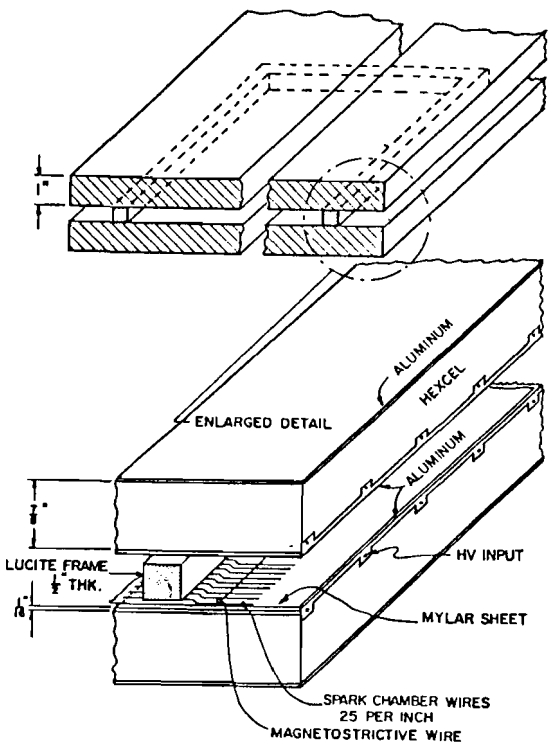

Figure 3.3

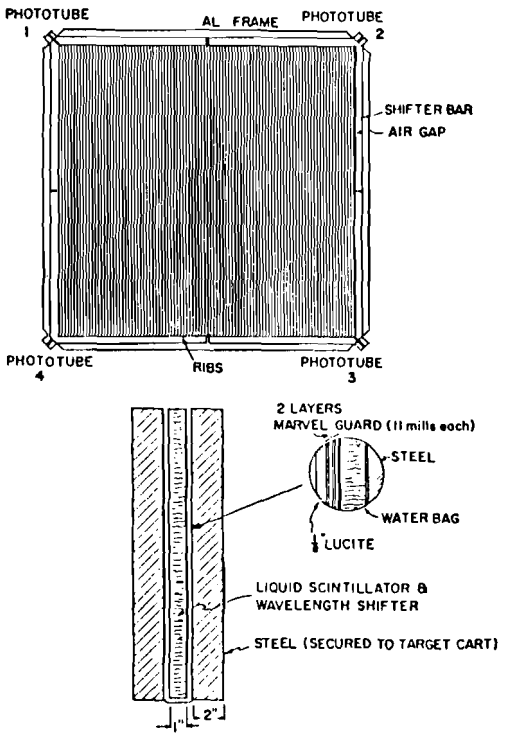

Figure 3.4

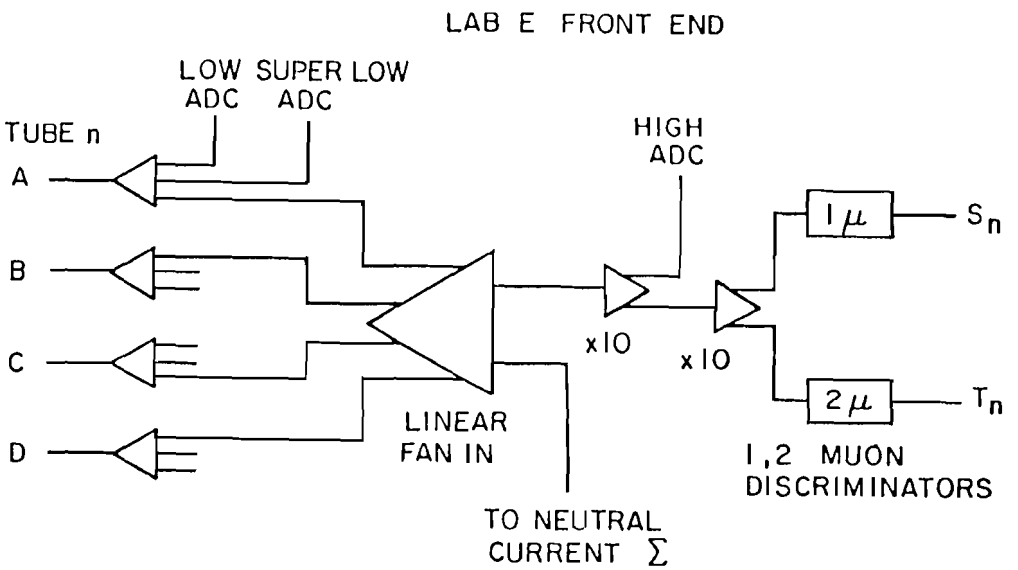

Figure 3.5

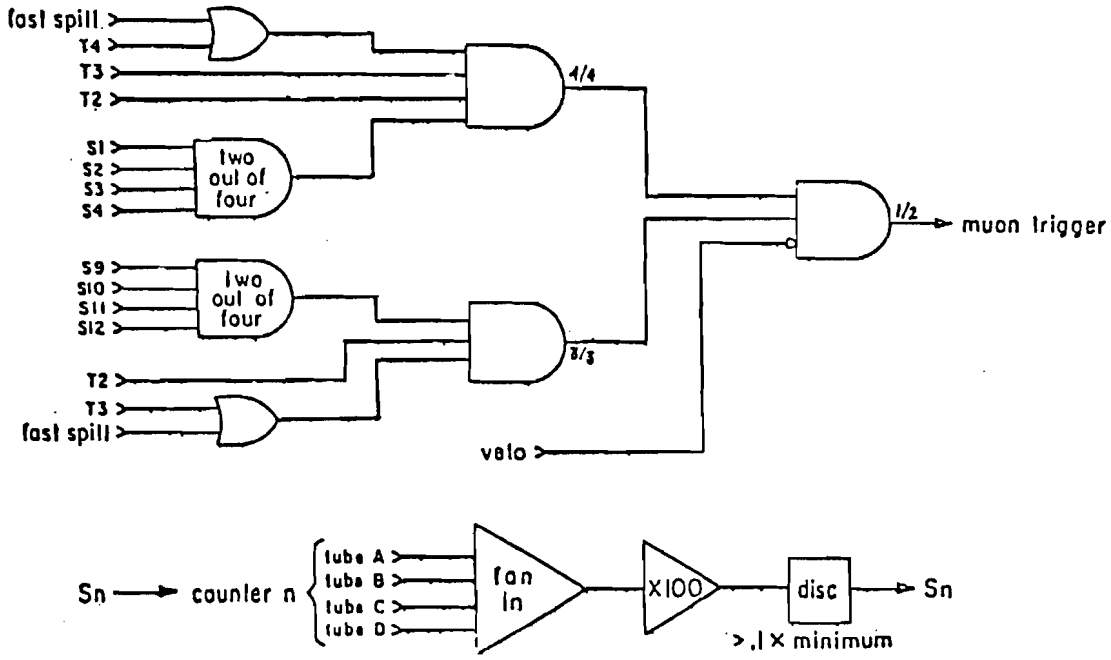

Figure 3.6

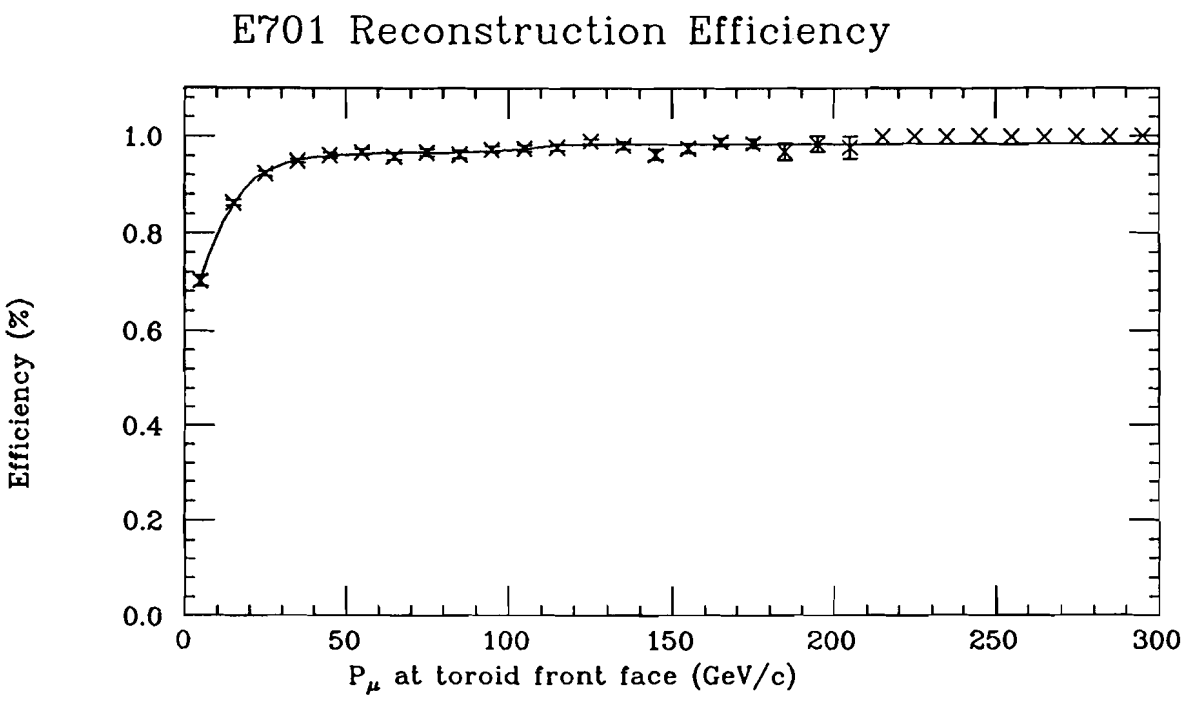

Figure 4.1

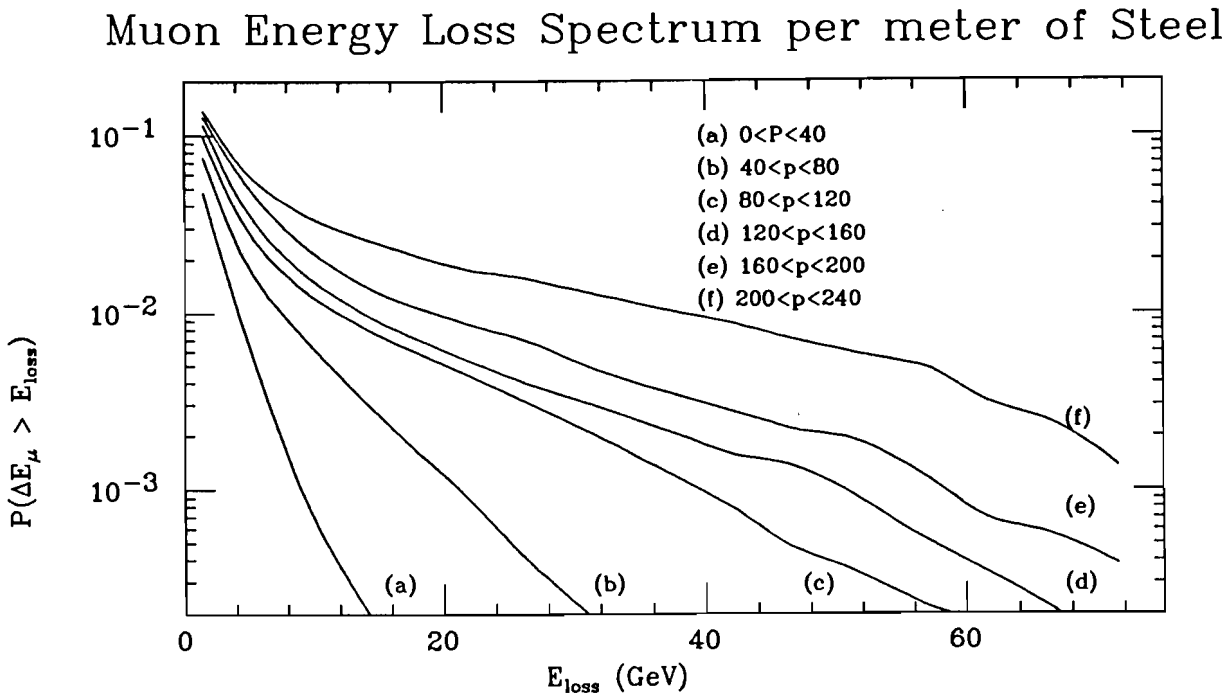

Figure 4.2

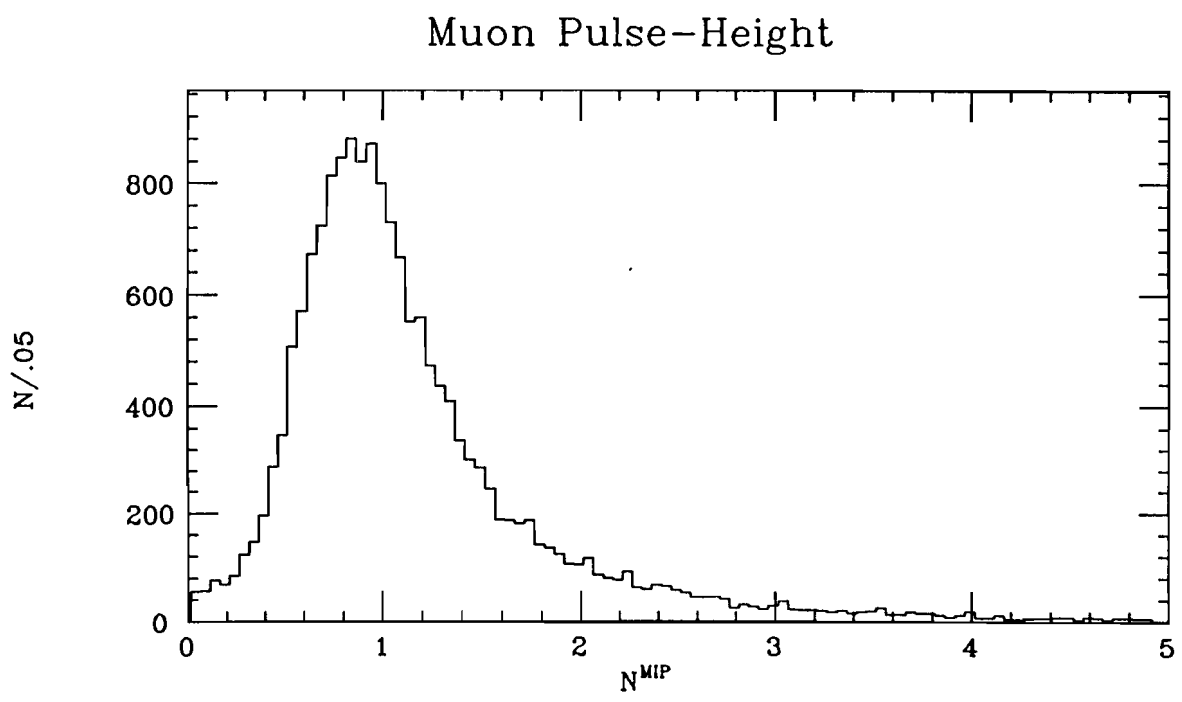

Figure 4.3

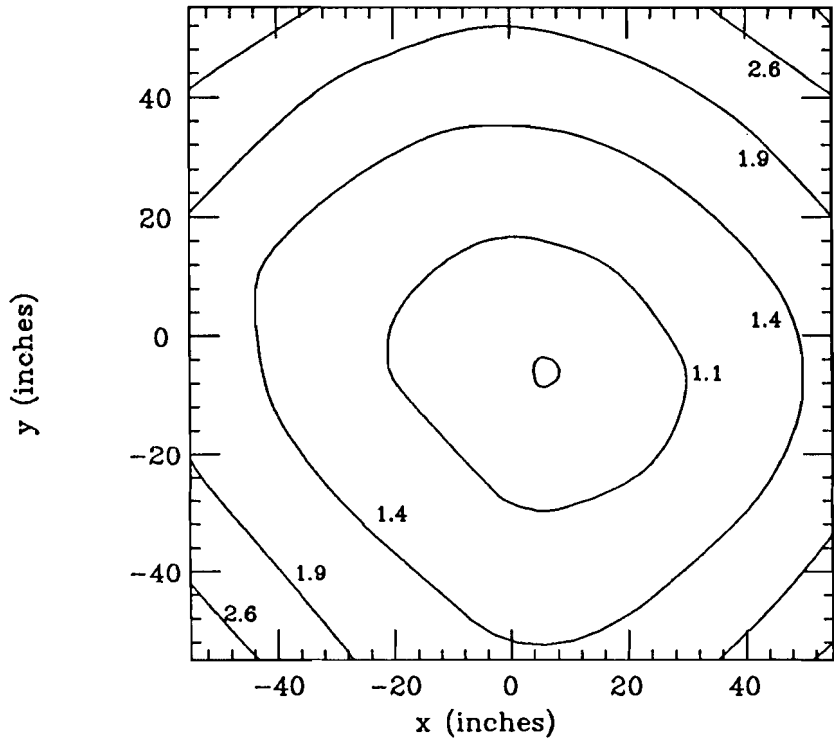

Figure 4.4

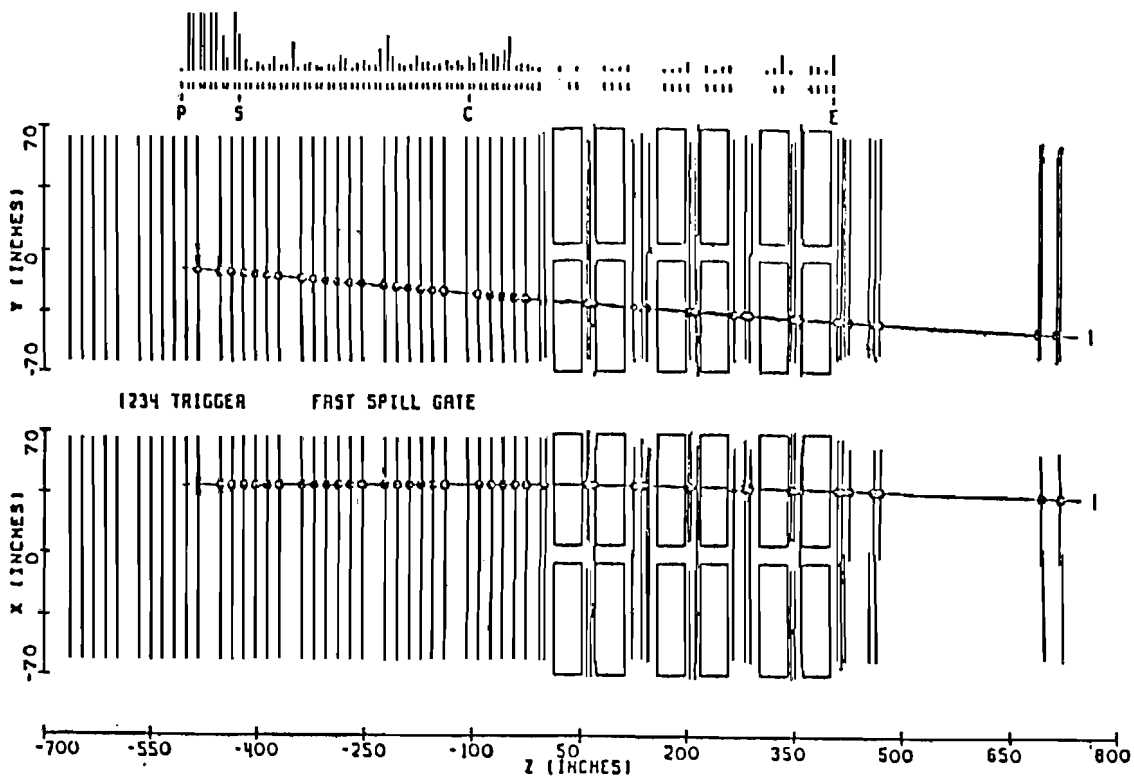

Figure 4.5

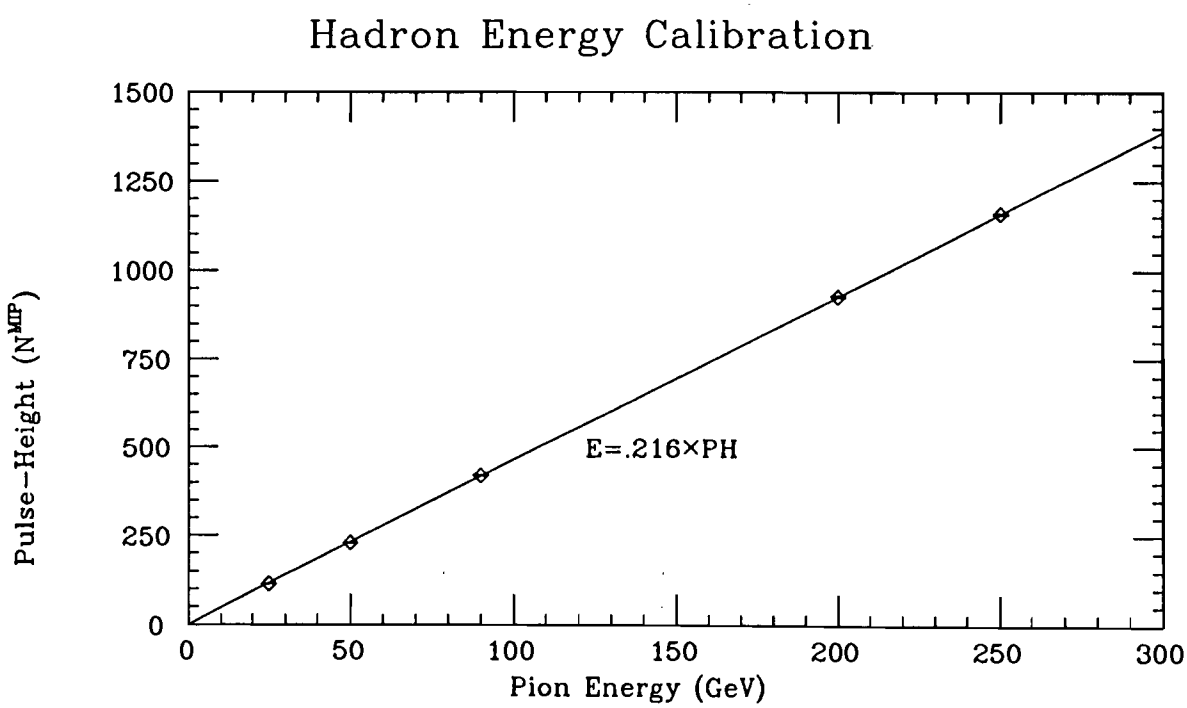

Figure 4.6a

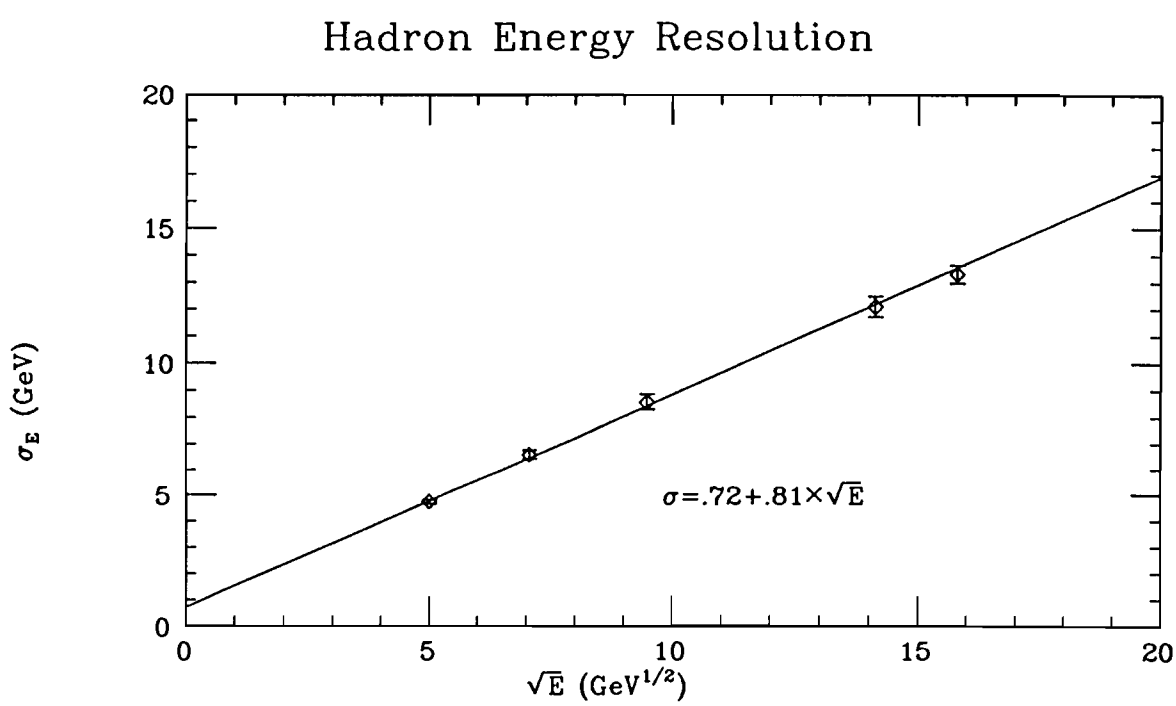

Figure 4.6b

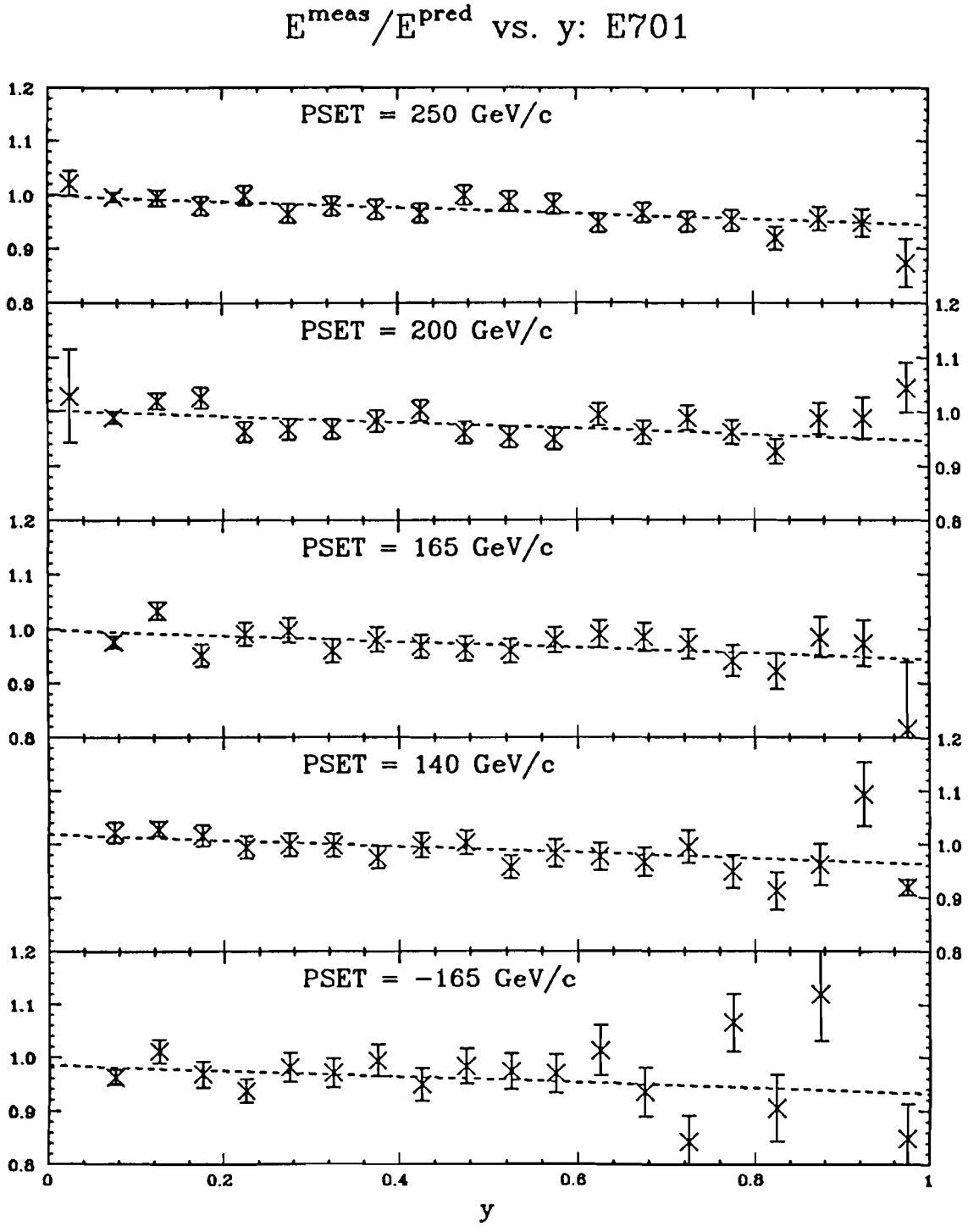
E^meas/E^pred vs. y: E701
PSET = 250 GeV/c
PSET = 200 GeV/c
PSET = 165 GeV/c
PSET = 140 GeV/c
PSET = −165 GeV/c
1.2
1.1
1.0
0.9
0.8
0
0.2
0.4
0.6
0.8
1
y

Figure 4.7

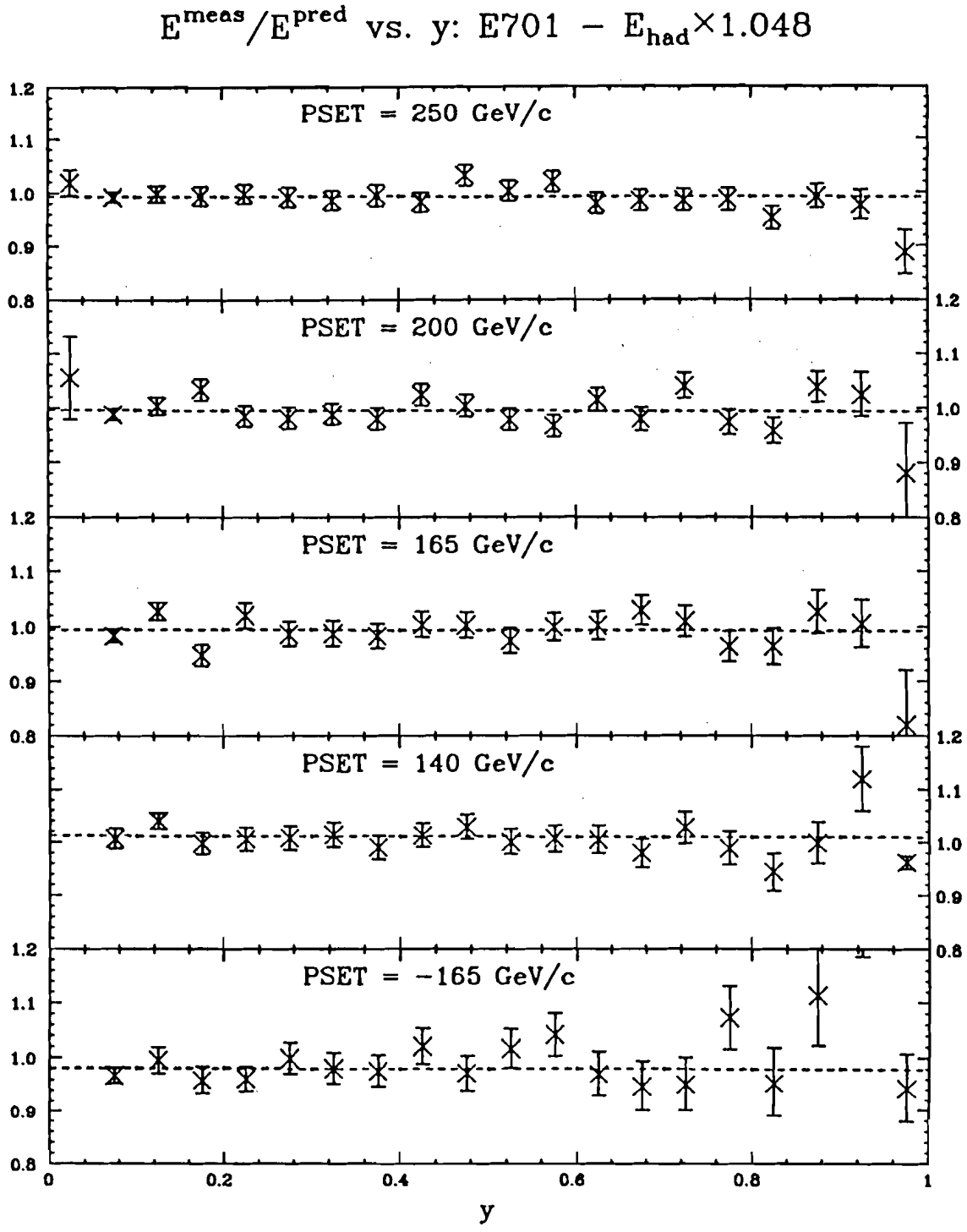
E^{meas}/E^{pred} vs. y: E701 − E_{had}×1.048
PSET = 250 GeV/c
PSET = 200 GeV/c
PSET = 165 GeV/c
PSET = 140 GeV/c
PSET = −165 GeV/c
1.2
1.1
1.0
0.9
0.8
0
0.2
0.4
0.6
0.8
1
y

Figure 4.8

x−Resolution

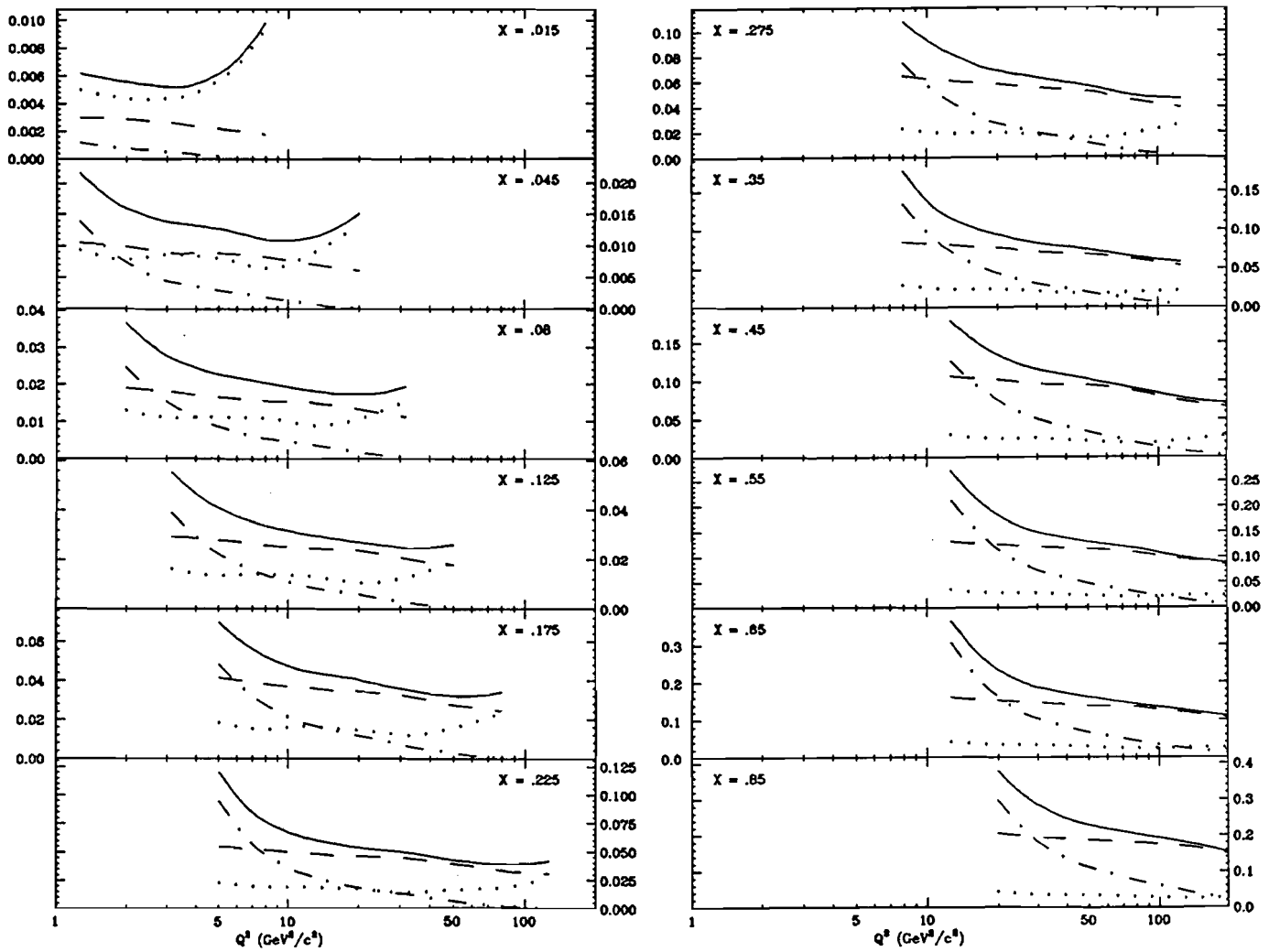

Figure 4.9a

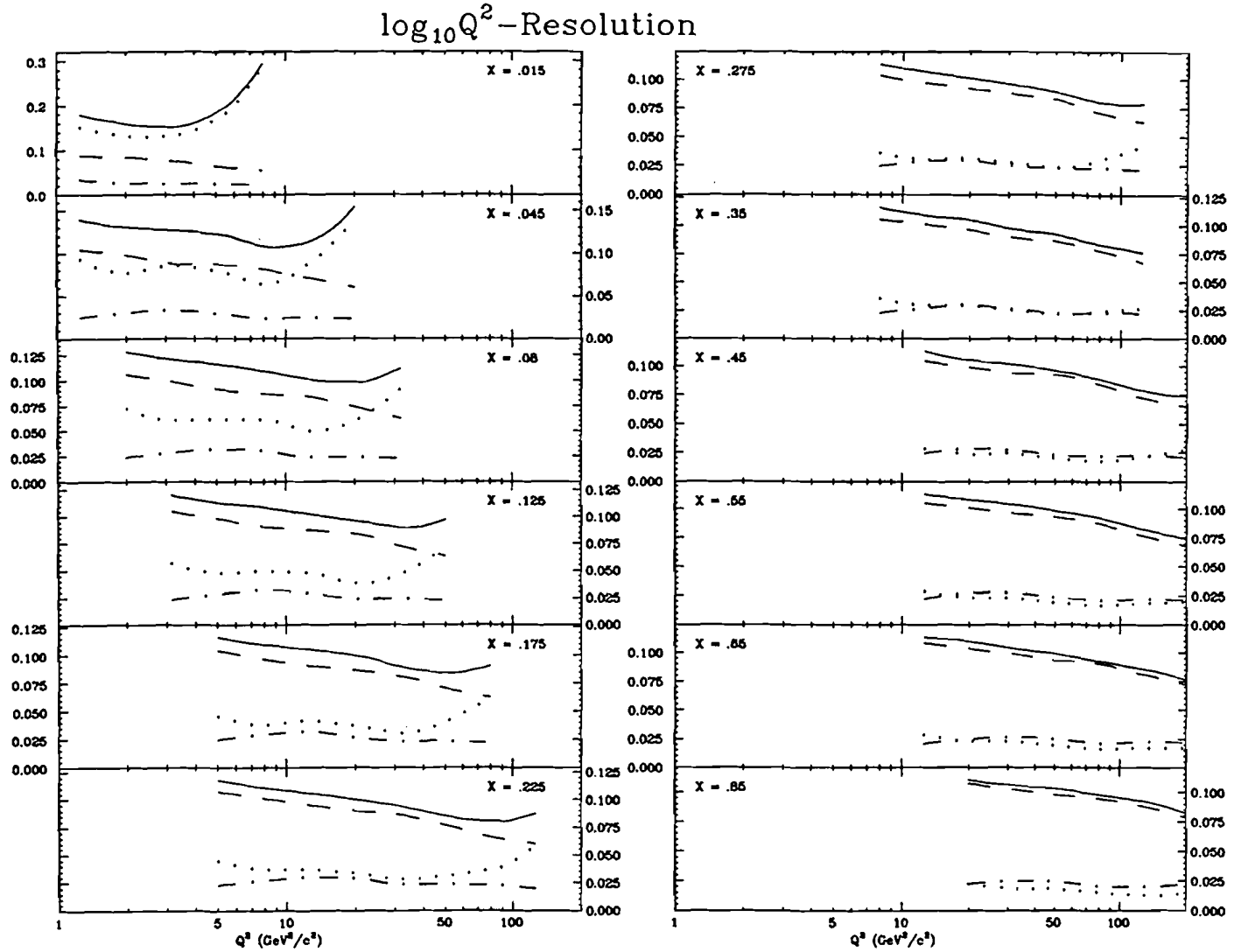
log10Q2−Resolution
X = .015
X = .045
X = .08
X = .125
X = .175
X = .225
X = .275
X = .35
X = .45
X = .55
X = .65
X = .85
Q2 (GeV2/c2)
Q2 (GeV2/c2)

Figure 4.9b

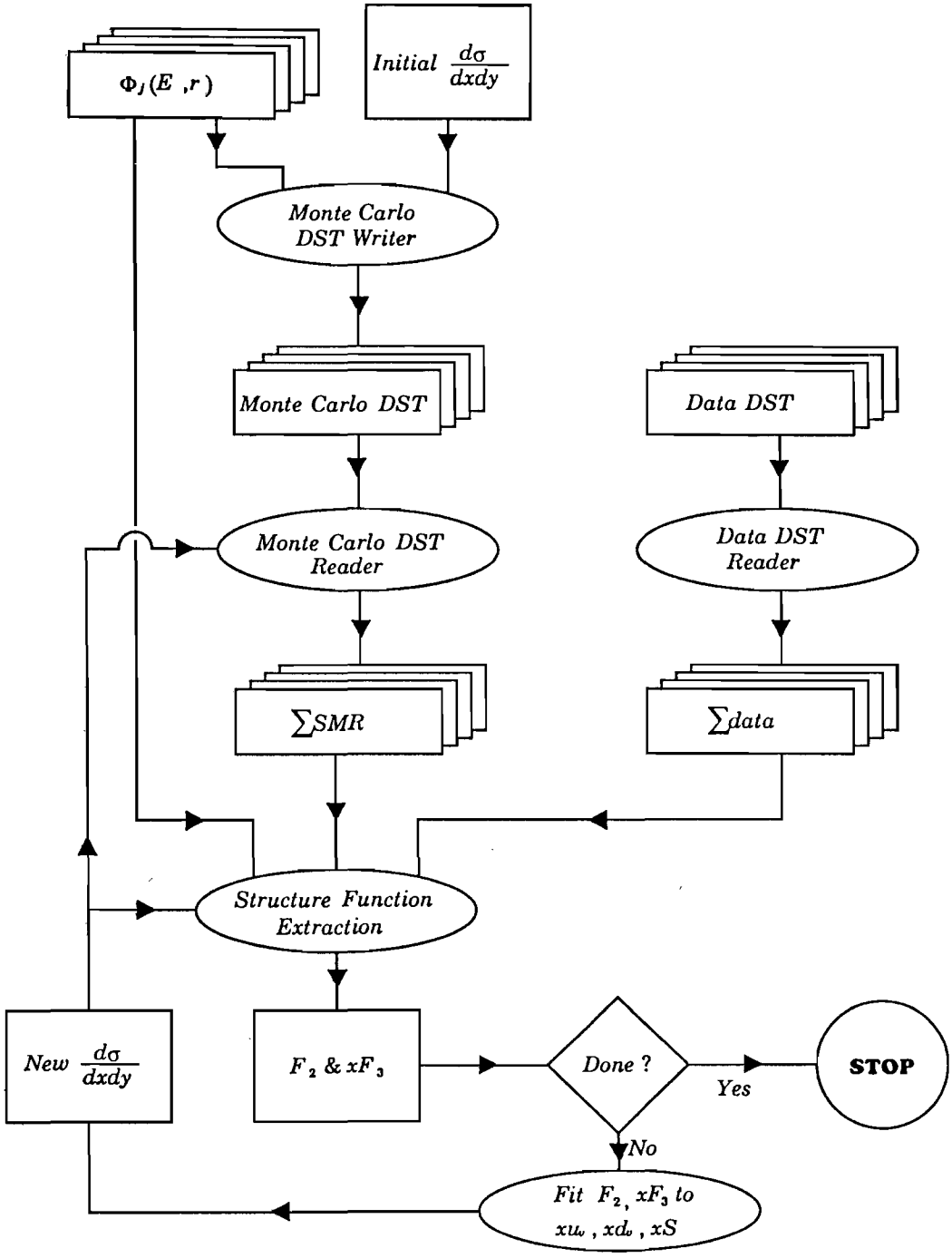
$\Phi_j(E, r)$
Initial $\frac{d\sigma}{dxdy}$
Monte Carlo DST Writer
Monte Carlo DST
Data DST
Monte Carlo DST Reader
Data DST Reader
$\sum SMR$
$\sum data$
Structure Function Extraction
New $\frac{d\sigma}{dxdy}$
F_2 & xF_3
Done ?
Yes
STOP
No
Fit F_2, xF_3 to xu_v, xd_v, xS

Figure 5.1

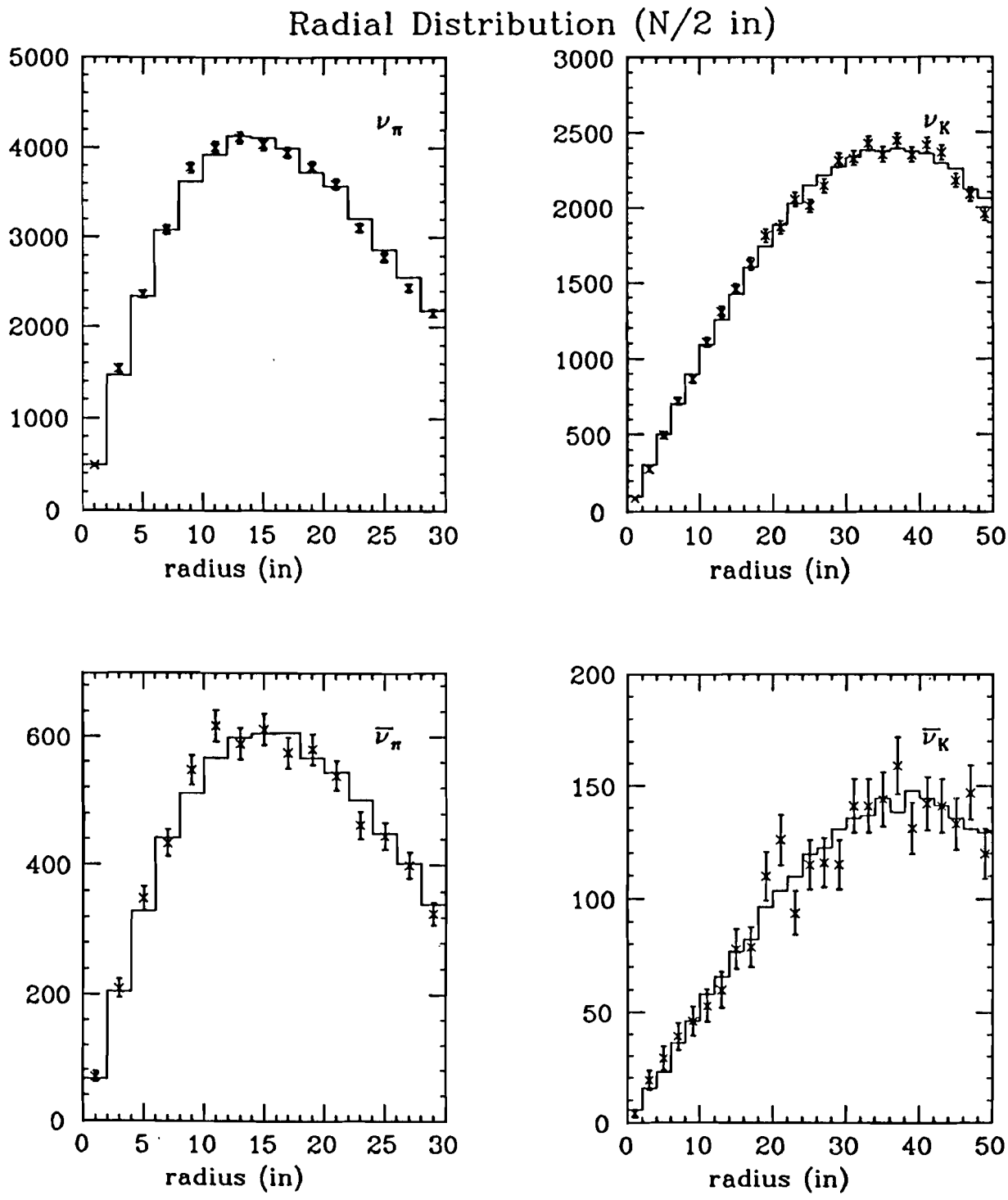
Radial Distribution (N/2 in)
ν_π
ν_K
$\bar{\nu}_\pi$
$\bar{\nu}_K$
radius (in)
radius (in)
radius (in)
radius (in)

Figure 5.2a

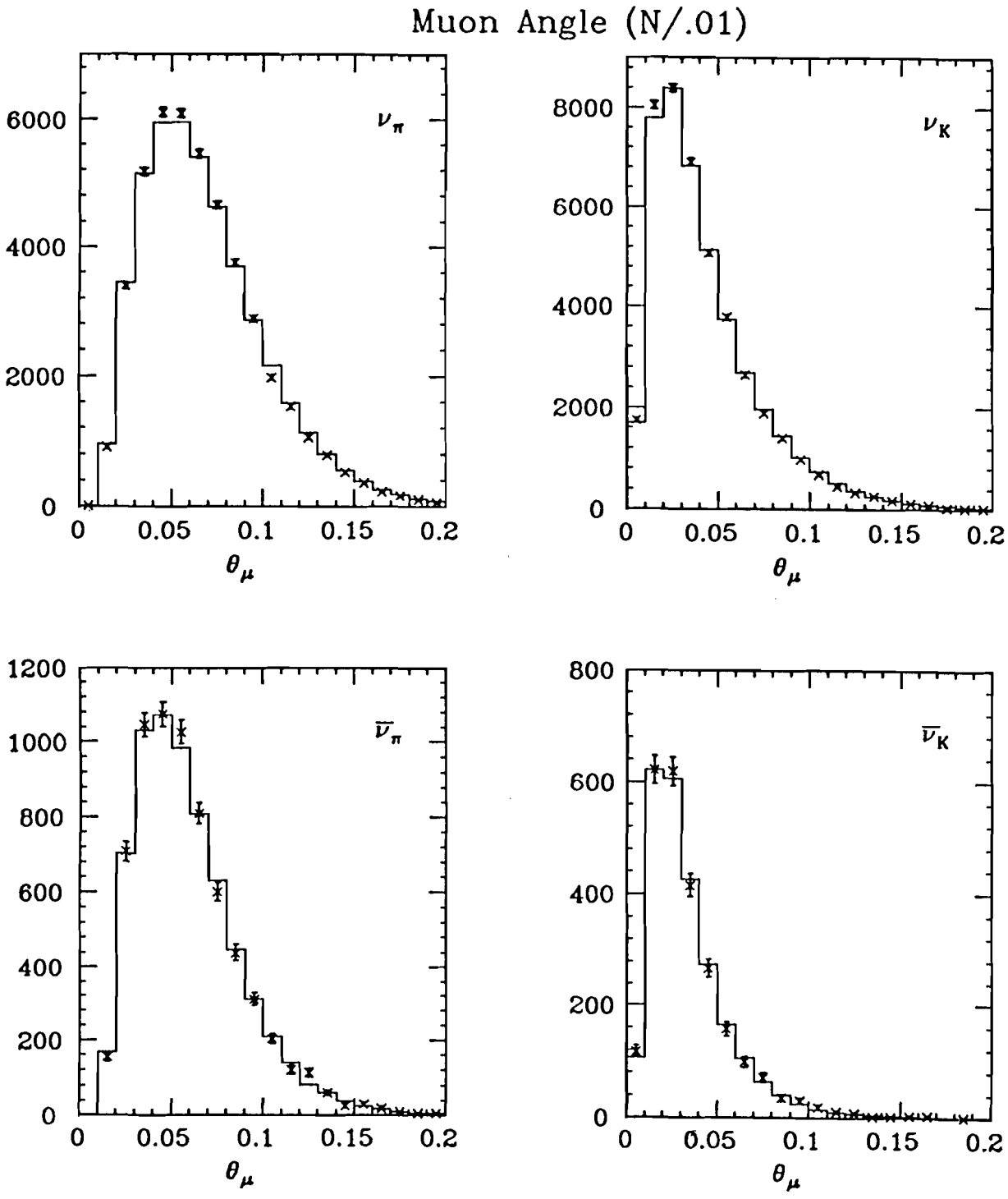
Muon Angle (N/.01)
ν_π
ν_K
$\overline{\nu}_\pi$
$\overline{\nu}_K$
θ_μ
0
0.05
0.1
0.15
0.2
2000
4000
6000
8000
200
400
600
800
1000
1200

Figure 5.2b

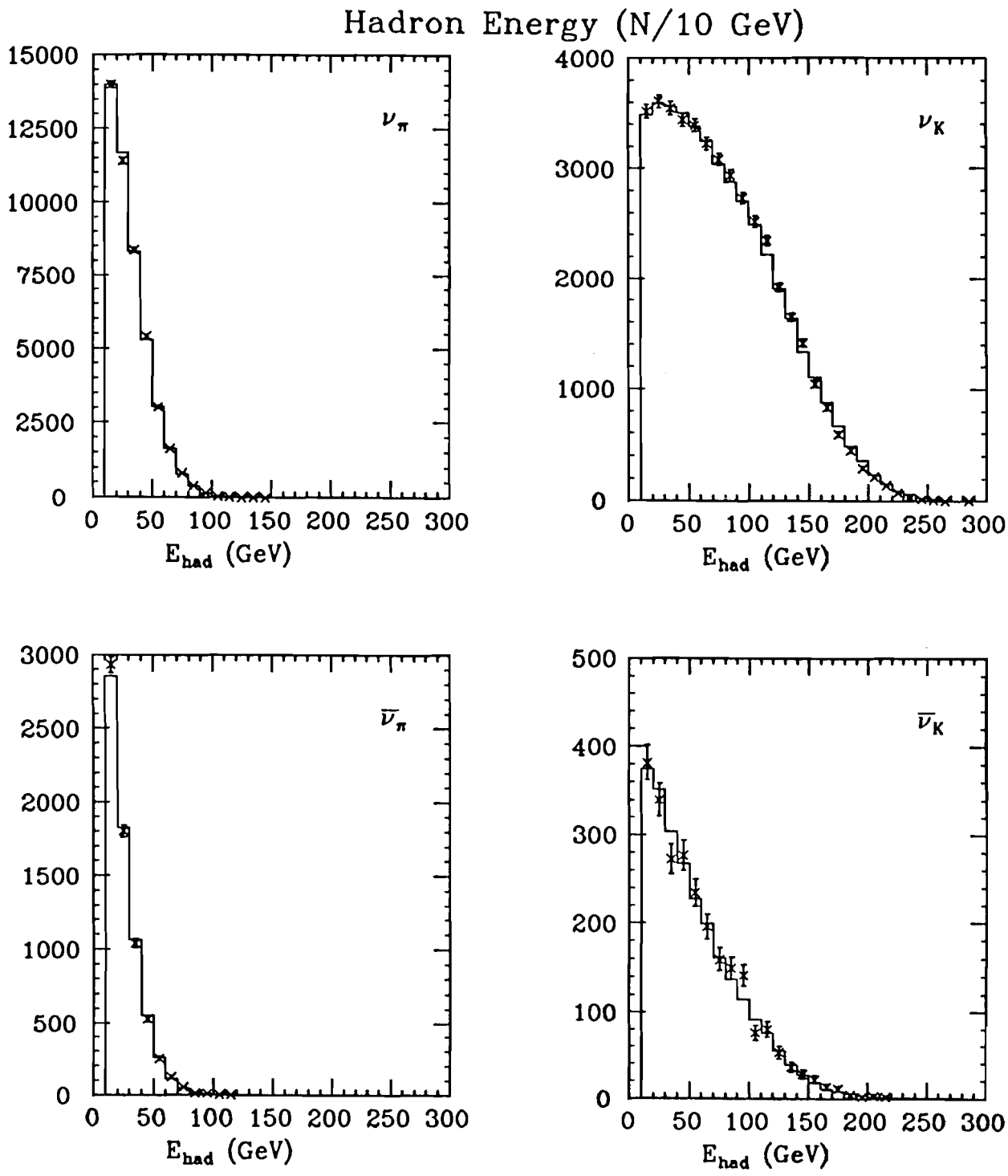
Hadron Energy (N/10 GeV)
ν_π
ν_K
$\bar{\nu}_\pi$
$\bar{\nu}_K$
E_{had} (GeV)
E_{had} (GeV)
E_{had} (GeV)
E_{had} (GeV)

Figure 5.2c

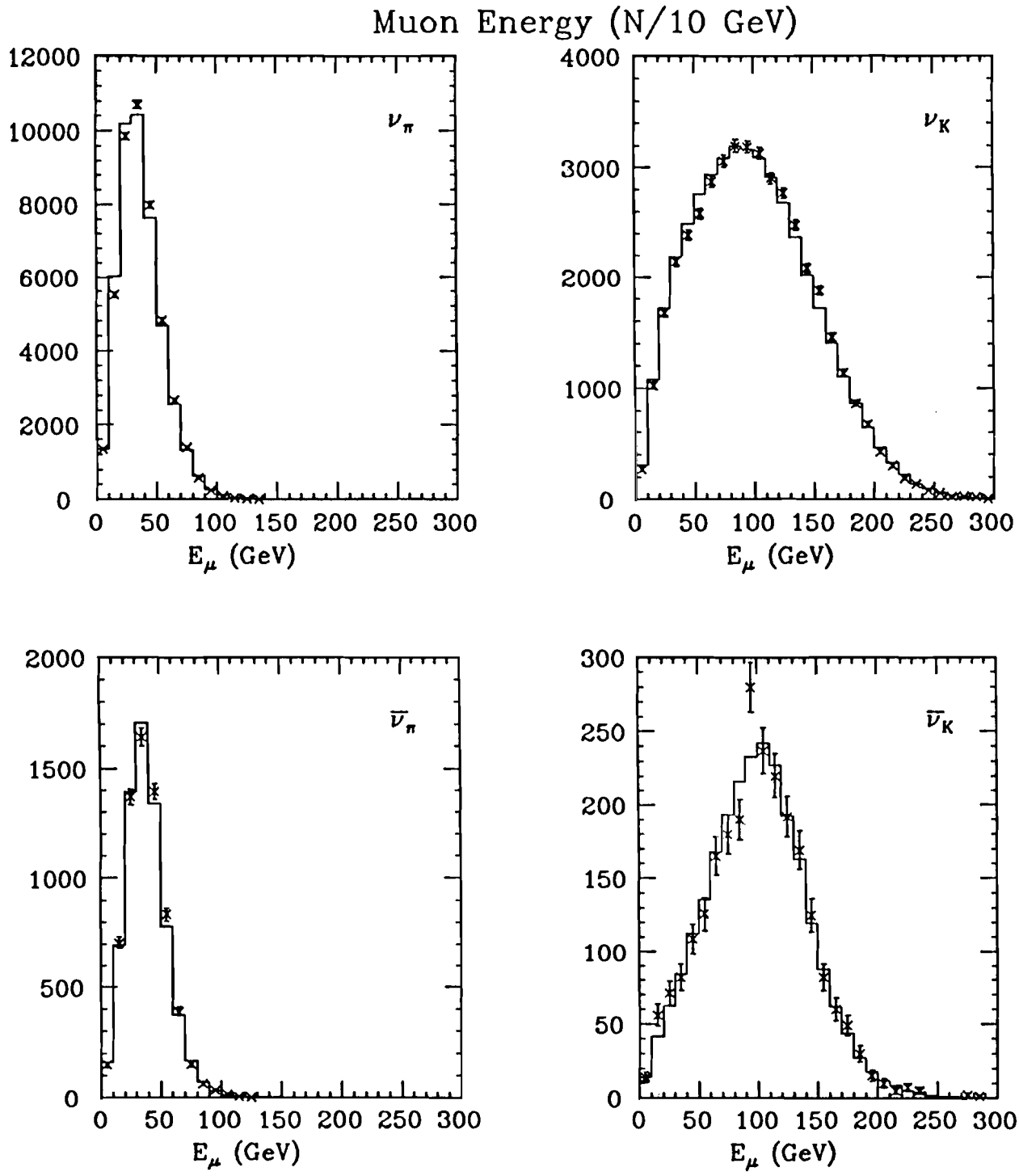
Muon Energy (N/10 GeV)
ν_π
ν_K
$\bar{\nu}_\pi$
$\bar{\nu}_K$
E_μ (GeV)
0
50
100
150
200
250
300
2000
4000
6000
8000
10000
12000
1000
3000
500
1500
250

Figure 5.2d

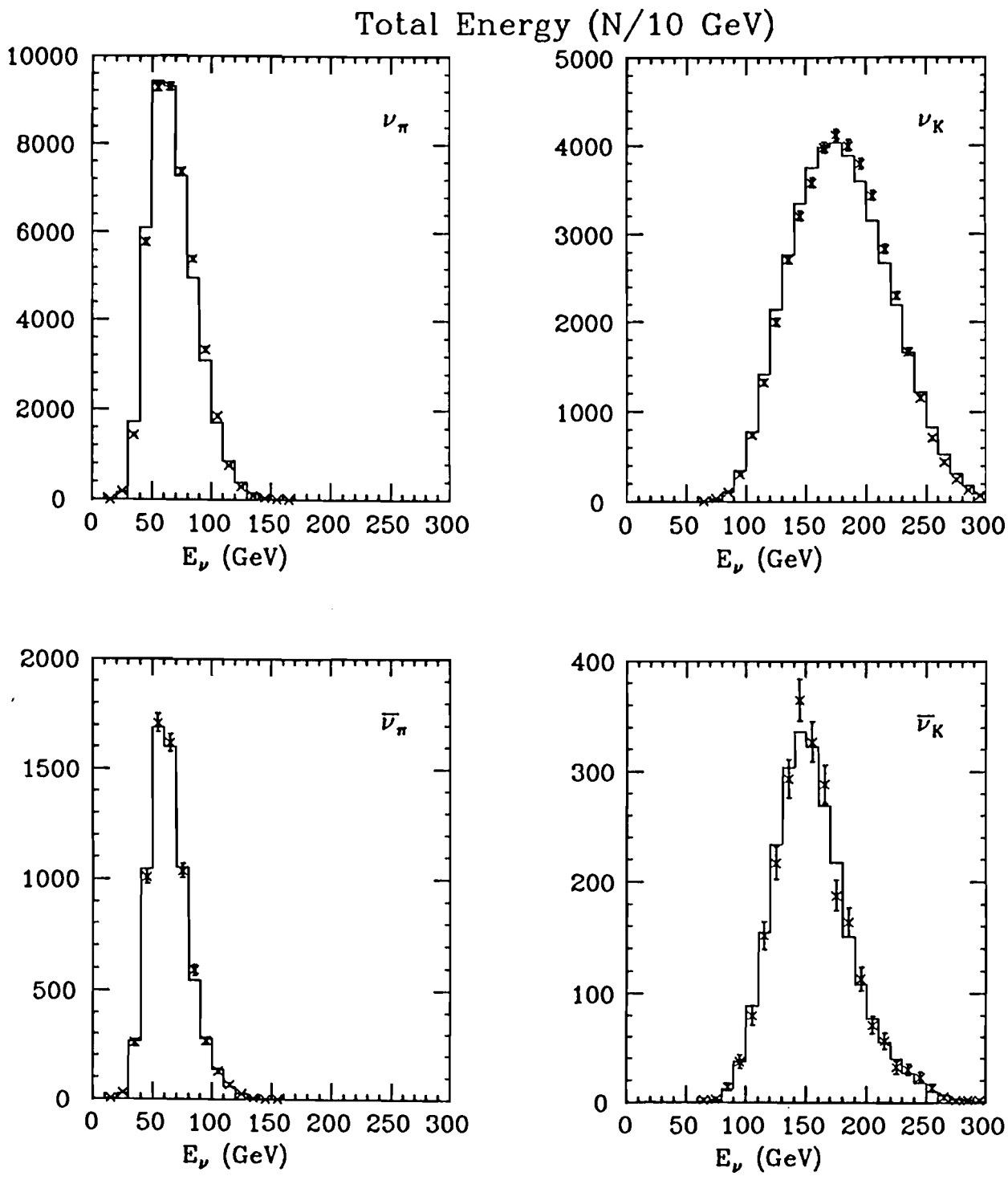
Total Energy (N/10 GeV)
ν_π
ν_K
$\bar{\nu}_\pi$
$\bar{\nu}_K$
E_ν (GeV)
0
50
100
150
200
250
300
2000
4000
6000
8000
10000
1000
3000
5000
500
1500
100
200
300
400

Figure 5.3a

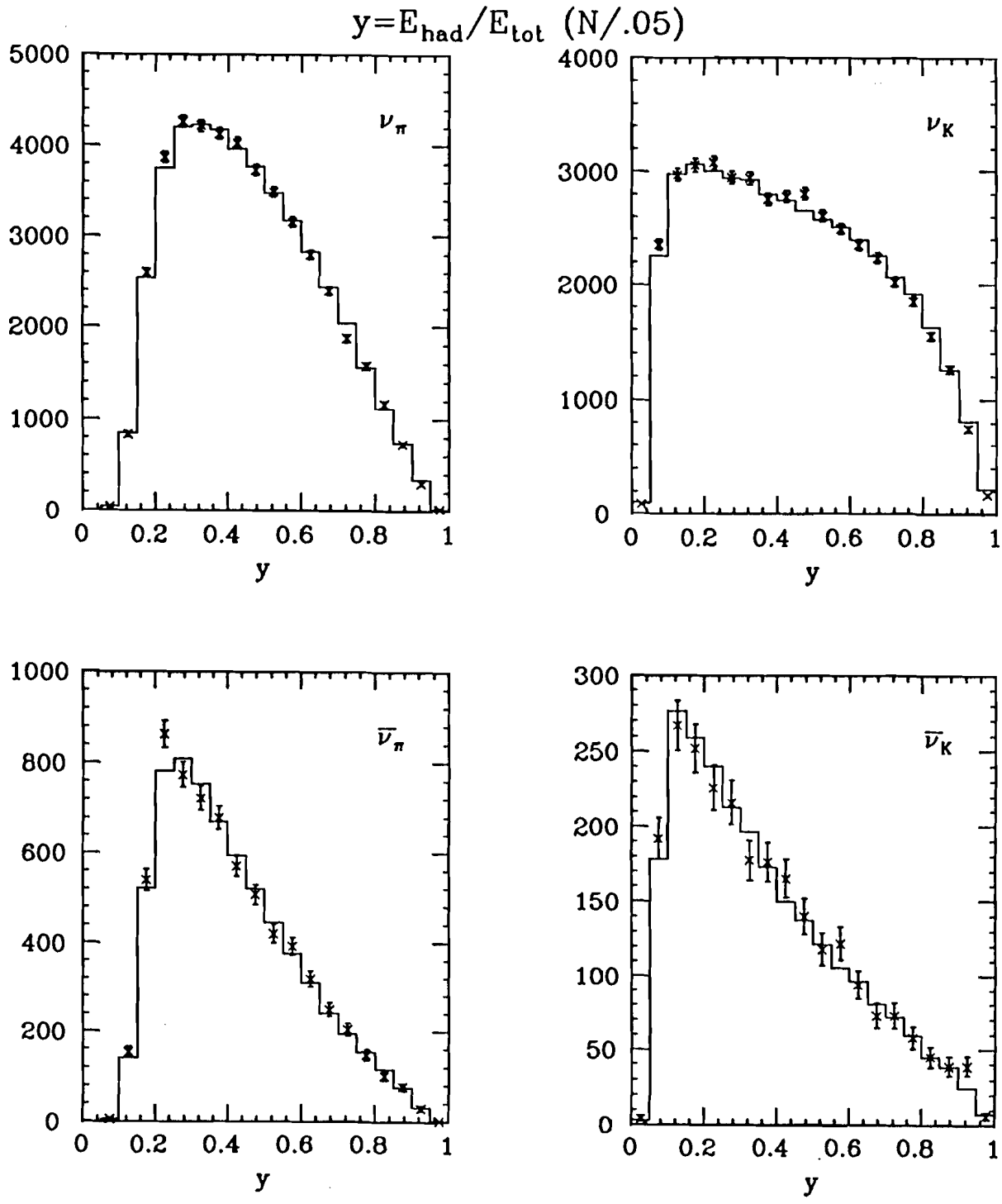

Figure 5.3b

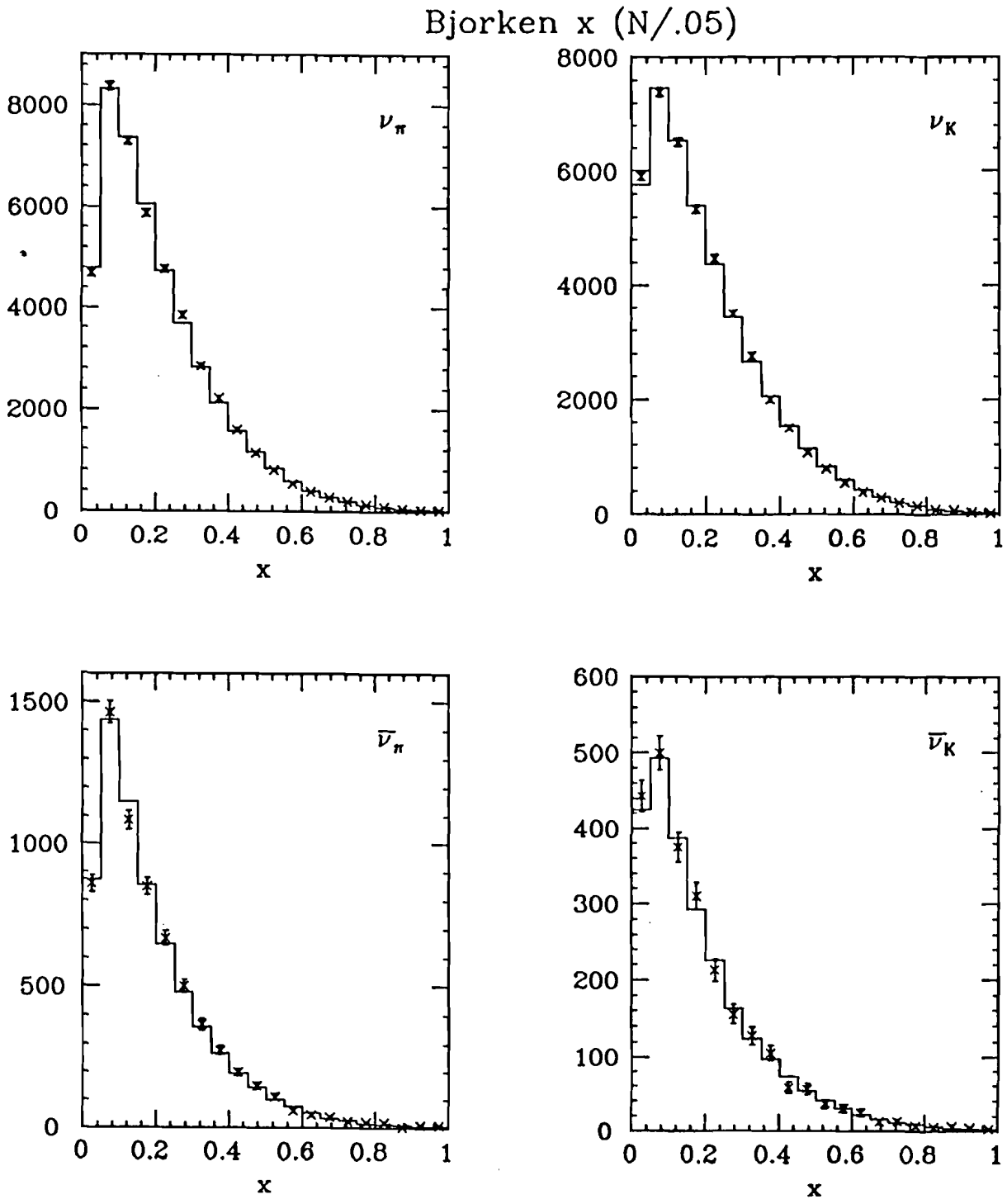

Figure 5.3c

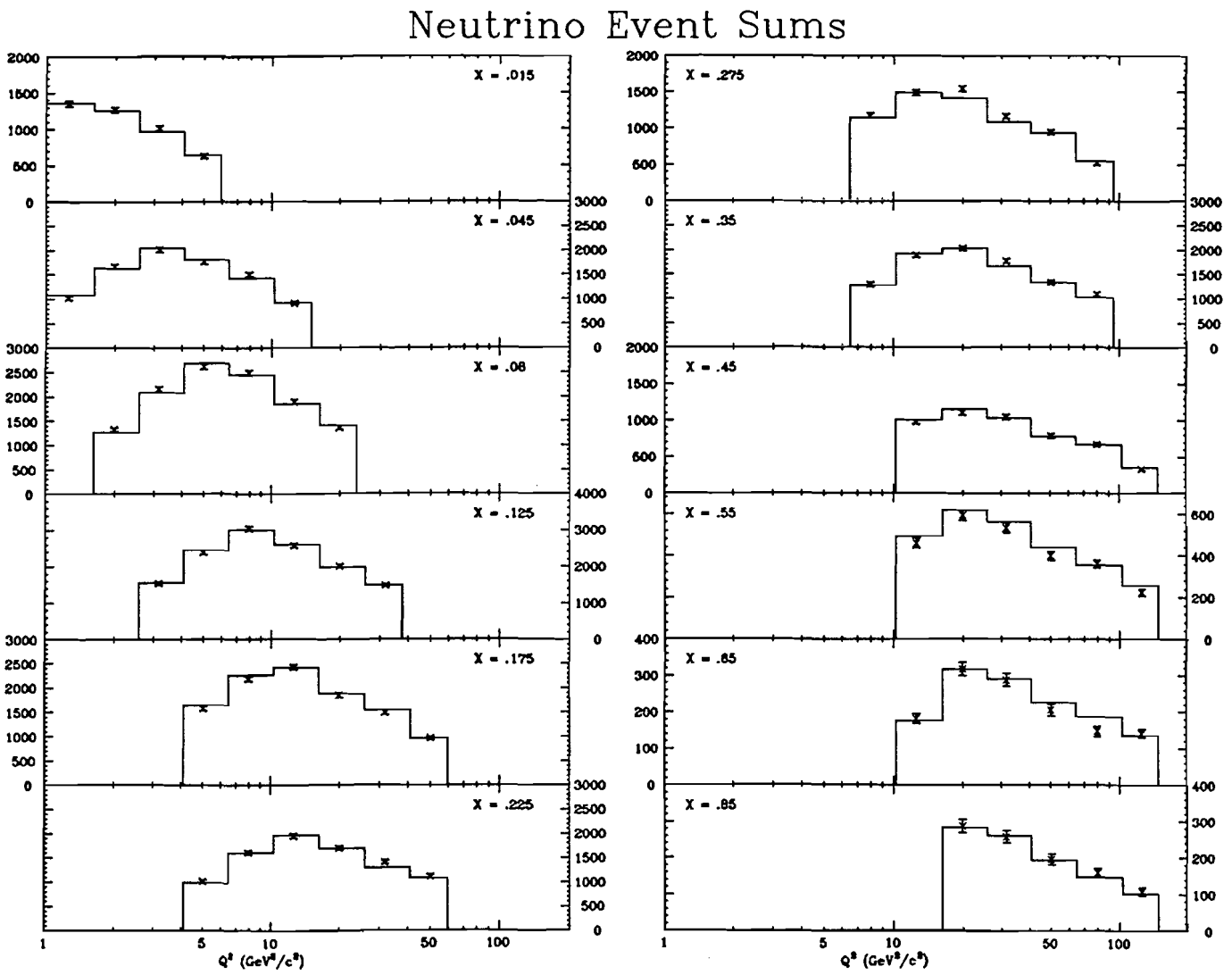
Neutrino Event Sums
X = .015
X = .045
X = .08
X = .125
X = .175
X = .225
X = .275
X = .35
X = .45
X = .55
X = .65
X = .85
Q² (GeV²/c²)
Q² (GeV²/c²)

Figure 5.4a

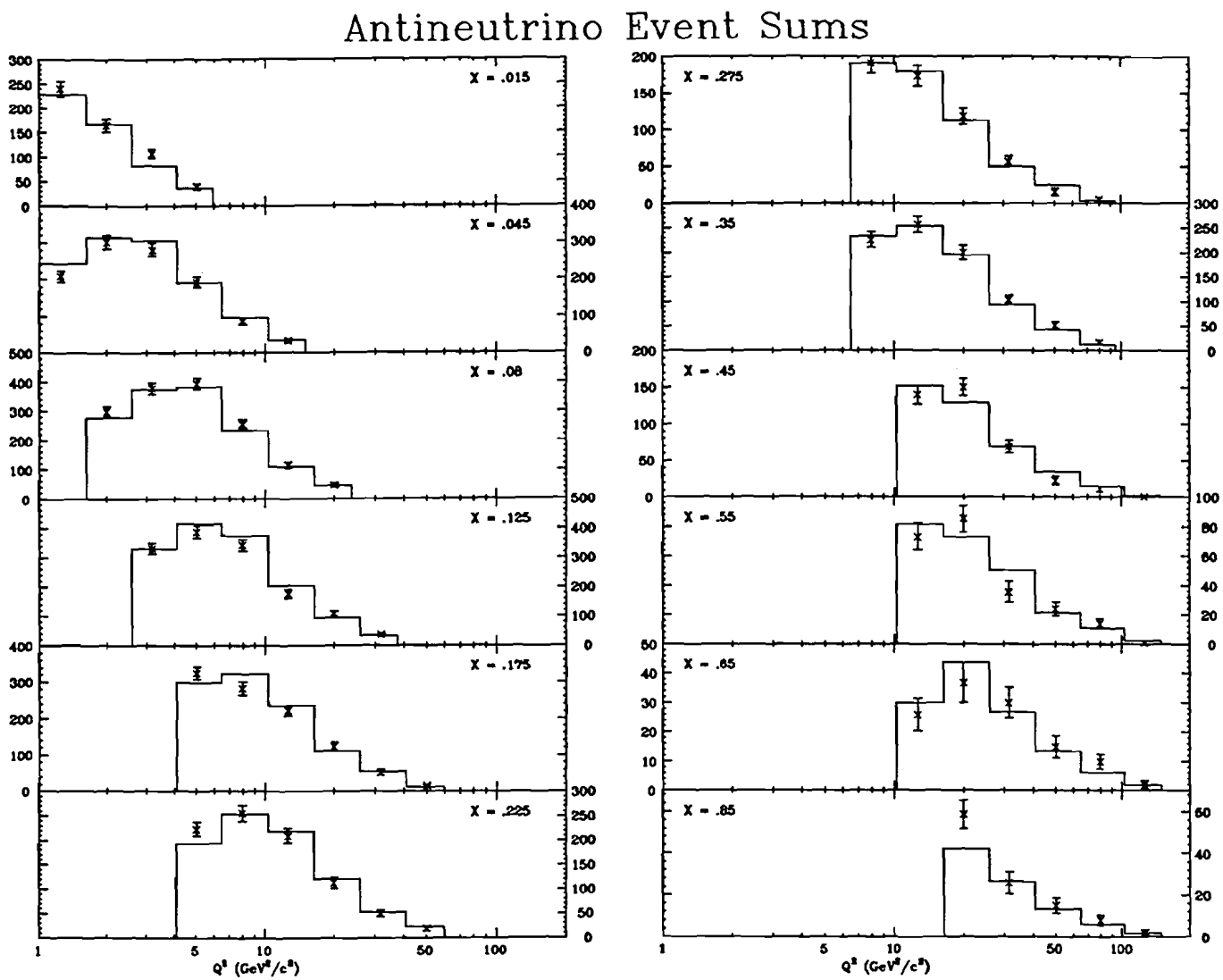
Antineutrino Event Sums
X = .015
X = .045
X = .08
X = .125
X = .175
X = .225
X = .275
X = .35
X = .45
X = .55
X = .65
X = .85
Q² (GeV²/c²)
Q² (GeV²/c²)

Figure 5.4b

F_2 Model Corrections

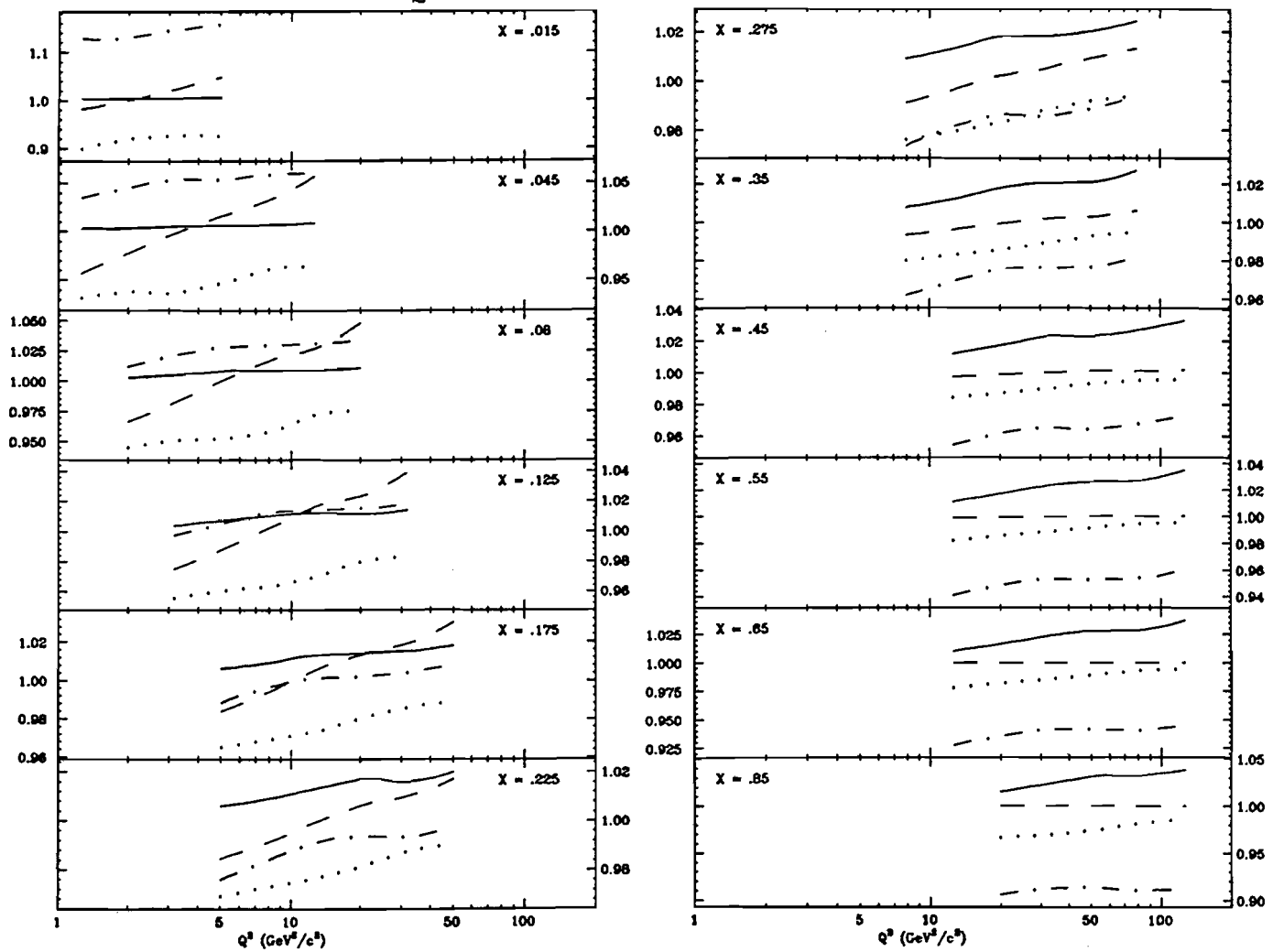

Figure 5.5a

xF_3 Model Corrections

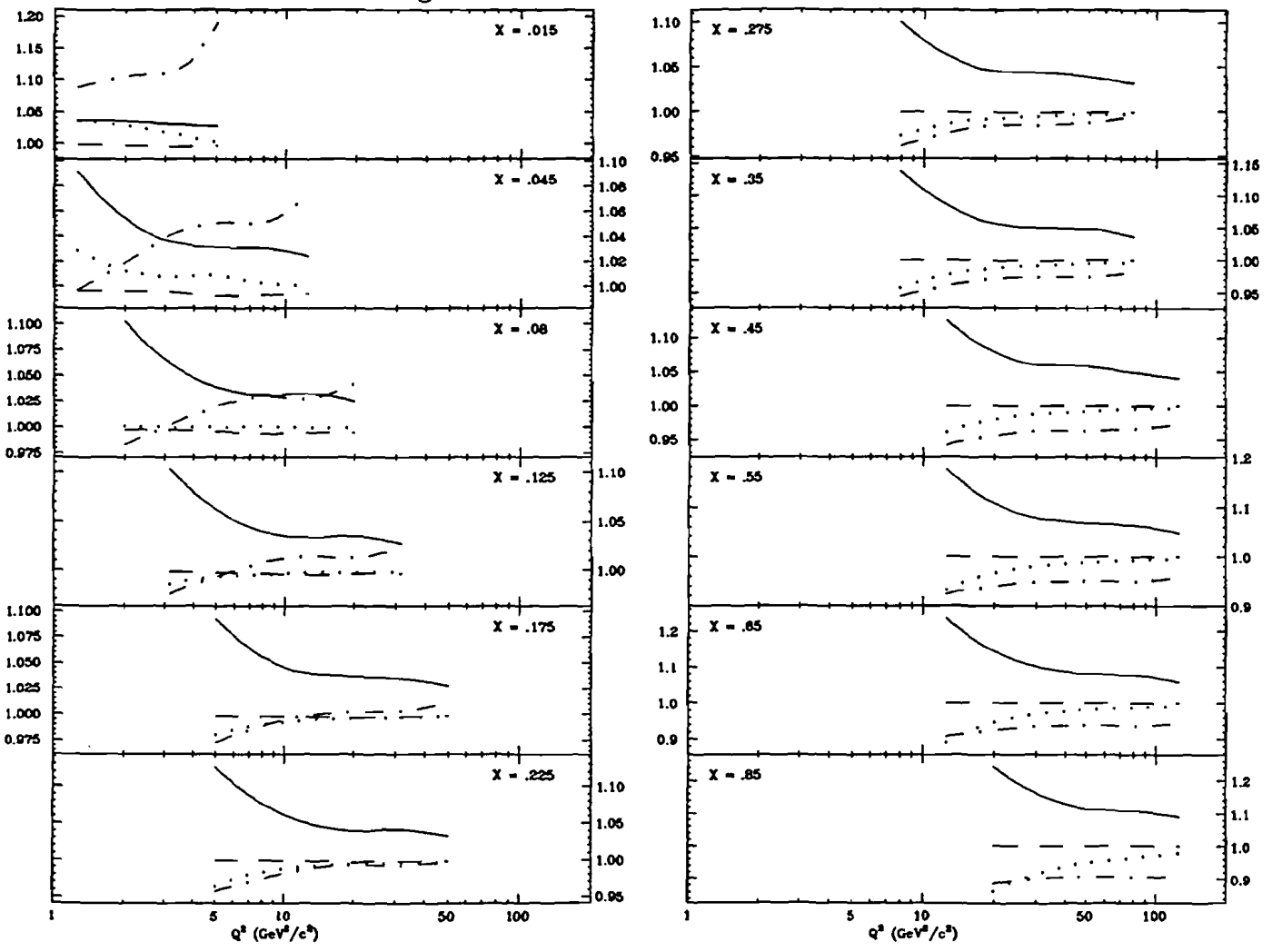

Figure 5.5b

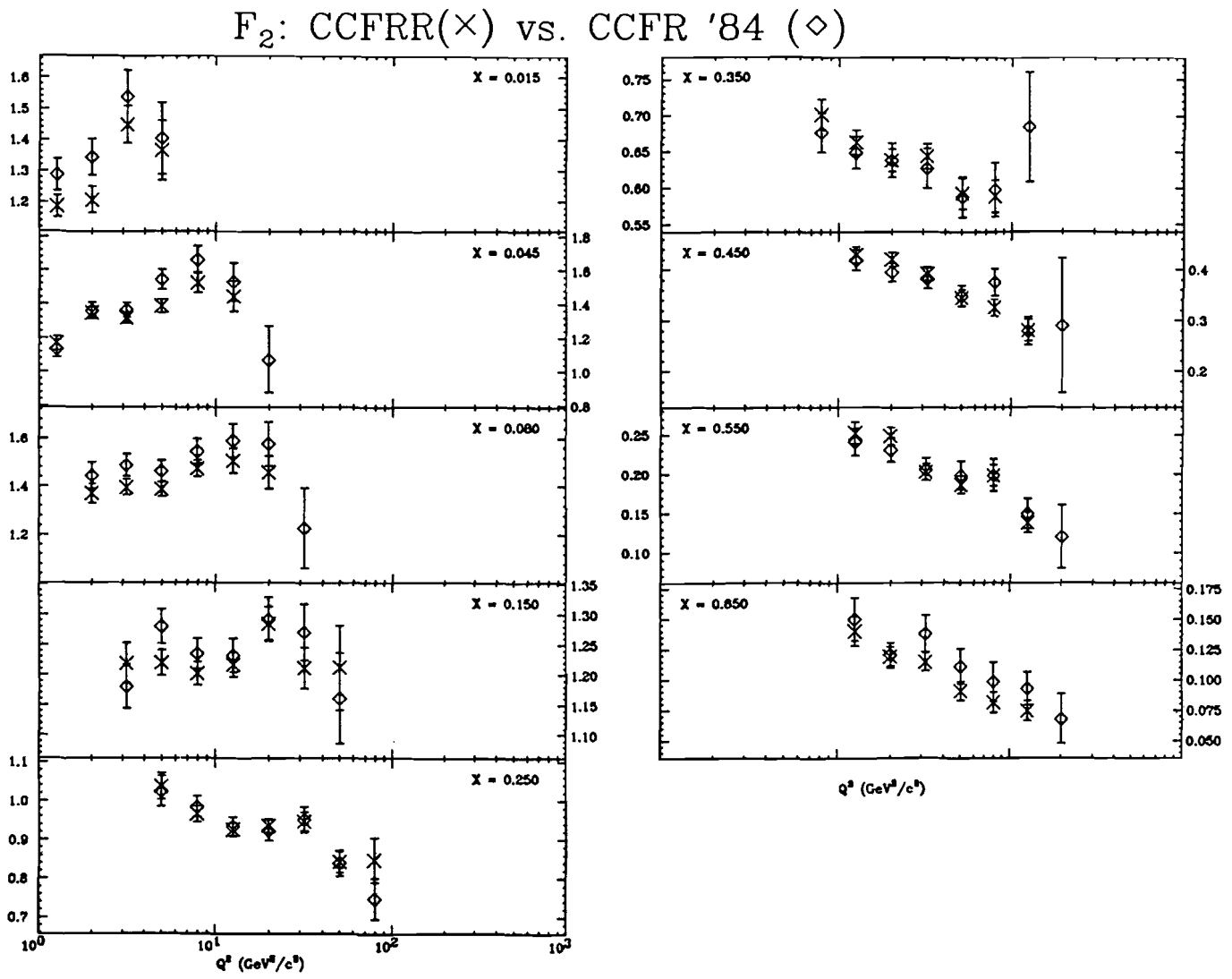
F2: CCFRR(×) vs. CCFR '84 (◇)
X = 0.015
X = 0.045
X = 0.080
X = 0.150
X = 0.250
X = 0.350
X = 0.450
X = 0.550
X = 0.650
Q² (GeV²/c²)
Q² (GeV²/c²)

Figure 6.1a

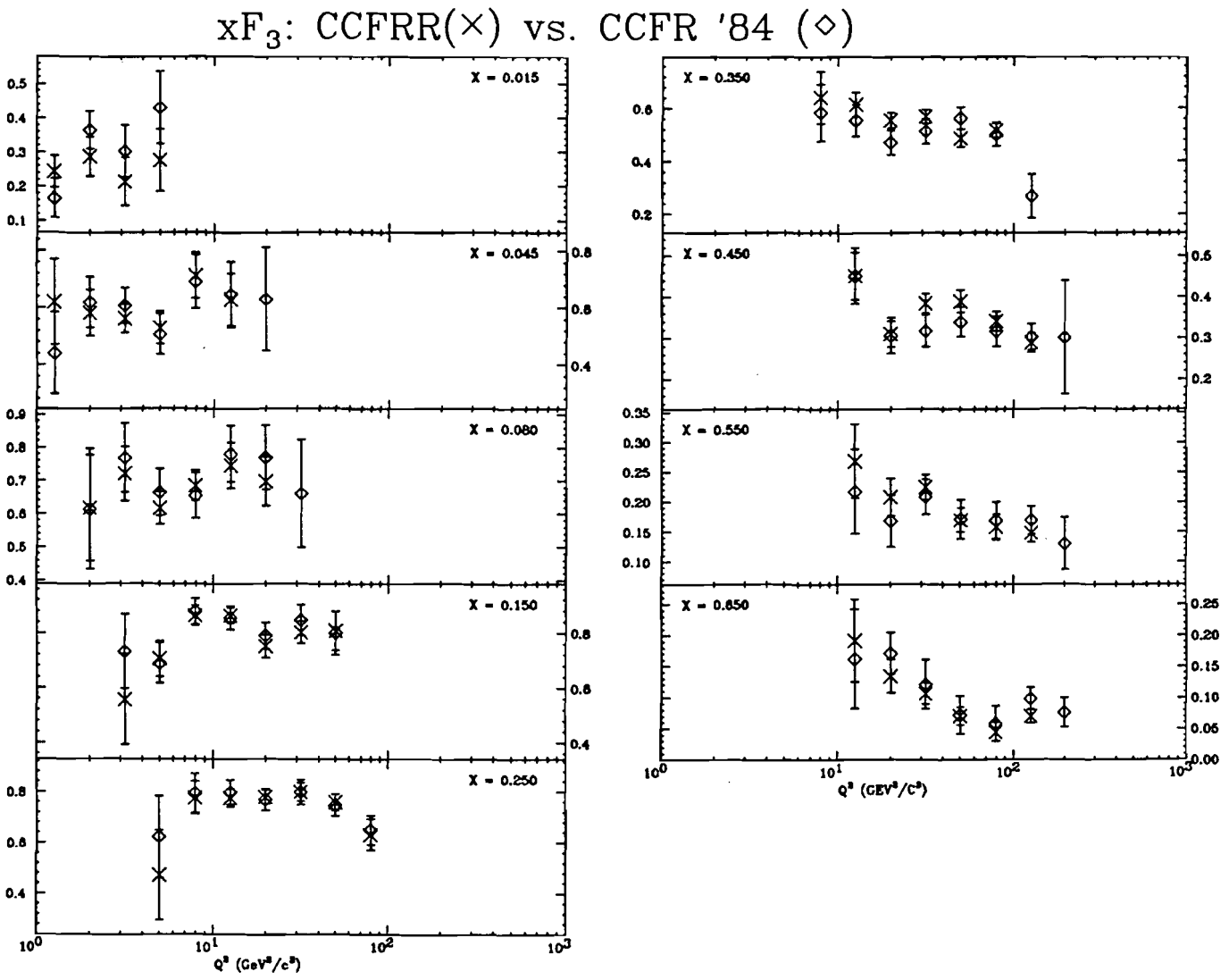
xF3: CCFRR(×) vs. CCFR '84 (◇)
X = 0.015
X = 0.045
X = 0.080
X = 0.150
X = 0.250
X = 0.350
X = 0.450
X = 0.550
X = 0.650
Q² (GeV²/c²)
Q² (GEV²/C²)

Figure 6.1b

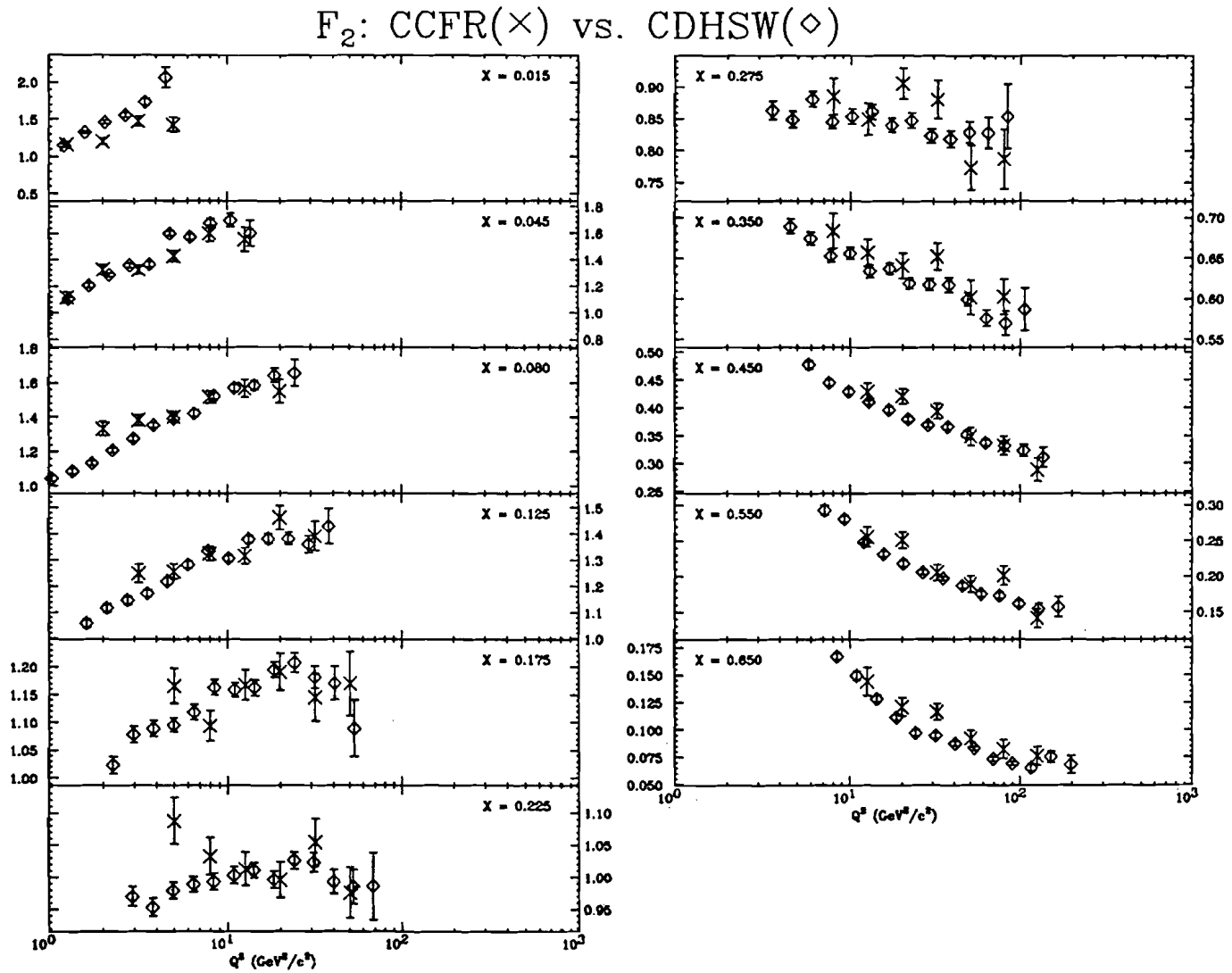
F2: CCFR(×) vs. CDHSW(◇)
X = 0.015
X = 0.045
X = 0.080
X = 0.125
X = 0.175
X = 0.225
X = 0.275
X = 0.350
X = 0.450
X = 0.550
X = 0.650
Q² (GeV²/c²)
Q² (GeV²/c²)

Figure 6.2a

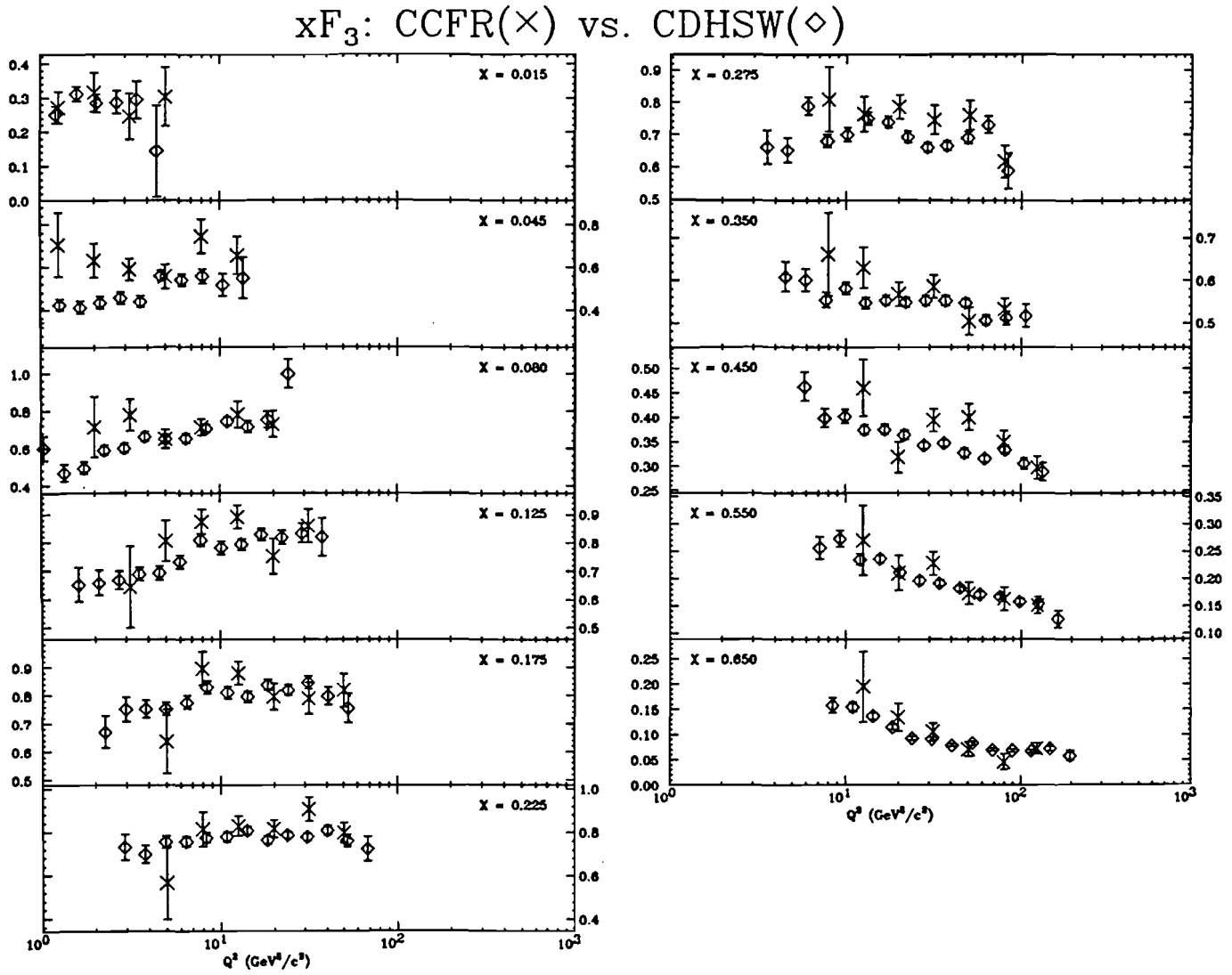
xF3: CCFR(×) vs. CDHSW(◇)
X = 0.015
X = 0.045
X = 0.080
X = 0.125
X = 0.175
X = 0.225
X = 0.275
X = 0.350
X = 0.450
X = 0.550
X = 0.650
Q² (GeV²/c²)
Q² (GeV²/c²)

Figure 6.2b

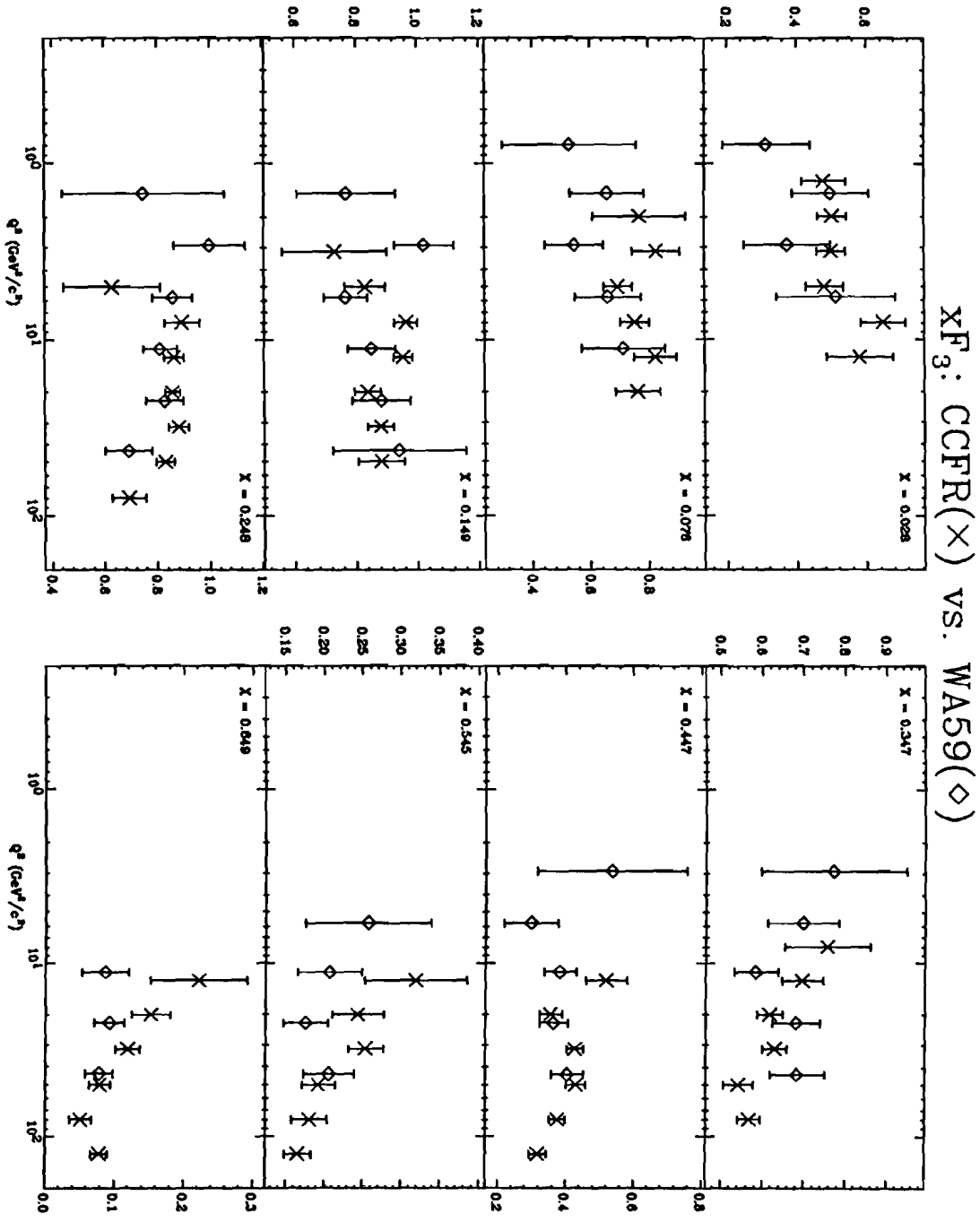
xF3: CCFR(×) vs. WA59(◇)
x = 0.028
x = 0.078
x = 0.149
x = 0.248
x = 0.347
x = 0.447
x = 0.545
x = 0.649
Q² (GeV²/c²)

Figure 6.3a

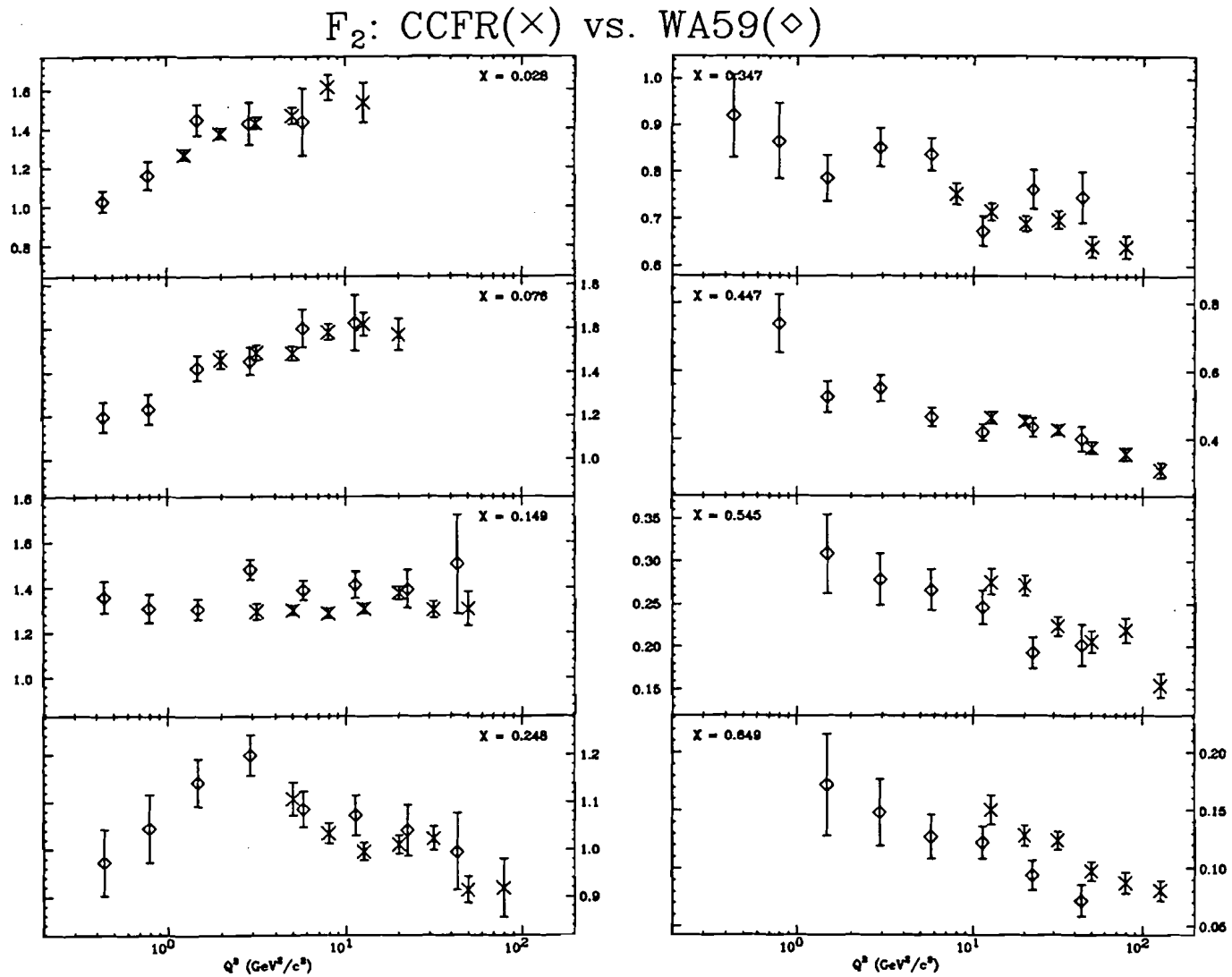
F2: CCFR(×) vs. WA59(◇)
X = 0.028
X = 0.076
X = 0.149
X = 0.248
X = 0.347
X = 0.447
X = 0.545
X = 0.649
Q² (GeV²/c²)
Q² (GeV²/c²)

Figure 6.3b

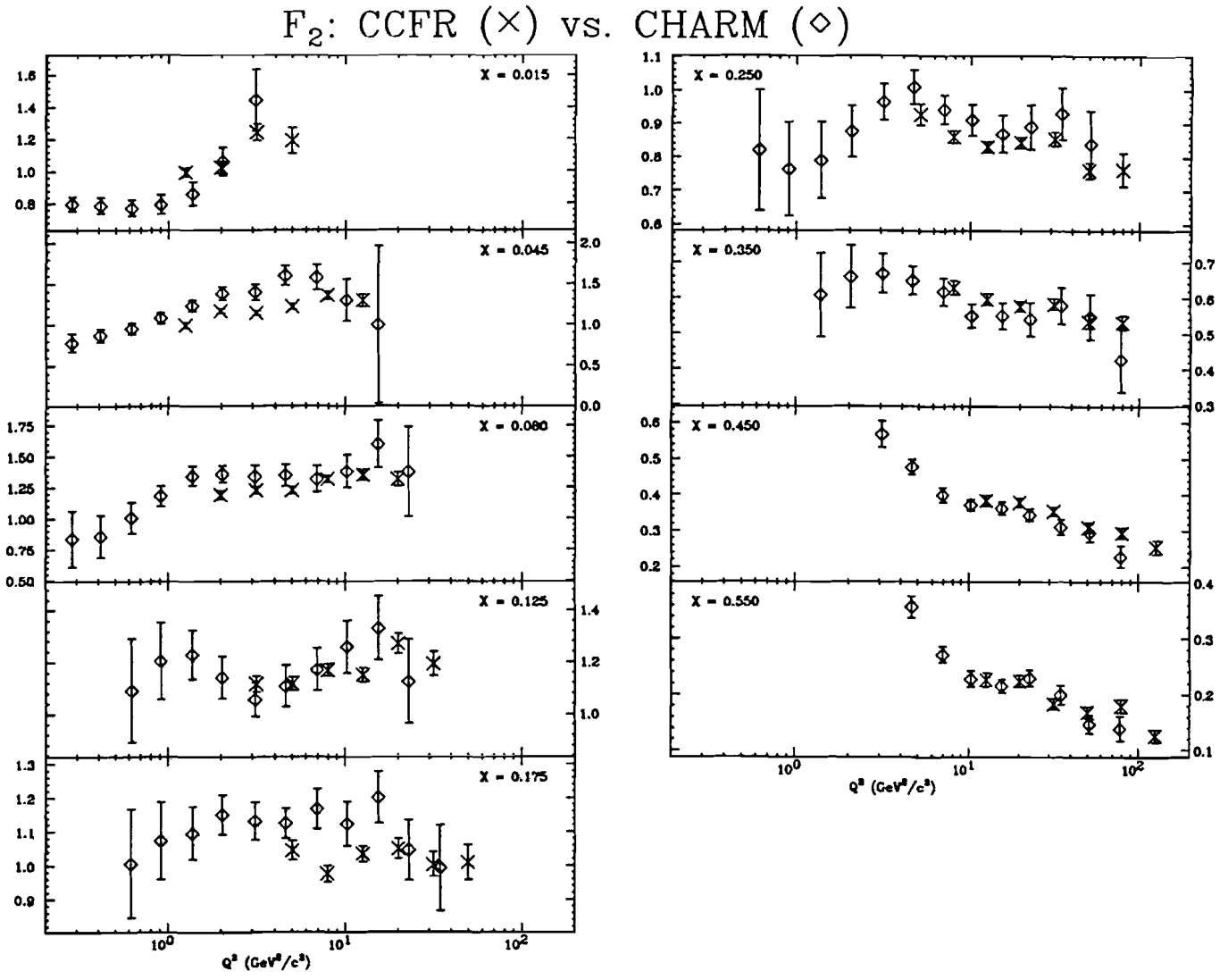
F2: CCFR (×) vs. CHARM (◇)
X = 0.015
X = 0.045
X = 0.080
X = 0.125
X = 0.175
X = 0.250
X = 0.350
X = 0.450
X = 0.550
Q² (GeV²/c²)
Q² (GeV²/c²)

Figure 6.4a

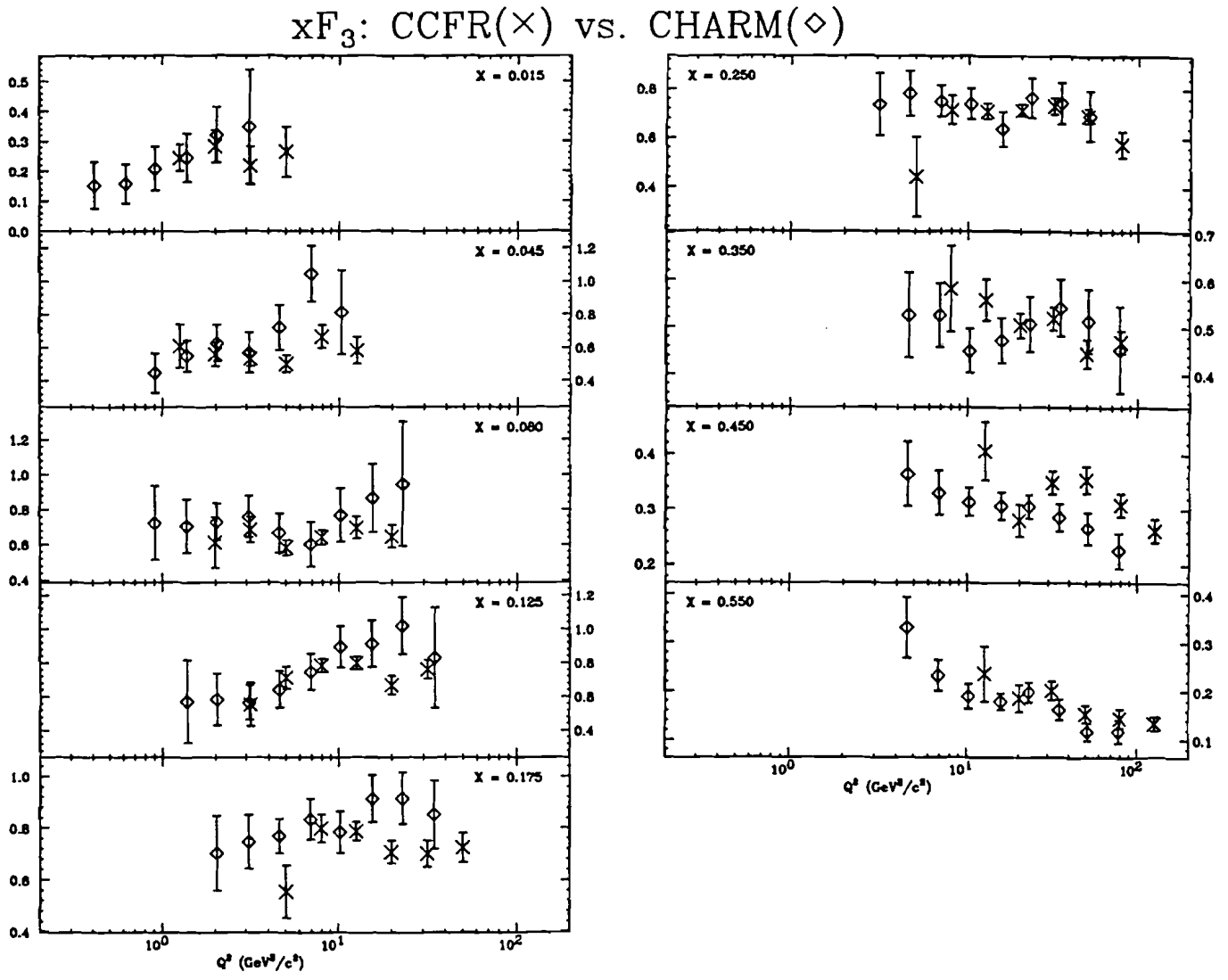
xF3: CCFR(×) vs. CHARM(◇)
X = 0.015
X = 0.045
X = 0.080
X = 0.125
X = 0.175
X = 0.250
X = 0.350
X = 0.450
X = 0.550
Q² (GeV²/c²)

Figure 6.4b

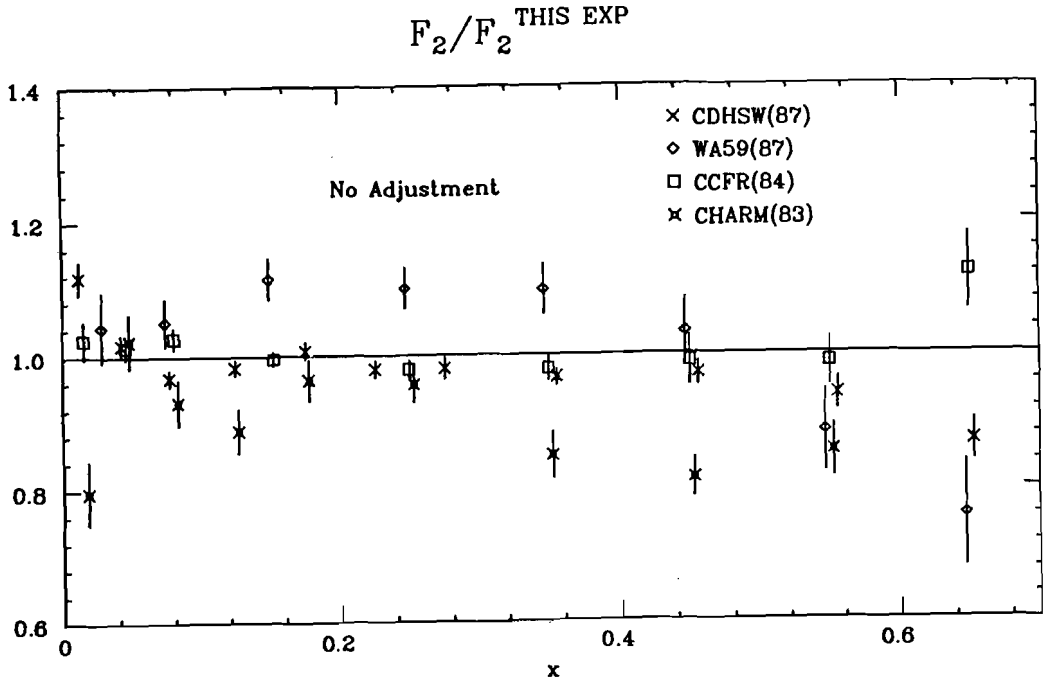

Figure 6.5a

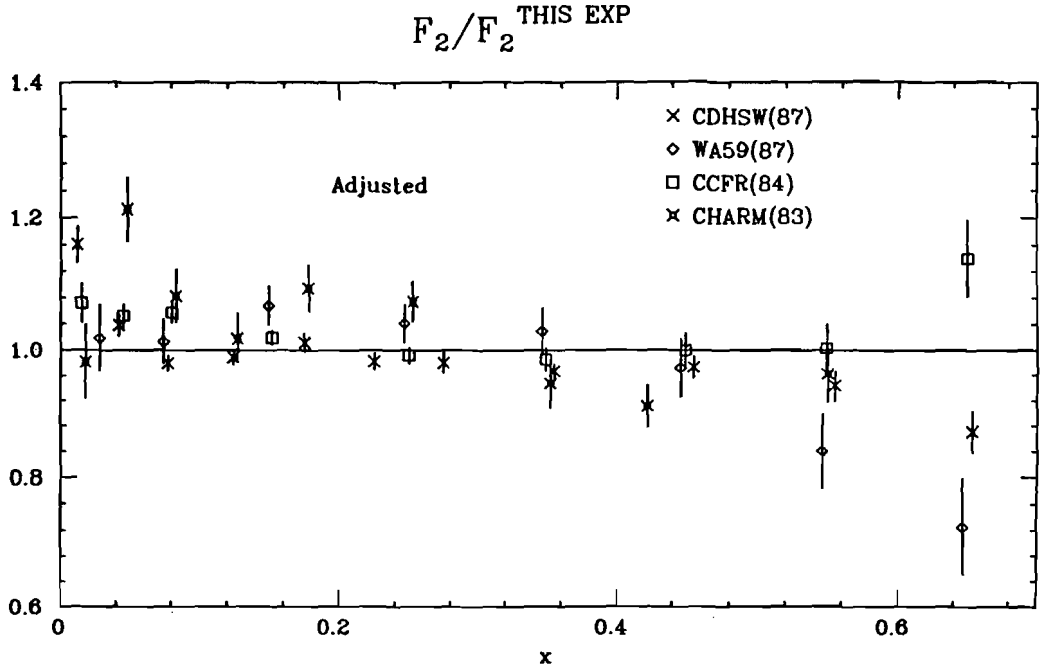

Figure 6.5b

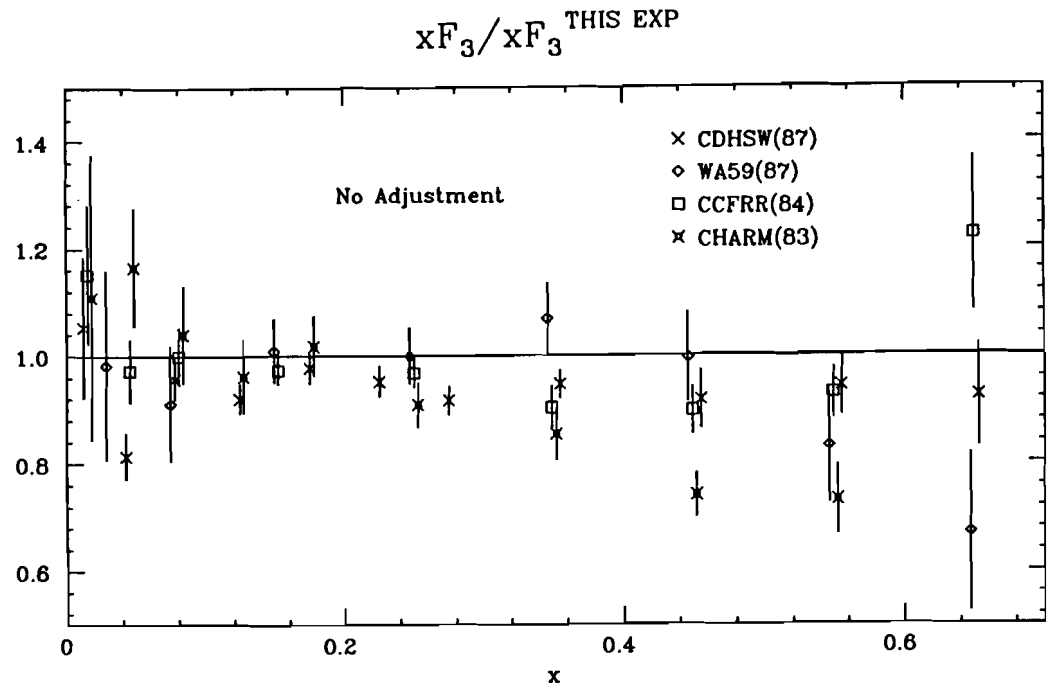

Figure 6.6a

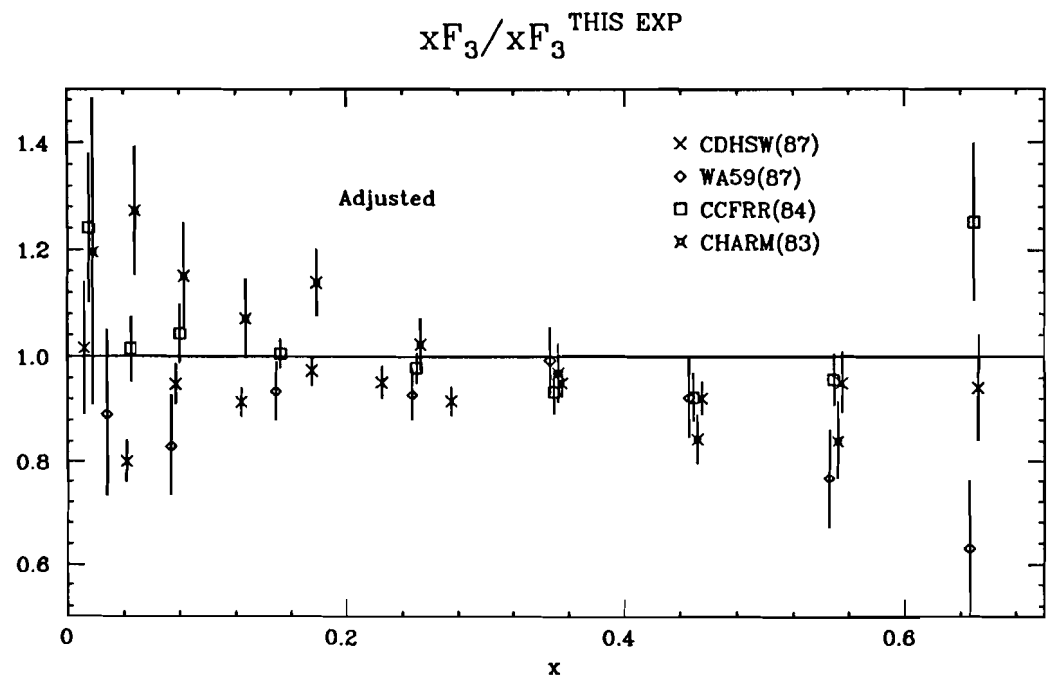

Figure 6.6b

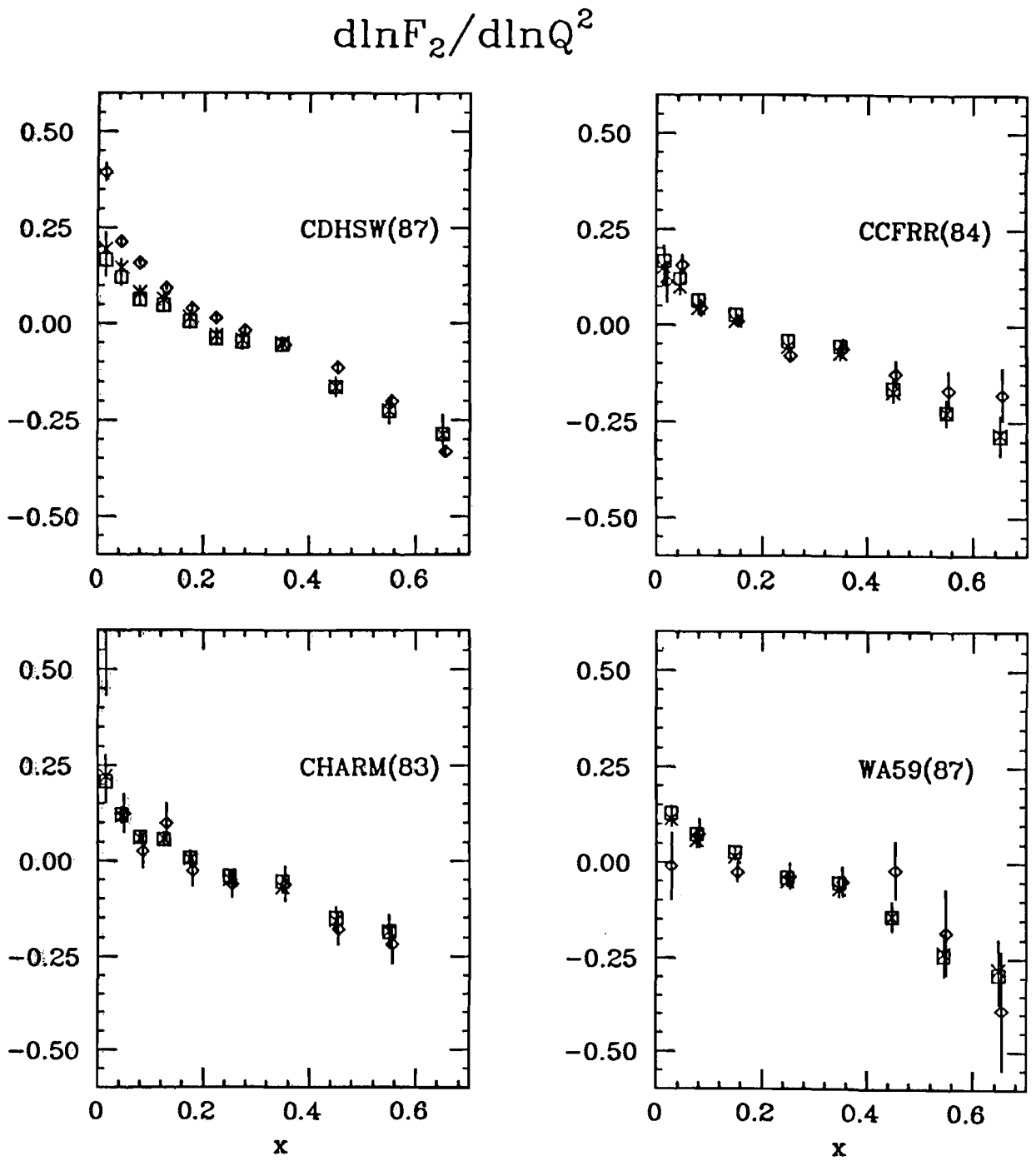
dlnF2/dlnQ2
CDHSW(87)
CCFRR(84)
CHARM(83)
WA59(87)
0.50
0.25
0.00
-0.25
-0.50
0
0.2
0.4
0.6
x

Figure 6.7

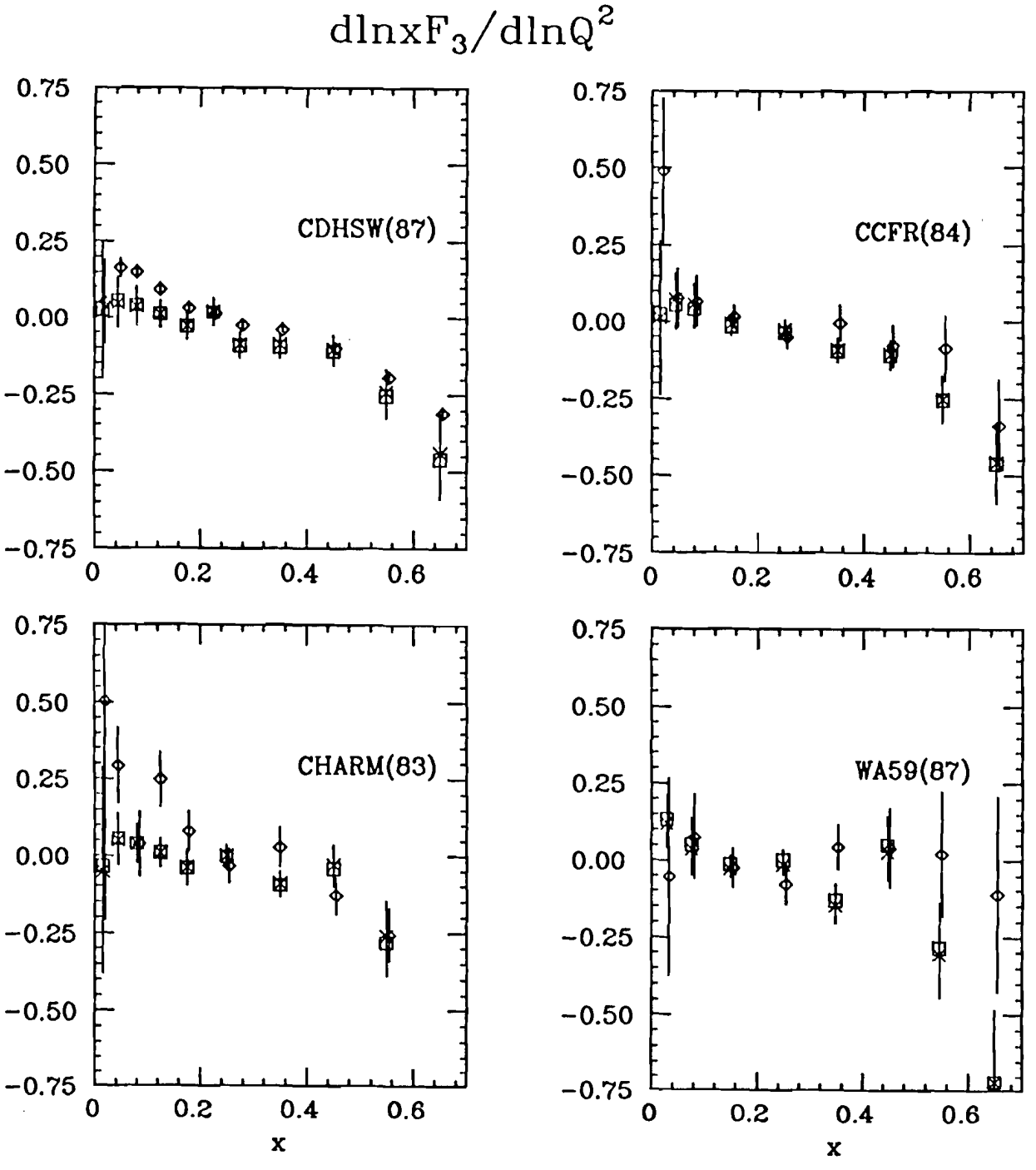
dlnxF3/dlnQ2
CDHSW(87)
CCFR(84)
CHARM(83)
WA59(87)
0.75
0.50
0.25
0.00
-0.25
-0.50
-0.75
0
0.2
0.4
0.6
x

Figure 6.8

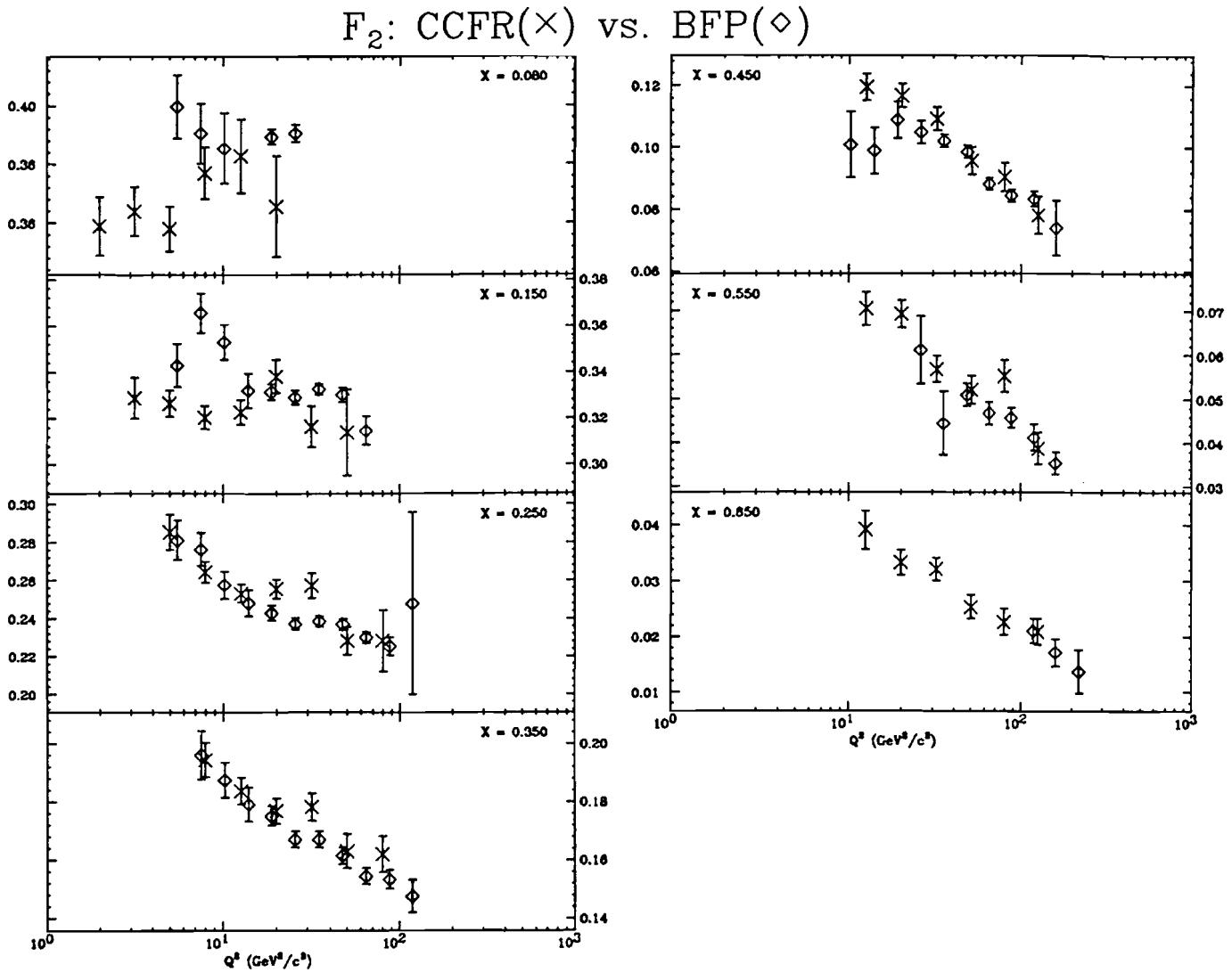
F2: CCFR(×) vs. BFP(◇)
X = 0.080
X = 0.150
X = 0.250
X = 0.350
X = 0.450
X = 0.550
X = 0.850
Q² (GeV²/c²)

Figure 6.9

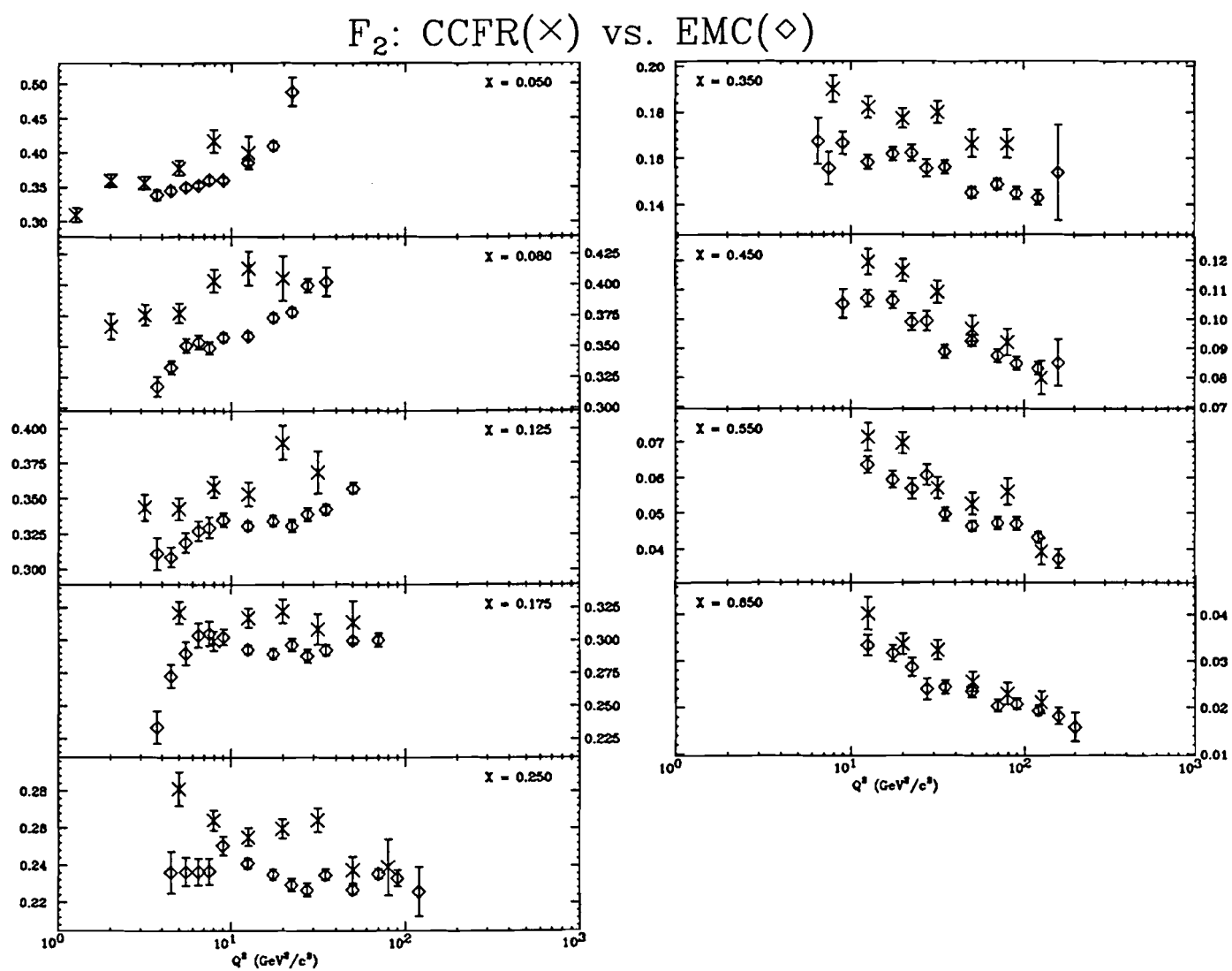
F2: CCFR(×) vs. EMC(◇)
X = 0.050
X = 0.080
X = 0.125
X = 0.175
X = 0.250
X = 0.350
X = 0.450
X = 0.550
X = 0.650
Q² (GeV²/c²)

Figure 6.10

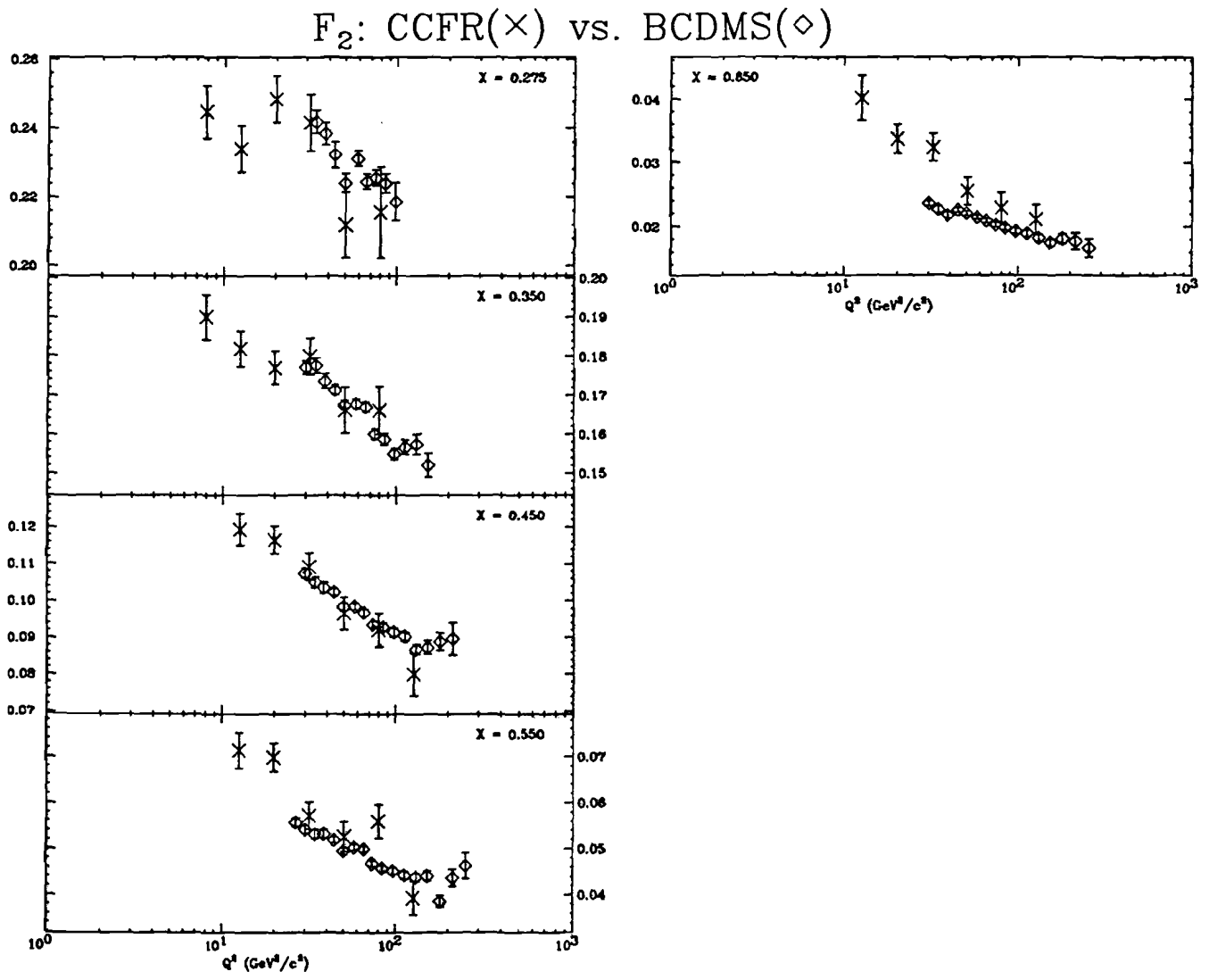

Figure 6.11

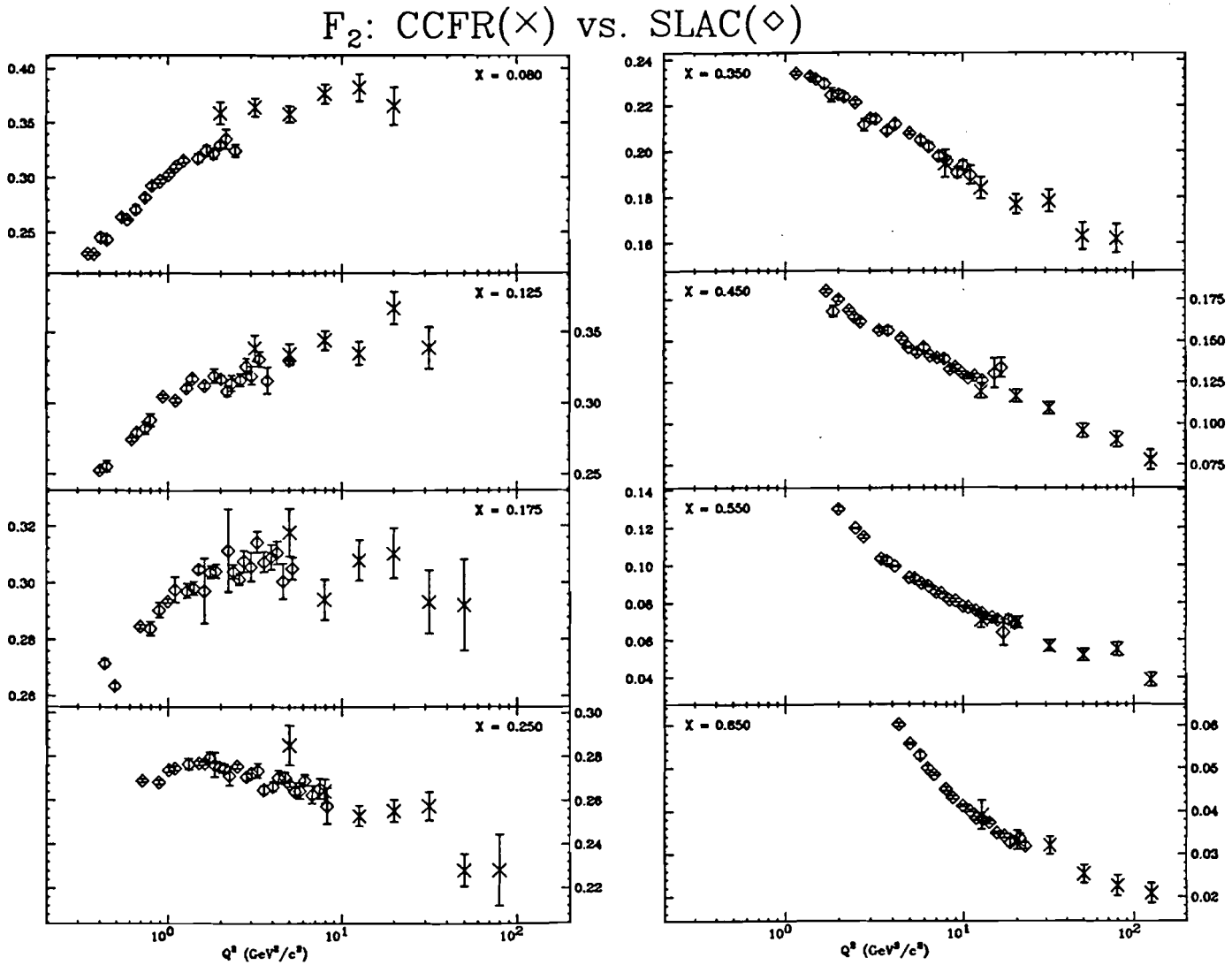
F2: CCFR(×) vs. SLAC(◇)
X = 0.080
X = 0.125
X = 0.175
X = 0.250
X = 0.350
X = 0.450
X = 0.550
X = 0.650
Q² (GeV²/c²)
Q² (GeV²/c²)

Figure 6.12

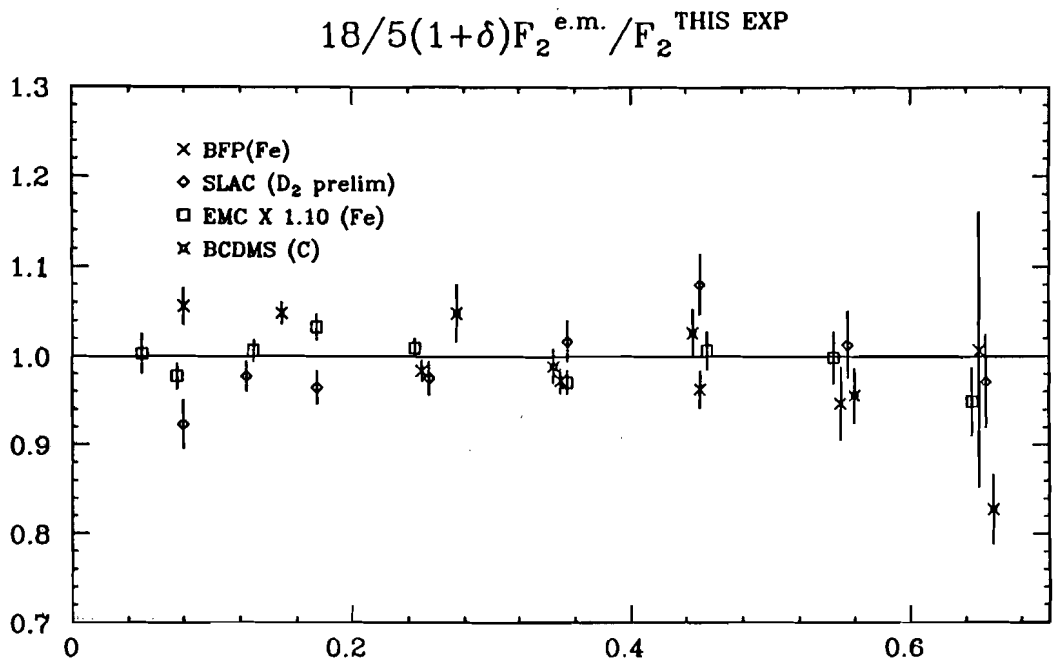

Figure 6.13

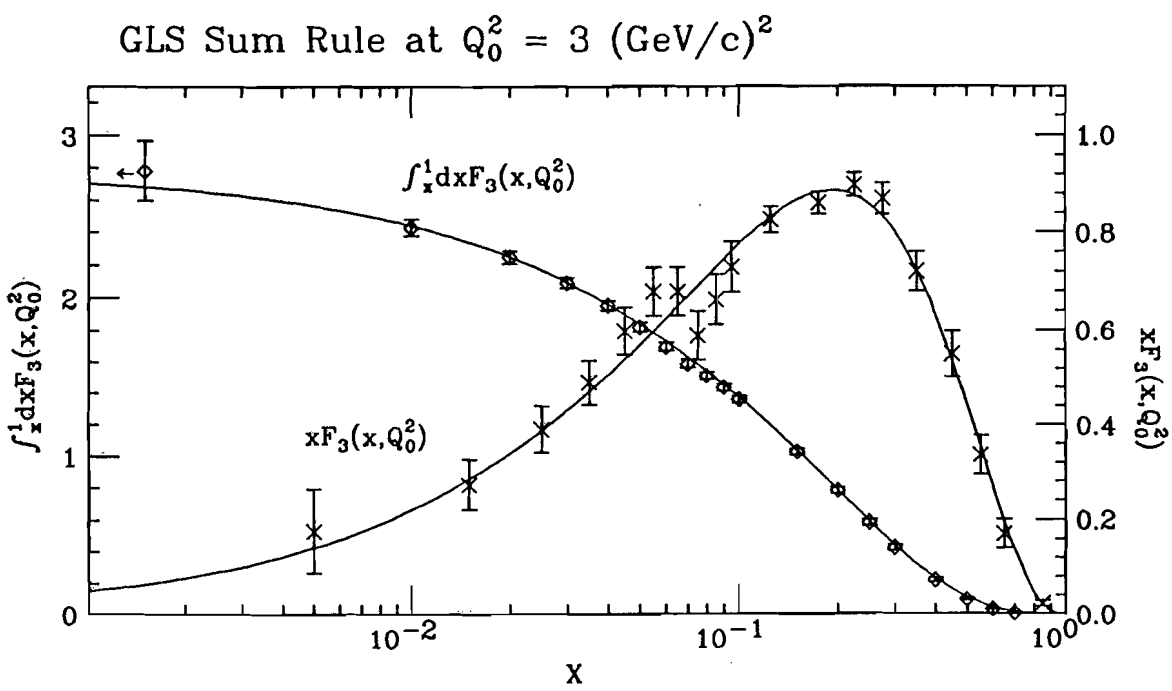

Figure 6.14

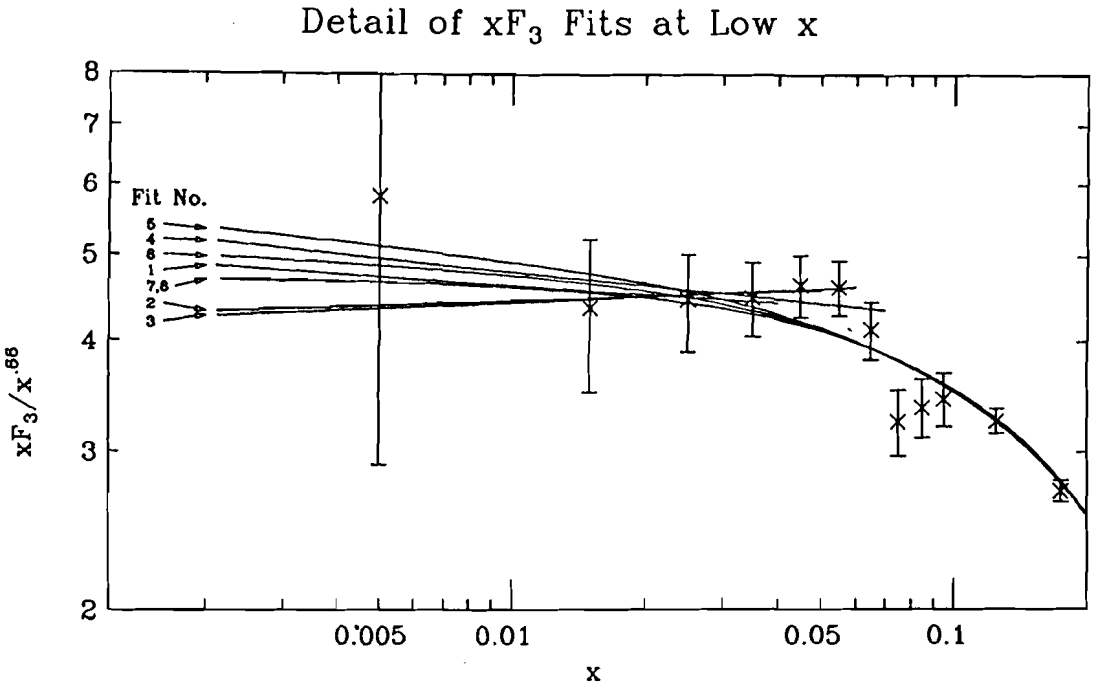
Detail of xF_3 Fits at Low x
Fit No.
5
4
6
1
7,8
2
3
8
7
6
5
4
3
2
$xF_3/x^{.66}$
0.005
0.01
0.05
0.1
x

Figure 6.15

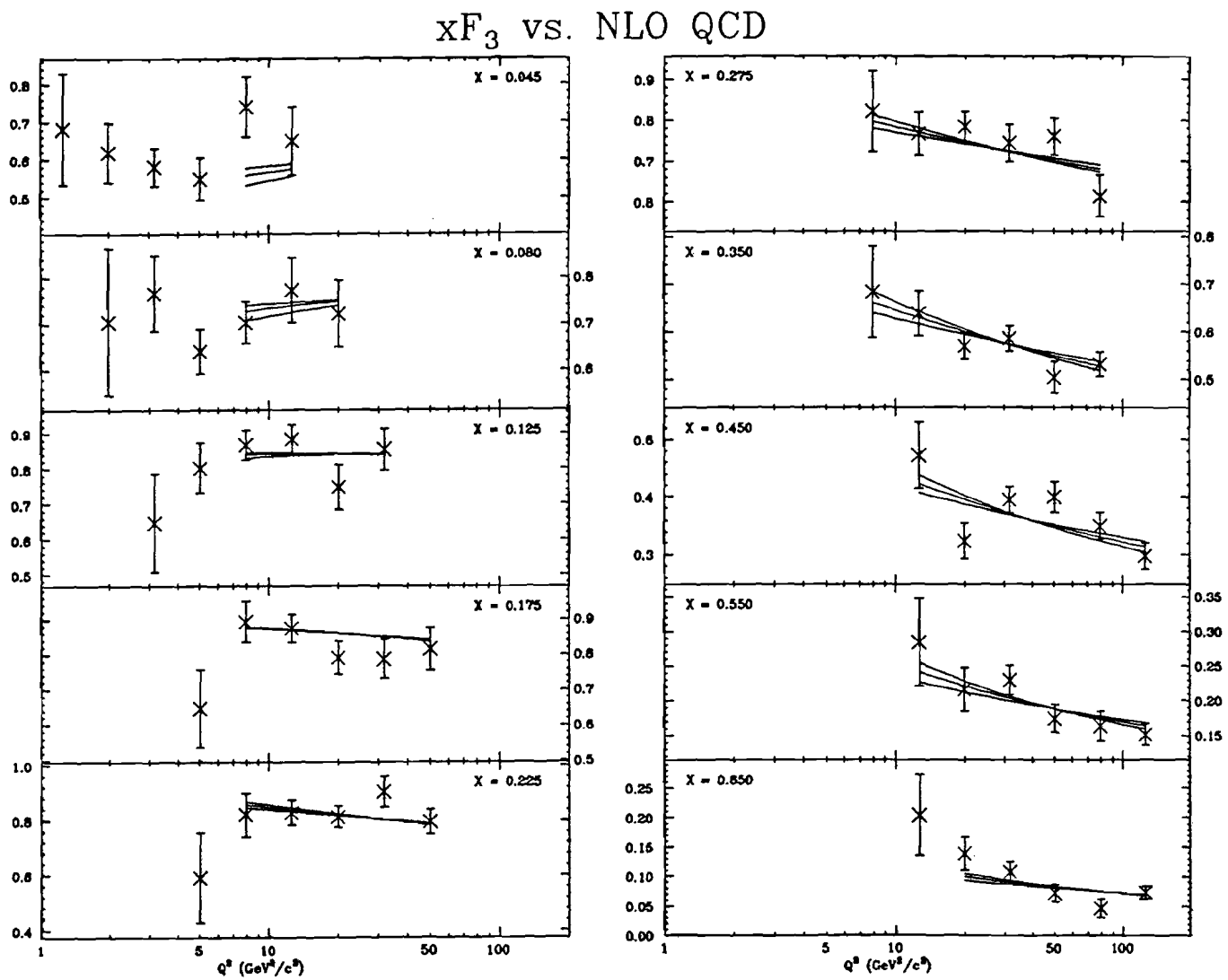
xF3 vs. NLO QCD
X = 0.045
X = 0.080
X = 0.125
X = 0.175
X = 0.225
X = 0.275
X = 0.350
X = 0.450
X = 0.550
X = 0.650
Q² (GeV²/c²)
Q² (GeV²/c²)

Figure 6.16

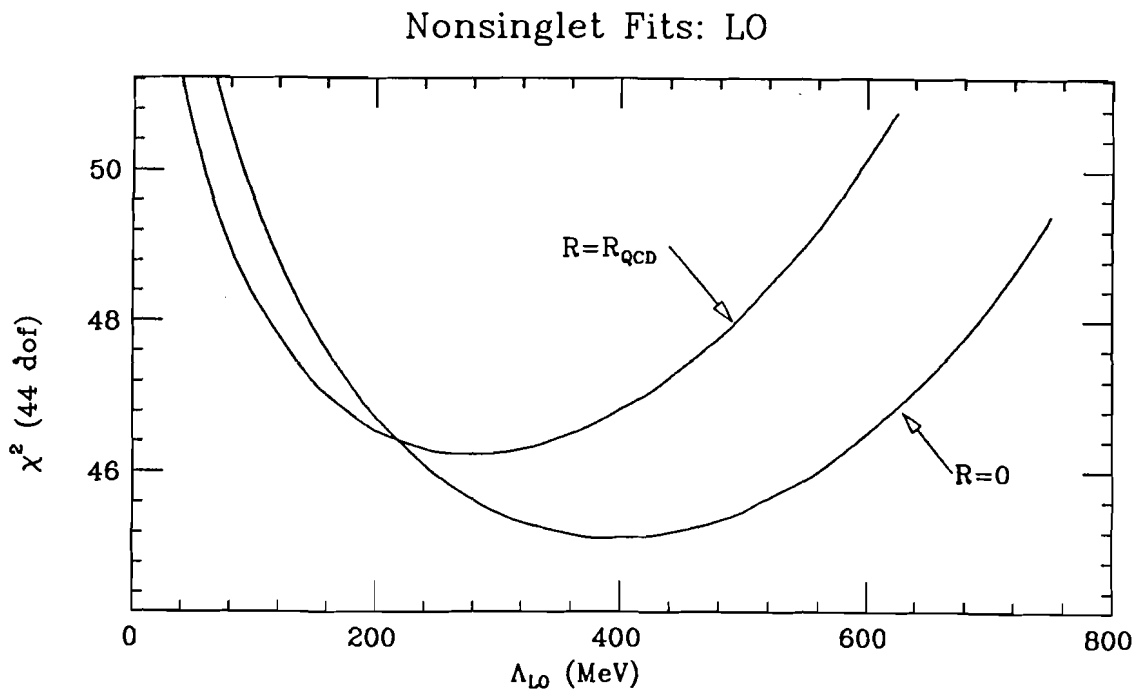

Figure 6.17a

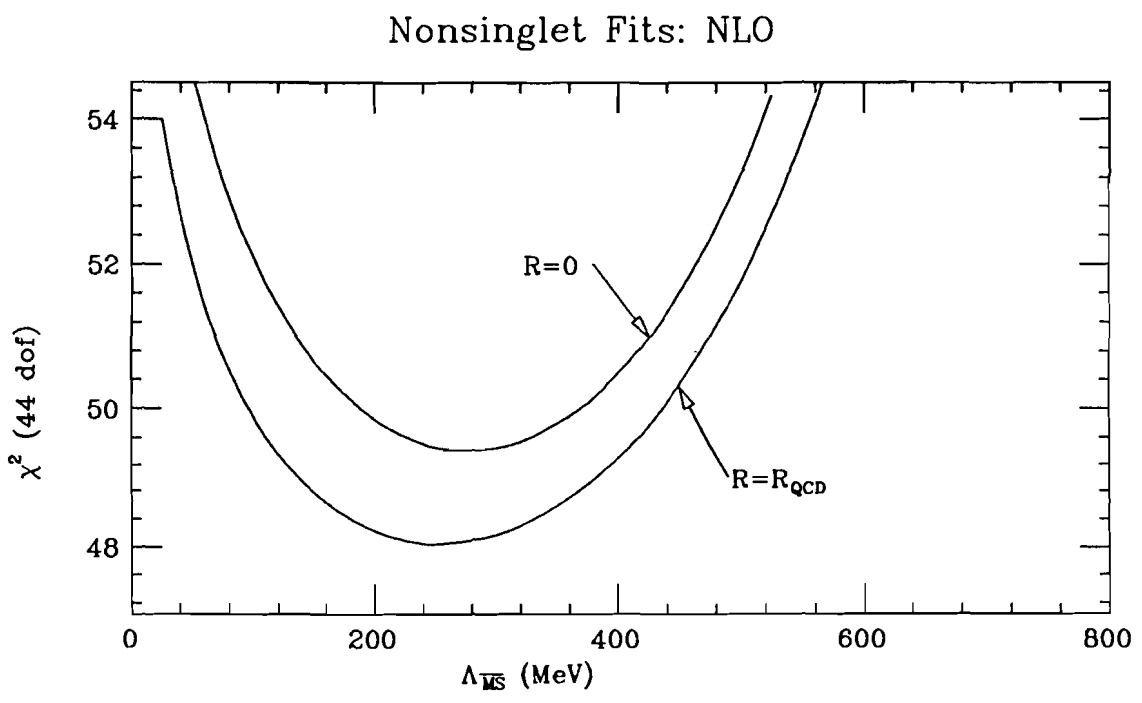

Figure 6.17b

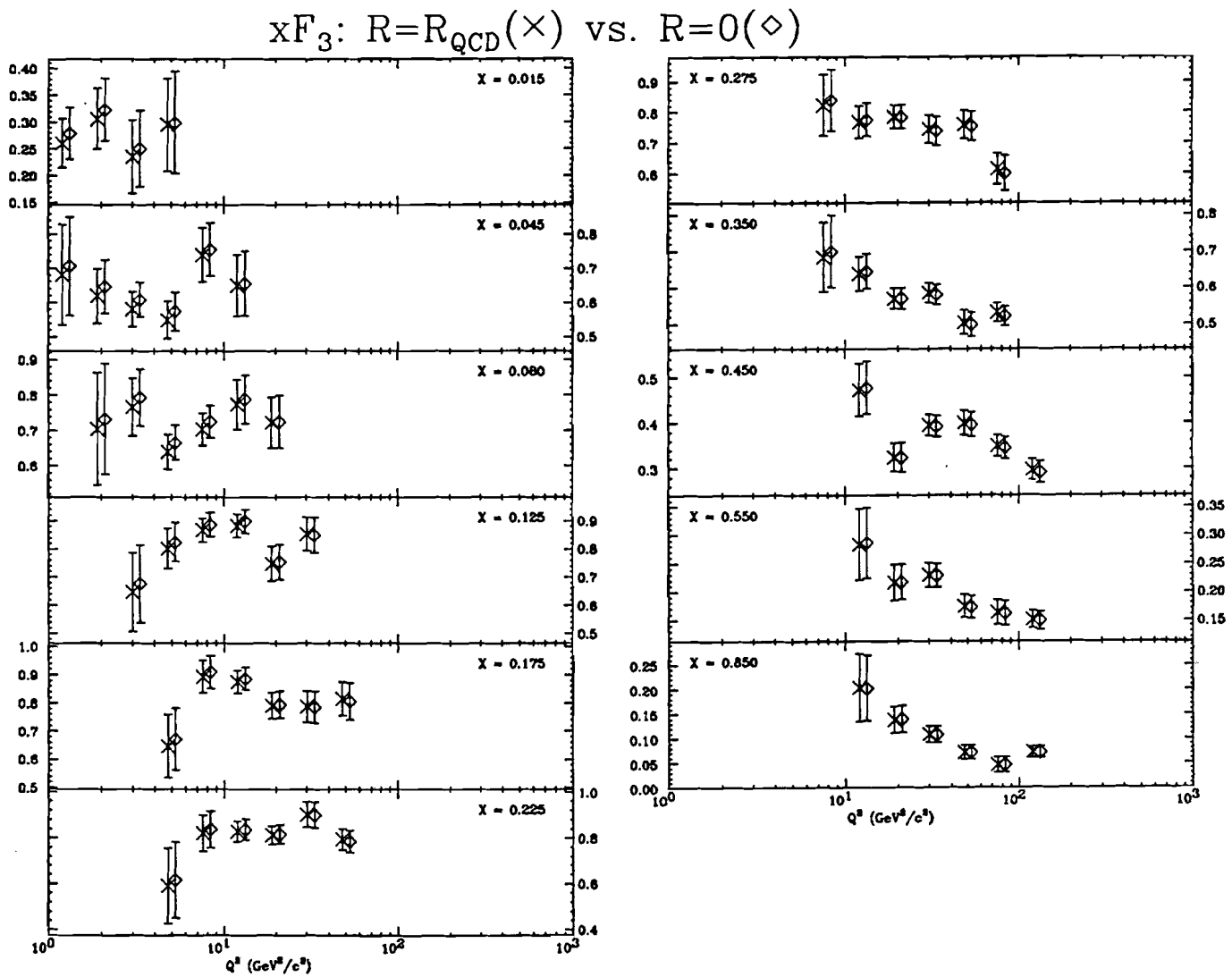
xF3: R=RQCD(×) vs. R=0(◇)
X = 0.015
X = 0.045
X = 0.080
X = 0.125
X = 0.175
X = 0.225
X = 0.275
X = 0.350
X = 0.450
X = 0.550
X = 0.850
Q² (GeV²/c²)
Q² (GeV²/c²)

Figure 6.18

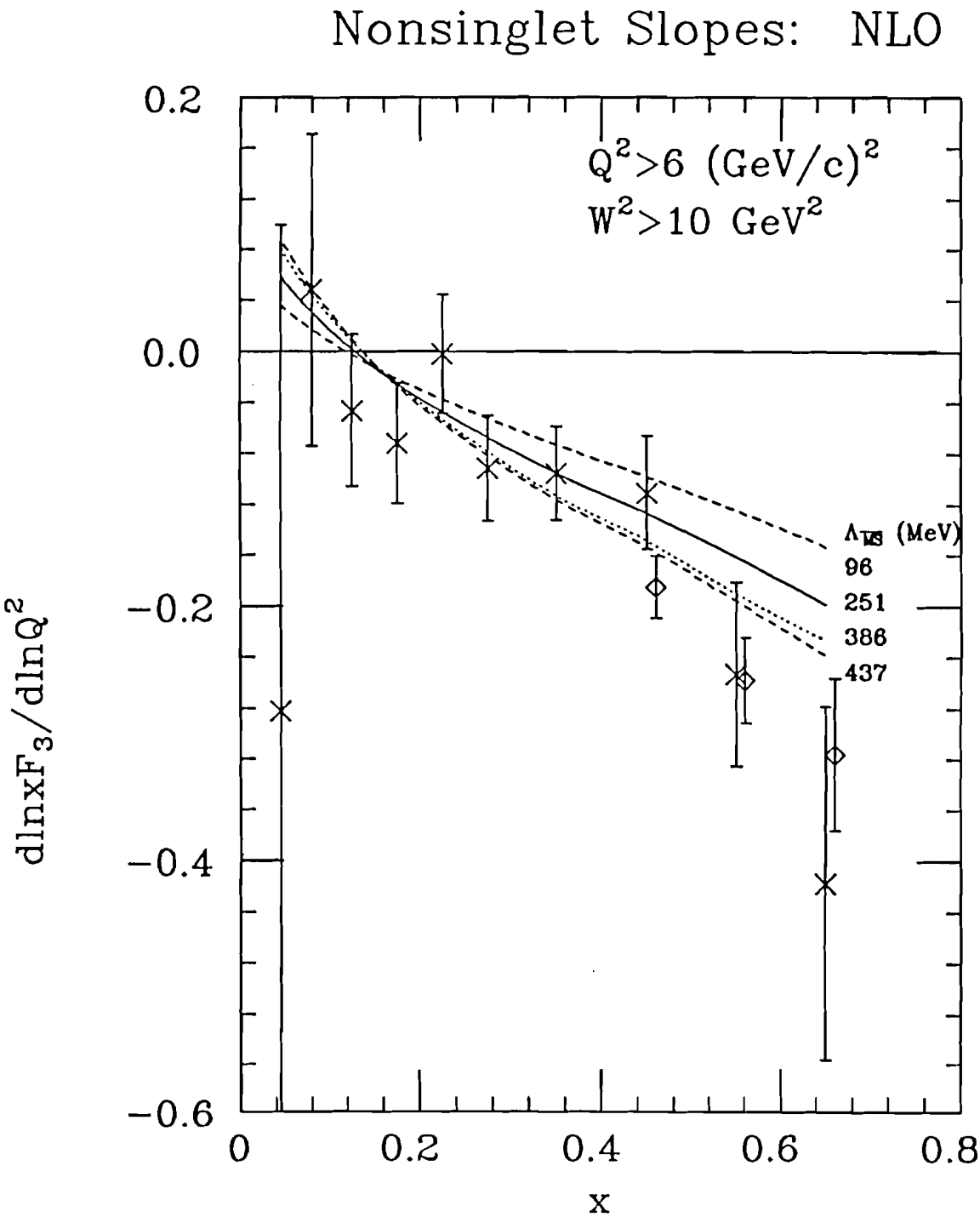
Nonsinglet Slopes: NLO
$Q^2>6$ (GeV/c)^2
$W^2>10$ GeV^2
$\Lambda_{\overline{MS}}$ (MeV)
96
251
386
437
0.2
0.0
−0.2
−0.4
−0.6
0
0.2
0.4
0.6
0.8
x
$d\ln xF_3/d\ln Q^2$

Figure 6.19

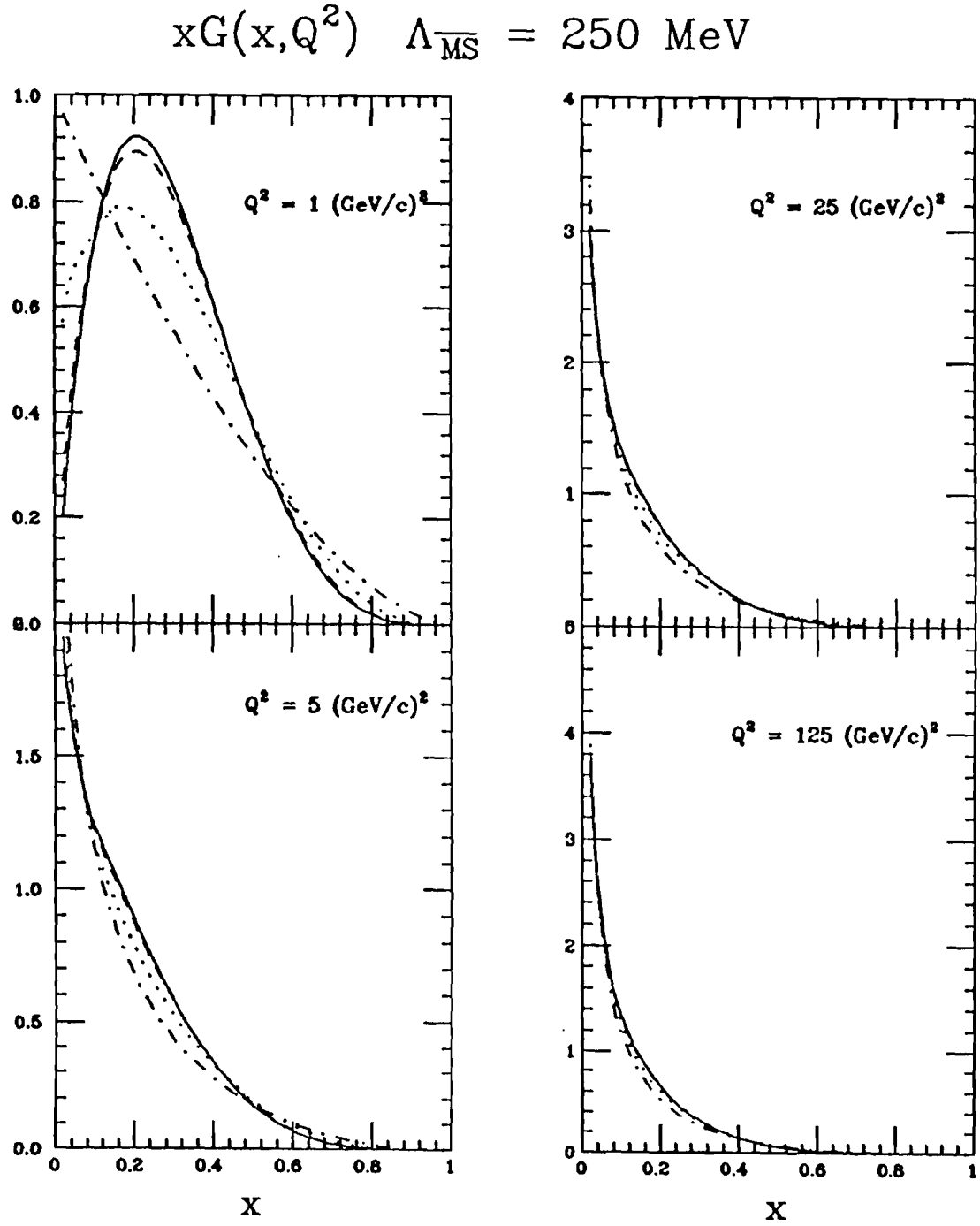
xG(x,Q²) Λ_MS = 250 MeV
Q² = 1 (GeV/c)²
Q² = 25 (GeV/c)²
Q² = 5 (GeV/c)²
Q² = 125 (GeV/c)²
X
X

Figure 6.20

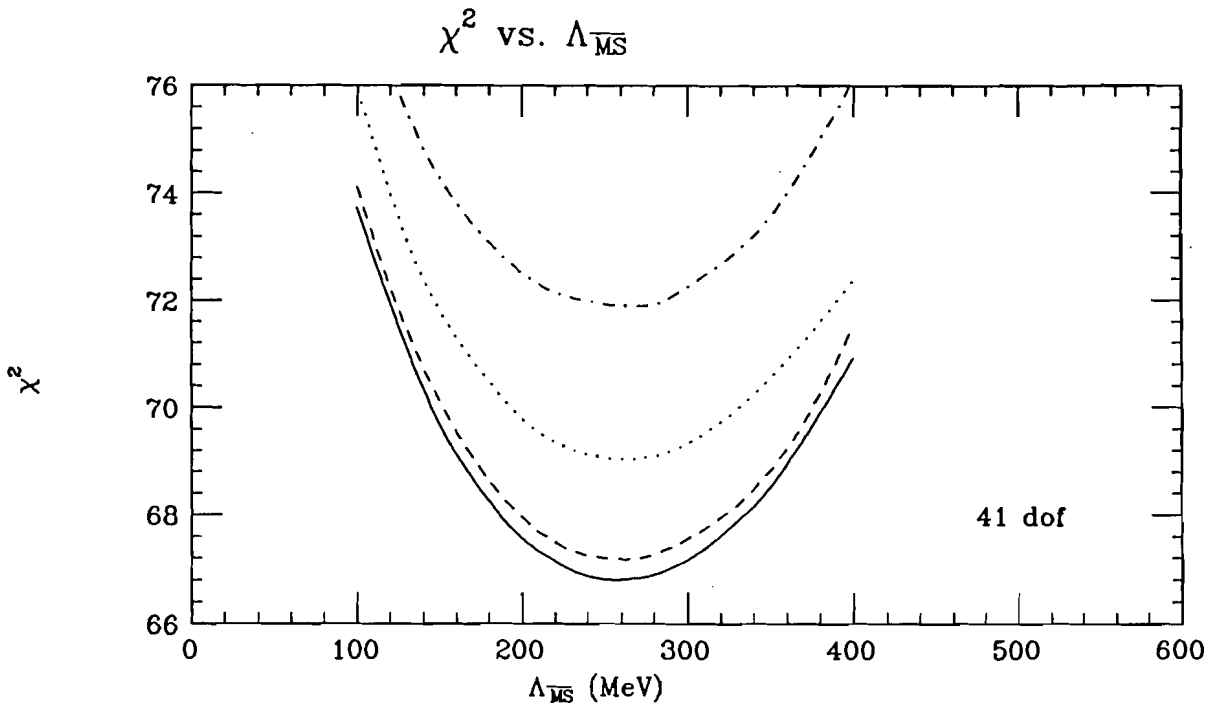

Figure 6.21

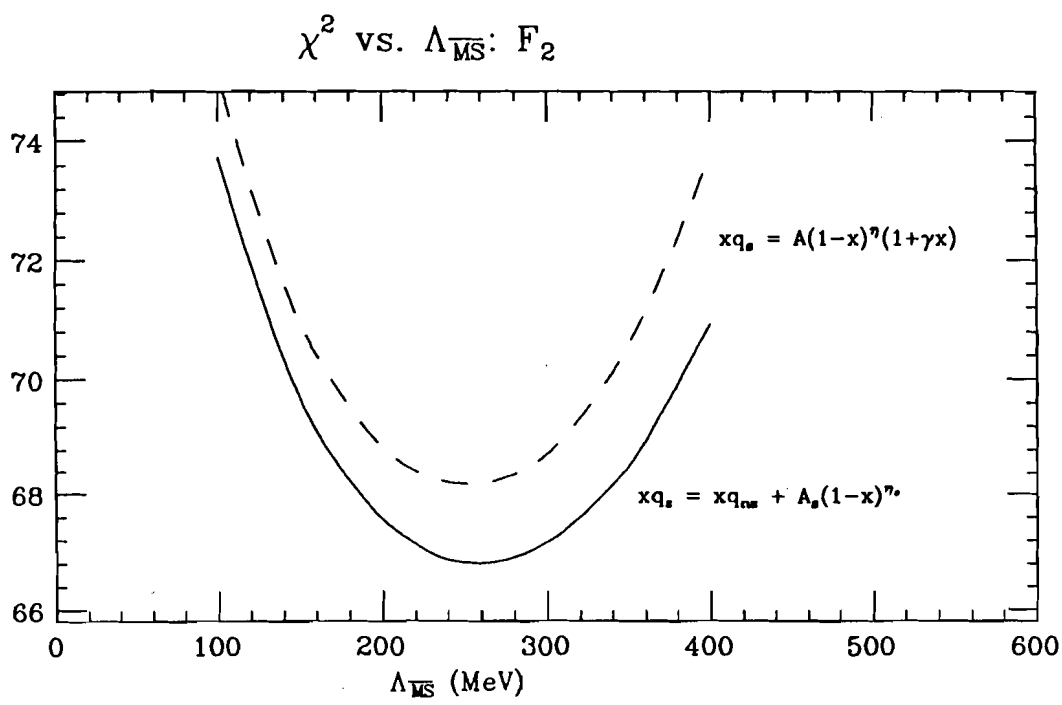

Figure 6.22

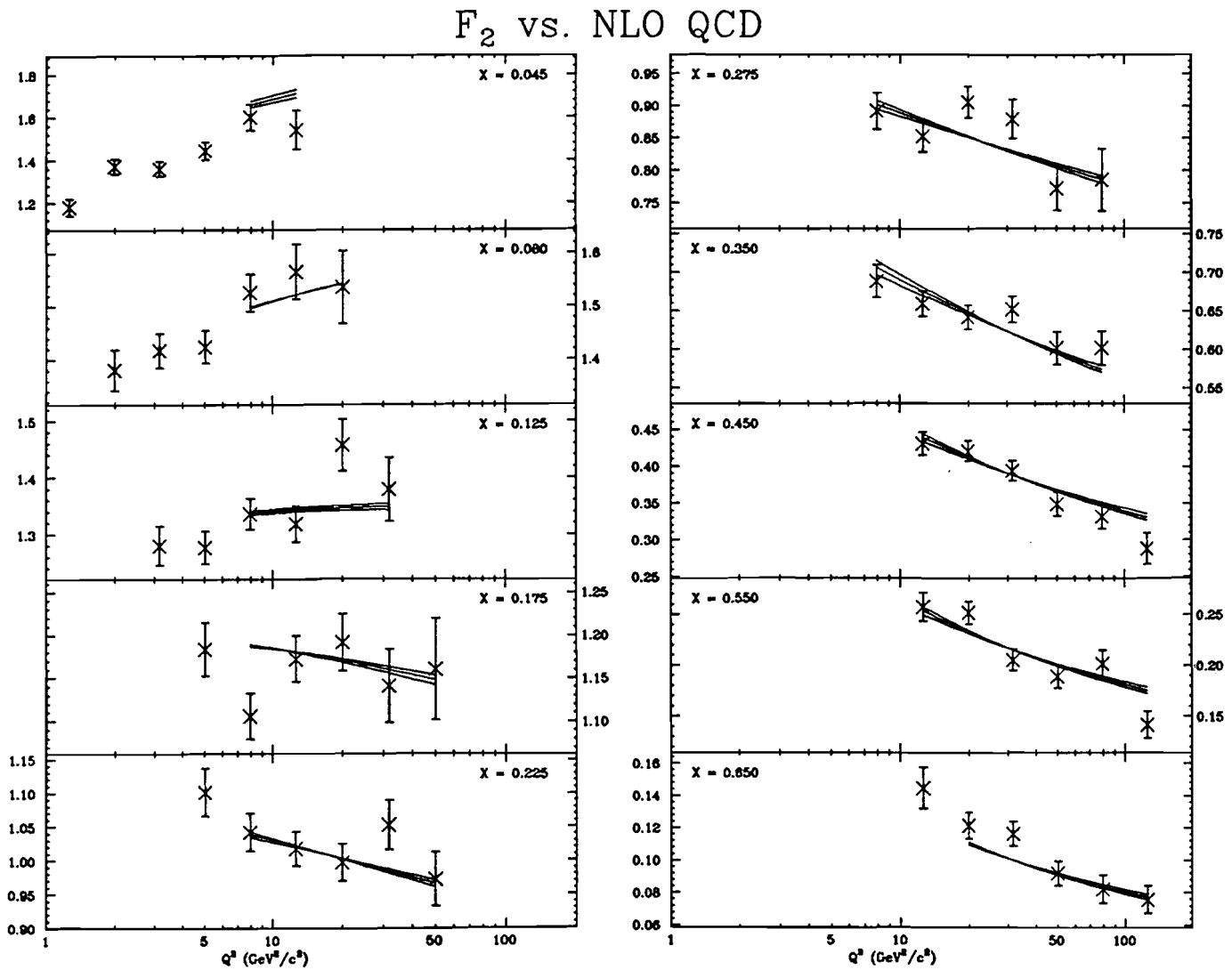
F2 vs. NLO QCD
X = 0.045
X = 0.080
X = 0.125
X = 0.175
X = 0.225
X = 0.275
X = 0.350
X = 0.450
X = 0.550
X = 0.650
Q² (GeV²/c²)
Q² (GeV²/c²)

Figure 6.23

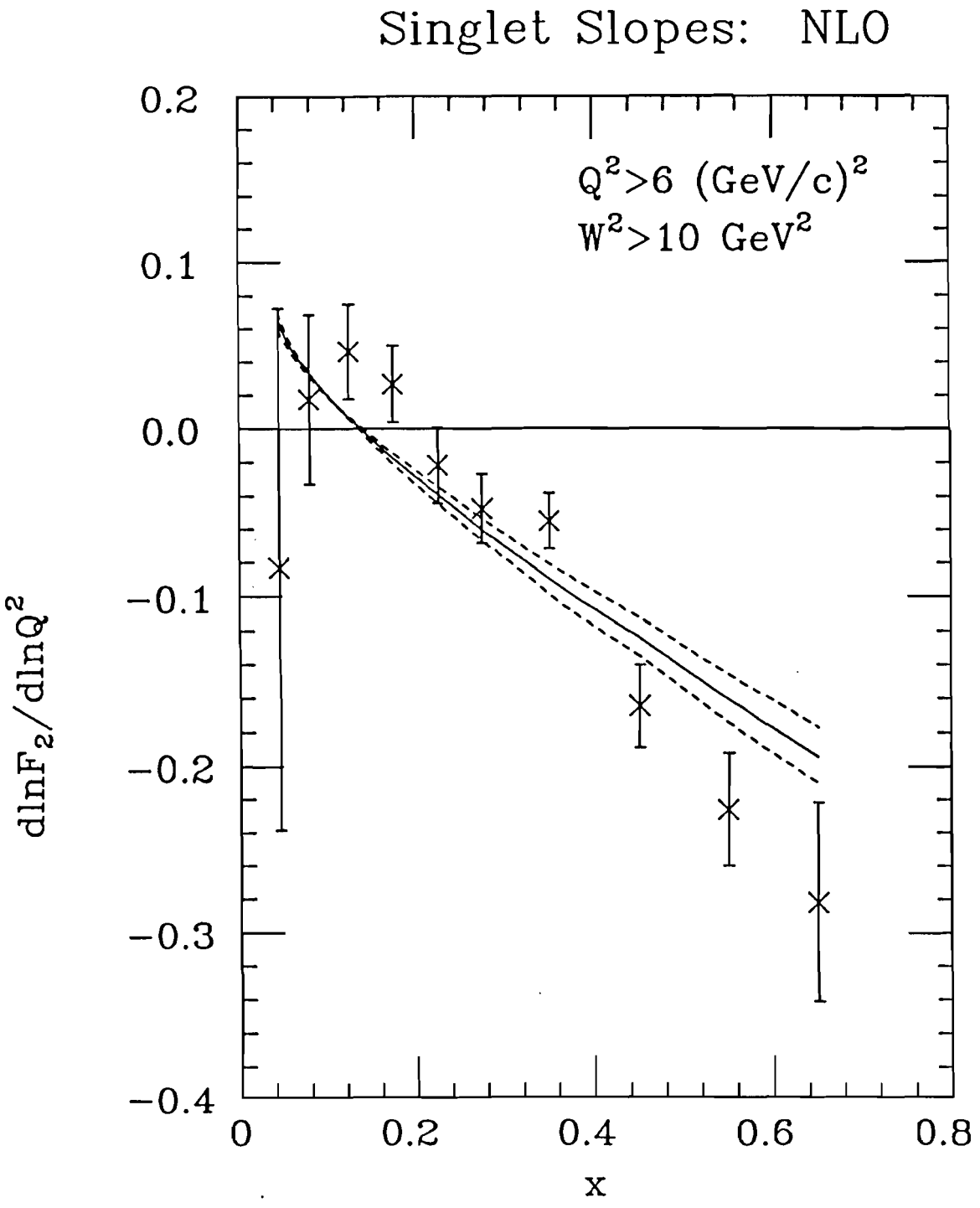
Singlet Slopes: NLO
$Q^2>6$ (GeV/c)^2
$W^2>10$ GeV^2
0.2
0.1
0.0
−0.1
−0.2
−0.3
−0.4
$d\ln F_2/d\ln Q^2$
0
0.2
0.4
0.6
0.8
x

Figure 6.24

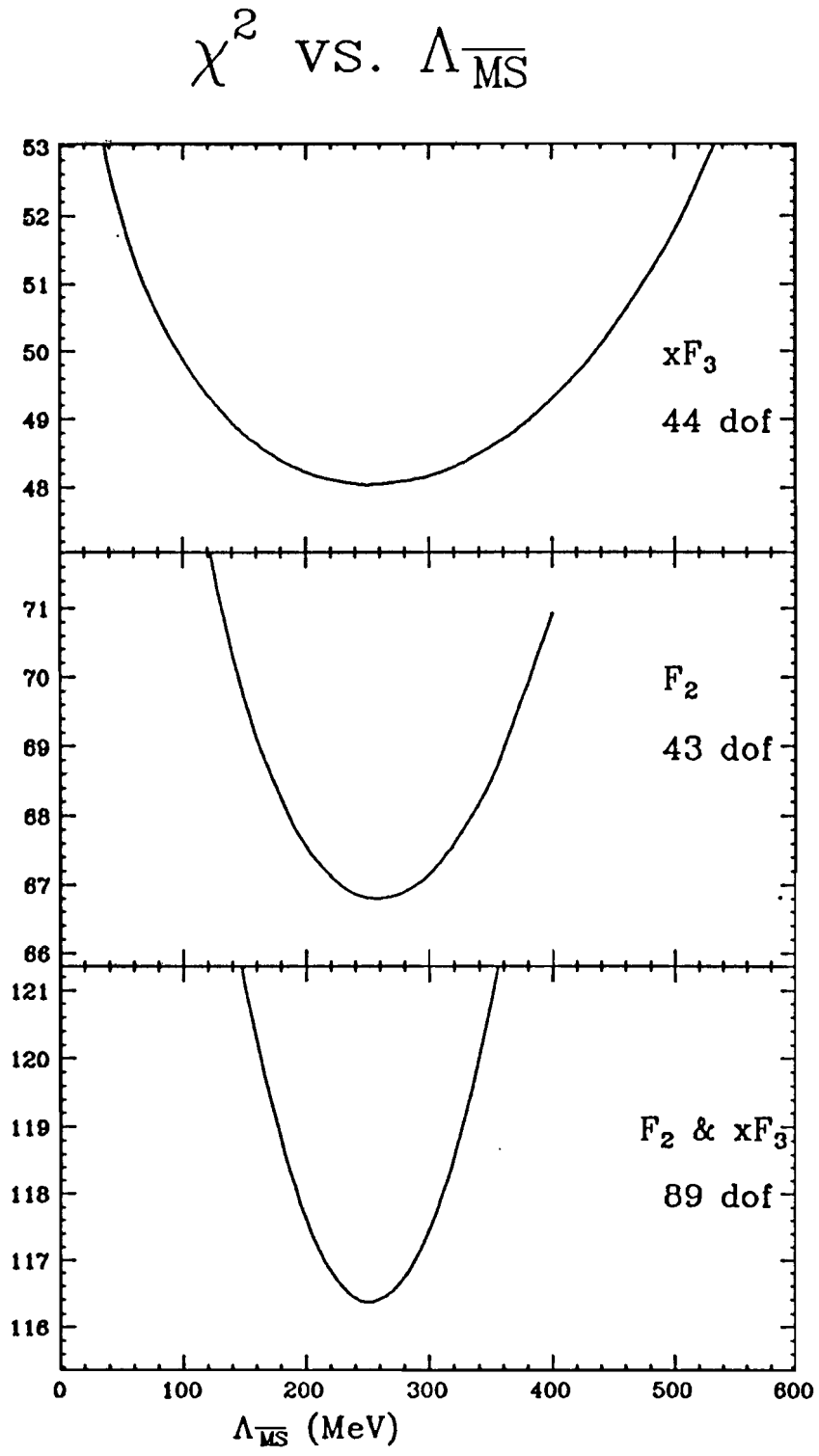
χ^2 vs. $\Lambda_{\overline{MS}}$
53
52
51
50
49
48
xF_3
44 dof
71
70
69
68
67
66
F_2
43 dof
121
120
119
118
117
116
F_2 & xF_3
89 dof
0
100
200
300
400
500
600
$\Lambda_{\overline{MS}}$ (MeV)

Figure 6.25

xF_3 vs. NLO QCD

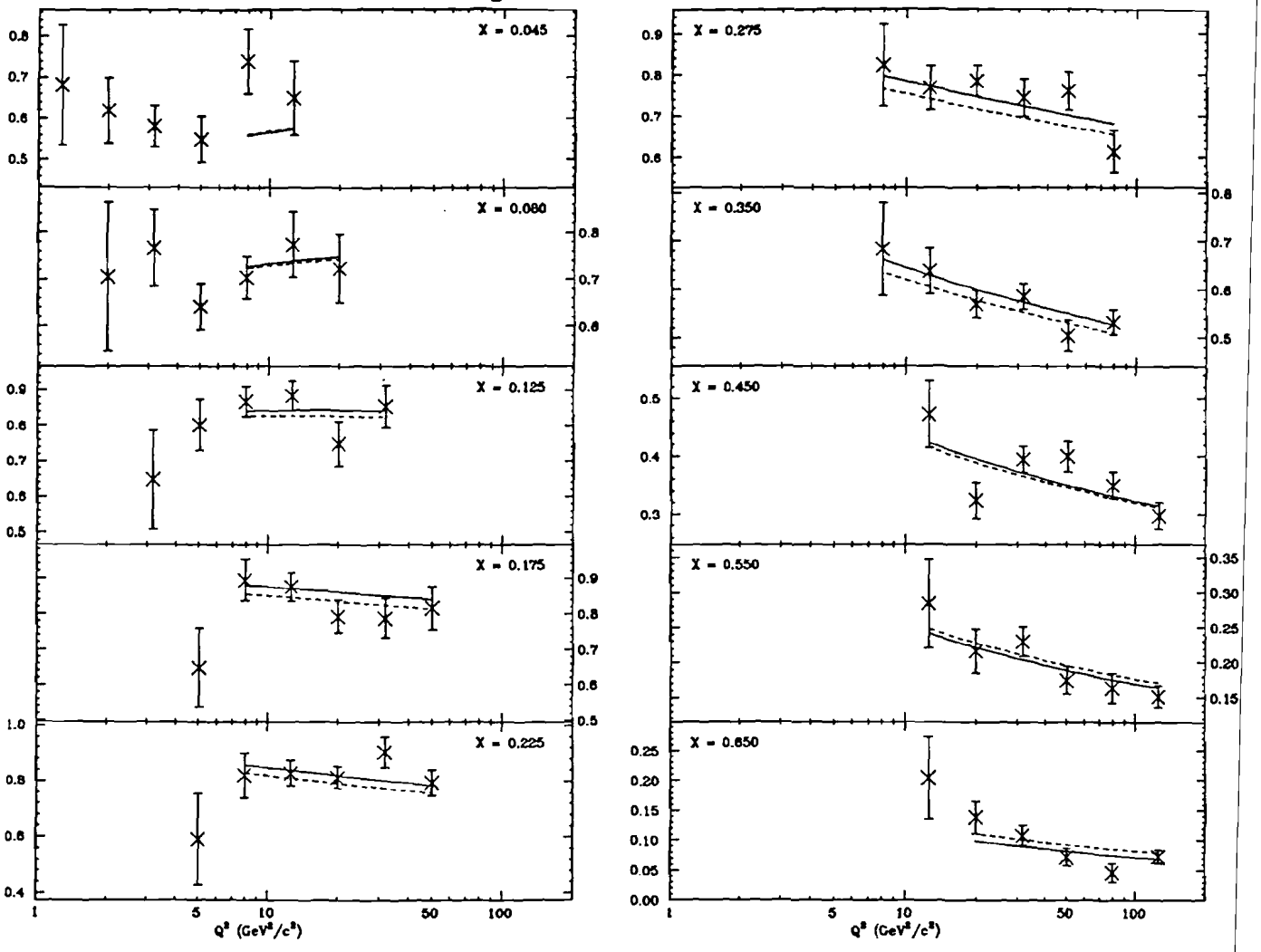

Figure 6.26

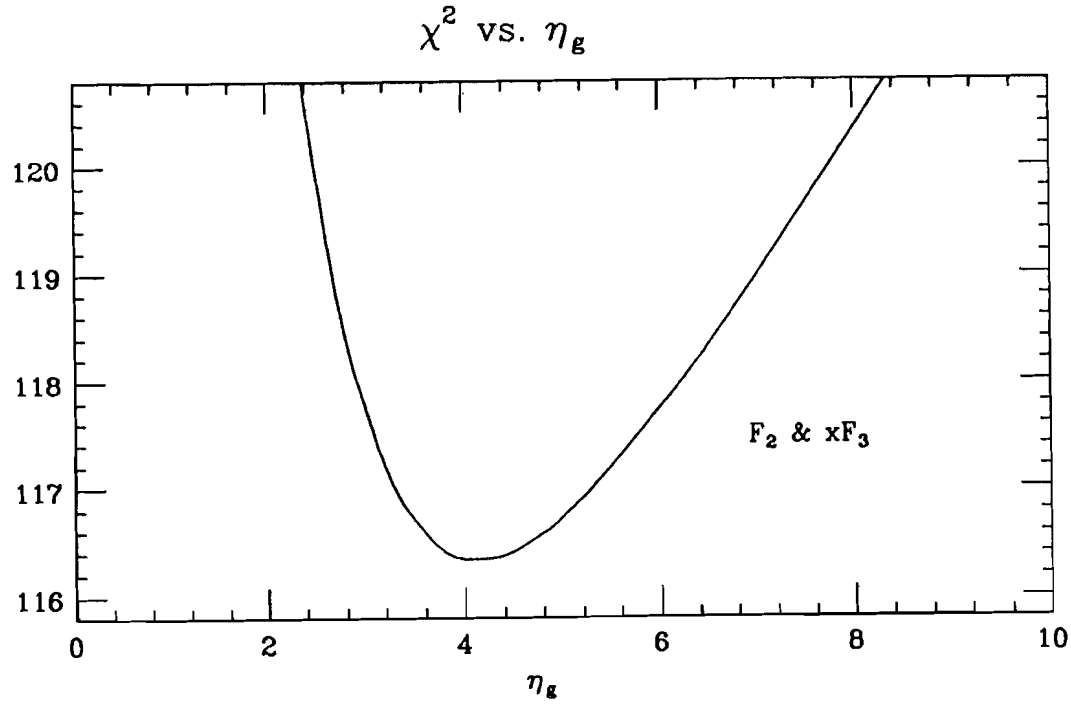

Figure 6.27a

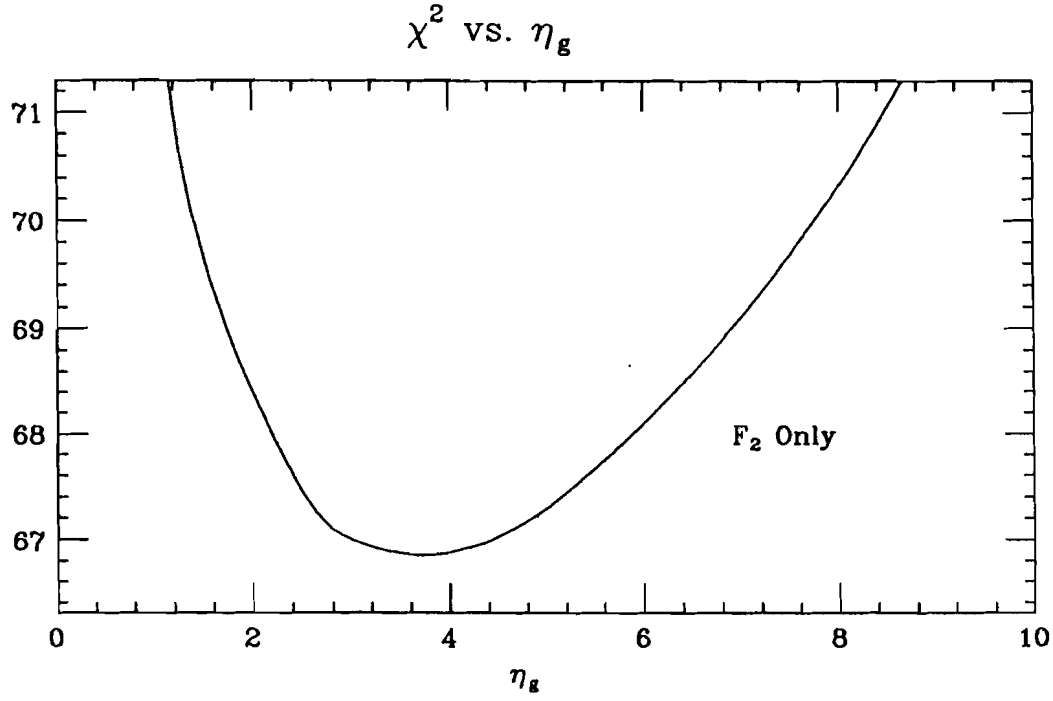

Figure 6.27b

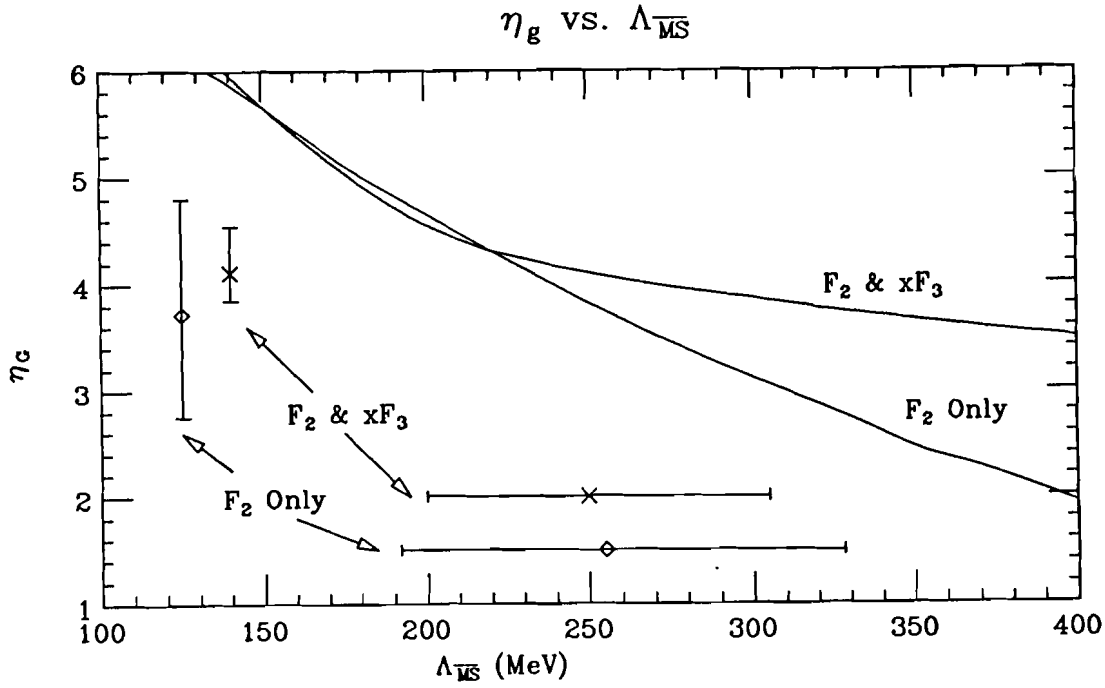

Figure 6.28

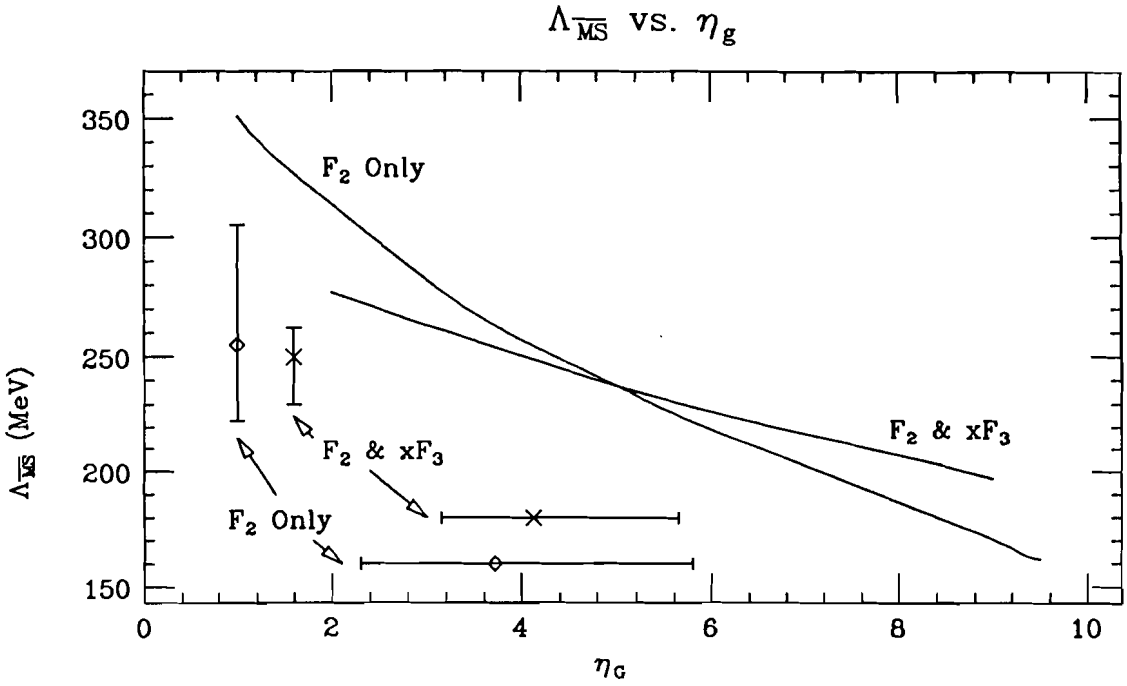

Figure 6.29

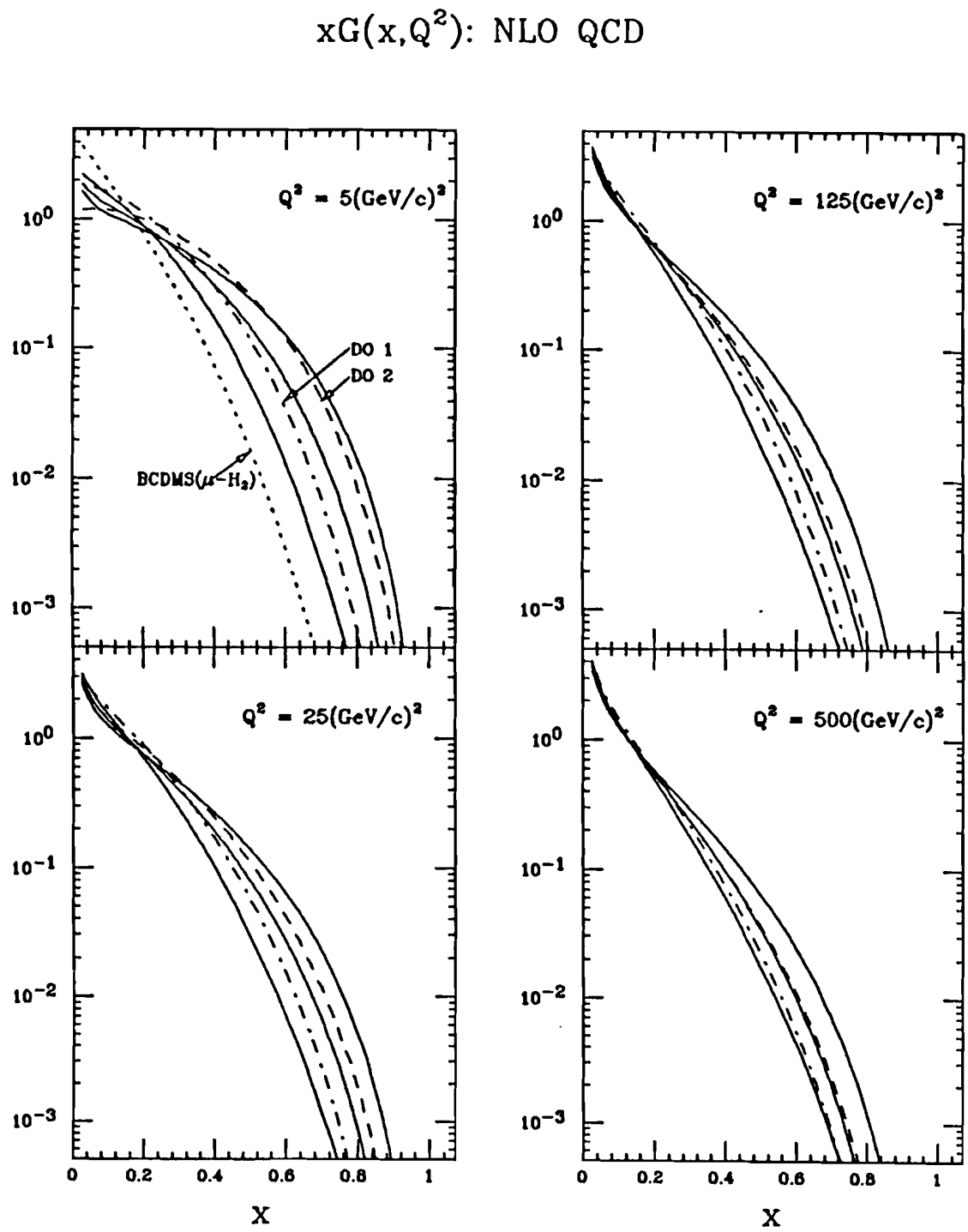
xG(x,Q²): NLO QCD
Q² = 5(GeV/c)²
Q² = 125(GeV/c)²
Q² = 25(GeV/c)²
Q² = 500(GeV/c)²
DO 1
DO 2
BCDMS(μ-H₂)
10⁰
10⁻¹
10⁻²
10⁻³
0
0.2
0.4
0.6
0.8
1
X

Figure 6.30

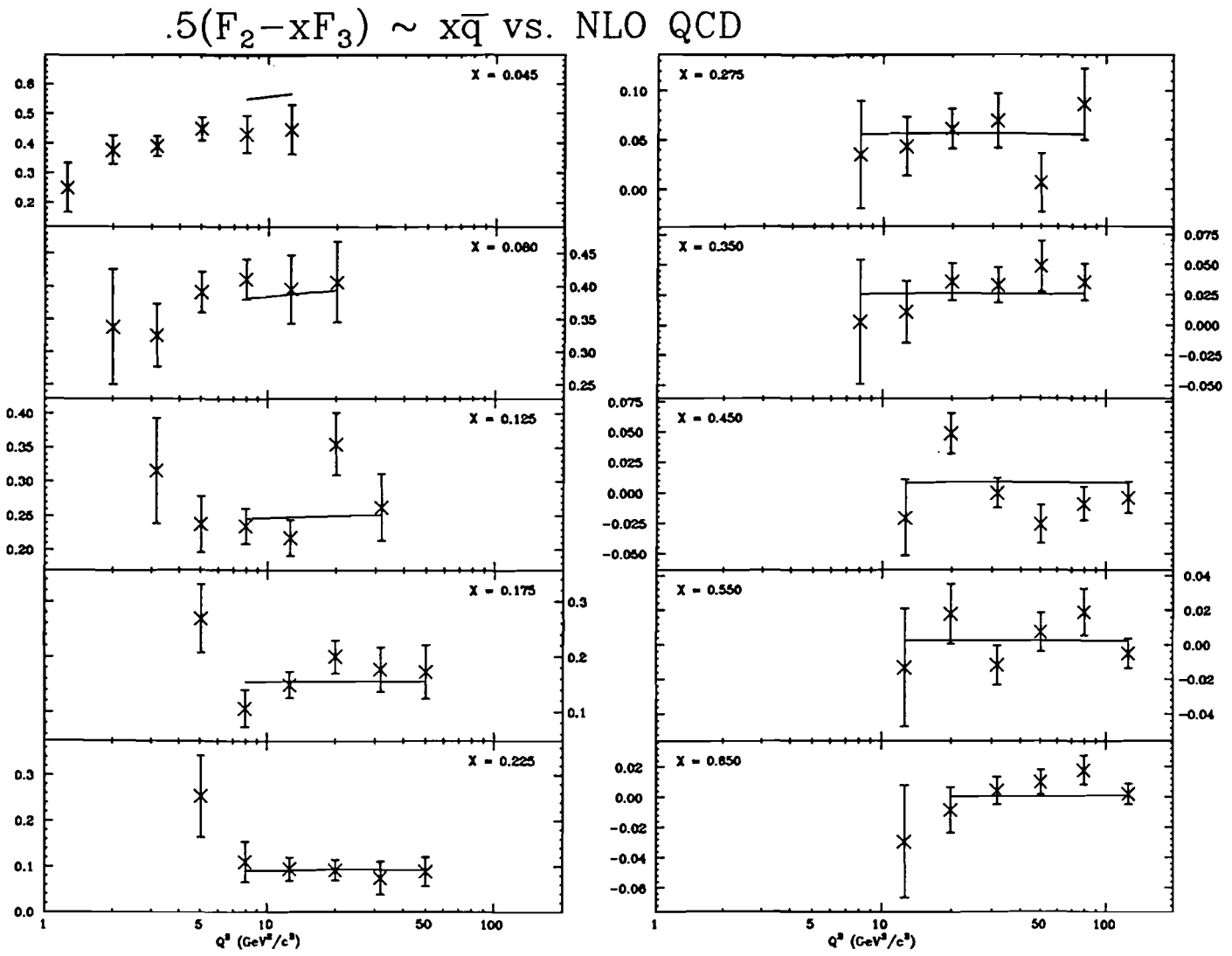
.5(F2−xF3) ~ xq̄ vs. NLO QCD
X = 0.045
X = 0.080
X = 0.125
X = 0.175
X = 0.225
X = 0.275
X = 0.350
X = 0.450
X = 0.550
X = 0.650
Q² (GeV²/c²)
Q² (GeV²/c²)

Figure 6.31

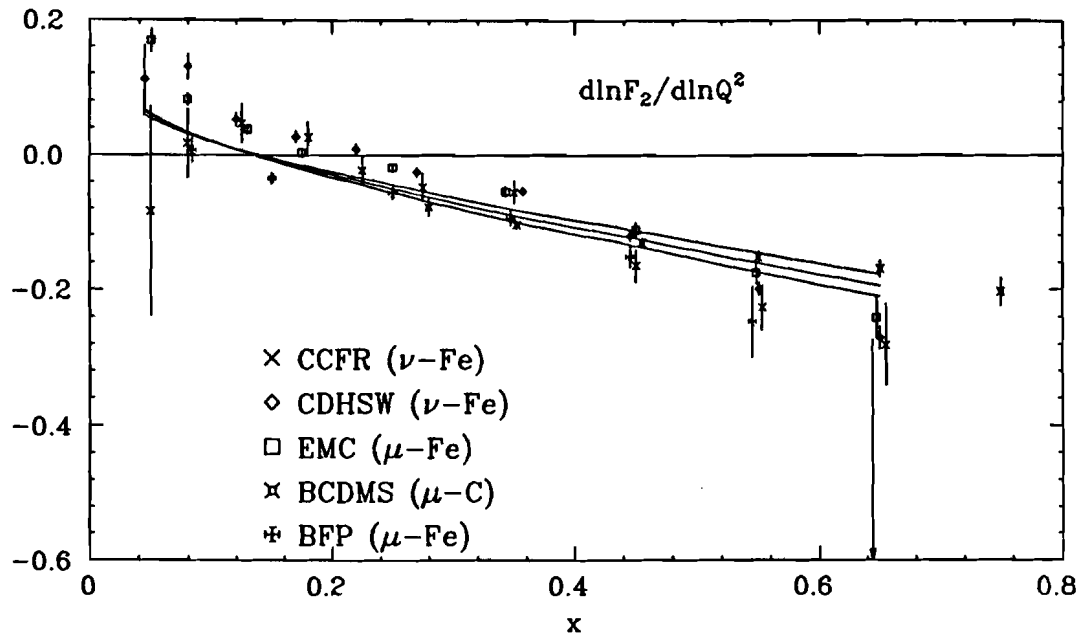

Figure 6.32a

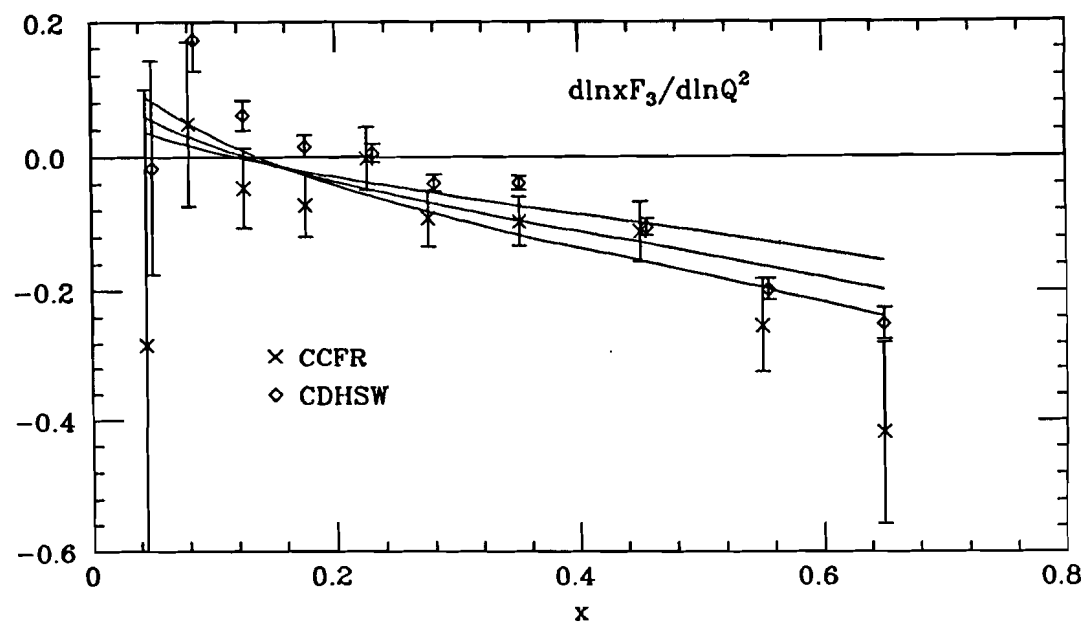

Figure 6.32b

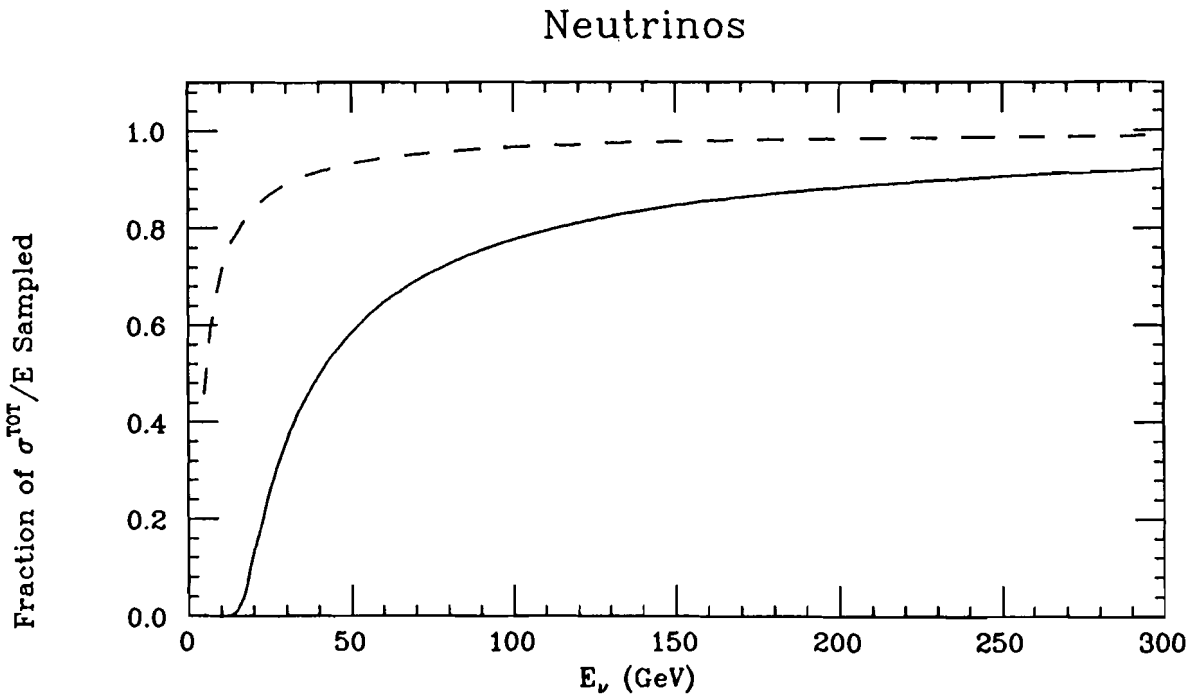

Figure A.1a

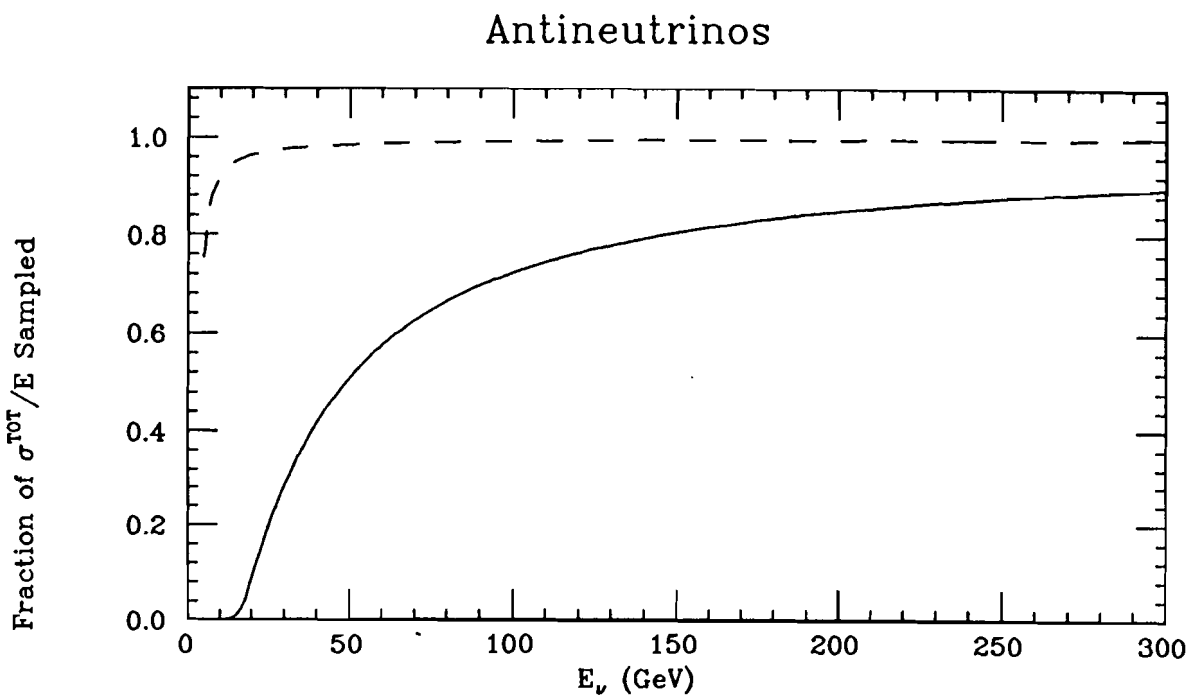

Figure A.1b

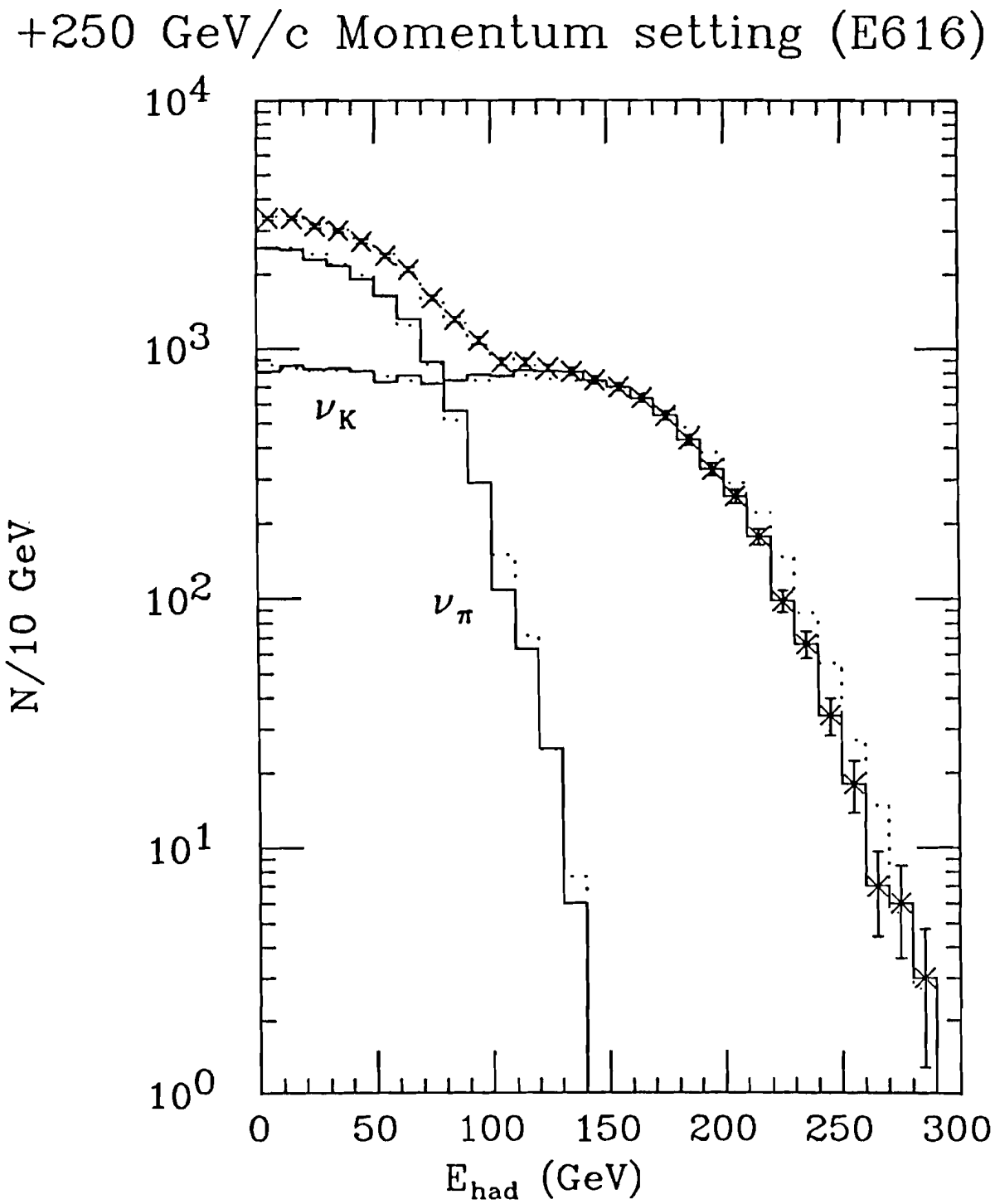
+250 GeV/c Momentum setting (E616)
10^4
10^3
10^2
10^1
10^0
N/10 GeV
ν_K
ν_π
0
50
100
150
200
250
300
E_{had} (GeV)

Figure A.2

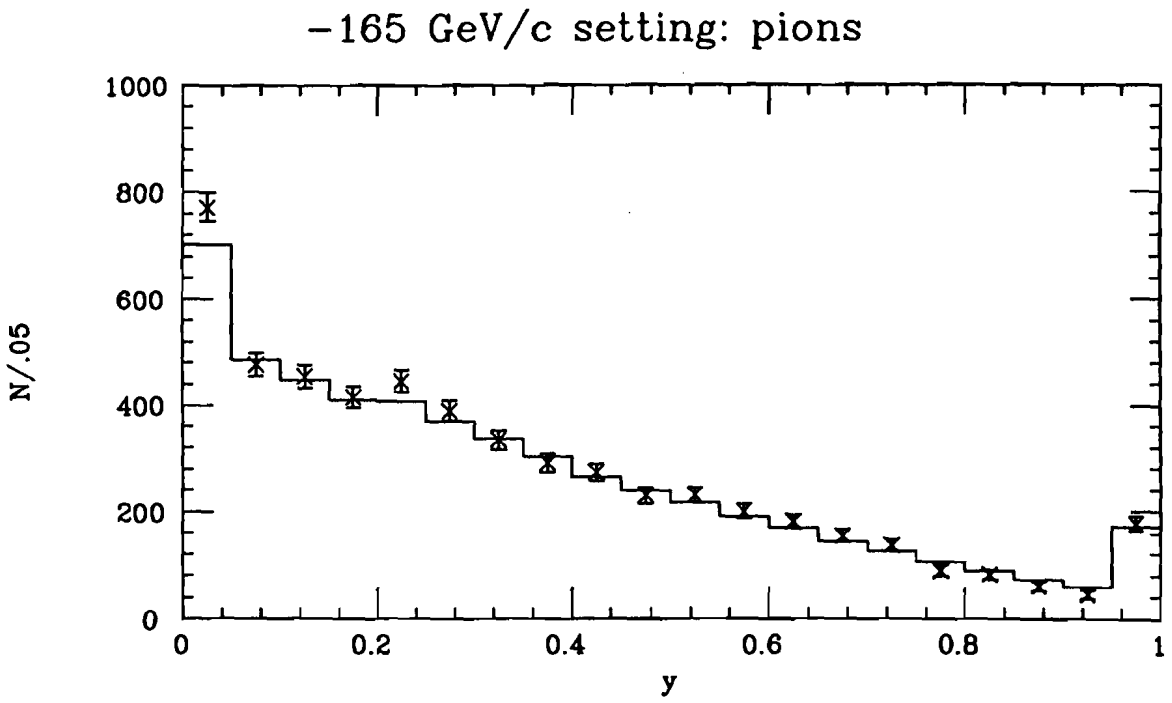

Figure A.3a

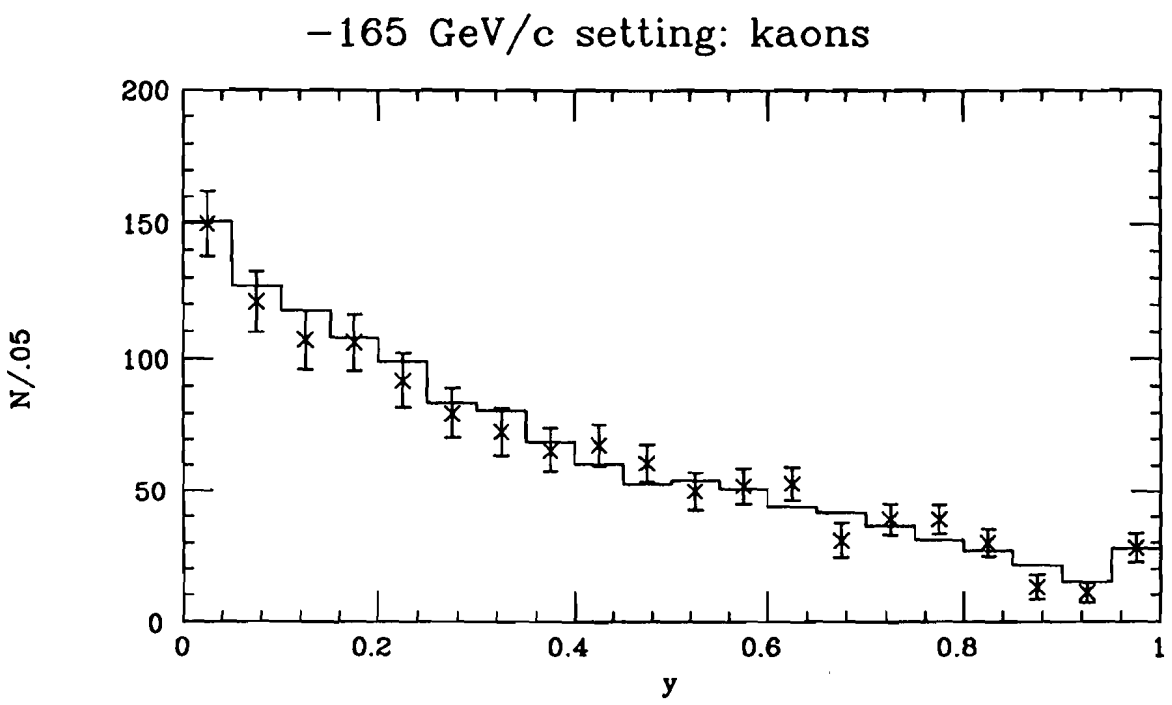

Figure A.3b

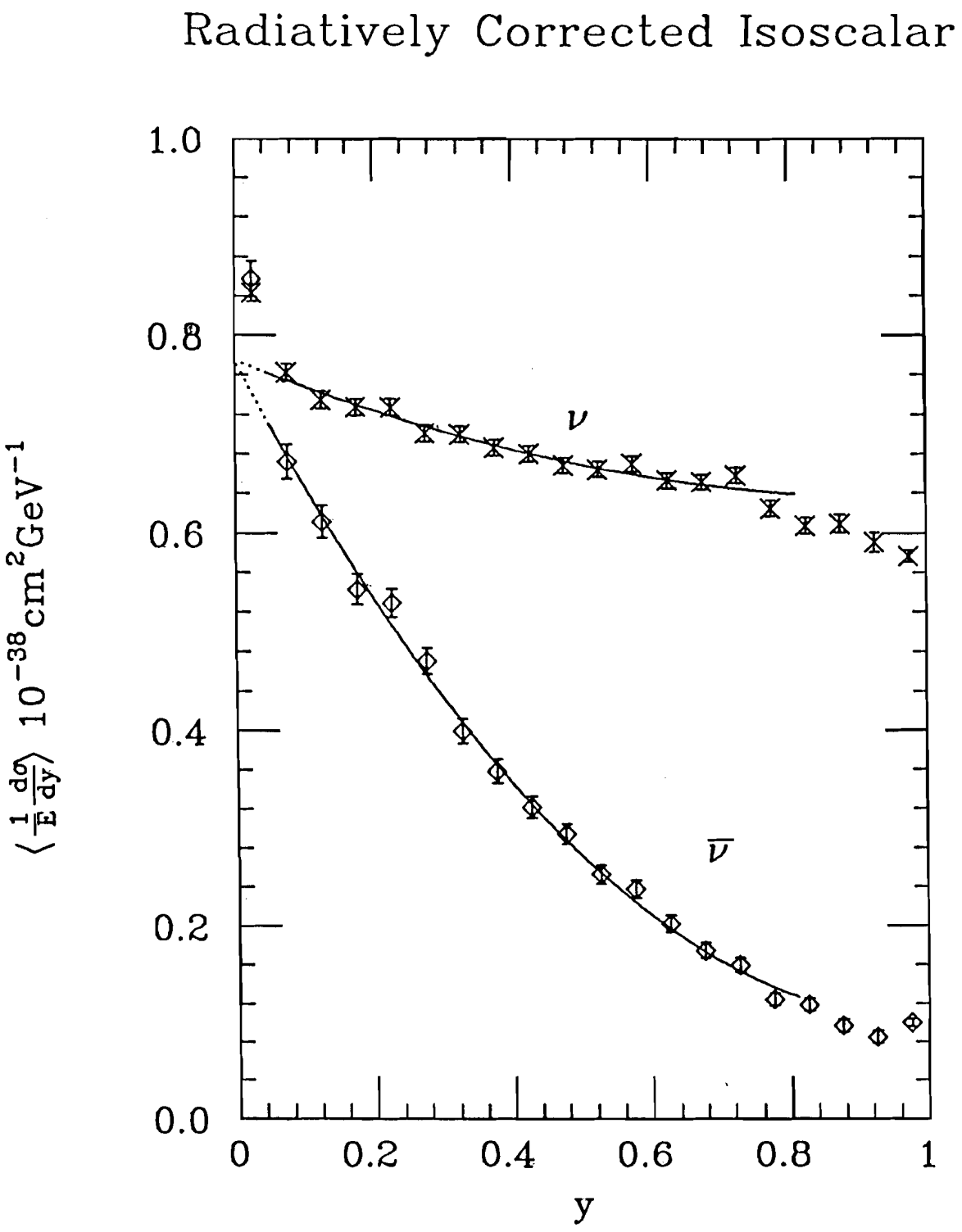
Radiatively Corrected Isoscalar
1.0
0.8
0.6
0.4
0.2
0.0
0
0.2
0.4
0.6
0.8
1
y
$\langle \frac{1}{E}\frac{d\sigma}{dy} \rangle$ 10^{-38}cm^{2}GeV^{-1}
ν
$\bar{\nu}$

Figure A.4

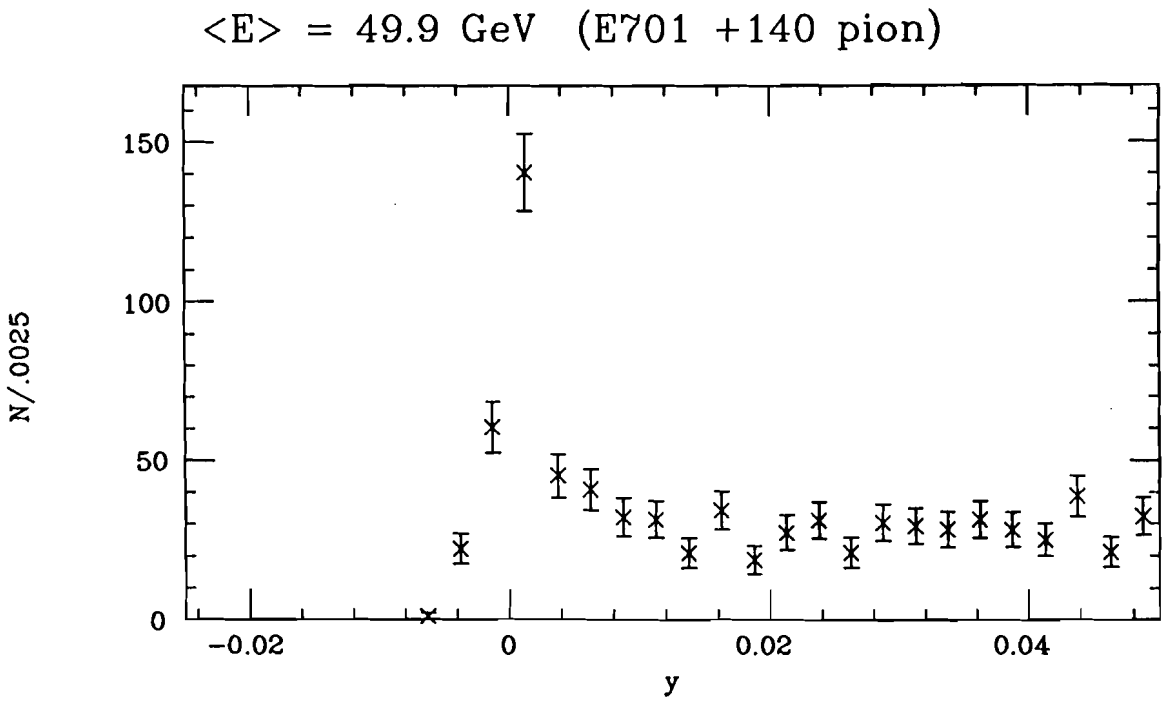

Figure A.5a

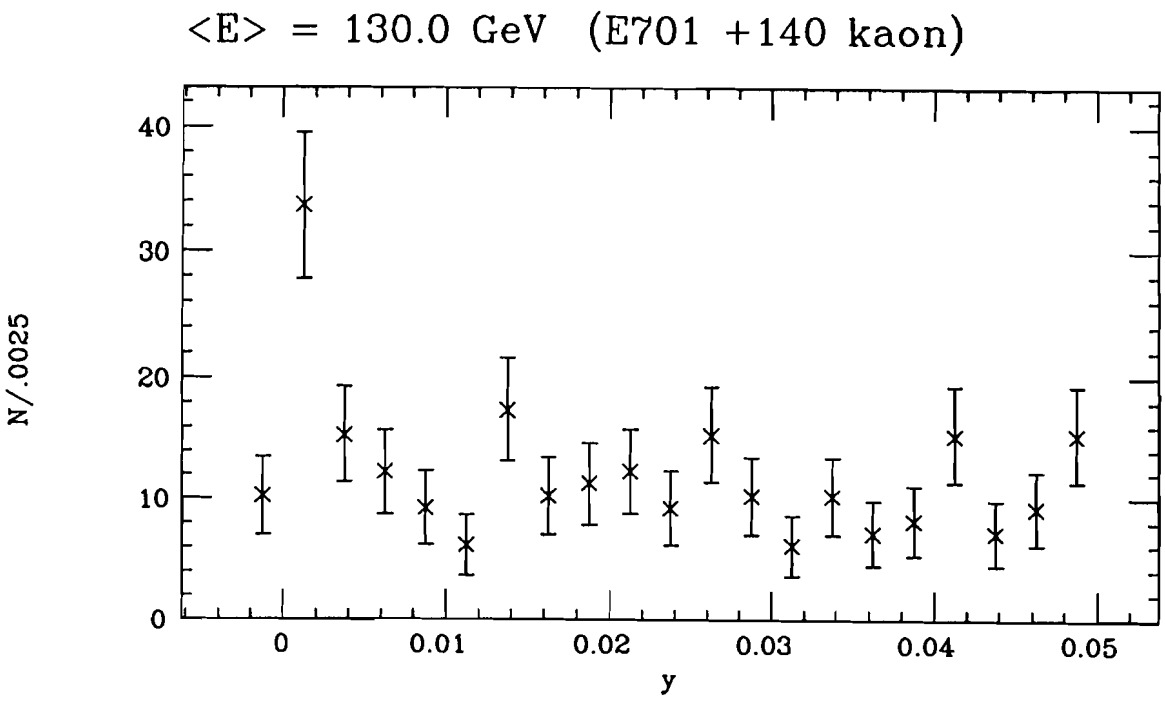

Figure A.5b

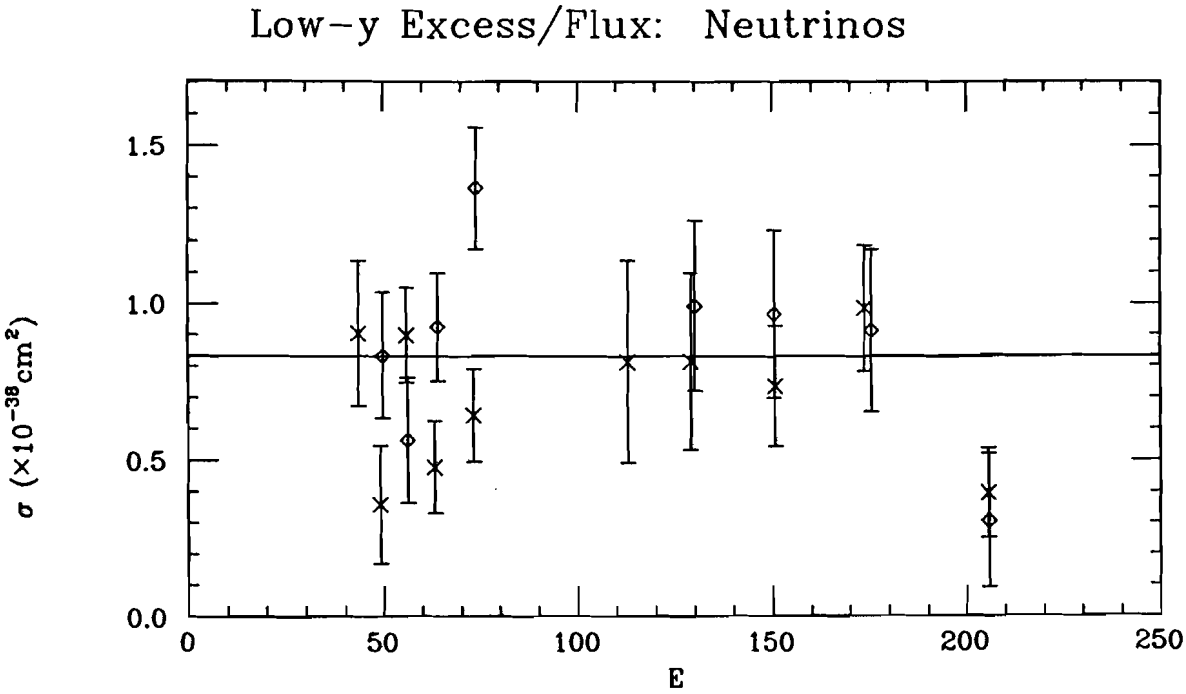

Figure A.6a

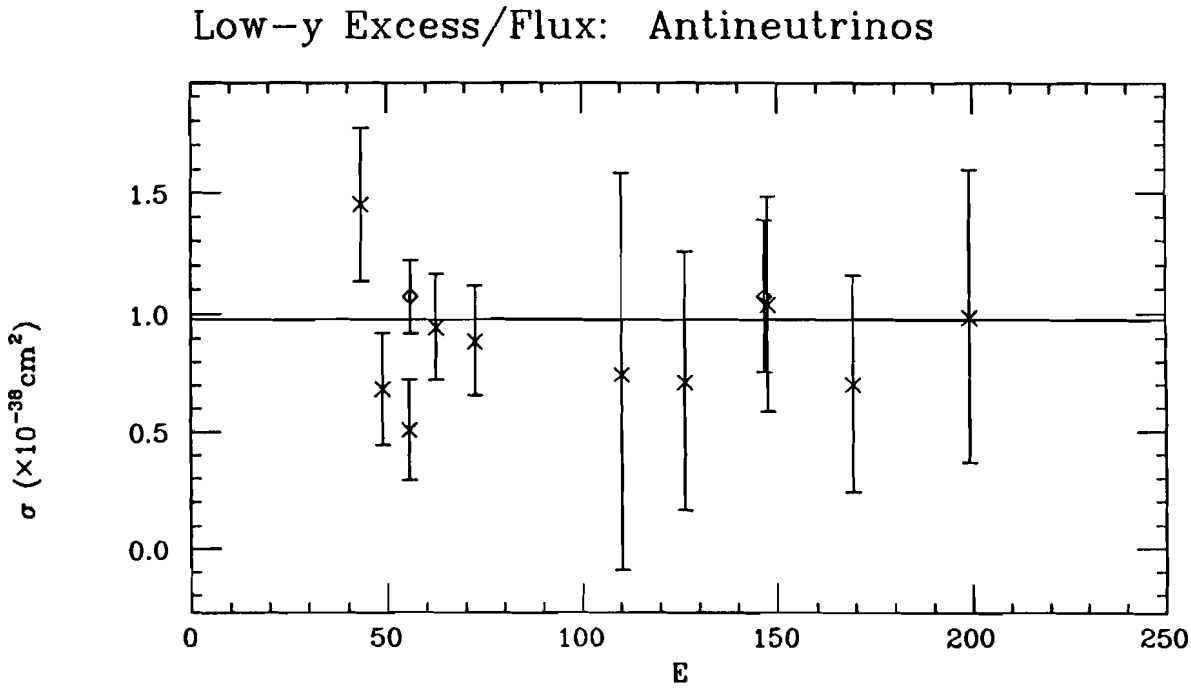

Figure A.6b

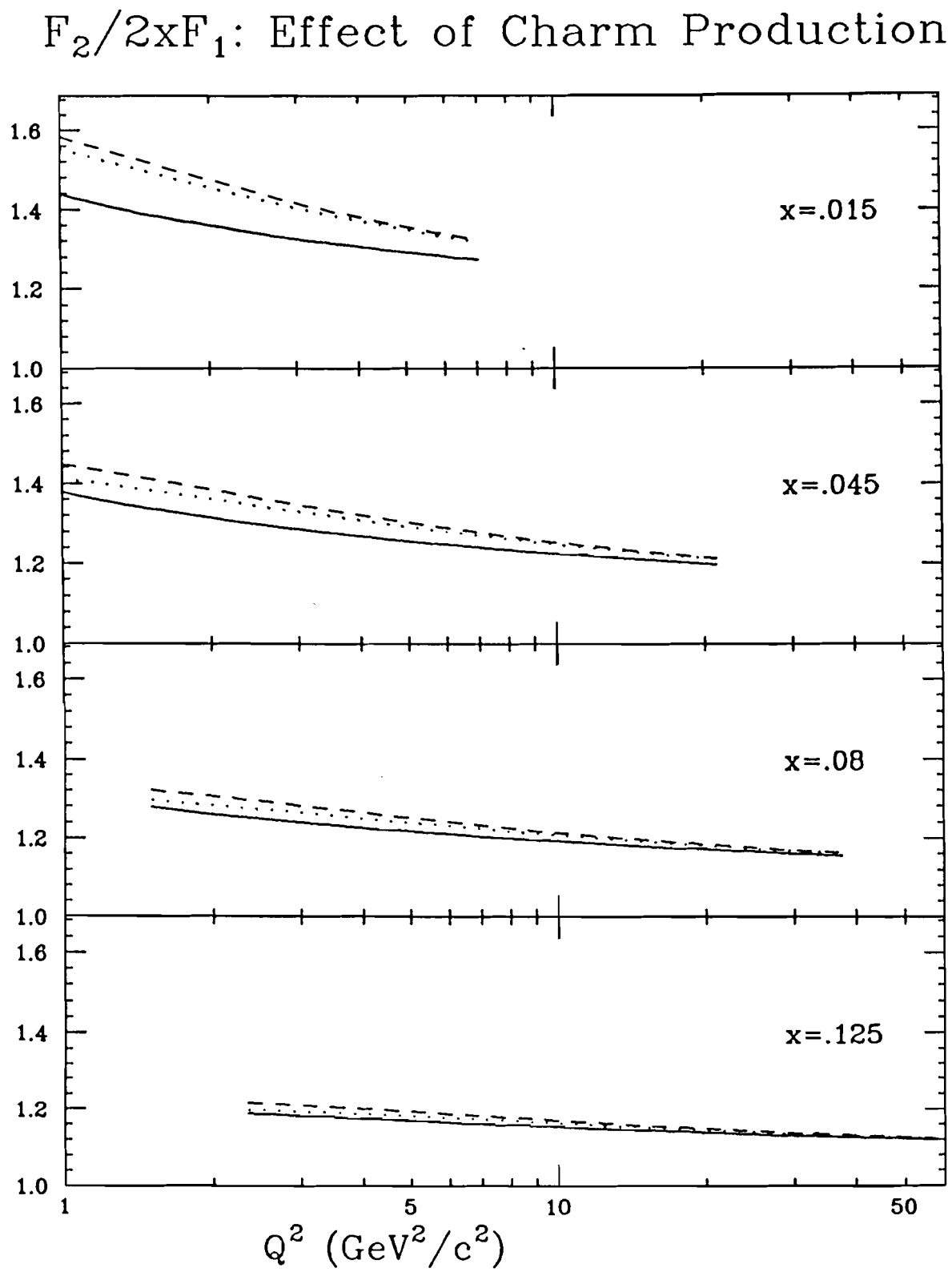
$F_2/2xF_1$: Effect of Charm Production
1.6
1.4
1.2
1.0
x=.015
x=.045
x=.08
x=.125
1
5
10
50
Q^2 (GeV^2/c^2)

Figure C.1